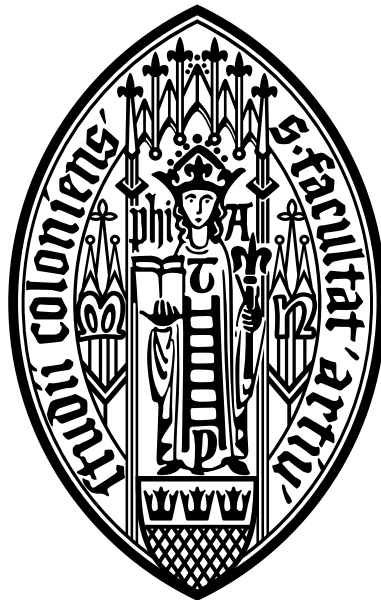


**Coulomb excitation of doubly-magic  $^{132}\text{Sn}$  at HIE-ISOLDE  
and development of escape-suppression shields for the  
MINIBALL spectrometer**

**Inaugural-Dissertation**

zur

Erlangung des Doktorgrades  
der Mathematisch-Naturwissenschaftlichen Fakultät  
der Universität zu Köln



Vorgelegt von

**David Pawel Rosiak**  
aus Solingen

Köln 2018

**Berichterstatter:**

Prof. Dr. Peter Reiter  
Prof. Dr. Jan Jolie

**Tag der mündlichen Prüfung:**

16. Juli 2018



# Abstract

Collective properties of the exotic doubly-magic nucleus  $^{132}\text{Sn}$ , in particular the first excited  $2^+$  and  $3^-$  states, were investigated via safe Coulomb excitation. The experiment was performed in October 2016 at the HIE-ISOLDE facility at CERN. The challenging Coulomb excitation was realized utilizing the new commissioned stage 1 HIE-ISOLDE accelerator in combination with the high resolution and high efficient MINIBALL array. The radioactive  $^{132}\text{Sn}$  beam was post accelerated up to 5.5 MeV/u and guided onto a  $3.1 \text{ mg/cm}^2$  thick  $^{206}\text{Pb}$  target. Projectile and target deexcitation were recorded in coincidence with the scattered nuclei to reduce the amount of background radiation in the  $\gamma$ -ray spectra and to perform the Doppler correction.  $B(E2)$ ,  $B(E3)$  and  $B(E1)$  values were determined for the corresponding transitions  $0_{\text{g.s.}}^+ \rightarrow 2_1^+$ ,  $0_{\text{g.s.}}^+ \rightarrow 3_1^-$ , and  $2_1^+ \rightarrow 3_1^-$  of  $^{132}\text{Sn}$ . The final reduced transition strengths are  $B(E2 \uparrow; 0_{\text{g.s.}}^+ \rightarrow 2_1^+) = 0.0869 \pm 0.019 \text{ e}^2\text{b}^2$ ,  $B(E3 \uparrow; 0_{\text{g.s.}}^+ \rightarrow 3_1^-) = 0.11 \pm 0.035 \text{ e}^2\text{b}^3$  and  $B(E1 \uparrow; 2_1^+ \rightarrow 3_1^-) = (9.05 \pm 3.04) \times 10^{-6} \text{ e}^2\text{b}$ . These experimental results were compared to state-of-the-art large-scale shell-model calculations, a relativistic random phase approximation and a random phase approximation calculation.

The second part of the present thesis deals with the manufacturing process and the first performance tests of the prototype escape-suppression-shield detector for the MINIBALL spectrometer. Measurements were performed with a stand-alone escape-suppression detector and with the assembled system in combination with a MINIBALL triple cluster. The performance of the combined system was quantified via the peak-to-total ratio of measured  $^{60}\text{Co}$   $\gamma$ -ray spectra. A comparison between the achieved results of the prototype detection system and prior performed GEANT4 simulations is presented. The achieved peak-to-total value of 41% with source measurements of the prototype detector is in good agreement with the predicted value of 44%.

# Zusammenfassung

Die kollektiven Eigenschaften des exotischen doppelt magischen Kerns  $^{132}\text{Sn}$ , insbesondere der ersten beiden angeregten Zustände  $2^+$  und  $3^-$ , wurden mit Hilfe von sicherer Coulomb Anregung untersucht. Das Experiment wurde im Oktober 2016 an der HIE-ISOLDE Einrichtung am CERN durchgeführt. Der neu in Betrieb genommene HIE-ISOLDE Beschleuniger (stage 1) in Kombination mit dem hochauflösenden und hocheffizienten MINIBALL Spektrometer ermöglichte die Durchführung des anspruchsvollen Experimentes. Damit konnte der radioaktive  $^{132}\text{Sn}$  Strahl auf bis zu 5.5 MeV/u nachbeschleunigt und auf ein  $3.1 \text{ mg/cm}^2$  dickes Target geleitet werden. Projektil- und Targetanregung wurden in Koinzidenz mit den gestreuten Teilchen detektiert, um die  $\gamma$ -Quanten der Coulomb-Anregung zu selektieren und um eine Doppler-Korrektur der emittierten Photonen durchzuführen.  $B(E2)$ ,  $B(E3)$  und  $B(E1)$  Werte wurden für die entsprechenden Übergänge  $0_{\text{g.s.}}^+ \rightarrow 2_1^+$ ,  $0_{\text{g.s.}}^+ \rightarrow 3_1^-$ , und  $2_1^+ \rightarrow 3_1^-$  in  $^{132}\text{Sn}$  bestimmt. Die reduzierten Übergangsstärken sind  $B(E2 \uparrow; 0_{\text{g.s.}}^+ \rightarrow 2_1^+) = 0.0869 \pm 0.019 \text{ e}^2\text{b}^2$ ,  $B(E3 \uparrow; 0_{\text{g.s.}}^+ \rightarrow 3_1^-) = 0.11 \pm 0.035 \text{ e}^2\text{b}^3$  und  $B(E1 \uparrow; 2_1^+ \rightarrow 3_1^-) = (9.05 \pm 3.04) \times 10^{-6} \text{ e}^2\text{b}$ . Die experimentell bestimmten Werte wurde mit modernen Schalenmodellrechnungen, einer relativistischen Random-Phase-Approximation und einer Random-Phase-Approximation verglichen.

Der zweite Teil der vorliegenden Arbeit beschreibt die Fertigung und die ersten Performance-Messungen des "Escape-Suppression Shields" (ESS) für das MINIBALL Spektrometer. Dafür wurde der ESS als auch die Kombination aus ESS und MINIBALL-Cluster-Detektor in der endgültigen Konfiguration vermessen und charakterisiert. Die Leistungsfähigkeit des kombinierten Systems wurde anhand des Peak-zu-Untergrund Verhältnisses von  $^{60}\text{Co}$  Spektren quantifiziert. Die erzielten Resultate wurden mit zuvor durchgeführten GEANT4 Simulationen verglichen. Der mit dem Prototypen-Detektor gemessene Peak-zu-Untergrund Wert von 41% ist in guter Übereinstimmung mit dem vorhergesagten Wert von 44%.

# Contents

<b>I. Coulomb excitation of doubly-magic <math>^{132}\text{Sn}</math></b>	<b>9</b>
<b>1. Nuclear structure and spectroscopic observables</b>	<b>11</b>
1.1. Magic numbers . . . . .	11
1.2. Nuclear shell model . . . . .	14
1.3. Experimental observables . . . . .	17
1.3.1. Binding energies . . . . .	17
1.3.2. Proton and neutron separation energies . . . . .	17
1.3.3. Electric quadrupole moment . . . . .	17
1.3.4. Transition strength . . . . .	20
1.4. Coulomb excitation . . . . .	22
<b>2. Physics case</b>	<b>32</b>
2.1. Properties of $Z = 50$ and $N = 82$ nuclei . . . . .	32
2.2. Previous Coulomb excitation of $^{132}\text{Sn}$ . . . . .	39
<b>3. Radioactive-beam physics at ISOLDE, CERN</b>	<b>41</b>
3.1. The HIE-ISOLDE facility . . . . .	43
3.1.1. Radioactive-ion beam production . . . . .	45
3.1.2. Ion sources . . . . .	46
3.1.3. Mass separators . . . . .	48
3.1.4. Post accelerator . . . . .	50
3.1.5. Beam time structure . . . . .	58
3.1.6. MINIBALL setup . . . . .	59
<b>4. Experimental details of experiment IS551</b>	<b>64</b>
<b>5. Data analysis</b>	<b>65</b>
5.1. Data acquisition and pre-processing . . . . .	65
5.2. Detector calibration . . . . .	66
5.2.1. DSSSD segment identification . . . . .	66
5.2.2. DSSSD energy calibration . . . . .	67
5.2.3. Energy calibration of MINIBALL . . . . .	76
5.2.4. Efficiency calibration of MINIBALL . . . . .	79
5.3. Doppler correction . . . . .	80

5.4. Kinematic conditions . . . . .	87
5.5. Particle- $\gamma$ coincidence . . . . .	89
5.6. Beam composition . . . . .	91
<b>6. Results</b>	<b>104</b>
6.0.1. Selection of projectile and target-like nuclei . . . . .	104
6.0.2. Yield calculation . . . . .	113
<b>7. Comparison with theoretical results</b>	<b>119</b>
7.1. Theoretical models . . . . .	119
7.1.1. Relativistic Quasiparticle-vibration coupling . . . . .	119
7.1.2. Hybrid configuration mixing model . . . . .	120
7.1.3. Shell-model calculation based on $^{110}\text{Zr}$ . . . . .	120
7.1.4. Monte Carlo shell-model calculation . . . . .	121
7.2. Comparison . . . . .	123
7.3. Summary and Outlook . . . . .	128
 <b>II. Development of escape-suppression shields for the MINI- BALL spectrometer</b>	 <b>131</b>
<b>8. Introduction</b>	<b>133</b>
<b>9. Geant4 simulations</b>	<b>135</b>
9.1. MINIBALL escape-suppression shield . . . . .	135
<b>10. Escape-suppression shield prototype</b>	<b>138</b>
10.1. Escape-suppression shield design . . . . .	138
10.1.1. BGO crystals . . . . .	138
10.1.2. BGO housing . . . . .	140
10.1.3. Photomultipliers for the escape-suppression shield . . . . .	141
10.1.4. Mechanics holding structure of ESS detectors . . . . .	143
10.2. Experimental setup . . . . .	145
10.2.1. BGO signal processing . . . . .	146
10.2.2. Electronics . . . . .	149

<b>11. Performance measurements with the ESS prototype</b>	<b>151</b>
11.1. Escape-suppression shield . . . . .	151
11.2. MINIBALL escape-suppression detector . . . . .	153
11.2.1. Coincidence mode . . . . .	153
11.2.2. Free run mode . . . . .	157
11.3. Summary and Outlook . . . . .	161
 <b>Bibliography</b>	 <b>165</b>
 <b>List of figures</b>	 <b>183</b>
 <b>List of tables</b>	 <b>186</b>
 <b>Acknowledgements</b>	
 <b>Erklärung zur Dissertation</b>	
 <b>Curriculum vitae</b>	



## Part I.

Coulomb excitation of doubly-magic  $^{132}\text{Sn}$





# 1. Nuclear structure and spectroscopic observables

Even today, the nuclear force and nuclear interactions are not completely understood. For a better understanding of atomic nuclei and the nuclear force one approach is to study the properties of nuclei depending on their proton-neutron configuration, which is known as nuclear structure. Doubly-magic nuclei are lighthouses along the whole chart of nuclei. Their basic properties like masses, binding energies and excited states are essential for a detailed understanding and theoretical description in a vast range of the nuclear chart. The doubly-magic nucleus  $^{132}\text{Sn}$  and its vicinity provide essential reference points for all theoretical approaches in order to improve their forecasting power for nuclei which are not yet accessible.

## 1.1. Magic numbers

One of the most important discoveries, during the pioneering studies of atomic nuclei and their nuclear structure, was that nuclei with specific numbers of protons or neutrons (semi-magic nuclei) or both (doubly-magic nuclei) exhibit remarkable properties, e.g. large binding and excitation energies [1, 2]. At this time, no theory was available to explain the origin of these phenomena. Thus, these configurations were called “magic numbers”. The magic numbers are  $Z = 2, 8, 20, 28, 50, 82$  and  $N = 2, 8, 20, 28, 50, 82, 126$ . It was observed that the trend of the separation energy for either protons or neutrons is generally smooth, except at certain specific nucleon numbers [2]. This is illustrated in Figure 1 where the two-neutron separation energy in MeV of O, Ca, Kr, Cd, Ce, Hf, Pt, Pb and U along their isotopic chains is shown. The separation energy exhibits discrete jumps at isotopes with neutron magic numbers; the same is observed for nuclei with proton magic numbers. Moreover, the energy of the first excited state of nuclei with magic numbers is much higher compared to their neighbors. This behavior is representatively shown, along the isotopic chain of lead, in Fig. 2 (a). Figure 2 (b) illustrates this property along the isotopic chains of nuclei in the vicinity of tin. The increased excitation energy for  $N = 82$  is caused by the magic configuration of neutrons in these nuclei. Furthermore, nuclei with configurations that correspond to magic numbers have more stable isotopes and isotones compared to their neighbors.

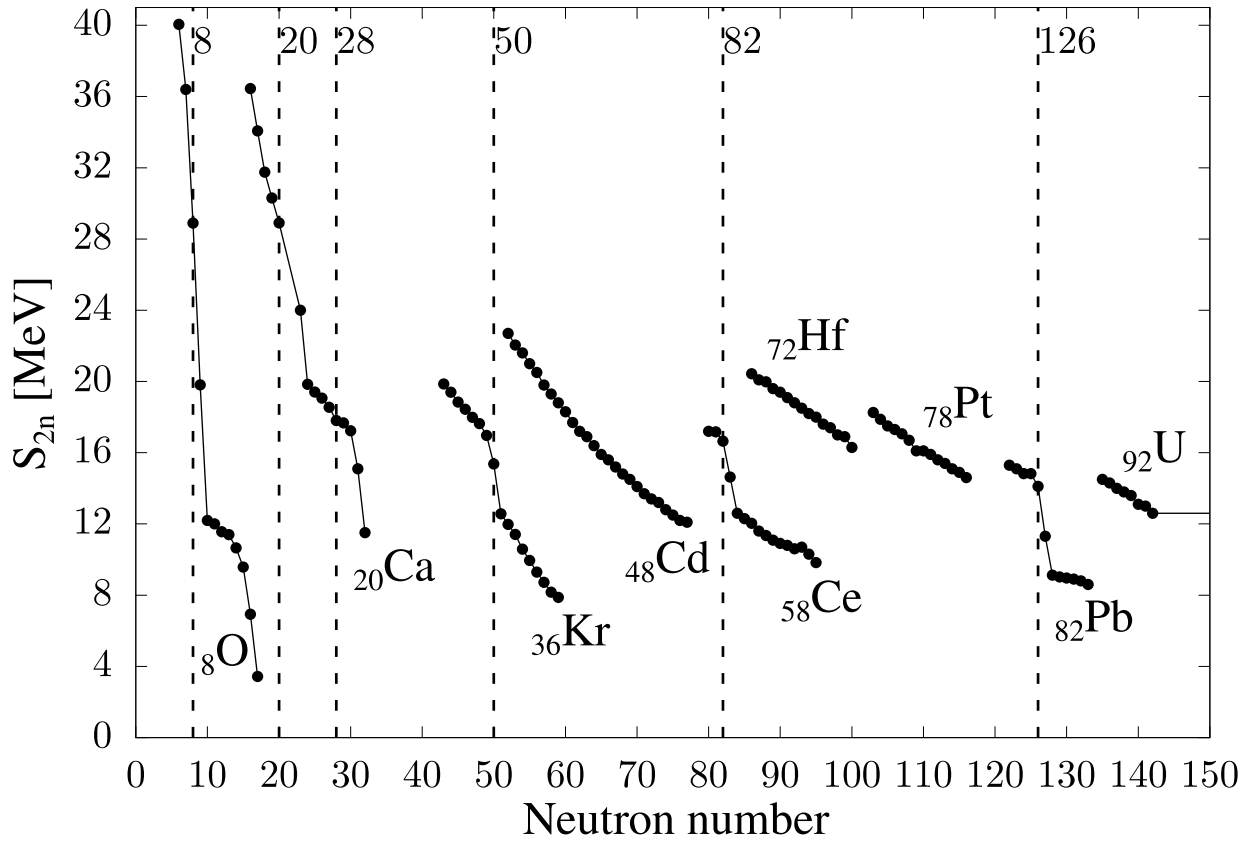


**Figure 1:** Two-neutron separation energy for isotopic chains including nuclei with magic neutron configuration. At the classical magic numbers, sharp changes of the two-neutron energy can be observed. Otherwise the trend of the two-neutron separation energy is smooth. Data taken from Ref. [3].

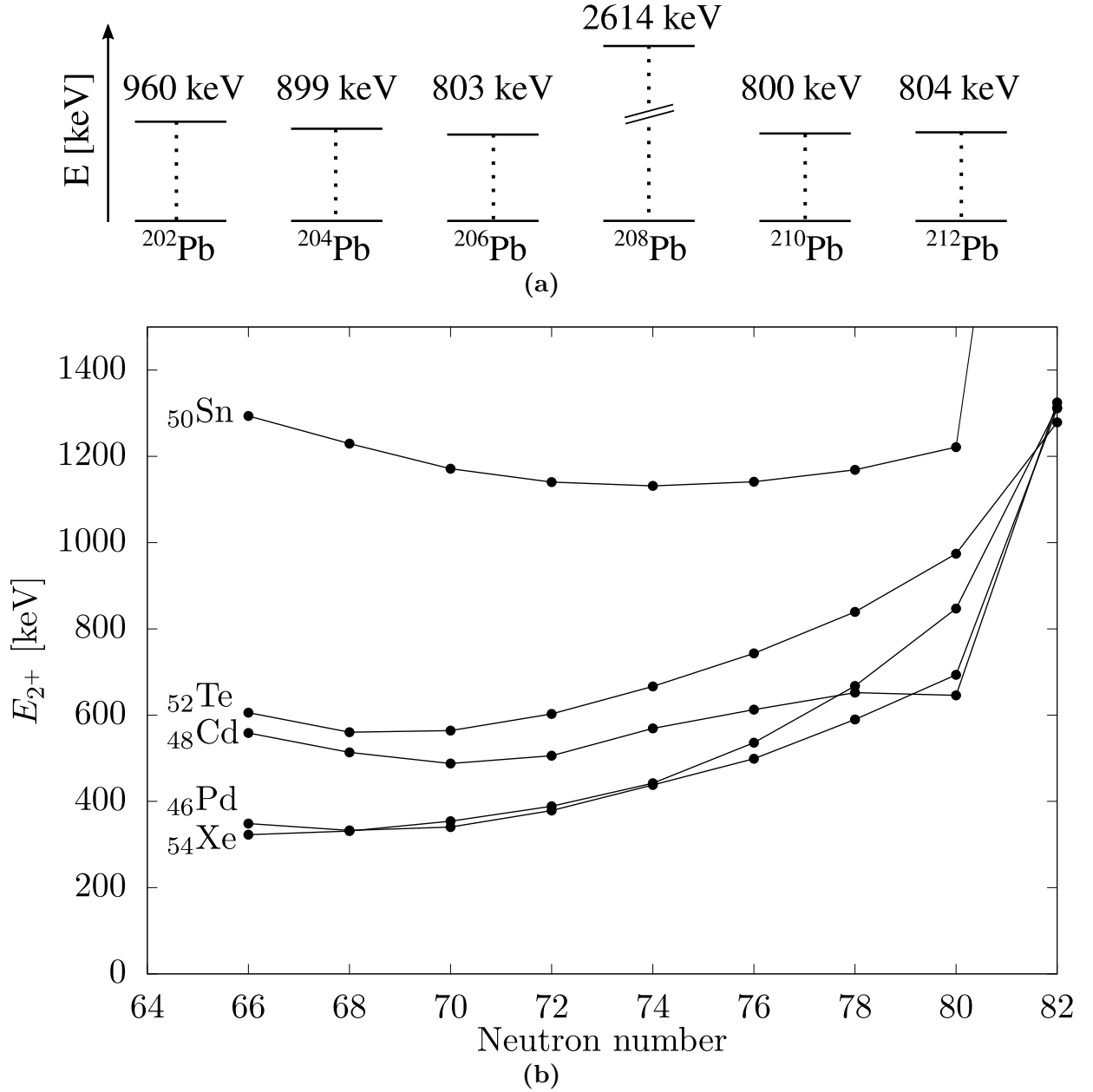


**Figure 2:** (a) Excitation energies for the first excited  $2_1^+$  state along the lead chain, including the doubly-magic  $^{208}\text{Pb}$ . (b) First excited  $2_1^+$  state for isotopes of Sn, Te, Xe, Cd, Pd. For the  $Z = 50$  shell closure (tin) the excitation energy is increased compared to the isotopes of the even-proton neighbors. The excitation energy of the doubly-magic tin amounts to  $\sim 4$  MeV. Data taken from Ref. [4].

## 1.2. Nuclear shell model

Atomic nuclei are many-body quantum systems, and can be partially compared to the electron cloud of an atom. The difference between this two systems, is the absence of a central potential inside a nucleus. Nevertheless, it is possible to treat protons and neutrons mathematically in a similar way, like it is done for the description of the electrons. For a nucleus with  $A$  interacting nucleons, the Hamiltonian can be written as a composition of kinetic energy and the interaction between all the nucleons. For protons also the Coulomb interactions has to be considered.

$$H = \sum_{i=1}^A T_i + \sum_{\substack{i,j=1 \\ i < j}}^A V_{ij} \quad (1.1)$$

In contrast to the electrons, the nucleon-nucleon interaction is not known from basic principles. However, binding-energy studies revealed that the nuclear interaction is predominantly effective between two nucleons (two body interaction). This allows to describe the Hamiltonian of a nucleus with a nucleon-nucleon interaction  $V_{ij}$ :

$$H = \sum_{i=1}^A T_i + \sum_{\substack{i,j=1 \\ i < j}}^A V_{ij} = \sum_{i=1}^A (T_i + V_i) + \left( \sum_{\substack{i,j=1 \\ i < j}}^A V_{ij} - \sum_{i=1}^A V_i \right) = H_0 + H_R, \quad (1.2)$$

where  $V_i$  is the mean field potential of the  $i$ th nucleon. For each nucleon the single-particle wave function  $\phi_i$  and the corresponding energy value  $\epsilon_i$  can be determined. A special solution for  $H_0$  can be written as,

$$\psi = \prod_{i=1}^A \phi_i(\vec{r}_i). \quad (1.3)$$

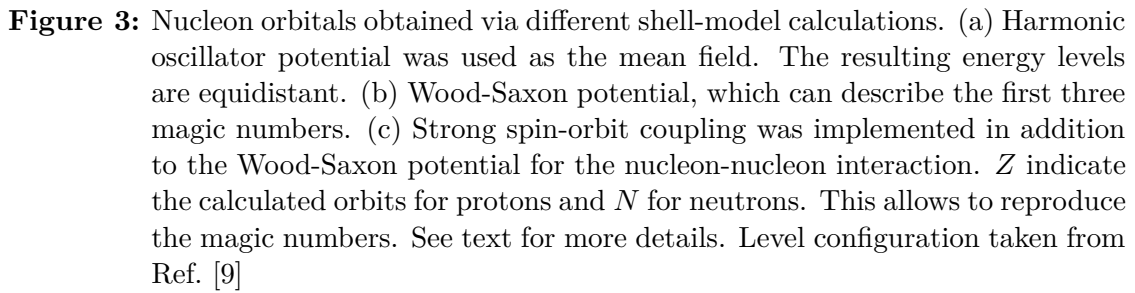
Protons and neutrons are fermions, thus they have to fulfill the Pauli-Principle. As a consequence, the complete solution of equation 1.2 has to be anti-symmetric. This can be achieved by the Slater-Determinant

$$\psi = \frac{1}{\sqrt{N!}} \text{Det}[\phi_i(\vec{r}_i)] \quad (1.4)$$

It can be shown that  $H_0$  is the dominant contribution to the energy spectrum and  $H_R$  is a small residual interaction [5]. In general  $H_0$  can be interpreted as the description of  $A$  non-interacting single particles moving in an average potential produced by all  $A$  nucleons. The residual interaction  $H_R$  comprises the nucleon-nucleon interactions neglected by the simple approach of  $H_0$ . For a theoretical treatment of the residual interaction see Ref. [5–7]. Thus, this approximation fits better for nuclei with closed shells rather than mid-shell nuclei where many valence nucleons contribute to the final configuration. The first calculations for the mean-field potential were done with a harmonic oscillator potential and the Wood-Saxon potential. These approximations were able to predict first energy spectra and avoided the issue of the repulsive feature of the nuclear force. However, the predictions were not able to reproduce the phenomena of the discovered higher magic numbers. In 1949 Haxel, Jensen, Suess [1], and independently Maria Goeppert-Mayer [2, 8], proposed a strong spin-orbit coupling as an additional term for the nucleon-nucleon interaction, as it is done for the electrons in an atom.

$$V_i = V(\vec{r}) + V_{ls}(\vec{r})(\vec{l} \cdot \vec{s}) \quad (1.5)$$

Where  $V(\vec{r})$  is the central potential,  $V_{ls}(\vec{r})$  is a radial potential, which is basically the amplitude of the spin-orbit coupling  $(\vec{l} \cdot \vec{s})$  with  $\vec{l}$  the angular momentum and  $\vec{s}$  the spin of the nucleon. This additional interaction enabled the theory to predict the nuclear magic numbers “2,8,20,28,50,82,126” and in addition other properties (spins and magnetic moments) of many nuclei available at this time [1, 8]. Therefore, this theory was called “nuclear shell model“. This modified nucleon-nucleon interaction induces an energy splitting for each state with total angular momentum  $j=l+s$ . Therein  $l$  is the orbital angular momentum and  $s$  is the spin, which can be parallel  $(+\frac{1}{2})$  or anti-parallel  $(-\frac{1}{2})$  to the orbital angular momentum. Energy spectra for the three different potentials are shown in Figure 3. Only the first three magic numbers can be reproduced by the Wood-Saxon potential. The energy spectra for protons and neutrons with the spin-orbit coupling look almost identical, as long as the Coulomb interaction is not taken into account. However, recent experimental and theoretical findings indicate that magic numbers are not constant and valid for all nuclei. For more exotic nuclei with high  $N/Z$  ratios new shell closures arise [10–13] indicating that the configuration of spherical and more stable nuclei is related to the neutron-proton ratio.



### 1.3. Experimental observables

The previous section indicated that there are still open questions in the understanding of nuclear structure, especially for exotic nuclei far from the so-called "valley of stability". The following sections focus on important observables that can be deduced from experiments and provide a better understanding of nuclear structure and nuclear force.

#### 1.3.1. Binding energies

For the identification of shell and sub-shell closures primarily nuclear masses and binding energies are used. Figure 4 illustrates the difference between measured masses and results of the Bethe-Weizsäcker mass formula. The largest deviations are observed for the magic numbers, irrespective of the nucleon type. The reason is the increased binding energy for nuclei towards shell or sub-shell closures.

#### 1.3.2. Proton and neutron separation energies

The two-nucleon separation energy is calculated from the binding energy  $S_{2n} = BE(A, Z) - BE(A - 2, Z)$  and  $S_{2p} = BE(A, Z) - BE(A - 2, Z - 2)$ . To compare the separation energy of neighboring nuclei the two-neutron and two-proton separation energy is considered, in order to neglect the effect of the pairing energy term in the Bethe-Weizsäcker formula. As already seen in Figure 1, nuclei with magic numbers show larger separation energies compared to their next neighbor nuclei. The drop of the two-proton/neutron separation energy and the high excitation energies of the first excited states for magic numbers can be explained by shell closures of these nuclei (see Figure 3 (c)). Separation energies provide crucial information about the location of shell and sub-shell closures along the chart of nuclei.

#### 1.3.3. Electric quadrupole moment

The nuclear shell model yields best results for nuclei with nearly or completely filled shells. Nucleons of closed shells occupy all possible magnetic sub-states and lead to a spherical density distribution of the nucleus. The nuclear electrical quadrupole moment  $Q$  is sensitive to the charge distribution of the nuclear state. Therefore,  $Q$  vanishes for nuclei with magic numbers and the absolute value increases towards mid-shell nuclei. Further information can be deduced from the sign of the electrical quadrupole moment.  $Q < 0$  corresponds to a oblate shape of the nuclei, in a simple model it is related to particles outside of closed

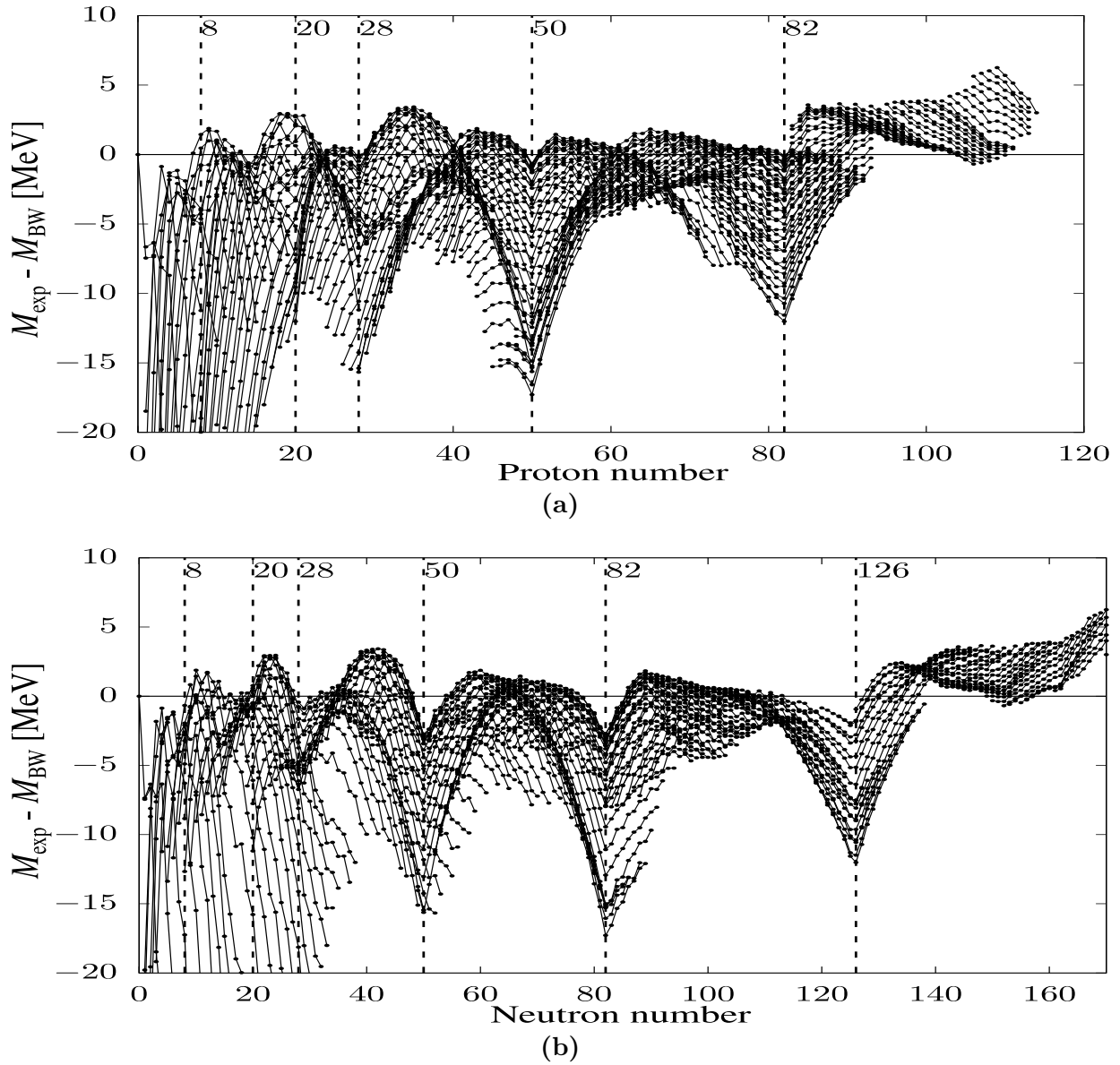


**Figure 4:** Mass difference between experimental measured ( $M_{\text{exp}}$ ) and calculated masses with the Bethe-Weizacker formula ( $M_{\text{BW}}$ ), for all measured isotones and isotopes. The largest deviations occur at magic numbers, due to the high binding energies at closed shells. Experimental values taken from Ref. [3].



shells.  $Q > 0$  corresponds to prolate shaped nuclei, induced by holes of fully filled shells. Thus,  $Q$  is the quantum mechanical representation of the nuclear charge distribution, including the nuclear spin  $I$  and the projection of  $I$  onto the z-direction. This description of the nuclear deformation is illustrated in Figure 5. The quantity  $\frac{Q}{ZR^2}$  is a measure for the nuclear deformation independent of the size of a nucleus. At all magic numbers the electric quadrupole moment reduce to zero and the deformation changes from prolate to oblate shaped nuclei. This behavior agrees with the aforementioned simple particle picture for the deformation. Therein, additional particles or holes in closed nuclei are related to the origin of nuclei deformation. In Figure 5 additional zero crossing points, besides the magic numbers, with  $Q > 0$  to  $Q < 0$  can be observed.

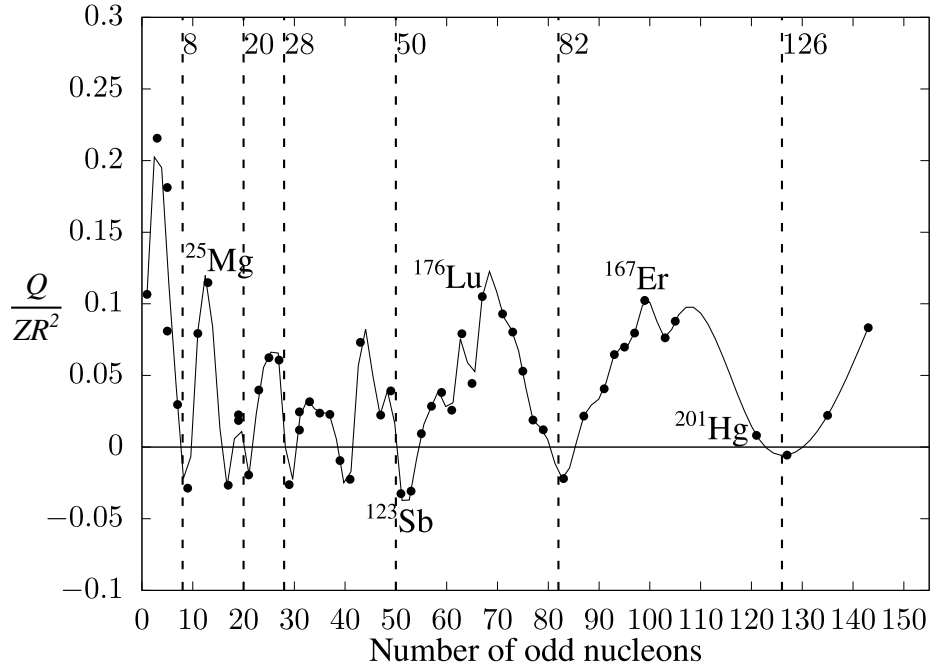


**Figure 5:** Quadrupole deformation of nuclei. The quantity  $\frac{Q}{ZR^2}$  is a size independent measure for the deformation of the nuclei with respect to a spherical nuclei. The deformations are shown for different nuclei with odd number of protons or odd number of neutrons. Magic numbers are illustrated by dashed lines. At the magic numbers the deformation get zero and a change from prolate to oblate shape is observed. This behavior is an indication for fully closed shells and, therefore, for magic numbers. Data taken from Ref. [14].

As mentioned before, new shell closures arise for nuclei far from stability. This was observed for neutron-rich nitrogen, oxygen and fluorine nuclei with  $N = 16$  [15, 16]. Nuclei with forty protons or neutrons, also show properties of a shell closure [17]; however, forty is not a classical magic number.

### 1.3.4. Transition strength

In section 1.1, energies of first excited states in nuclei demonstrated a clear increase at magic numbers. In addition to excitation energies also transition strengths of the electromagnetic radiation between nuclear states yield useful information about the underlying nuclear structure [18, 19]. Both quantities, excitation energy  $E(I_f)$  and reduced transition strength  $B(\sigma\lambda; I_i \rightarrow I_f)$ , provide a signature for nuclear collectivity in even-even nuclei [9, 20].

The variables  $I_i$  and  $I_f$  denote the total angular momentum of the initial and final state of the nucleus, respectively. The character of the electromagnetic transition is represented by  $\sigma$  and can be electric E or magnetic M. The angular momentum carried by the emitted radiation is described by  $\lambda$ . The parity of electric multipole transition  $E\lambda$  is given by  $(-1)^\lambda$  and for magnetic multipole transition  $M\lambda$  the parity is determined by  $(-1)^{\lambda+1}$ . Therefore, even electric multipole transitions conserve the parity, whereas odd electric multipole transitions change the parity. For magnetic multipole transitions it is vice versa. Most low-lying nuclear states decay via electromagnetic processes i.e.  $\gamma$ -ray emission. These transitions can be described by reduced matrix elements  $\langle \Psi_f | |\mathfrak{M}(\sigma\lambda)| | \Psi_i \rangle$ , which provide information on the wavefunction of the initial and final states [18, 19, 21]. Reduced matrix elements are identical for exciting and de-exciting transitions with the same electromagnetic multipole operator  $\mathfrak{M}(\sigma\lambda)$ . The reduced transition probabilities are given by

$$B(\sigma\lambda, I_i \rightarrow I_f) = \frac{1}{2I_i + 1} \left| \langle \Psi_f | |\mathfrak{M}(\sigma\lambda)| | \Psi_i \rangle \right|^2 \quad (1.6)$$

with  $\Psi_i$  and  $\Psi_f$  the initial and final state of the transition, respectively [9]. Reduced transition strengths for excitation and de-excitation, for the same set of states, are related by

$$B(\sigma\lambda, I_i \rightarrow I_f) = \frac{2I_f + 1}{2I_i + 1} B(\sigma\lambda, I_f \rightarrow I_i). \quad (1.7)$$

The reduced transition strength for electric multipole character is typically given in units of  $e^2 b^\lambda$  and for magnetic multipole transitions  $\mu_N^2 b^{\lambda-1}$  units are used. Thus,  $e$  denotes the electric charge and  $\mu_N$  the nuclear magneton. Complementary to the "direct" measurement of the transition strength via e.g. Coulomb excitation [22], it is possible to measure the lifetime  $\tau$  of an excited state. From the lifetime it is possible to determine the reduced transition strength. The partial  $\gamma$ -decay rate of the emission of a  $\gamma$  ray of multipole  $\lambda$ ,

from the initial state  $I_i$  into the final state  $I_f$  can be calculated with

$$T(\sigma\lambda; I_i \rightarrow I_f) = \frac{8\pi(\lambda+1)}{\lambda\hbar[(2\lambda+1)!!]^2} \left(\frac{E_\gamma}{\hbar c}\right)^{2\lambda+1} \times B(\sigma\lambda; I_i \rightarrow I_f). \quad (1.8)$$

If the decay, of the initial state into several final states is possible, these states have to be taken into account. Furthermore, the decay could also proceed via electron conversion. Therefore, the conversion coefficient  $\alpha(\lambda)$  has to be considered as well. Thus, the lifetime of the state  $I_i$  can be described by:

$$\tau(I_i) = \left( \sum_{I_f} \sum_{\lambda} T(\sigma\lambda; I_i \rightarrow I_f) [1 + \alpha(\lambda)] \right)^{-1} \quad (1.9)$$

If only one final state and one multipole transition is possible, the reduced transition strength can be determined from the lifetime. For almost all even-even nuclei the first excited state is a  $2^+$  state and, therefore, a  $\gamma$ -ray decay only via a E2 transition into the  $0^+_{\text{g.s.}}$  ground state is possible. In this special case the reduced transition strength can be written as:

$$B(E2; 2^+ \rightarrow 0^+) = \frac{8.16 \times 10^{-24}}{[1 + \alpha(E2)] E_\gamma^5 \tau(2^+)}. \quad (1.10)$$

The number of nucleons which contribute to an excitation of the nucleus can be roughly estimated with the so called Weisskopf units (W.u.) [9]. Therefore, the  $B(E\lambda)$  and  $B(M\lambda)$  values are reevaluated in the following way:

$$B(E\lambda; I_i \rightarrow I_f)_{\text{Weisskopf}} = \frac{1.2^{2\lambda}}{4\pi} \left(\frac{3}{\lambda+3}\right)^2 A^{\frac{2\lambda}{3}}, \quad (1.11)$$

$$B(M\lambda; I_i \rightarrow I_f)_{\text{Weisskopf}} = \frac{1.2^{2\lambda-2} 10}{\pi} \left(\frac{3}{\lambda+3}\right)^2 A^{\frac{2\lambda-2}{3}}. \quad (1.12)$$

Equation 1.11 is expressed in  $e^2 \text{fm}^{2\lambda}$ , whereas equation 1.12 in  $\mu_N^2 \text{fm}^{2\lambda-2}$  units. Weisskopf units are used for single-particle transitions, where it is assumed that only one nucleon in an average potential changes its orbit and contributes to the excitation. This is called the

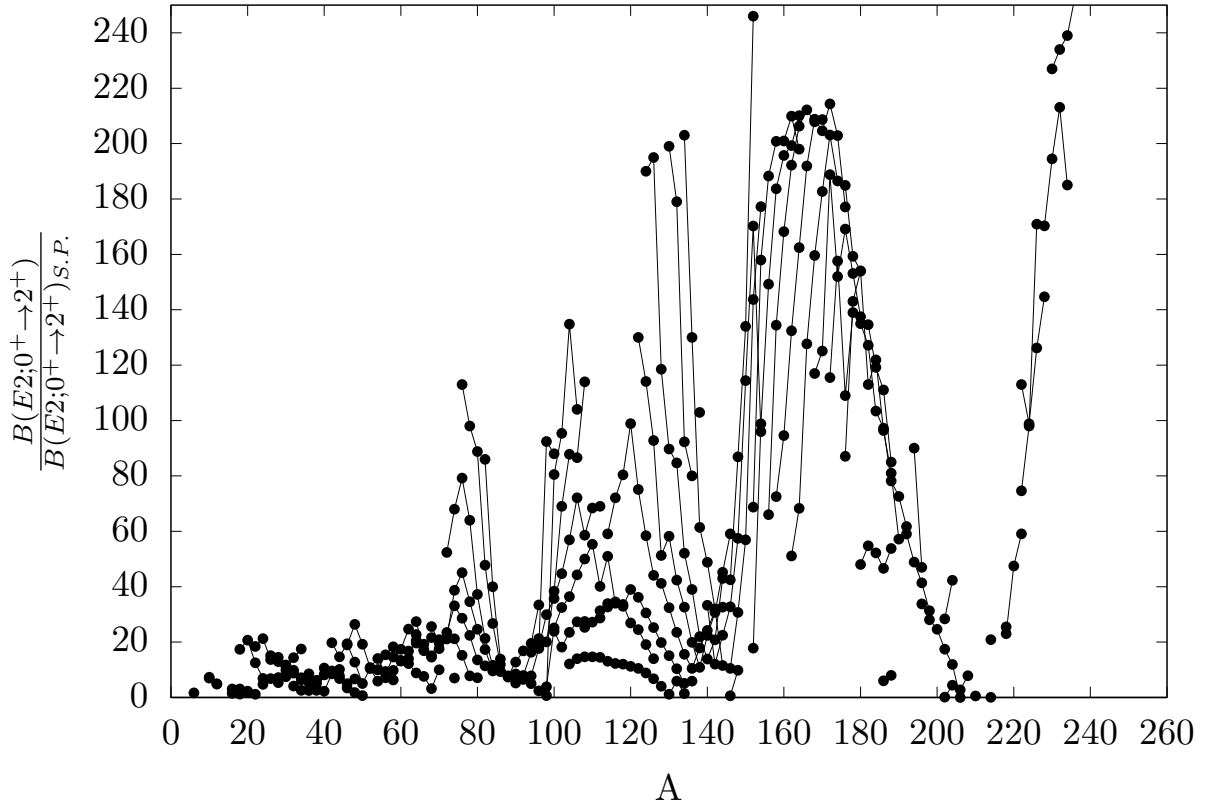


**Figure 6:** The reduced transition strength in Weisskopf units for  $2_1^+ \rightarrow 0_{g.s.}^+$  transitions for all even-even nuclei. Nuclei with equal  $Z$  are connected by lines. The highest values are reached in mid-shell nuclei, whereas values around 1 are observed in closed-shell nuclei. This behavior can be explained by the high collectivity of mid-shell nuclei and the single-particle excitation of closed-shell nuclei. Data taken from Ref. [4].

single-particle picture [20]. A reduced transition strength of  $B(E2) \sim 1$  W.u. corresponds to a single-particle transitions, whereas higher values are expected for collective transitions with multiple nucleons contribute to the excitation. In Figure 6 the reduced transition strength is plotted in Weisskopf units. Peak maxima correspond to mid-shell nuclei and, hence, to collective excitation. The smallest values can be observed at magic numbers or closed-shell nuclei, where single-particle excitation is expected to dominate.

#### 1.4. Coulomb excitation

Since the introduction of the Coulomb-excitation technique during the 1950s [18], this method provided outstanding insight into e.g. collective properties of nuclei. In particular,

Coulomb excitation allowed to deduce a major part of the currently known transition probabilities and deformation parameters of atomic nuclei. Especially for exotic radioactive isotopes far from stability, Coulomb excitation provides a tool to access to  $B(\sigma\lambda)$  values and potentially quadrupole moments, which are difficult to obtain via inelastic scattering and direct lifetime measurements.

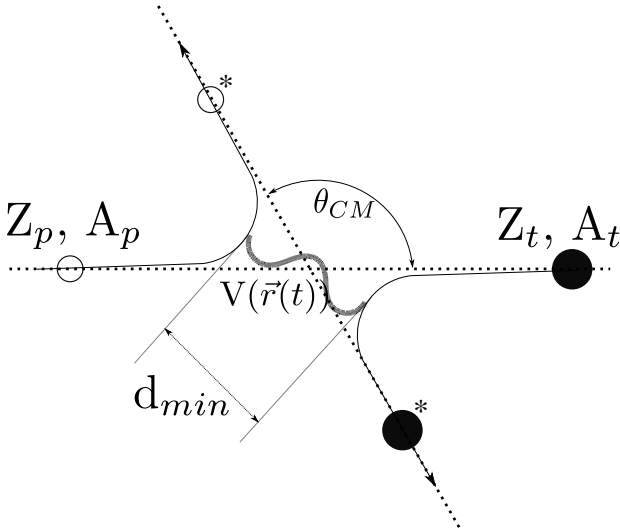


**Figure 7:** Schematic illustration of a Coulomb scattering event in the center-of-mass system. At the point of closest approach ( $d_{min}$ ) the interaction potential  $V(\vec{r}(t))$  is strongest. After the inelastic scattering, projectile and target nuclei are excited indicated by asterisks.

The goal of Coulomb excitation is to determine nuclear transition matrix elements by exciting atomic nuclei via pure electromagnetic interaction. This implies, only the well understood electromagnetic interaction is contributing to the excitation and nuclear force effects can be neglected. Therefore, a projectile nucleus with atomic number  $Z_1$  is guided onto a target nucleus with atomic number  $Z_2$ . If the energy of the incident particle  $E_1$  is below the Coulomb barrier, the distance of closest approach  $d_{min}$  will be large enough to ensure no contribution of the nuclear-force to the excitation process. A schematic illustration of this process is shown in Figure 7, in the center-of-mass frame. It is immediately clear that the excitation depends on  $E_1$ ,  $Z_1$ ,  $Z_2$ , the nuclei distance or the scattering angle  $\theta$  of the particles. The strongest inter-

action potential is reached at the point of closest approach and, hence, the excitation probability is highest (see Fig. 7). To obtain the total excitation probability, the complete particle trajectory has to be included in the calculation as the Coulomb force is a long-range force. This boundary conditions and the well understood electromagnetic force allow an accurate calculation of this processes involved i.e. the complex single and multiple excitations. The theoretical procedure, which is used in Coulomb excitation calculation codes e.g. GOSIA/GOSIA2 [23–25], was developed in the mid 50s and is presented in detail in the paper of K. Alder *et. al.* [18]. In the following sections the basic concept will be discussed.

**Semiclassical approach**

Apart of the quantum-mechanical approach in Ref. [18], Coulomb excitation can be treated in the semi-classical approximation, which presumes classical Rutherford trajectories along the whole scattering and excitation process. The electromagnetic excitation has a negligible effect on the trajectories. Nevertheless, the excitation itself is treated fully quantum mechanically. This implies that the Coulomb-excitation cross section is a composition of the classical Rutherford scattering  $\left(\frac{d\sigma}{d\Omega}\right)_{RUTH}$  and the quantum-mechanical probability for the excitation in which the particle was scattered into the solid angle  $d\Omega$ . The quantum-mechanical probability  $\mathfrak{P}$  depends on the contributing nuclear states [19]. For a two-state model with initial level  $i$  and final level  $f$  the cross section is given by:

$$\left(\frac{d\sigma}{d\Omega}\right)_{COULEX} = \left(\frac{d\sigma}{d\Omega}\right)_{RUTH} \times \mathfrak{P}_{i \rightarrow f}. \quad (1.13)$$

The classical Rutherford trajectories are preserved, if the size of the impinging projectile is much smaller than the size of the hyperbolic trajectory. This condition is expressed by the Sommerfeld parameter

$$\eta = \frac{d_{\min}}{2\lambda_{\text{proj}}}, \quad (1.14)$$

where  $\lambda_{\text{proj}}$  is the de Broglie wavelength of the particle wave packet and  $d_{\min}/2$  is half the distance of closest approach with

$$d_{\min} = \frac{Z_1 Z_2 e^2}{E_{CM}} = \frac{2Z_1 Z_2 e^2}{mc^2 \beta^2}, \quad (1.15)$$

where  $\beta = \frac{v}{c}$  is their impact velocity,  $m$  the reduced mass and  $Z_1, Z_2$  describe the proton number of projectile and target, respectively. The Sommerfeld parameter can be written as [9, 19]

$$\eta = \frac{Z_1 Z_2 e^2}{\hbar v} = \alpha \frac{Z_1 Z_2}{\beta} \approx \frac{Z_1 Z_2 A_1^{1/2}}{6.32 E_1^{1/2}}, \quad (1.16)$$

with  $\alpha = e^2/\hbar c$  the unitless fine-structure constant and  $\beta = \sqrt{2E/mc^2}$ . For the present case

of  $^{132}\text{Sn}$  with a beam energy of 5.5 MeV/u impinging onto a  $^{206}\text{Pb}$  target, the Sommerfeld parameter equals  $\eta = 272$ . Hence, the semi-classical approach  $\eta \gg 1$  is applicable.

### First-order perturbation theory

The excitation energy  $\Delta E$  also has impact on the excitation cross section. It is useful to define the adiabaticity parameter  $\xi$ , as the difference between incoming  $\eta_i$  and outgoing  $\eta_f$ ,

$$\xi = \eta_i - \eta_f = \frac{Z_1 Z_2 A_1^{1/2} \Delta E}{12.65 E^{3/2}} = \frac{\eta \Delta E}{2 E_1}. \quad (1.17)$$

For  $\xi \leq 1$  and small  $\Delta E$  a large excitation probability is expected, whereas for  $\xi \gg 1$  a vanishing excitation cross section will be the case, because high  $\Delta E$  hamper the Coulomb excitation [9]. Moreover,  $\xi$  can be interpreted as the ratio of the collision time relative to the time scale of internal motion of the nucleus.

$$\xi = \frac{\tau_{\text{collision}}}{\tau_{\text{nucleus}}} \quad (1.18)$$

If the collision time is much longer than the internal motion of the nucleus, the change of the electromagnetic field strength per time approaches the adiabatic limit and, hence no excitation is possible (adiabatic theorem) [26].

Considering the aforementioned semiclassical theory, excitation probabilities are determined in time-dependent perturbation theory. Therefore, the condition of classical trajectories of the scattered particles has to be fulfilled. As equation 1.13 is valid for the projectile as well as for the target, both excitation probabilities and cross sections can be determined in an analog way by interchanging the corresponding properties of the calculated nucleus. In perturbation theory the motion of the two particles is treated classically. The time-dependent interaction potential  $V(r(\vec{t}))$  originating from one collision partner influencing the second one, is used to calculate the excitation probability along the whole trajectory [21]. For unpolarized particles the probability  $\mathfrak{P}_{i \rightarrow f}$  from the state  $|i I_i M_i\rangle$  to state  $|f I_f M_f\rangle$  is expressed by

$$\mathfrak{P}_{i \rightarrow f} = \frac{1}{2 I_i + 1} \sum_{M_i M_f} \left| \langle f I_f M_f | b | i I_i M_i \rangle \right|^2 = \left| c_{i \rightarrow f}^{(1)} \right|^2, \quad (1.19)$$

with  $I_i$ ,  $M_i$  and  $I_f$ ,  $M_f$ , the spin and magnetic quantum number of the initial and final

state, respectively. The matrix elements  $b$  are given by

$$\langle f I_f M_f | b | i I_i M_i \rangle = \frac{1}{i\hbar} \int_{-\infty}^{+\infty} \langle f I_f M_f | V(r(\vec{t})) | i I_i M_i \rangle e^{i\omega_{if}t} dt, \quad (1.20)$$

with  $\frac{\Delta E}{\hbar} = \omega_{if}$ . The excitation of the particles can be induced by either the electric  $V(r(\vec{t}))_E$  or the magnetic  $V(r(\vec{t}))_M$  component of the electromagnetic field. Thus, it is convenient to separate them. In the following the electric component is discussed and later on the magnetic contribution is reviewed. Performing a multipole expansion on the single components of the electric interaction potential the transition amplitude can be written as

$$\langle f I_f M_f | b | i I_i M_i \rangle = \frac{4\pi Z_1 e}{i\hbar} \sum_{\mu\lambda} \frac{1}{2\lambda + 1} \langle f I_f M_f | \mathfrak{M}(E\lambda, \mu) | i I_i M_i \rangle S_{\mu\lambda}, \quad (1.21)$$

where  $S_{\mu\lambda}$  denotes the orbital integral along the classical trajectory  $r(\vec{t})$ :

$$S_{\mu\lambda} = \int_{-\infty}^{+\infty} e^{i\omega_{if}t} Y_{\mu\lambda}(r(\vec{t})) \left( \frac{1}{r(\vec{t})} \right)^{\lambda+1} dt, \quad (1.22)$$

with  $Y_{\mu\lambda}(r(\vec{t}))$  the spherical harmonics [21]. The information about the nuclear structure is completely contained in the electric multipole matrix elements

$\langle f I_f M_f | \mathfrak{M}(E\lambda, \mu) | i I_i M_i \rangle$ , which can be defined as independent of the geometry of both nuclei by applying the Wigner-Eckart-Theorem:

$$\langle i I_i M_i | \mathfrak{M}(E\lambda, \mu) | f I_f M_f \rangle = (-1)^{I_i - M_i} \begin{pmatrix} I_i & \lambda & I_f \\ -M_i & \mu & M_f \end{pmatrix} \langle i I_i | \mathfrak{M}(E\lambda, \mu) | f I_f \rangle. \quad (1.23)$$

with the Clebsch-Gordan coefficient  $\begin{pmatrix} I_i & \lambda & I_f \\ -M_i & \mu & M_f \end{pmatrix}$ . The total transition probability is expressed as follows:

$$\mathfrak{P}_{i \rightarrow f} = \sum_{\lambda} \mathfrak{P}_{i \rightarrow f}(E\lambda) = \sum_{\lambda} \left( \frac{4\pi Z_1 e}{\hbar} \right)^2 \frac{B(E\lambda; I_i \rightarrow I_f)}{(2\lambda + 1)^3} \sum_{\mu} |S_{E\lambda, \mu}|^2, \quad (1.24)$$



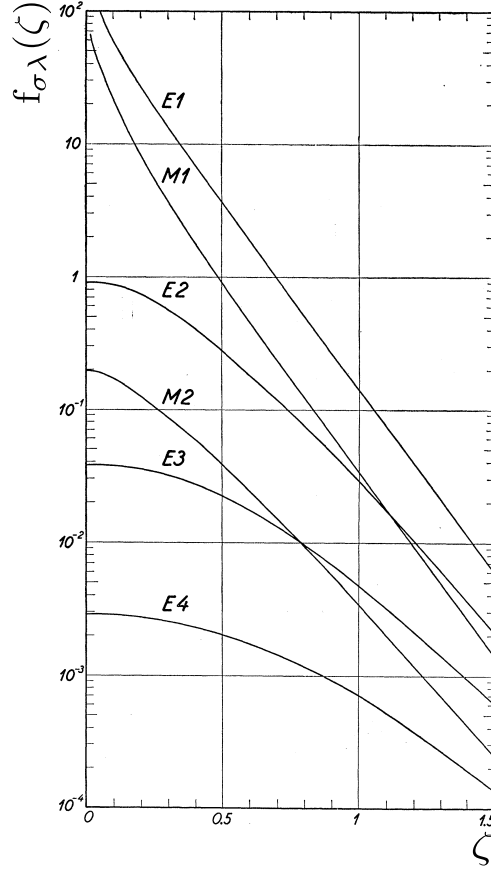


**Figure 8:** The integrated non-relativistic Coulomb-excitation function in dependency of the adiabaticity parameter  $\xi$  for electric multipole transitions with  $\lambda = 1, 2, 3, 4$ . Figure taken from [18] with kind permission from APS.

with the reduced transition strength  $B(E\lambda; I_i \rightarrow I_f)$  defined in equation 1.6. The resulting differential cross section for a given electrical multipolarity  $\lambda$  is then described by

$$\left(\frac{d\sigma}{d\Omega}\right)_{E\lambda} = \left(\frac{Z_1 e}{\hbar\nu}\right)^2 \left(\frac{d_{min}}{2}\right)^{-2\lambda+2} B(E\lambda; I_i \rightarrow I_f) f_{E\lambda}(\theta, \xi), \quad (1.25)$$

with the dimensionless non-relativistic Coulomb-excitation function  $f_{E\lambda}(\theta, \xi)$  containing all information about the classical trajectory of the scattered particles. The dependency as a function of  $\xi$  is illustrated in Figure 8 for electric transitions up to  $\lambda = 4$ . For the magnetic part the excitation cross section is similar:

$$\left(\frac{d\sigma}{d\Omega}\right)_{M\lambda} = \left(\frac{Z_1 e}{\hbar c}\right)^2 \left(\frac{d_{min}}{2}\right)^{-2\lambda+2} B(M\lambda; I_i \rightarrow I_f) f_{M\lambda}(\theta, \xi), \quad (1.26)$$

From equation 1.25 and 1.26 can be deduced that a magnetic transition of the same multipolarity is suppressed by a factor of  $\beta^2 = (v^2/c^2)$ , compared to a electric transition. At beam energies of 5.5 MeV/u for  $^{132}\text{Sn}$  and a corresponding  $\beta \sim 11\%$ , electric transitions will dominate the Coulomb excitation process.

## Second-order perturbation theory

In the framework of first-order perturbation theory, Coulomb-excitation probabilities are typically quite small  $\mathfrak{P}_{i \rightarrow f} \ll 1$ . However, for heavy-ion collisions the transition probability increases with the ion energy and, thus, the condition  $\mathfrak{P}_{i \rightarrow f} \ll 1$  may not longer be satisfied and second-order effects have to be considered. This implies two consequences, i.e. first-order transition probabilities can be affected by second-order terms and states which were not accessible for example due to selection rules, can be populated via double excitation [27]. In this case the transition to the final state proceed via a multi-step excitation process. For multi-step excitation the probability increases with increasing beam energy [18, 19, 21]. To incorporate these effects, the perturbation of the nucleus by the changing electromagnetic field has to be considered up to higher orders, keeping the classical trajectories. The transition probability for a multi-step excitation from the initial state  $i$  via an intermediate state  $m$  into the final state  $f$  is given by

$$\mathfrak{P}_{i \rightarrow f} = \left| c_{i \rightarrow f}^{(1)} + \sum_m c_{i \rightarrow m \rightarrow f}^{(2)} \right|^2 = \left| c_{i \rightarrow f}^{(1)} \right|^2 + 2\Re(c_{i \rightarrow f}^{(1)} \cdot \sum_m c_{i \rightarrow m \rightarrow f}^{(2)}) + \left| \sum_m c_{i \rightarrow m \rightarrow f}^{(2)} \right|^2, \quad (1.27)$$

where  $c_{i \rightarrow f}^{(1)}$  is defined in equation 1.19 and

$$c_{i \rightarrow m \rightarrow f}^{(2)} = \frac{1}{i\hbar} \int_{-\infty}^{+\infty} \langle f I_f M_f | V(r(\vec{t})) | m I_m M_m \rangle e^{i\omega_{mf}t} \times \langle m I_m M_m | V(r(\vec{t})) | i I_i M_i \rangle e^{i\omega_{im}t} dt. \quad (1.28)$$

From Equation 1.27 follows that the first-order and the second-order processes interfere [21]. Thus, it is important to include the second-order effects in the calculation, even for low multi-step excitation probabilities. The interference between first-order and second-order terms lead, e.g. to the reorientation effect. A typically occurrence of this effect is observed by E2 absorption in even-even nuclei, where a transition from  $|m I_m M_m\rangle$  to  $|f I_f M_f\rangle$  with

$m = f$   $I_m = I_f$  can arise. Both state differ only in the magnetic sub-state of the same excited state (usually  $2^+$ ). In this case the matrix element  $\langle f I_f M_f | \mathfrak{M}(E2) | m I_m M_m \rangle$  is proportional to the spectroscopic quadrupole moment

$$Q_s^I = \sqrt{\frac{16\pi I(2I-1)}{5(I+1)(2I+1)(2I+3)}} \times \langle I | \mathfrak{M}(E2) | I \rangle. \quad (1.29)$$

For a spherical nucleus, e.g. the doubly-magic  $^{132}\text{Sn}$  the quadrupole moment should be close to zero, as the quadrupole moment is a measure for the deformation of the nucleus. With a precise determination of  $\mathfrak{P}_{i \rightarrow f}$ , the magnitude and the sign of  $Q_s^I$  indicate the structure of the excited state.

Another consequence of second-order contribution is the two-step E2 excitation. In even-even nuclei the first  $4^+$  state can be excited either directly via an E4-transition or via a two-step excitation following the excitation scheme

$$0^+ \xrightarrow{\text{E2}} 2^+ \xrightarrow{\text{E2}} 4^+. \quad (1.30)$$

Due to the much lower excitation probability of E4 compared to a E2 transition (cf. Fig. 8), the second-order contribution is essential. In almost all heavy-ion collisions the E4 first-order transition is superimposed by a much stronger excitation via the second-order two-step E2 transition. Both examples of the second-order perturbation theory are illustrated in Figure 9.

### “Safe” Coulomb excitation

The so-called “safe” Coulomb excitation is characterized by a negligible effect of the nuclear force on the excitation of particles in a scattering experiment. The excitation of one or both scattering particles is induced by pure Coulomb interaction. A sufficient large distance between the two nuclear surfaces is necessary to satisfy this condition. The point of closest approach is restricted to

$$d_{\min} > R_{\text{target}} + R_{\text{proj}} + \Delta D = 1.25(A_{\text{proj}}^{1/3} + A_{\text{target}}^{1/3}) + \Delta D, \quad (1.31)$$

where  $R_{\text{Proj}}$ ,  $R_{\text{target}}$  describes the nuclear radii of projectile and target, and  $\Delta D$  an additional “safe” distance.

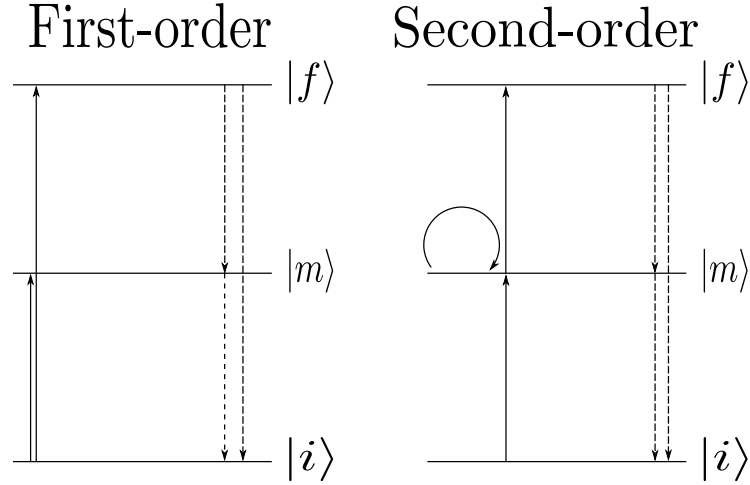


**Figure 9:** Solid lines represent excitation, whereas dashed lines the de-excitation process. The schematic diagram show on the left side a one-step excitation from the initial level  $|i\rangle$  to the final states  $|m\rangle$  and  $|f\rangle$ . On the right hand side the second-order processes are illustrated. The excitation to the final state  $|f\rangle$  proceed via the intermediate state  $|m\rangle$ . In addition, transitions within one state are possible, due to magnetic sub-state transitions. Further information in the text.

In reference [22] Cline *et. al.* determined an effect of less than 0.1% contribution of the nuclear interaction in a Coulomb scattering experiment, with a safe distance of  $\Delta D = 5.0$  fm. Furthermore, the safe bombarding energy as a function of the scattering angle is calculated by

$$E(\theta_{CM}) = 0.72 \frac{Z_{\text{proj}} Z_{\text{target}}}{d_{\text{min}}} \frac{A_{\text{proj}} + A_{\text{target}}}{A_{\text{target}}} \left( 1 + \frac{1}{\sin\left(\frac{\theta_{CM}}{2}\right)} \right), \quad (1.32)$$

with the scattering angle in the center-of-mass system  $\theta_{CM}$ . Considering the conditions of the  $^{132}\text{Sn}$  experiment, the point of closest approach for safe Coulomb excitation amounts to 18.75 fm. This would correspond to a safe bombarding energy of 3.9 MeV/u. To increase the Coulomb excitation cross section, an impinging energy of 5.5 MeV/u was chosen to facilitate the challenging experiment. However, for such beam energies the center-of-mass scattering angle has to be restricted to fulfill the safe Coulomb-excitation criterion. The particle-scattering angles were restricted to  $67.6^\circ$  in the center-of-mass frame. This corresponds to forward angles up to  $42^\circ$  with respect to the direction of the beam in the laboratory frame.

### Relative measurement of the transition strength

In Coulomb excitation experiments with insufficient knowledge of the beam current and its intensity, the Coulomb-excitation cross section can be determined relative to a well-studied transition. In the previous section it was explained that the number of scattered nuclei in a Coulomb-excitation experiment provides a direct measure for the excitation probability of the corresponding nuclei. This observable can be deduced from the measured  $\gamma$ -ray intensity after the de-excitation of the scattered particles.

$$N_{\gamma,\text{proj}}(f \rightarrow i) = \epsilon_{\gamma,\text{proj}} b_{f \rightarrow i}^{\text{proj}} \sigma_{\text{proj}}(f) I \frac{\rho d_{\text{target}} N_A}{A_{\text{target}}} \quad (1.33)$$

The total number of detected  $\gamma$ -rays after an excitation of the projectile from an initial state  $|i\rangle$  to the final state  $|f\rangle$  followed by the deexcitation is determined by equation 1.33. Therefore, the detection efficiency for the emitted  $\gamma$ -ray  $\epsilon_{\gamma,\text{proj}}$ , the branching ratio of the transition  $b_{f \rightarrow i}$ , the excitation cross section  $\sigma_{\text{proj}}(f)$  for the final state, the beam intensity  $I$  and the number of scattering target nuclei  $(\rho d_{\text{target}} N_A)/A_{\text{target}}$  has to be considered. The number of target nuclei is expressed as the ratio of the product of target density times target thickness and the Avogadro constant divided by the atomic mass of the target nuclei. The analog equation holds for the target excitation:

$$N_{\gamma,\text{target}}(f \rightarrow i) = \epsilon_{\gamma,\text{target}} b_{f \rightarrow i}^{\text{target}} \sigma_{\text{target}}(f) I \frac{\rho d_{\text{target}} N_A}{A_{\text{target}}}. \quad (1.34)$$

From this follows that the ratio of the  $\gamma$ -ray intensities from projectile and target deexcitation is independent from the beam intensity. As the transition of the target nuclei is well known, all properties like branching ratios or excitation cross section are established with small errors. Thus the relevant excitation cross section can be written as

$$\sigma_{\text{proj}}(f) = \sigma_{\text{target}}(f) \frac{N_{\gamma,\text{proj}}(f \rightarrow i)}{N_{\gamma,\text{target}}(f \rightarrow i)} \frac{b_{f \rightarrow i}^{\text{target}}}{b_{f \rightarrow i}^{\text{proj}}} \frac{\epsilon_{\gamma,\text{target}}}{\epsilon_{\gamma,\text{proj}}}. \quad (1.35)$$

Using equations 1.25 and 1.26 the reduced transition strength can be determined with the classical trajectories of the scattered particles and the corresponding solid angle. This calculations are done with coupled-channel codes like CLX [28, 29] or GOSIA2 [23–25].

## 2. Physics case

The physics motivation for the Coulomb-excitation experiment of the doubly-magic  $^{132}\text{Sn}$  is described. In addition, previous results on a  $^{132}\text{Sn}$  Coulomb-excitation experiment at HRIBF (Holifield Radioactive Ion Beam Facility) at ORNL are briefly discussed [30].

### 2.1. Properties of $Z = 50$ and $N = 82$ nuclei

More than 7000 nuclides are predicted to exist within the proton and neutron drip lines [31], until October 2016, nuclear ground-state properties for 3437 nuclei were observed in different experiments [32]. Astrophysical processes like the r-process (rapid neutron capture), which has a curcile role in the production of neutron-rich isotopes heavier than iron far from stability [33], proceed predominantly outside the area of known nuclei (cf. Figure 10).

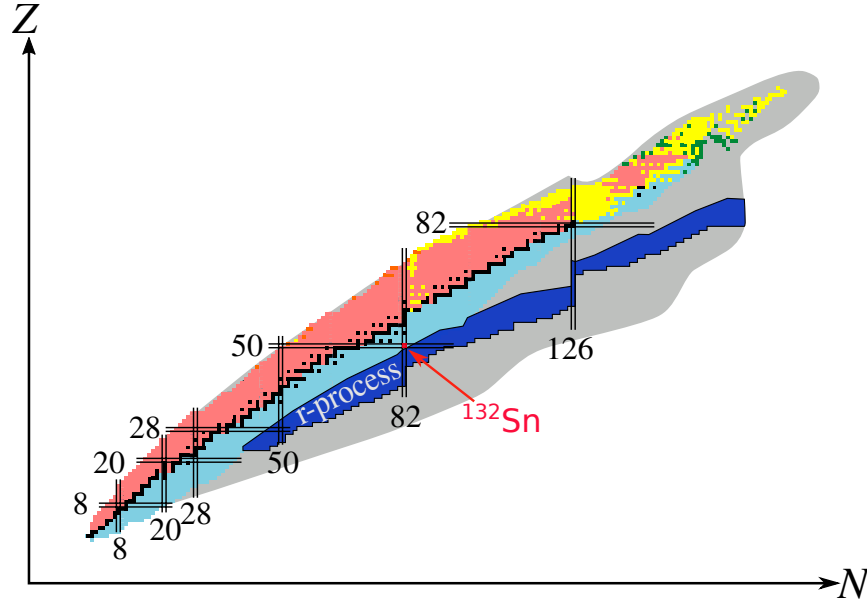


**Figure 10:** Nuclear chart with the magic numbers marked. The crossing points of magic proton and neutron numbers indicate the doubly-magic nuclei. Neutron-rich nuclei are marked in blue, neutron-deficient nuclei in red, stable nuclei in black and unknown nuclei in grey. One predicted r-process region is shown in blue. At  $N = 50, 82$  and  $126$  the “waiting points” of the r-process are indicated. The r-process approaches very close to the doubly-magic  $^{132}\text{Sn}$ .  $^{132}\text{Sn}$  is the only neutron-rich doubly-magic nuclei above  $Z = 28$  in the region of the r-process predictions.

Thus, the origin and the exact progression of the r-process path are still unknown and remain an open question. The r-process proceeds along nuclei with constant neutron-separation energies to nuclei with increasing proton numbers, until the so called "waiting points" are reached. These "waiting points" correspond to nuclear-shell closures at  $N = 50$ , 82 and 126 [34], at which capture reactions and photodisintegration are in competition and further capture reactions to more neutron-rich nuclei get unlikely. Thus, the production of these nuclei are increased, and characteristic peaks in the mass abundance around  $A \simeq 80$ , 130 and 195 are observed. The mass abundance in the solar system is illustrated in Figure 11 (a).

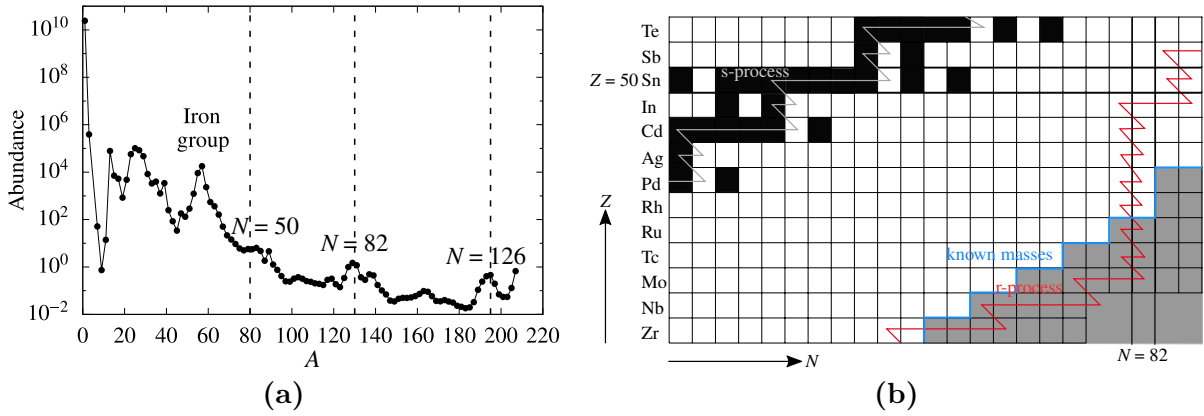


**Figure 11:** (a) Nuclear abundance of the solar system. The characteristic peaks are produced by the r- and s-process of the nucleosynthesis. This increase in the abundance at  $A \simeq 80$ , 130, 195 is related to the neutron shell closures at  $N = 50$ , 82 and 126. Data taken from Ref. [35]. Due to the increase of the neutron-separation energy and decrease of the neutron-capture cross section, the r-process proceeds along this so called "waiting points", mainly via  $\beta$ -decay and neutron capture. (b) Theoretical r-process path (red) along the  $N = 82$  magic number predicted in Ref. [36]. The white-grey path marks the s-process (slow-neutron capture) at the neutron-rich side of the valley of stability.

After reaching the "waiting points", the weak interaction, in particular the  $\beta^-$ -decay, drives the r-process along the chain of isotones up to nuclei with a magic proton configuration. A theoretically predicted path of the described r-process around the shell closure  $N = 82$  is shown in Figure 11 (b). For a detailed insight into this phenomenon, the knowledge of nuclear properties, like the neutron-separation energy, the mass, the half-life ( $T_{1/2}$ ) and the neutron-capture cross section, especially at  $N = 50$ , 82, and 126 are mandatory in order to perform r-process calculations, predictions and in order to improve the astrophysical understanding of the nucleosynthesis [37]. Therefore, extrapolations from theoretical models

(e.g. nuclear shell model), based on experimentally determined quantities of nuclei, are used to calculate the properties of unknown/unobserved nuclei. To perform extrapolations without exceeding the available computational power, closed-shell nuclei are essential, to accomplish the calculations for high nuclear masses. Including closed-shell nuclei in nuclear shell-model calculations, enables the investigation of nuclides in their vicinity by reducing the required model space. This limits the size of the Hamiltonian and the necessary computational power. Hence, the properties of doubly-magic nuclei are of particular importance. Out of the huge amount of today's known nuclides, merely ten nuclei are observed that are classically doubly magic and, thus, exhibit fully filled proton and neutron shells (see section 1). Five of this nuclei i.e.  ${}^4\text{He}$ ,  ${}^{16}\text{O}$ ,  ${}^{40}\text{Ca}$ ,  ${}^{48}\text{Ca}$  and  ${}^{208}\text{Pb}$  are stable. The remaining five nuclei  ${}^{48}\text{Ni}$ ,  ${}^{56}\text{Ni}$ ,  ${}^{78}\text{Ni}$ ,  ${}^{100}\text{Sn}$  and  ${}^{132}\text{Sn}$  are radioactive. The properties of the stable doubly-magic nuclei are quite well studied [6]. For radioactive doubly-magic nuclei the situation is much more difficult, as the production of radioactive doubly-magic nuclei is challenging and in addition the experimental observation, too (see section 3). Nowadays,  ${}^{132}\text{Sn}$  ( $Z = 50$  and  $N = 82$ ) is the only observed doubly-magic nucleus above  $Z = 28$  in the neutron-rich region far from stability and in immediate proximity to the r-process path. Thus, this nucleus is essential for efficient theoretical descriptions in this region. The single-particle properties of this nucleus were already studied in the one particle/hole proton and neutron neighbors [38–41]. Besides single-particle properties, collective characteristics of nuclei are essential to develop and benchmark theoretical models e.g. nuclear shell-model interactions. The investigation of the collective properties of the doubly-magic  ${}^{132}\text{Sn}$  nucleus, via Coulomb excitation, is presented in this work. In the following a brief summary of the experimentally determined characteristics of the shell closures at  $Z = 50$  and  $N = 82$  is given.

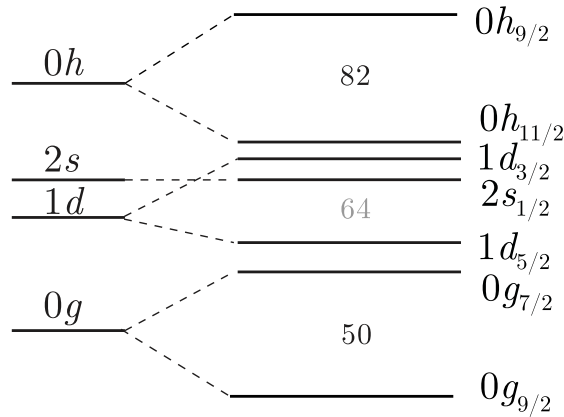


**Figure 12:** Shell-model orbitals forming the shell gaps at the magic numbers 50 and 82.



### Shell closure along $Z = 50$

The nuclear shell gap at  $Z = 50$  was investigated along the chain of tin isotopes, which includes the two doubly-magic nuclei  $^{100}\text{Sn}$  and  $^{132}\text{Sn}$ . This shell closure is created by fully filled orbitals up to the  $0g_{9/2}$  orbital and the first empty orbitals  $0g_{7/2}$  and  $1d_{5/2}$ . Figure 12 illustrates the orbital configuration around the shell closures for  $Z = 50$  and  $N = 82$ .

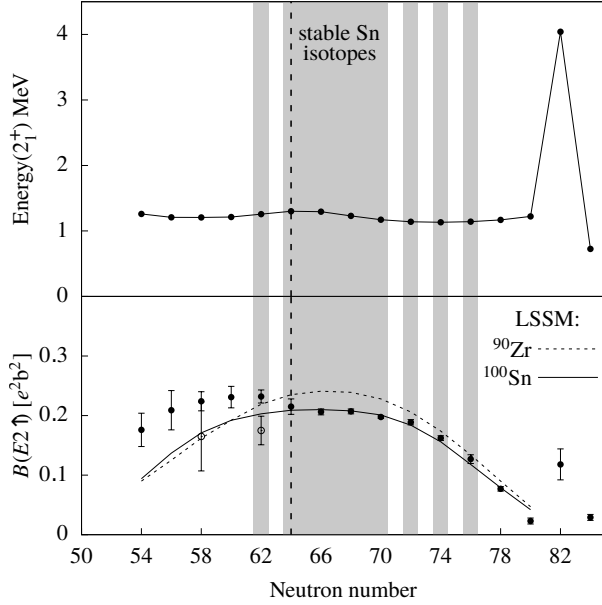


**Figure 13:** Top: Excitation energy of the first excited state  $2_1^+$  in even-even Sn nuclei along  $Z = 50$ . Bottom:  $B(E2 \uparrow)$  values along the isotopic Sn chain are illustrated. Data taken from Ref. [4]. Shell-model calculations are from Ref. [42]. Values for  $^{132}\text{Sn}$  were taken from Ref. [43].

In even-even tin nuclei the excitation energy of the first excited  $2_1^+$  state is nearly constant between  $N = 52$  and  $N = 84$ , except for the magic number  $N = 82$ . The upper plot of Figure 13 illustrates the measured excitation energies of the first excited state along the Sn chain. The constant behavior of the excitation energies can be explained by the dense neutron-orbit distribution between the shell gap  $N = 50$  and  $N = 82$ . The high density of states allows for pairing correlations, which result in similar excitation configurations [6]. Thus, the  $2_1^+$  states around  $\simeq 1.2$  MeV are caused by pure-neutron excitation. The small increase of the excitation energy around  $N = 64$  is an indication for a potential sub-shell closure and a sub-shell gap between the  $1d_{5/2}$  and  $1d_{3/2}$  orbitals. At  $N = 82$  the excitation energy is increased, because the excitation requires high energy for both, proton and neutron particles, to overcome the shell gap. Hence, the  $2_1^+$  state of the doubly-magic  $^{132}\text{Sn}$  is probably no longer of pure neutron character, it is rather a combination of neutron and proton excitations. Further prove for the doubly-magic character of  $^{132}\text{Sn}$  can be deduced from the experimentally determined  $B(E2 \uparrow)$  value (preliminary value from Ref. [43, 44]). In the bottom Figure 13, the  $B(E2 \uparrow)$  values for the even-even nuclei along the isotopic tin chain are presented. For  $N > 64$  the reduced transition strength follows the parabolic trend of generalized seniority [45, 46], predicted by large-scale shell model calculations [42]. For  $N < 64$  a more constant behavior is apparent and, thus, indicate an

increase in collectivity with decreasing neutron number (black dots) [42, 43, 47, 48]. In contrast, the data drawn with empty circles were obtained from an experiment employing the Doppler-shift attenuation method [49], suggesting a decrease of collectivity with decreasing  $N$ . This data is in better agreement with the large-scale shell-model calculation [42] and with the observed reduced binding energy of the orbits around  $Z = 50$  [6].

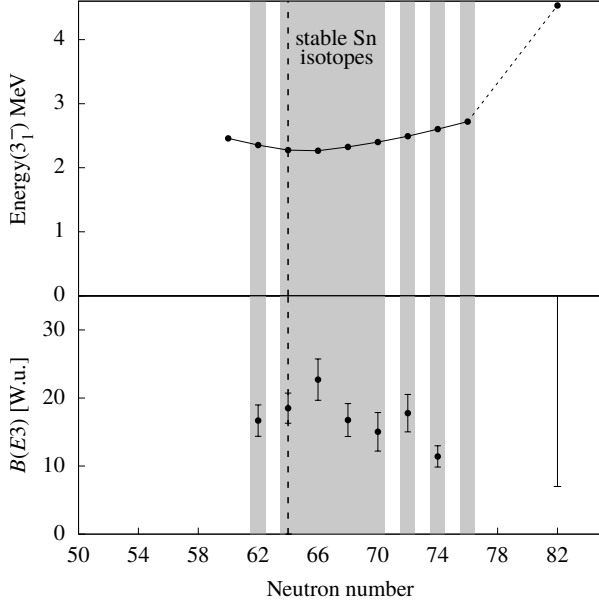


**Figure 14:** Top: Excitation energies for the second excited state  $3_1^-$  in the even-even tin isotopic nuclei. Bottom:  $B(E3)$  values in W.u. are presented. Values taken from Ref. [50]. See text for more details.

Due to the ambiguity of the experimental results for  $N < 64$ , further experimental clarification is essential, as the properties of the  $Z = 50$  isotopic chain are key ingredients for theoretical calculations of  $B(E2)$  values in the middle of the nuclear chart. The observed local rise at  $N = 82$  of the  $B(E2 \uparrow)$  value (see section 2.2) is related to the negative-parity intruder orbital  $0h_{11/2}$ . The same behavior is also observed in the doubly-magic  $^{208}\text{Pb}$  [38, 51, 52] and was predicted applying different quasi-particle random-phase approximation (QRPA) calculations [53–55]. Nevertheless, the  $B(E2 \uparrow)$  for  $^{132}\text{Sn}$  is small compared to “mid-shell” tin isotopes and, hence, a further indication of the doubly-magic structure of  $^{132}\text{Sn}$ . The second excited state in the doubly-magic  $^{132}\text{Sn}$  is the

$3_1^-$ . The excitation energy along the isotopic chain (see upper Figure 14) is nearly constant at  $\simeq 2.5$  MeV, which also originate from the dense neutron orbit configuration. Experimental values for  $N = 78$  and  $N = 80$  are not available. The  $B(E3)$  values, shown in the bottom Figure 14, between  $\simeq 10$ -25 W.u. implicate a collective structure of the  $3_1^-$  state. The negative-parity intruder  $0h_{11/2}$ , which has to be included in possible neutron configurations, allows for  $E2$  and  $E3$  collective transitions via the possible  $\nu 0h_{11/2}0g_{7/2}$  and  $\nu 0h_{11/2}1d_{5/2}$  particle-hole excitations.

### Shell closure along $N = 82$

Along the  $N = 82$  isotonic chain seven nuclei are stable. This emphasizes the strong nature of the shell gap at  $N = 82$  for  $Z \geq 50$ . Moreover, this shell-closure is affected by proton-neutron interactions. This interactions can modify e.g. binding energies and, thus, change the orbit energy and influence the shell gap.

The  $\pi\nu$ -interactions are restrained to the proton-neutron configurations. Therefore, several possible  $\pi\nu$ -interaction mechanisms can affect the structure of nuclei alongside  $N = 82$ . Thus, it is significant to study certain properties of the isotonic chain  $N = 82$  as a function of the proton number. In Figure 15 the excitation energy of the first excited state as a function of the proton number is presented. A similar pattern, as for the isotopic chain  $Z = 50$ , can be observed (see Figure 13). The highest excitation energy of the first excited state is reached for  $Z = 50$ , followed by a smooth behavior for higher  $Z$ . The increase towards  $Z = 64$  is slightly more pronounced, than along the isotopic chain. The reason is the sub-shell closure with its larger energy gap between

the proton orbitals, originating from the additional contribution from the Coulomb force. Furthermore, the aforementioned reduced transition strength along  $N = 82$  for  $Z \geq 50$ , demonstrates that the  $B(E2 \uparrow)$  of  $^{132}\text{Sn}$  is small compared to the neighboring isotones and, hence, reinforce the doubly-magic character of this nucleus. The equality of the  $B(E2 \uparrow)$  for tin and tellurium is related to the local increase of the  $B(E2 \uparrow)$  for  $^{132}\text{Sn}$ .

The second excited state for nuclei with 82 neutrons is the  $3_1^-$  state. This state is generated by proton excitation, as the large neutron-shell gap hinder neutron excitation. As expected and presented in Figure 16, the excitation energy is the largest for  $^{132}\text{Sn}$ . The minimal excitation energy for the  $3_1^-$  level is observed for  $N = 64$ . The proton orbit distribution at the sub-shell closure induces the lowering of the  $3_1^-$  state. Thus, in this case the  $3_1^-$  is

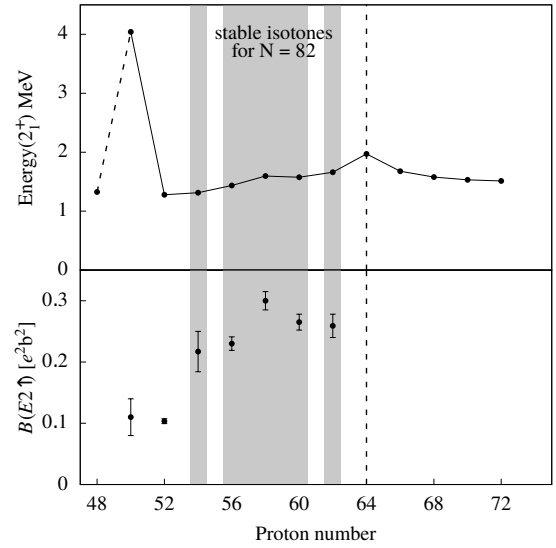


**Figure 15:**  $E(2_1^+)$  and  $B(E2 \uparrow)$  along the  $N = 82$  isotonic chain are presented. The dashed line connecting  $Z = 48$  and  $Z = 50$  is set, as the spin assignment at  $Z = 48$  is preliminary. Data taken from Ref. [4].

lowered to around 2 MeV. The  $B(E3 \uparrow) \simeq 10 - 40$  W.u. values indicate clearly a collective behavior with a maximum value at the sub-shell closure at  $Z = 64$ . At  $Z = 64$  the possible number of particles/holes that contribute to the excitation is largest between the two shell closures  $Z = 50$  and  $Z = 82$ .

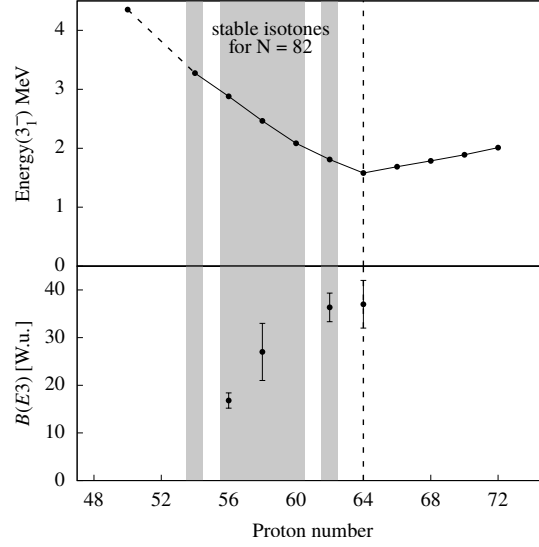


**Figure 16:** Measured  $E(3_1^-)$  and  $B(E3)$  values are shown. Adapted from Ref. [56–60].  
The values for  $Z = 50, 52$  are unknown.

## 2.2. Previous Coulomb excitation of $^{132}\text{Sn}$

The first Coulomb-excitation experiment with a radioactive-ion  $^{132}\text{Sn}$  beam was performed at HRIBF at ORNL and reported in Ref. [43, 44]. The challenge to excite the doubly-magic  $^{132}\text{Sn}$ , arises on the one hand from the required high excitation energy and on the other hand from the small transition strengths. Nevertheless, with the opportunity of post-accelerating radioactive-ion beams (cf. Sec. 3), it is possible to produce the  $^{132}\text{Sn}$  beam and facilitate the excitation of the first  $2^+$  state. The  $^{132}\text{Sn}$  Coulomb-excitation experiment at ORNL used a post-accelerated radioactive-ion beam in two consecutive runs with 470 MeV (3.6 MeV/u) and 495 MeV (3.75 MeV/u). Both runs utilized a  $1.3\text{ mg/cm}^2$  thick  $^{48}\text{Ti}$  target, which yield a high cross section for the inverse kinematic and beam energies [44]. For monitoring the beam quality a carbon-foil-MCP beam counter as well as a Bragg counter were positioned 57 cm and 2 m in the beam axis downstream the target, respectively. The beam intensity at the  $^{48}\text{Ti}$  target amounted up to  $1.4 \times 10^5$  ions/s and a beam purity of 96% was achieved. The beam time was approximately two weeks. To detect the high-energetic  $\gamma$  rays from the first excited  $2_1^+$  state at 4.04 MeV, the ORNL-MSU-TAMU  $\text{BaF}_2$  array was used to guarantee a high total-photopeak efficiency of  $\sim 30\%$ . Therefore, 150  $\text{BaF}_2$  detectors were placed in a compact geometry surrounding the target. In addition to the scintillators an annular double-sided silicon strip detector (DSSSD) with 7 cm diameter was employed to detect the scattered beam-like and target-like particles. The distance between the target and the Si-detector was 8 cm along the beam direction. Thus, the full range of possible center-of-mass angles was covered. The particle Doppler-correction was done with the positron sensitive Si-detector with 48 radial strips and 16 horizontal strips. Considering the high energies of both reactions and the safe Coulomb-excitation (COULEX) criterion of 5 fm distance between projectile and target nuclei, a limitation of possible scattering angles was required to eliminate the influence of nuclear interactions [22]. The maximum scattering angle in the center of mass frame at 3.75 MeV/u beam energy amounts to  $85^\circ$ , whereas at 3.6 MeV/u an angle of  $90^\circ$  was the limit. Both angles correspond to  $\simeq 20^\circ$  in the laboratory frame. The final  $\gamma$ -ray spectrum for  $^{132}\text{Sn}$  was obtained with a particle-gamma coincidence trigger to reduce the  $\gamma$ -ray background. The forward scattered tin particles, within the safe COULEX angles, were used as a valid trigger. "Unsafe" events were discriminated by coincidences between Sn and Ti particles (see Figure 17 (b)), by making use of the inverse kinematics. The advantage of a high efficiency of the  $\text{BaF}_2$  array for 4 MeV  $\gamma$  rays, goes along with a poor energy resolution of 25% at 4 MeV (Figure 17 (a)). Considering the second excited state  $3_1^-$ , with an excitation

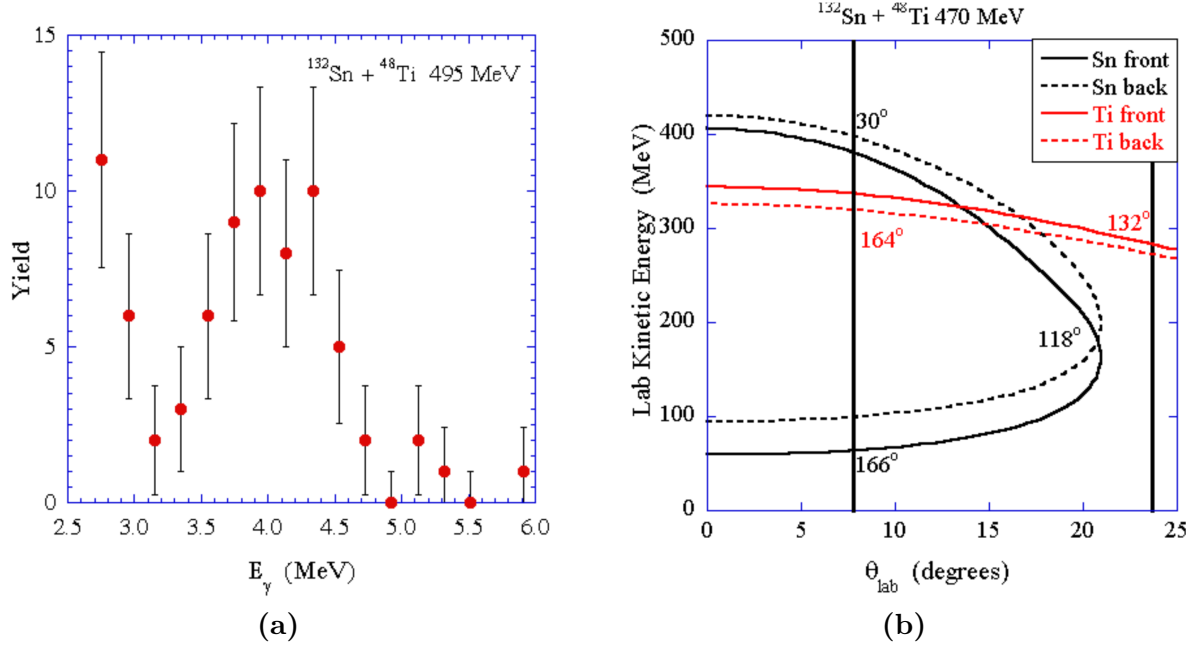


**Figure 17:** (a)  $\gamma$ -ray spectrum obtained from the  $^{132}\text{Sn}$  experiment in inverse kinematics at HRIBF. The spectrum was generated with a particle-gamma coincidence trigger between the DSSSD detector and the  $\text{BaF}_2$  array, to reduce the  $\gamma$ -ray background. (b) Calculated kinematics of the reaction. The dashed lines represent the energy at the “back” of the target, whereas the solid lines show the energy at the “front” of the target with respect to the scattering angle. Figures taken from Ref. [44] with kind permission of The European Physical Journal (EPJ).

energy of 4.35 MeV (and even the  $4_1^+$  at 4.42 MeV), it is impossible to separate the  $2_1^+$  and  $3_1^-$  transitions with the achieved energy resolution. The preliminary reduced transition strength  $B(E2 \uparrow; 0_{\text{g.s.}}^+ \rightarrow 2_1^+) = 0.11(3)/0.14(6) e^2\text{b}^2$  was determined with the obtained yield shown in Figure 17 (a) [43, 44]. A final  $B(E2)$  value was not given. No efficiency calibration was available for the  $\text{BaF}_2$  array. The preliminary values were calculated with a simulated response function for the  $\text{BaF}_2$  array.

### 3. Radioactive-beam physics at ISOLDE, CERN

Ground-state properties are already observed for more than 3400 bound nuclei. Only a small fraction of this nuclei, i.e. 253 are stable. Further 33 radioactive nuclei occur naturally on earth. Thus, more than 91% of the observed nuclei are only short-lived and have to be produced in-situ by nuclear reactions. Therefore, nuclear reactions are indispensable to create and study unstable nuclei, to understand their nuclear structure and astrophysical processes like the r- and p-process. Different techniques are applied to produce nuclei towards the proton and neutron drip lines. For example neutron-rich nuclides are mainly produced via fission reactions of heavy nuclei, whereas proton-rich residuals can be created via fusion-evaporation reactions.

One experimental approach to study radioactive nuclei are "in situ" experiments. Thereby stable nuclear beams are guided onto stable target materials, followed by the immediate investigation of the reaction products and their properties. With this technique high production cross sections for radioactive nuclei are achieved. However, for fusion-evaporation reactions the potential residuals are limited by the beam-target combination and are produced among other nuclei in the same reaction. Investigation of radioactive nuclei after induced fission reactions suffer from high fission background. The created radioactive nuclei of both reactions are restricted to highly excited states and the consecutive decays.

A complementary experimental method is the production of post-accelerated Radioactive Ion Beams (RIBs). For this method two reaction processes are needed, first the radioactive nuclei are generated at a primary target. Consecutively these nuclei are ionized, mass separated, accelerated and guided to a secondary target, where the second nuclear reaction of interest is induced and the measurement is performed. This technique reduces the background stemming from possible contamination during the primary reaction and allows, due to the variable beam energy and the available specific nuclei of interest, the investigation of low-energy properties. However, for exotic nuclei far from the valley of stability the production of radioactive-ion beams deals with very low production cross sections, unwanted contamination and very short half-lives of the produced nuclei. Hence, the production of qualitative high radioactive-ion beams requires high production rates. A precise selection of the nuclei of interest is essential to cope with the overwhelming amount of undesirable nuclides produced in the primary reaction. Thus, the extraction and manipulation (ionization, purification) of the radioactive-ion beam has to be very efficient. After the extraction of the desired radioactive nuclei, the focus lies on the half-life of the

created nuclides. For short-lived nuclei fast processing is an important aspect, as these products have to be guided timely to a scientific experimental setup. Another important aspect is the variable beam energy of the radioactive ions, which determines the variety of approachable nuclear properties. These considerations and requirements lead to the following possibilities of producing RIBs. The production and investigation of radioactive nuclei with life-times smaller than microseconds is performed via the so-called In-Flight (IF) technique. The IF method uses heavy-ion beams at energies between 100 MeV/u and 4.5 GeV/u, which are guided onto light targets (typically  $^9\text{Be}$ ). Therefore, the resulting nuclei still hold high energies and high forward momentum (beam direction). Separation and identification of the nuclei is achieved via a fragment separator. A second production method is the “Isotope Separation On-Line” (ISOL) technique utilized for example at the ISOLDE facility at CERN, which is one of the most commonly applied method for investigating low-energy properties of exotic nuclei. It allows for the production of neutron-rich as well as proton-rich radioactive nuclei at very low recoil velocities. The ISOL method is associated with the following steps: (i) bombardment of a thick heavy target with protons (deuterons or neutrons after neutron conversion), including the production of nuclei caused by e.g. fission, spallation or fragmentation, (ii) the diffusion of these nuclei out of the target (typically  $\text{UC}_x$ ) into an ion source and (iii) ionization, extraction and mass separation of the desired beam. For the production of radioactive nuclei the extraction and processing time from the bombardment of the primary target to the final delivery at the experimental setup, is of major importance. This limits the application of this method to experiments with nuclei with half-lives greater than  $T_{1/2} \geq 4 \text{ ms}$  [61]. In Figure 18 the isotopes and the corresponding intensities measured at the ISOLDE facility at CERN are illustrated.

In contrast to the doubly-magic tin nuclei i.e.  $^{100}\text{Sn}$ , the production of the exotic radioactive  $^{132}\text{Sn}$  nucleus is feasible with a high cross section by asymmetric fission of actinides via the ISOL technique. Thus, the  $^{132}\text{Sn}$  nuclei was studied exploiting different techniques like,  $\beta^-$ -decay of  $^{132}\text{In}$ ,  $\beta^-$ -decay of  $^{133}\text{In}$  with following neutron evaporation, internal-conversion decay and spontaneous fission of  $^{248}\text{Cm}$ . From these measurements the level scheme up to 7.2 MeV, spins of the ground and the first-excited state, branching ratios and conversion coefficients of  $^{132}\text{Sn}$  are documented [64]. At HRIBF, Oak Ridge a first Coulomb-excitation experiment was performed to determine reduced transition strengths, which was briefly described in Section 2.2. In contrast to the Coulomb excitation at ORNL, the approach of this experiment is based on a high resolution  $\gamma$ -ray spectrometer to determine the quadrupole and octupole collectivity of  $^{132}\text{Sn}$ .



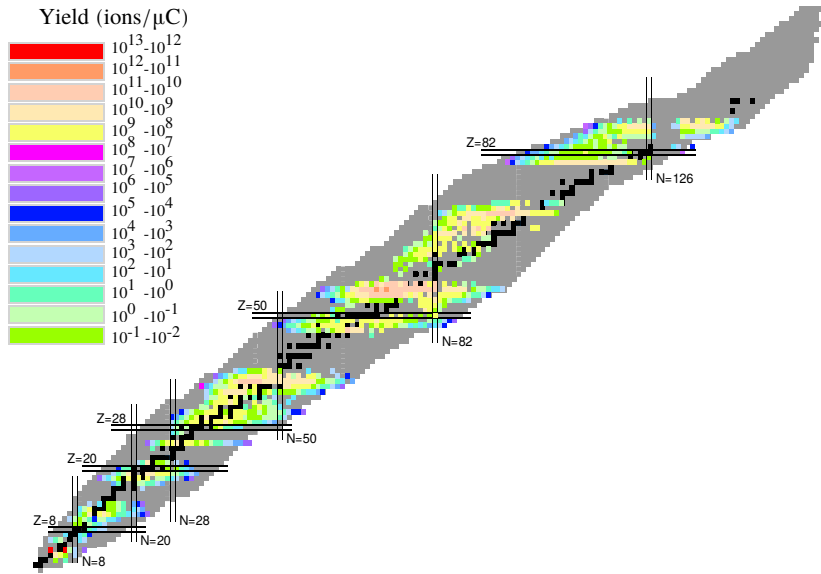


**Figure 18:** (a) Nuclear chart (grey area) with available nuclei, illustrated with a color code, and the corresponding intensities measured at ISOLDE, CERN. Data taken from Ref. [62, 63].

The reduced detection efficiency, compared to the BaF<sub>2</sub> array, is compensated by an increased Coulomb-excitation cross section due to the high beam energy of <sup>132</sup>Sn delivered by the HIE-ISOLDE accelerator (stage 1). A more detailed description of the experimental setup is given in the subsequent sections.

### 3.1. The HIE-ISOLDE facility

The initial intention for operating the ISOLDE facility at CERN, was the production of short-lived radioactive isotopes, which were not accessible at this time [65]. After the first experiments at the late 1960s, it was realized that the ISOL technique provides immense opportunities for studying nuclear physics and properties of unknown nuclei far from stability [66]. At this time the primary protons were delivered by the synchro-cyclotron (SC) with an energy of 600 MeV and intensities up to 4 μA [65, 67]. In 1992 the ISOLDE facility was upgraded, moving from the SC to CERNs Proton-Synchrotron Booster (PSB). The PSB delivers a 1.4 GeV proton beam with a maximum average intensity of 2 μA. Approximately 1300 nuclei of more than 70 isotopes can be produced at ISOLDE with intensities between 10<sup>-1</sup> to 10<sup>13</sup> ions/s. Typical energies of the singly-charged ions of the primary

ion source are between 30 keV and 60 keV. Within this range the low-energy physics at ISOLDE (e.g. solid-state, biophysics, laser spectroscopy, mass measurements, medicine experiments etc.) take place. In 2001 a further major upgrade was put into operation, the REX (Radioactive beam EXperiment) post-accelerator, which expanded the possible nuclear structure and nuclear astrophysics studies of radioactive-ion beams to energies up to 3 MeV/u. This enabled e.g. nuclear reaction studies at the Coulomb barrier [68].

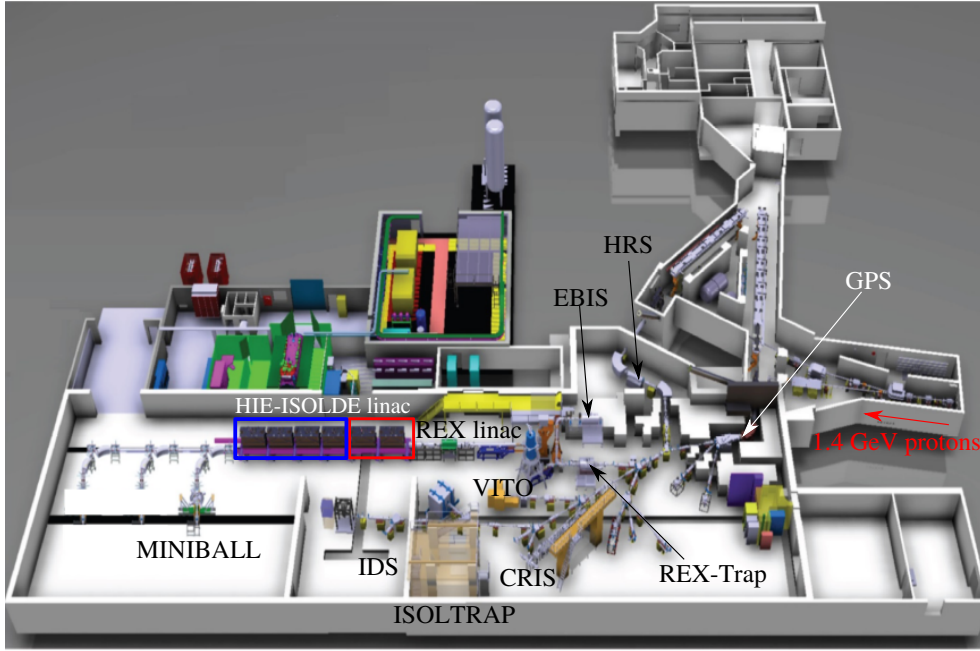


**Figure 19:** Schematical overview of the ISOLDE facility after the final HIE-ISOLDE upgrade with its various experimental setups. Marked in the red frame are the existing super conducting cryomodules (2016) and in the blue frame the missing one. Figure adapted from Ref [69] with kind permission of CERN.

The next step towards higher beam energies and new physics was in 2015, with the successive ISOLDE upgrade to HIE-ISOLDE (High Intensity and Energy). An additional super-conducting accelerator extends the post-acceleration of the radioactive-ion beam after the REX accelerator. This super conducting accelerator consists, in its final version, of four high- $\beta$  cryomodules plus two low- $\beta$  cryomodules replacing parts of REX, which will accelerate ion beams up to 10 MeV/u for nuclei with mass-over-charge ratios of 4.5. In October 2016 the first stage (stage 1) of this upgrade was finished and successfully operating, by accelerating radioactive-ion beams up to 5.5 MeV/u for nuclei with  $A/q \approx 4.5$  [68, 70, 71]. The new HIE-ISOLDE facility with its various experimental and instrumental setups is shown schematically in Figure 19.

### 3.1.1. Radioactive-ion beam production

The ISOL beam-development program started simultaneously with the operation of the ISOLDE facility [65]. This beam development is still a key player for the physics at ISOLDE and contributed to a major part to the evolution of the ISOLDE facility. Thus, continuously new target materials, target-handling techniques as well as enhanced ion sources are required to increase the beam intensity, beam purity and variety of the available radioactive ion beams at ISOLDE.

ISOLDE is integrated in the main CERN accelerator complex and profits from the pulsed 1.4 GeV proton beam of the PSB. The proton beam is guided from the PSB to the ISOLDE target with a minimum spacing of 1.2 s between the proton pulses. Its intensity can reach up to  $3.2 \times 10^{13}$  protons per pulse. This would result in a maximum integrated intensity of 4  $\mu$ A. Due to safety regulations the average integrated intensity amounts to 2  $\mu$ A, which is caused by an average 2.4 s spacing between the proton pulses impinging at the ISOLDE target [72]. At ISOLDE two separate targets can be operated simultaneously, as each target station is coupled to a different mass separator (cf. Section 3.1.3). In Figure 20 (a) a typical ISOLDE target is illustrated and a schematical cross section of this target is shown in Figure 20 (b).

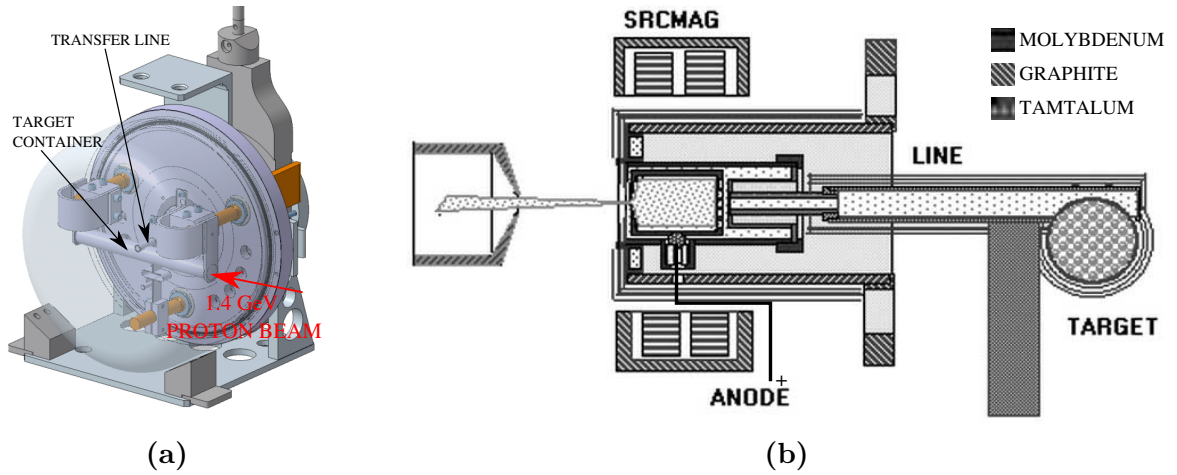


**Figure 20:** (a) CAD drawing of a typical target station at ISOLDE. Figure adapted from [73] with permission of CERN. (b) Cross section of a FEBIAD hot plasma ion source (labeled MK5). Figure adapted from [74] with permission of CERN.

As seen in Figure 20 (a) the proton beam is impinging into the target container with a length of 20 cm and 2 cm in diameter. Inside the target container, which typically consists of graphite or tantalum, the target can be stored as a powder, metal, molten metal or carbide fibers pressed in pill form. Concerning the target material many parameters have to be considered, e.g. production cross sections, release characteristics, density, mechanical and thermal resistance, melting point, target structure and the electrical conductance. These properties are important for the target selection, to maximize the beam intensity, which depends on the requested isotope. The high-energy proton beam impinging onto the thick target, produces, via fission, fragmentation and spallation processes, a variety of radioactive isotopes. Neutron-rich isotopes are produced by fission and spallation processes of heavy neutron-rich elements. Neutron-deficient isotopes are generated in fragmentation reactions with the ISOL technique. For some isotopes neutron-induced fission can yield higher beam intensities or an improved beam purity. Therefore, a proton-to-neutron converter is placed 25 mm (center to center) apart of the ISOLDE target. The converter, which typically is made of a heavy metal, e.g. tungsten, with a diameter of 12.7 mm and a length of 125 mm, is directly irradiated with the proton beam from the PSB [75]. The neutrons created by spallation reactions are used subsequently to induce fission in the ISOLDE target material.

A frequently used target is  $\text{UC}_x$  (uranium carbide), because it provides high production cross sections and fast release characteristics for many neutron-rich nuclei [76]. The target material can be heated to enhance the effusion and diffusion processes in order to increase the beam intensity. Moreover, the purity of some beams can be improved by extracting the required isotope as a molecular beam. Therefore, the chemical properties of the desired isotope are used to create a molecule predominantly with the desired isotope. Thereby possible contaminants are reduced, as the production of a chemical compound with the remaining isotopes is suppressed.

### 3.1.2. Ion sources

Three possible ion sources are used at ISOLDE to ionize the isotopes or molecules produced in the primary reaction. The simplest setup is the surface ion source, which uses a heavy metal tube (tungsten or tantalum) with a high work function. For isotopes with a low ionization potential the heated metal tube is able to strip down an electron from the atomic shell and, hence, ionize it. Tin isotopes with a relative high ionization energy of 7.3 eV [77] can not be surface ionized to a sufficient amount. The ionization energy

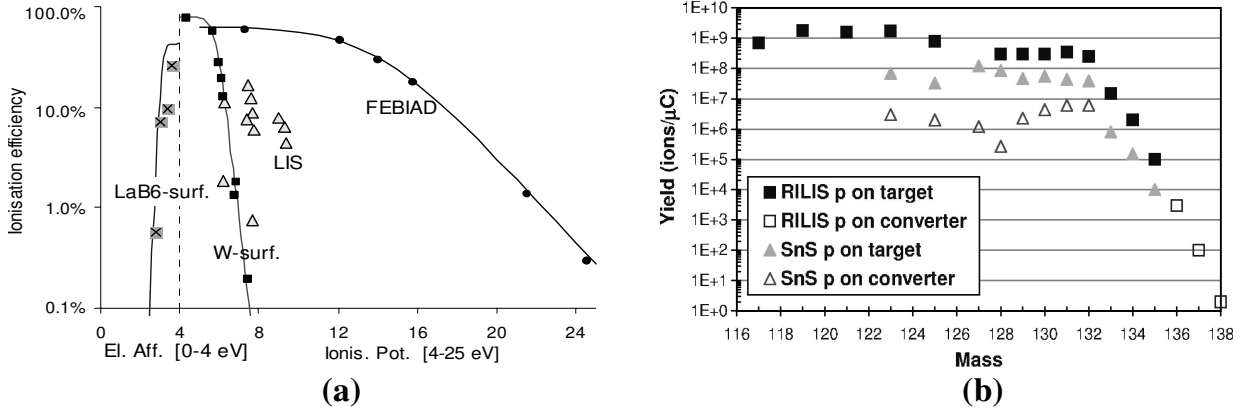


**Figure 21:** (a) Ionization efficiency as a function of the ionisation potential for different ion sources. Surface ionization is marked with squares, negative surface ionization with crossed-squares and laser ionization with triangles. For the FEBIAD source (circles) the ionization efficiency between 7-10 eV is almost constant at 80%. Figure taken from Ref. [78]. (b) Obtained yields at ISOLDE for tin isotopes with direct and indirect target irradiation with a proton beam following ionization of atomic tin with RILIS and molecular tin sulfid with a hot plasma source. The RILIS ionization of tin shows a yield which is one order of magnitude higher than the yield of SnS obtained with plasma ionization. The difference in the intensity is caused mainly by a conservative operation of the hot plasma source to avoid damages of the tantalum cathode. Nevertheless, the purity of the beam extracted with SnS molecules is much higher. Figures taken from [75] with kind permission of Elsevier.

of SnS amounts to 9.13 eV, thus making surface ionization not applicable [75] (compare Fig. 21 (a)).

A more advanced method is the laser ionization. Intense laser pulses are tuned in resonance to strong excitation transitions of the specific atom to remove one electron from its shell. Typically laser ionization is a multi-step process. The Resonance Ionization Laser Ion Source (RILIS) method was already used successfully for ionization of light tin isotopes at ISOLDE [79]. This procedure allows to suppress the heavier Sb, Te, I and Xe isotopes as their ionization energy is greater than 8.6 eV. Nevertheless, Cs, Ba and In with ionization energies smaller than 6 eV are also produced very efficiently and lead to a contamination of the beam. However, the ionization efficiency via the RILIS is not applicable for SnS (Figure 21 (a)), as the energy transfer to the molecule would cause a photodissociation of the molecules. For more details concerning these two methods see Ref. [80].

### Plasma ion source

As previously mentioned, to enhance the beam purity and obtain a high intensity of  $^{132}\text{Sn}$ , it is possible to synthesize and extract SnS [81]. This will reduce the main contamination caused by caesium, as caesium will not build a chemical compound molecule with sulfur. The same is true for the noble gas Xe. A further advantage is the desorption time of SnS, which is two orders of magnitude smaller than the desorption time of tin [75]. This reduces the release time of SnS out of the target significantly and improves the efficiency, i.e. the beam intensity at this point, especially for short-lived isotopes [75]. The synthesized molecules are ionized with a hot plasma source. The tantalum transfer line is heated up to  $1900^\circ\text{C}$ , as higher temperatures will not improve the ionization efficiency due to higher background from material evaporation [82]. The transfer line is equipped with a thin molybdenum tube with enriched sulfur to allow the production of SnS. The plasma is typically generated with Xe and Ar, via accelerated electron impact.

The SnS molecules as well as the electrons are produced in the heated transfer line and diffuse into the plasma chamber. The electrons are accelerated between a disc-shaped cathode inside the transfer line and the extraction anode inside the plasma chamber. Typical voltages applied for the electron acceleration are between 100 V and 200 V. This enables for an efficient ionization of elements with high ionization potentials. The plasma temperature  $T_p$  has to be maintained in the way that  $k_B T_p \geq W_{\text{SnS}}$ , where  $W_{\text{SnS}}$  denotes the ionization energy of SnS [80]. The ionization of the molecules is caused by electron impact, stripping and pick-up collisions with the plasma ions. The ionization efficiency is enhanced by an additional magnetic field, perpendicular to the beam axis, which increases the molecules persistence in the plasma. For the present experimental setup, the Forced Electron Beam Induced Arc Discharge (FEBIAD) source was used (see Fig. 20 (b)). This type of plasma source provides an ionization efficiency of around 80% for tin sulfide (cf. Fig. 21 (a)) and operates successfully at low gas pressures of  $10^{-4}$  to  $10^{-5}$  mbar [83]. The ion beam intensities of the FEBIAD ion source are in the range of 1-10  $\mu\text{A}$  [82]. For more details of the FEBIAD ion source see Ref. [83, 84].

#### 3.1.3. Mass separators

The molecules are ionized to a charge state  $q = +1$  and extracted by an external electric field of 30 keV to 60 keV at the extraction anode of the ion source. After the extraction, it is important to select the desired molecules and guide these to the experimental setup.

The mass-over-charge ( $A/q$ ) selectivity is achieved with two different mass separators, the General Purpose Separator (GPS) and the High Resolution Separator (HRS). Each of these mass separators is connected to an individual target station, allowing for a very flexible operation and RIB delivery. Both separators are feeding one common beam line, which in turn delivers the beam to the majority of all available experimental setups at the ISOLDE facility. In the following subsection the HRS will be described in more detail, as this separator was in operation during the presented experiment. For a specification of the GPS, see Ref. [72].

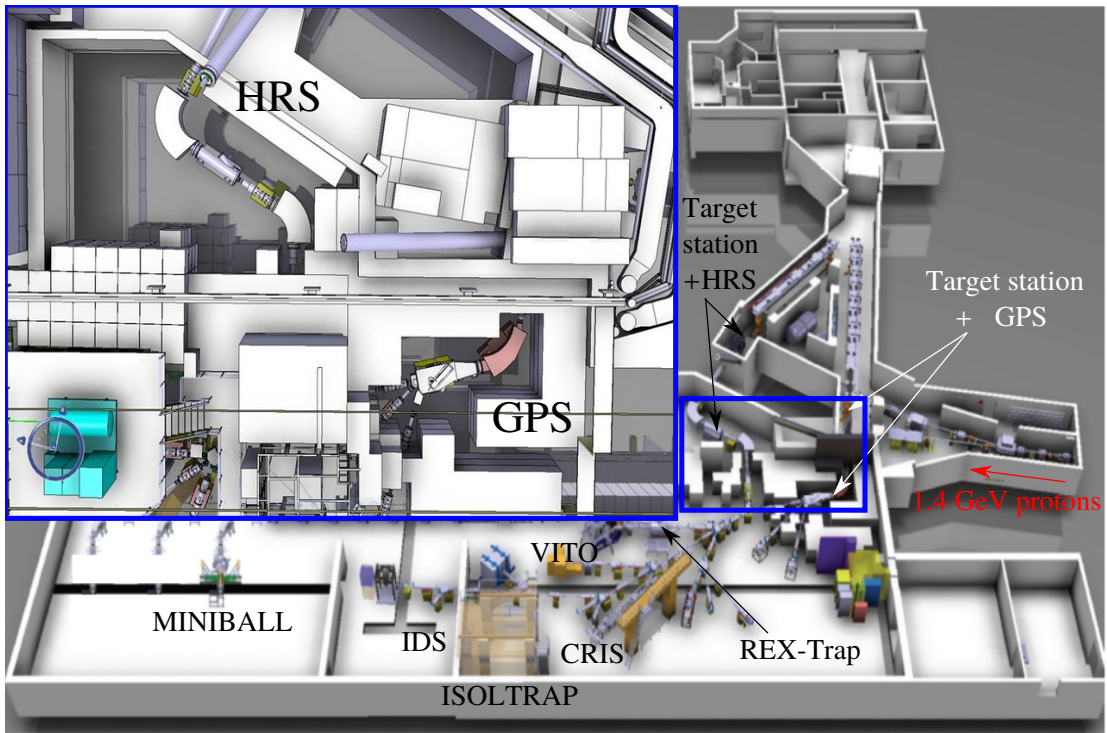


**Figure 22:** CAD drawing of the ISOLDE hall with an inset of the mass separators HRS and GPS. More details about the setup are given in the text. Figure adapted from Ref. [69] with kind permission of CERN.

## HRS

The High Resolution Separator can be divided in two separator stages. The first stage comprises three electrostatic quadrupole lenses, followed by the double focusing  $90^\circ$  C-magnet with 1 m bending radius and higher-order correction elements. These correction elements consist of a 32-pole electrostatic multipole in octopole configuration together with pole face windings in the magnet in hexapole configuration. The second stage has a



comparable structure. Two electrostatic lenses and a second dipole magnet with a bending angle of  $60^\circ$  are followed by two electrostatic multipoles (32-poles in octopole configuration) for higher-order corrections. As illustrated in Figure 22, the magnets of the HRS are positioned in opposite directions, which has the advantage that no additional focussing element is needed between the two stages. The total mass resolving power of the HRS is  $M/\Delta M = 7000$  with higher-order correction elements turned off, while reaching up to  $M/\Delta M = 15000$  with higher-order corrections [72].

### 3.1.4. Post accelerator

After mass separation, the radioactive ion beam is delivered to several experimental setups at the low-energy area of ISOLDE with its initial beam energy of typically 30-60 keV. Radioactive ion beams with these low energies are used for investigations of ground-state properties,  $\beta$ -decay studies, solid-state physics, biophysics or medicine experiments. During the mid 1990s, after ISOLDE had been moved to the PS Booster, the REX project was approved by the CERN Research Board. This was the consequence of the interesting new physics opportunities with post-accelerated radioactive ion beams with energies of a few MeV/u [67]. The Radioactive beam EXperiment (REX) project was devoted to bunching, charge breeding and post acceleration of the low-energy beam at ISOLDE. The post-acceleration unit comprises a penning trap (REXTRAP) for decelerating and bunching of the beam, followed by a charge-breeding system (REXEBS). The setup is illustrated on the right side of Figure 23.

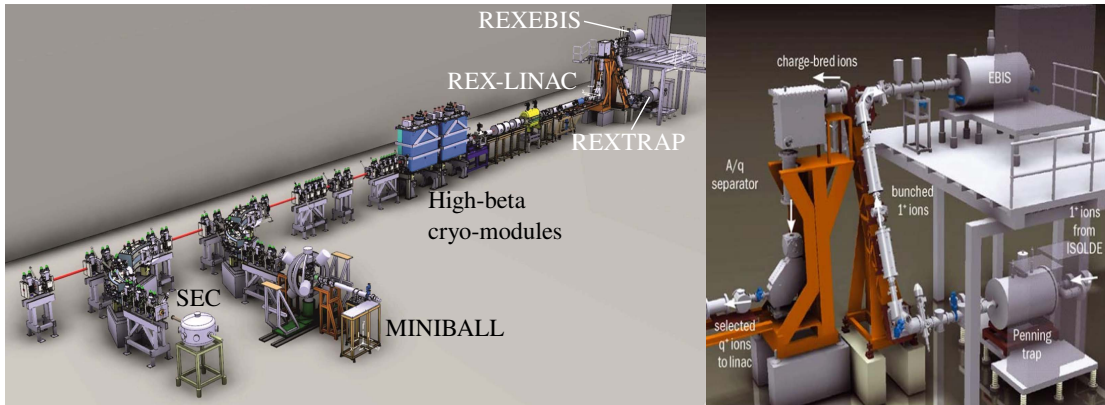


**Figure 23:** Left: Schematic illustration of the experimental setup of the REX-ISOLDE and first stage HIE-ISOLDE instruments. Right: Schematic drawing of the charge breeding system with the basic work-flow description. Figures taken from [68] with permission of CERN.



Inside REXEBIS the singly-charged ion beam is processed to higher charge states via electron-beam ionization. This procedure is essential to avoid a large-scale accelerator and instead be able to reach moderate energies with a compact and effective accelerator (REXLINAC). The REX linear accelerator is coupled to the charge breeding system via an  $A/q$  separator. Since the operational start of REX-ISOLDE in 2001 over 100 isotopes, from  ${}^6\text{He}$  up to  ${}^{224}\text{Ra}$ , were post-accelerated and studied in Coulomb excitation or transfer reactions [61, 70]. In order to achieve even higher beam energies, the HIE-ISOLDE project was initiated [71]. A schematical configuration of the REX- and current HIE-ISOLDE setup is shown in Figure 23 (Left). The first stage of the new super-conducting linear accelerator, with two newly installed high-beta cryo-modules, which are mounted behind the REX-LINAC, allowed to enhance the beam energy from 3.0 MeV/u up to 5.5 MeV/u. The first stage of the HIE-ISOLDE project was finished in 2016 and started successful operation in September of the same year [70]. Further stages will upgrade the super-conducting LINAC to comprise finally six cryomodules, which will be able to accelerate the radioactive ion beam to energies up to 10 MeV/u for nuclei with  $A/q \approx 4.5$  [68].

## REXTRAP

A Penning trap can be employed to provide cooled and bunched ion beams. These are essential for operating charge-breeding systems with high efficiency, e.g. EBIS and radio-frequency accelerators, which are also used at ISOLDE.

The mass-separated singly-charged ion beam is continuously injected into the cylindrical shaped Penning trap REXTRAP, which has a diameter of 5 cm and a length of 0.9 m [87]. REXTRAP is divided in a stopping and a trapping region, both filled with Ne and/or Ar as a buffer gas [87, 88] (cf. Fig. 24 (a) top left). Incoming ions are cooled by collisions with the buffer gas and trapped by an applied High-Voltage (HV) field. This process typically takes  $\sim 20$  ms [85]. Charge exchange collisions are avoided, due to the high ionization potential of Ne/Ar noble gases. The pressure in the trapping region amounts to around  $10^{-4}$  mbar, whereas the pressure in the stopping area is one order of magnitude larger to increase the energy loss of the ions. In addition, an applied 3 T magnetic field allows the confinement of ions in the center of the trap. Within the applied electric and magnetic fields, the ions are forced to a magnetron motion around the trap center, a reduced cyclotron motion and an axial motion (harmonic oscillation). The cooling via collisions with the buffer gas, disturbs the magnetron motion of the ions and increase their orbits. Recentering of the

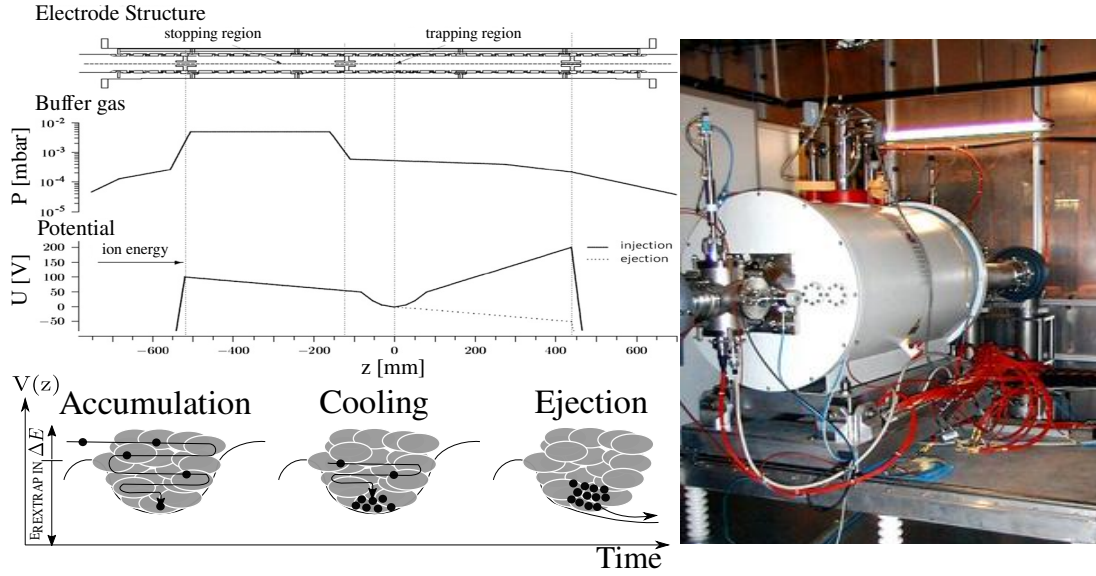


**Figure 24:** Top left: Schematic drawing of the Penning trap with the used electrode configuration. Middle: Corresponding gas pressure and potential along REXTRAP. The left bottom Figure illustrates schematically the working principle of the Penning trap. Right: Image of REXTRAP at ISOLDE, CERN. Figures adapted from [85, 86] with permission from Elsevier and CERN.

ions of interest is achieved by applying a radio-frequency field with the cyclotron frequency matching the desired ions mass  $\omega_C = q/mB$ . This procedure, which improves the purity of the beam, is called side band cooling [87]. The typical mass resolution of the side band cooling amounts to  $M/\Delta M \approx 500$  [87] and depends on the gas pressure in the trapping region.

## REXEBS

After the continuous beam is decelerated and bunched, the ions are injected via an efficient electrostatic achromatic transport line into the Electron Beam Ion Source (EBIS) for charge breeding [89]. This charge breeding is essential, to facilitate a post acceleration up to 5.5 MeV/u with the subsequent compact linear accelerator. As illustrated in Figure 23 the connection to REXEBIS is realized by two 90° kicker benders. REXEBIS allows for an  $A/q$  ratio in the range between  $2.5 \leq A/q \leq 4.5$ . The upper limit of the  $A/q$  ratio is limited by the REXLINAC properties (see Sec. 3.1.4). The charge breeding in the EBIS is achieved by electron impact. The incoming ions are confined in a 0.8 m big trapping region and bombarded with an electron beam, which is provided by an electron gun (cathode). The electron beam is transversally focused by employing a 2 T magnetic

field of a 1.2 m long superconducting solenoid [90]. The confinement of the ions is generated by the negative space charge of the electron beam inside the magnetic field and the electric field of electrodes at the front and back side of the REXEBIS (cf. Fig. 25). This trapping enhances the phase-space overlap between the electron beam and the confined ions, which leads to an improved breeding efficiency of the EBIS. For a successful injection of the beam into the EBIS a low extraction emittance of REXTRAP  $< 15 \text{ mm}\cdot\text{mrad}$  is required [91]. The electron gun produces 3-6 keV electrons with a typical current of 200 mA, that can be increased up to 460 mA. A high current beam density of  $100 \text{ A/cm}^2$  is accomplished by the external magnetic field [89]. The breeding time depends on the mass-over-charge ratio, which is needed for the isotope of interest. Between 5 ms, for  $A < 10$  nuclei, up to some hundreds of milliseconds for  $A > 200$  isotopes are necessary to reach the proper  $A/q$  ratio [68]. The extraction time out of the EBIS is manipulated by adjusting the extraction barrier. For light nuclei the extraction time is typically in the range of tens of microseconds, whereas for heavy nuclei  $A > 150$  it will take longer than 100  $\mu\text{s}$ .

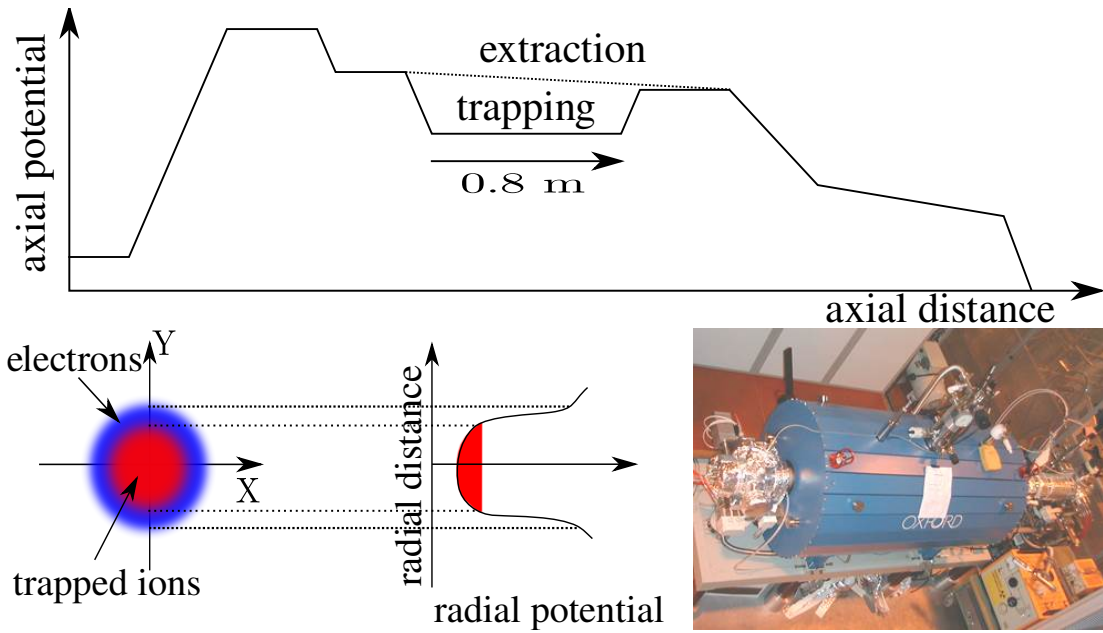


**Figure 25:** Top: Axial potential along the EBIS with the 0.8 m long magnetic field for the confinement of the ions. For the ejection the potential is lowered to about 20 kV. Bottom left: Radial potential caused by the space charge of the electron beam. See text for more details. Figure adapted from [92] with kind permissions of CERN. Bottom right: Picture of REXEBIS at ISOLDE inside the 1.2 m long solenoid. Figure taken from [92] with kind permission from CERN.

This has an impact on the instantaneous particle rates at the experimental setup [89]. It is possible to increase the extraction time up to 800  $\mu\text{s}$  [91] to obtain an equal/constant count rate over the extraction time. This is relevant in order to avoid a huge dead time of the DAQ system or pile-up signals in the recorded data. Following the extraction from REXEBIS the beam has to be separated with respect to the  $A/q$  ratio, as contaminations may overweight the desired radioactive isotopes. Most contaminations, e.g. carbon, oxygen, nitrogen, neon and argon are mainly caused by residual gas inside REXEBIS. Hence, an ultra-high vacuum of  $10^{-11}$  mbar inside the EBIS is required to improve charge breeding and simultaneously suppress the production of contaminations due to ionization of residual gas atoms.

### $A/q$ separator

The mass separator connecting the REXEBIS with the REXLINAC is mounted in a vertical S-shape structure. A  $90^\circ$  electrostatic deflector followed by a  $90^\circ$  magnetic bender are used to select the proper  $A/q$  ratio and suppress contaminations. The ions released by REXEBIS exhibits an energy spread of  $\Delta E/E = 5 \times 10^{-3}$ , which can be restricted by the electrostatic deflector. The beam is limited in energy, independent of the ions masses. The selective  $A/q$  filter is the subsequent bending magnet, which sufficiently eliminates a major amount of contaminants. The typical mass resolving power for this system amounts to  $M/\Delta M \sim 150$  [94]. Nevertheless, contaminants with similar energy as well as with similar  $A/q$  ratio will pass the mass separator and reach the final experimental setup. The expected contaminations from the REXTRAP and REXEBIS were mentioned in the previous section. Figure 26 shows an example of the EBIS beam after charge breeding  $^{129}\text{Cs}$ .

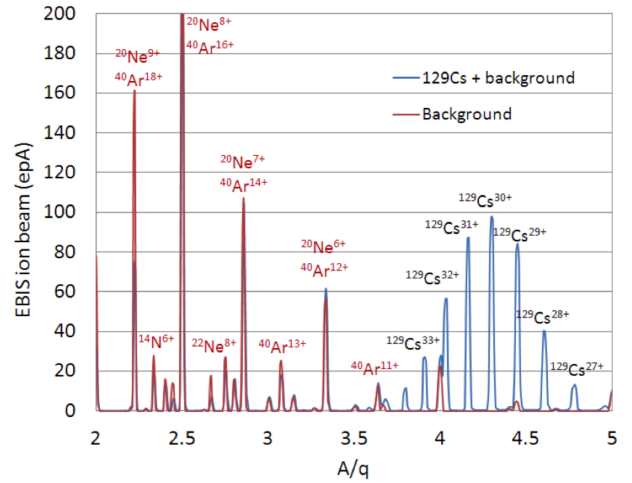


**Figure 26:** Intensity of the extracted ion beam from EBIS as a function of the  $A/q$  ratio. In blue, the injected and charged breed  $^{129}\text{Cs}$  isotope with a maximum intensity at a charge state of  $q = 30^+$  is shown. Furthermore, the residual gases inside REXTRAP and REXEBIS are present in the extracted beam. For this case  $^{129}\text{Cs}^{30+}$  can be well separated from the contaminations. Figure taken from [93] with kind permission of CERN.

## REXLINAC

The bunched and separated ion beam is injected into the compact linear accelerator of REX. The REXLINAC is a room-temperature linear accelerator, which was designed to post-accelerate radioactive-ion beams with  $A/q \leq 4.5$ . The structure of the REXLINAC is composed out of a radio-frequency quadrupole accelerator (RFQ), an interdigital H structure (IH), three 7-gap resonators and a 9-gap resonator. The ion beam is injected into the four-rod  $\lambda/2$  RFQ accelerator with an energy of 5 keV/u. The RFQ unit accelerates the beam up to 300 keV/u and injects it into the IH structure, by passing a split-ring rebuncher to modify the longitudinal beam parameters. The 20-gap IH cavity operates at a frequency of 101.228 MHz and increases the beam energy up to 1.2 MeV/u [95].

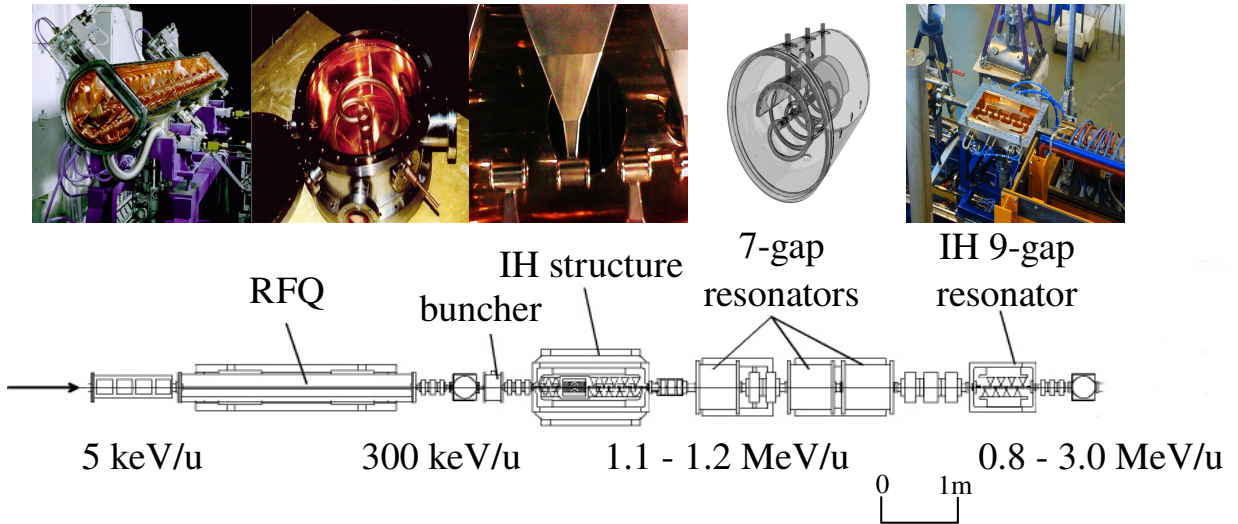


**Figure 27:** Schematical structure of the REXLINAC with images from maintenance work in open status for the single units. Further information is given in the text. Figures taken from [96] with kind permission of CERN.

The adjacent system of three 7-gap split-ring resonators, operating at the same frequency, allows to adjust the beam energy in the range from 0.8 MeV/u up to 2.2 MeV/u. The last boost in beam energy can be achieved with the 9-gap IH unit, operating at twice the frequency of the 7-gap resonators. This can enhance the beam energy up to 3.0 MeV/u ( $A/q < 3.5$ ).

The beam intensity and the time structure is constrained by several parameters. These are the proton repetition time, release characteristics of the primary ISOLDE target, the charge breeding and bunching as well as the duty cycle (typically 10%) of the accelerator [97].

The beam intensity can vary between few 100 up to  $10^7$  ions/s, which is measured with Faraday cups, multi-channel plates (MCP) and phosphor screens [68]. If the intensity of the desired beam is below 0.1 pA the measuring devices are not able to directly detect the beam. Therefore, the accelerator adjustments are performed with a stable beam with sufficient intensity and similar  $A/q$  as the final isotopes, to obtain the set of accelerator parameters [68].

## **HIELINAC**

An additional energy improvement will increase the scientific opportunities of the ISOLDE facility. The energy upgrade includes the expansion of the existing REXLINAC with an additional superconducting linear accelerator, high energy beam transfer lines (installed 2015) and three experimental beam lines [68].

In 2006 it was decided to build a superconducting (SC) linear post-accelerator to achieve HIE-ISOLDE's energy upgrade. The large electric gradients, provided by this kind of accelerator, allow for a compact, space-effective construction and positioning in the limited space of the ISOLDE hall [101]. The design of the cryomodules benefited from the experience of the LHC, TRIUMPH and ALPI facilities. This composition of REXLINAC and the newly installed first stage superconducting accelerator, which is based on quarter-waver resonators, is the ISOLDE HIELINAC. In total six cryomodules with in total 32 radiofrequency cavities will be assembled to the final superconducting linear post-accelerator at ISOLDE.

The upgrade of the post-accelerator is divided into three stages [71]: (I) The first stage included the process from designing up to commissioning of two cryomodules. In 2015, the first beam was delivered by HIE-ISOLDE with one cryomodule operating. The second cryomodule was installed in 2016. Both cryomodules comprised five superconducting high-beta ( $\beta = 10.3\%$ ) cavities, with 300 mm diameter, operating at 101.28 MHz, and a superconducting solenoid magnet [71]. The operation of both cryomodules in 2016 allowed to enhance the beam energy up to 5.5 MeV/u for nuclei with  $A/q \leq 4.5$ . The aim of the solenoid, with a maximum strength of 7 T, is to decouple the transverse and longitudinal motion of the ions inside the cavities and, hence, reduce the beam emittance and losses. (II) Subsequently the next two cryomodules, with the same specification, will be mounted. Already in 2017 the third cryomodule was mounted in the ISOLDE hall (cf. Fig. 28) [68, 70]. Completion in 2018 was achieved! The ultra-high vacuum coating chambers of the



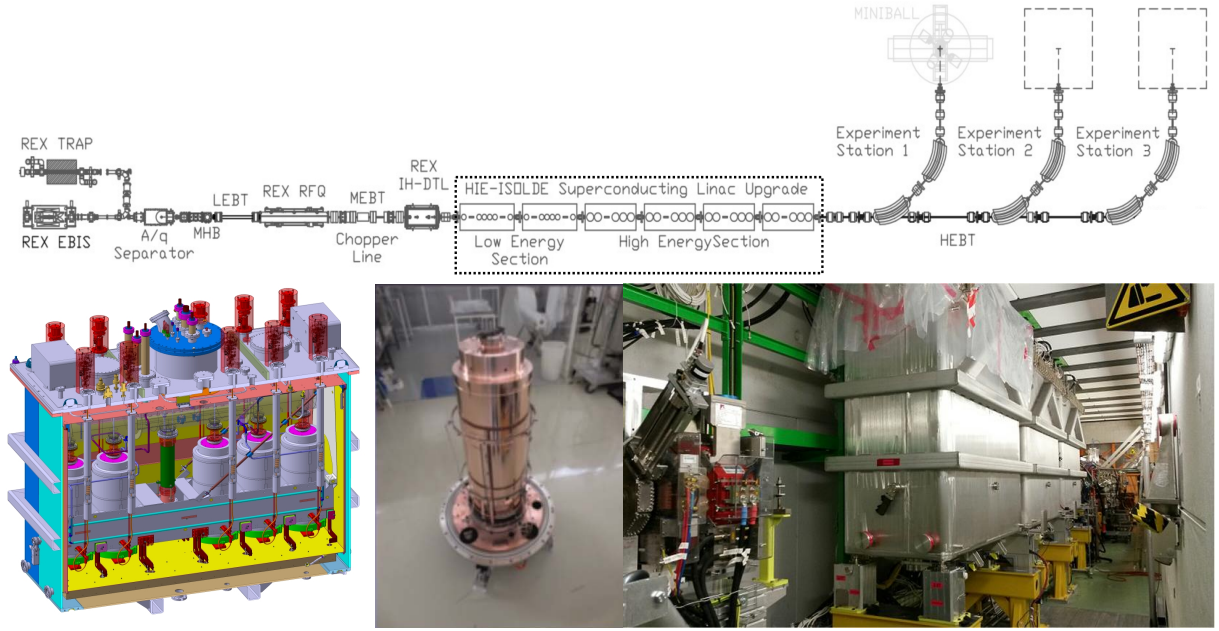


**Figure 28:** Top: Schematic setup of the final HIE-ISOLDE beam line. Bottom left: CAD drawing illustrates the installation of one high-beta cryomodule. Five high-beta RF cavities are mounted under the liquid He reservoir and divided in two groups by the superconducting solenoid. For the low-beta cryomodules a similar configuration will be realized, however they will contain six RF cavities and two solenoids. Bottom middle: Image shows a RF cavity after assembly in a clean room. Bottom right: Picture represent the status of the HIELINAC at ISOLDE at the beginning of 2017 with three cryomodules already mounted at their final position. Figures taken from [68, 98–100] with kind permission of CERN.

cryomodules operate at  $10^{-10}$  mbar at cooled state. Accelerator gradients are specified to be 6.0 MV/m with less than 10 W power dissipation at 4.5 K operational temperature [68, 71]. (III) The final step will replace the 7-gap and 9-gap structures from REXLINAC with two cryomodules. Each of this modules will contain six low-beta ( $\beta = 6.3\%$ ) cavities (180 mm diameter) and two superconducting solenoid magnets. During this stage the remaining REXLINAC will be upgraded by the installation of a pre-buncher and beam copper at the RFQ, to increase the transmission and efficiency of REXLINAC. After this upgrade the HIELINAC will be able to provide post-accelerated ion beams with energies up to 10.0 MeV/u and variable energy without degradation of the beam quality.

The intensity upgrade of HIE-ISOLDE is dedicated to a more effective use of the improved proton beam from the upgraded PSB [102]. Therefore, efforts are ongoing to improve the target and ion source system, the mass separators and other related instruments to this section [68].

### 3.1.5. Beam time structure

As discussed in the previous sections the radioactive ion beam at HIE-ISOLDE is bunched. In Figure 29 a typical time structure at ISOLDE is illustrated. The time structure of the ion depends on different factors e.g. time of the delivered proton beam, release characteristics of the target and ion source, decay of the desired radioactive ions and the duty cycle of the bunching, breeding and accelerating devices. To keep control over the whole sequence from the proton impact to the radioactive ion-beam delivery at the experimental setup, various timing signals are provided. The first signal is available at the start of each super-cycle of the PSB. A super cycle is a sequence of individual preset cycles with a length of  $n \times 1.2$  s,  $n \in \mathbb{N}$ . This time signal is auxiliary if laser ionization is used to estimate the beam composition. Therefore, the signal is used as a trigger for a shutter, which blocks the laser and allow for the estimation of contaminants in the extracted radioactive-ion beam. In each super cycle

proton pulses with a  $n \times 1.2$  s margin are delivered to the ISOLDE facility. For the  $^{132}\text{Sn}$  experiment 8 out of 22 possible proton pulses were available for ISOLDE. The second marker T1 is correlated to the proton-beam impact onto the ISOLDE target. The time difference between T1 and the detection

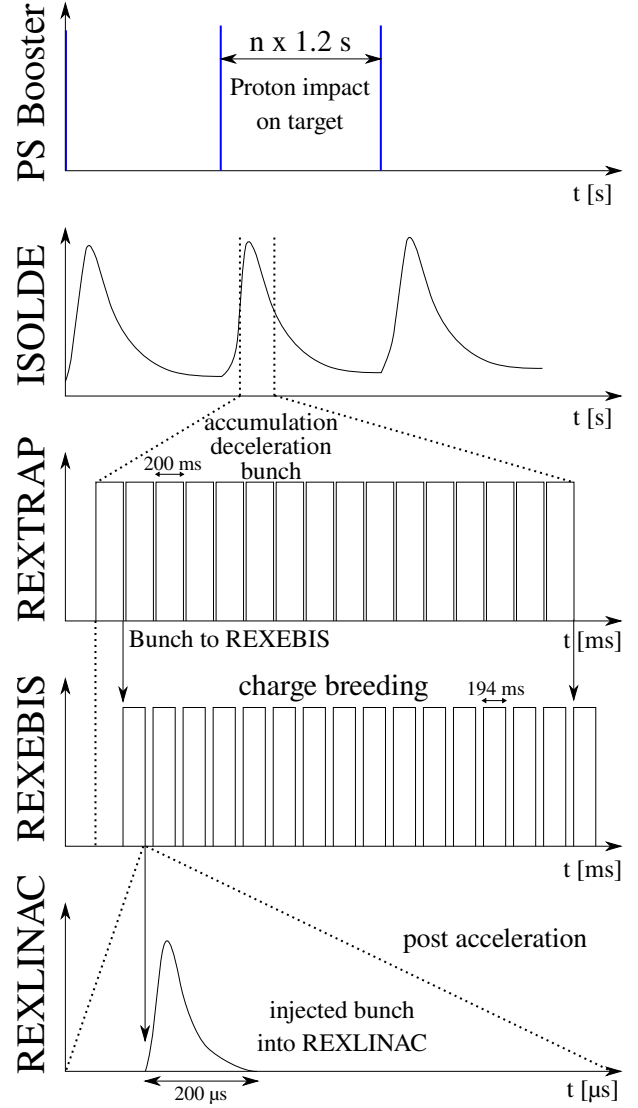


**Figure 29:** Time structure of the radioactive-ion beam at ISOLDE. For more details see text.



of the radioactive ion beam at the experimental setup, can be used to discriminate constant background or to identify contaminations, as radioactive nuclei have characteristic lifetimes and release times. Thereby, the measurement can be restricted to the desired isotope. Longer-lived and stable isotopes can be suppressed or vice versa. A third flag is set by the ion ejection from REXEBIS. This signal is used to synchronize the injection into the REXLINAC and enables a proper acceleration and transmission. Further, it is used to start a 1 ms long "ON beam" window for the data acquisition system (DAQ) of the MINIBALL detection system (see section 3.1.6). Depending on the release time and beam distribution out of REXEBIS a further discrimination can be achieved to suppress background radiation. Typical length of the beam bunch out of the EBIS is 200  $\mu\text{s}$  with fast extraction and 800  $\mu\text{s}$  for slow extraction.

### 3.1.6. MINIBALL setup

Unlike stable isotopes, the beam intensity of rare radioactive isotopes far from stability can be quite low. In addition, doubly-magic nuclei, e.g.  $^{132}\text{Sn}$ , have high transition energies and, thus, low excitation cross sections which impede the measurement of excited states via Coulomb excitation.

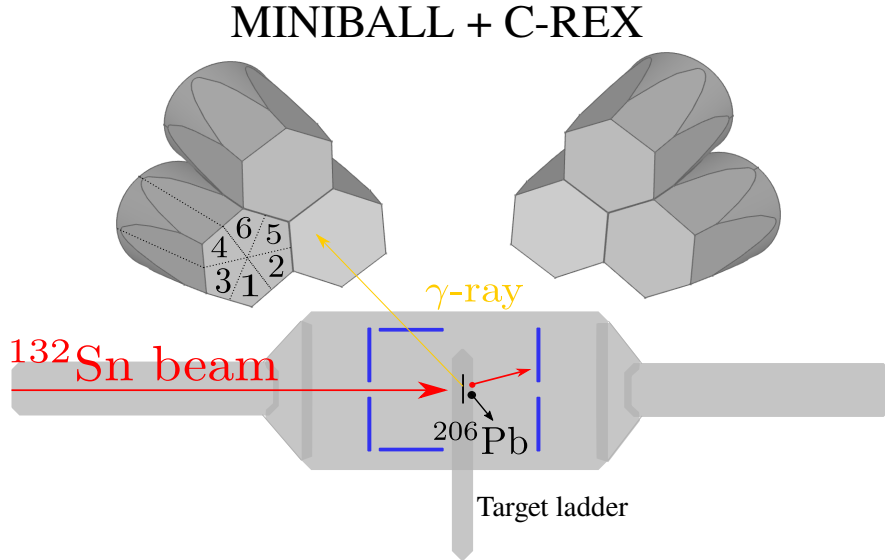


**Figure 30:** Schematic illustration of the MINIBALL + C-REX setup used in the experiment. DSSSD particle detectors are illustrated with blue elements. The particle information was obtained with the forward CD, whereas the  $\gamma$ -rays were detected with the highly efficient MINIBALL spectrometer consisting of eight triple-cluster HPGe detectors. The segmentation of the HPGe detectors is illustrated for one crystal.

Furthermore, the high beam energy of 5.5 MeV/u and related  $^{132}\text{Sn}$  ion velocity ( $\frac{v}{c} \approx 10\%$ ) result in a significant Doppler shift and broadening of the interesting transition  $\gamma$ -rays. The combination of low radioactive ion-beam intensity, high transition energies and low excitation cross sections require a highly efficient and position sensitive  $\gamma$ -ray detection system. Therefore, the MINIBALL array in conjunction with the so-called C-REX setup was utilized at HIE-ISOLDE to allow such a demanding measurement. A schematical overview of the experimental setup is illustrated in Figure 30.

### The MINIBALL Spectrometer

The MINIBALL array started operation at ISOLDE in 2001 and is used since then successfully for multiple Coulomb-excitation and transfer-reaction experiments [103]. The MINIBALL array comprises eight triple cluster detectors, which are mounted inside the MINIBALL frame. This frame was constructed to guarantee maximum flexibility for positioning the MINIBALL cluster detectors. The triple clusters are mounted on arms enabling the positioning of the detectors in three dimensions (see Fig. 31).

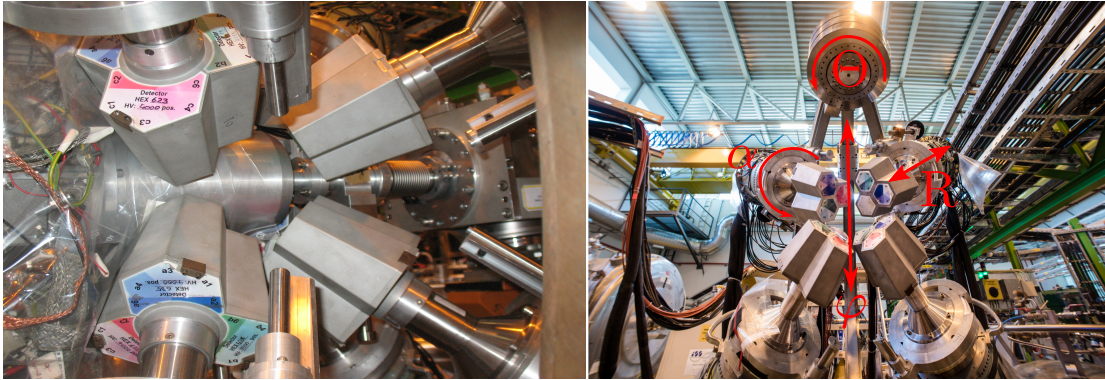


**Figure 31:** Left: Picture of the MINIBALL spectrometer arranged around the target chamber used for the C-REX setup. Figure from Ref. [104]. Right: Four triple cluster detectors mounted on one half of the MINIBALL frame. The degrees of freedom for the positioning of the triple cluster are marked. The flexibility of the frame allows the adjustment of the detectors as close as possible to the target, which results in a highly efficient setup. Figure adapted from Ref. [105] with kind permission of CERN.

Each triple cluster detector contains three individually encapsulated six-fold segmented High-Purity Germanium crystals (HPGe). Fig. 32 illustrates a triple cluster and a schematic picture of three encapsulated HPGe crystals. The tapered germanium crystals are 78 mm long and have a diameter of 70 mm. The tapering angle amounts to  $4.125^\circ$ . The weight

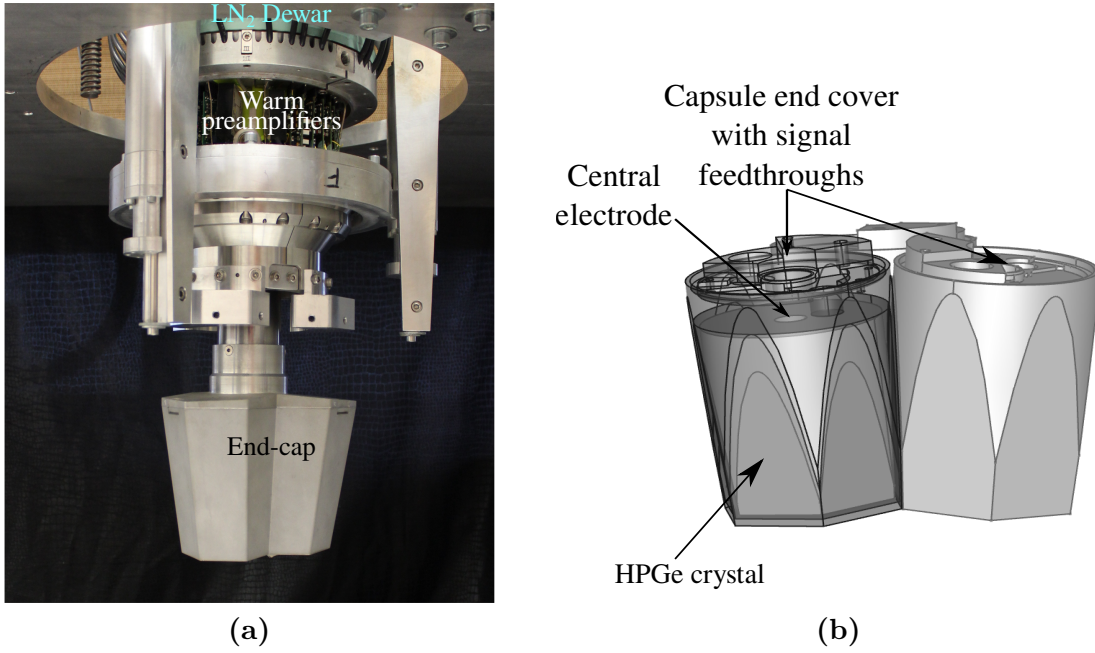


**Figure 32:** (a): Picture of one MINIBALL triple-cluster detector inside a scanning table. Right: Schematical drawing of a triple configuration of the six-fold segmented encapsulated HPGe detectors. The HPGe detectors are mounted in a 0.7 mm thin aluminum can with 0.7 mm spacing between the HPGe crystal and the can. The signal cabling inside the capsule as well as the mechanical mounting is not shown. The cold electronics is mounted on top of the capsule lid.

of one HPGe crystals amounts to approx. 1 kg. In total 144 individual segment signals and 24 additional signals from the central electrode are measured. The high granularity of the system reduces the opening angle of the detection and, therefore, enhances the position sensitivity [103, 106]. In particular this aspect is important for in-flight emitted  $\gamma$ -rays with  $\frac{v}{c} \sim 10\%$ , as they are detected with large Doppler shifts which have to be corrected. Especially for close detector-target distances the position sensitivity is valuable. As the beam intensities and excitation cross sections are quite low for radioactive isotopes far from stability, high detection efficiency is an indispensable condition. Thus, the MINIBALL array operates at close as possible detector-target distances to maximize the detection efficiency. In an experiment with a spherical target chamber and a detector-target distance of approx. 12 cm, the MINIBALL array provides a photopeak efficiency of about 8% at 1.332 MeV, by covering 60% of the total solid angle [106]. The C-REX target chamber (see Fig. 31) is not spherical but barrel-like. The absolute efficiency is decreased to about 5 – 6% as the detector-target distances increase [107]. The energy resolution of

the MINIBALL spectrometer after addback, measured with a  $^{60}\text{Co}$ , amounts to 2 – 3 keV at 1.332 MeV. This good energy resolution is achieved by operating the detector system and the charge-depending electronics at almost liquid-nitrogen temperature ( $\sim 90$  K). The signals from the detector system are processed with digital electronics (“Digital Gamma Finder”, DGF XIA electronics), to enable high count rates and allow for a proper event building [106].

### Particle detector

To perform Doppler-correction, the emission angle information of the emitted  $\gamma$ -ray has to be combined with the momentum vector of the deexciting emitting particle. A Double-Sided Silicon Strip Detector (DSSSD) was installed additionally to the HPGe array to measure the ion position and energy. The DSSSD was composed out of four identical quadrants, that were assembled to an annular structure (cf. Fig 33). The thickness of each quadrant is 138  $\mu\text{m}$  with a typical dead layer of 200 nm. The inner diameter of the annular detector amounts to 9 mm and the outer diameter to 40.9 mm. Each quadrant is divided on one side into 16 annular strips (front side) and on the other side in 24 strips (back side). The 16 annular rings at the front side have a pitch of 2.0 mm. On the back side the 24 strips are arranged in a  $3.5^\circ$  pitch with a  $3.4^\circ$  opening angle [108]. For this experiment the 24 strips on the back side of each quadrant were interconnected to 16 strips. The 16 innermost strips were shorted to 8 strips. The back side effectively consists out of 16 strip with  $3.4^\circ$  opening angle for the outermost strips on each side and  $6.9^\circ$  for the innermost eight strips. In total  $4 \times 256$  pixels were available for the detection of the scattered ions, which allows for a two dimensional tracking of the particles perpendicular to the beam axis. This high granularity causes an improvement of the Doppler-correction. The DSSSD was place 32 mm downstream the target with respect to the incoming beam. Hence, the DSSSD detector covered forward scattering angles between  $16^\circ$  up to  $53^\circ$  in the laboratory system, with respect to the beam axis. The backward barrel and backward CD silicon detectors were mounted but not in operation, as the desired scattering range is limited by the kinematics of the reaction below  $42^\circ$  in the laboratory frame (cf. Sec. 5.4). Details about the detector properties of the backward DSSSD system can be found in Ref. [107].

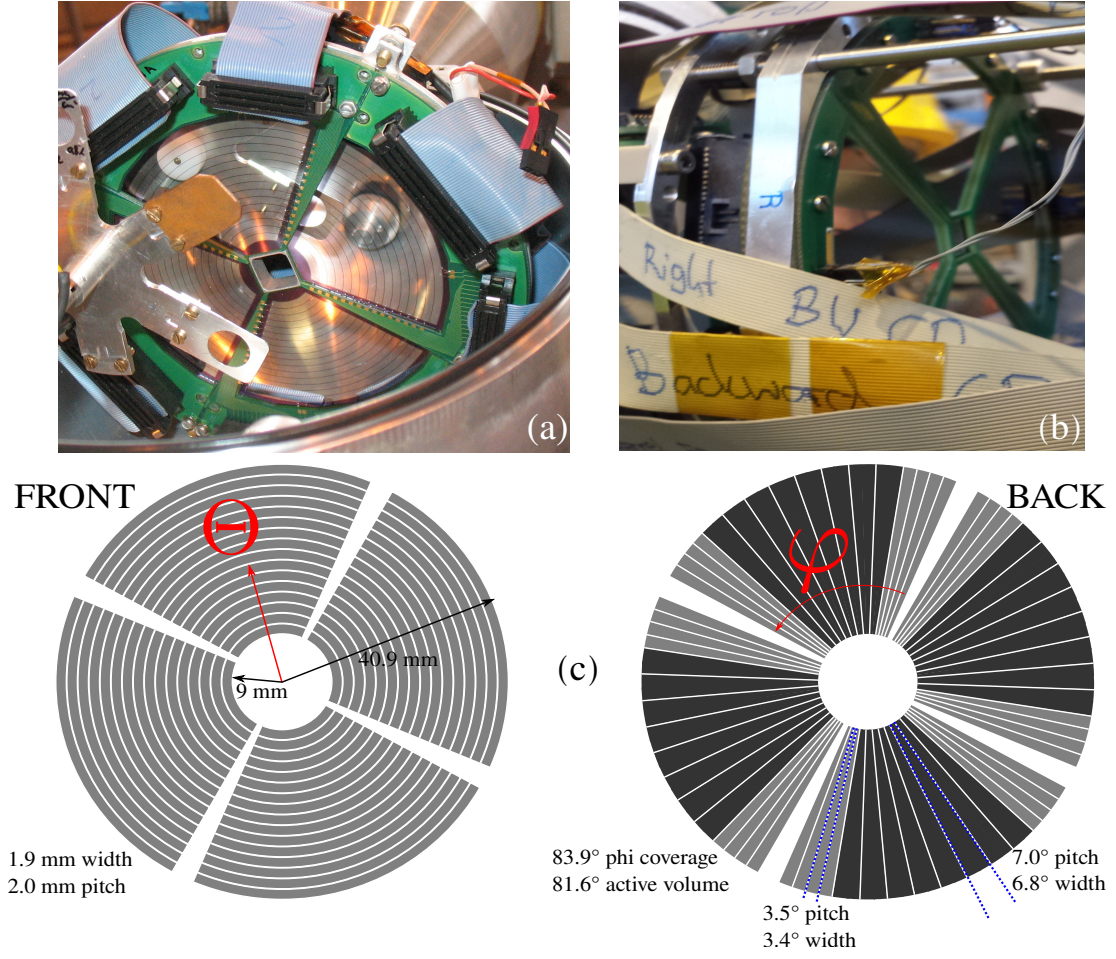


**Figure 33:** (a) Picture of an assembled DSSSD with a front side view mounted inside a target chamber. The 16 annular rings and the cable connectors are shown. Figure from Ref. [104] (b) The DSSSD built in the C-REX setup which was used for the measurement. (c) A schematical illustration of the DSSSD segmentation and the physical detector properties and dimensions.



## 4. Experimental details of experiment IS551

The Coulomb-excitation experiment was performed in October 2016 at the HIE-ISOLDE facility at CERN. For the exotic doubly-magic  $^{132}\text{Sn}$  the 44 g/cm<sup>2</sup> thick UC<sub>x</sub>/graphite target was irradiated directly with the 1.4 GeV proton beam from the CERN PS Booster (PSB) [72] with an average current of 2  $\mu\text{A}$ . To suppress contaminants that are produced with a high cross section, e.g.  $^{132}\text{Cs}$ ,  $^{132}\text{Sn}$  was extracted as a tin sulfide ( $\text{SnS}^+$ ) molecular beam. The transfer line of the hot plasma ion source was complemented with a thin molybdenum tube, which contained 61 mg enriched sulfur (99.9%  $^{34}\text{S}$ ). In addition, the transfer line was heated up to 1900 °C. The target temperature was 2000 °C to increase the effusion and diffusion of tin and consequently improve the beam intensity. The ionization and extraction of the molecules for further processing is done with the ion source, which is coupled to the target container. Surface ionization and laser ionization (RILIS) were not possible for the  $\text{SnS}^+$  beam, as it would not ionize or break-up the molecule, respectively. Hence, the plasma ionization technique was used to ionize the molecules.

The molecular beam was processed by the consecutive HRS mass separators and subsequent cooled for the SnS molecule mass  $A = 166$  in REXTRAP. The repetition time was 200 ms. It was recognized that the molecular beam was disassociated within REXTRAP. In the Time of Flight (ToF) spectrum between REXTRAP and REXEBIS predominantly  $A = 132$  ions were measured and only a small fraction of  $A = 166$  ions. Thus, the disassociation of tin sulfide occurred most likely after the recentering and immediately before the extraction of the ions.

After the charge breeding of the  $^{132}\text{Sn}$  beam in REXEBIS for 194 ms, the highly-charged radioactive tin nuclei were guided into the new superconducting high-beta cryomodules of HIE-ISOLDE. The efficiency of REXTRAP and REXEBIS amounted to 10%, producing an  $A/q$  ratio of the tin ions of 4.258 with the charge state of  $q = 31^+$ . The bunch length of the ion beam into the post accelerator was 200  $\mu\text{s}$ . The beam energy, reached with completion of stage I of HIE-ISOLDE, was  $5.49 \text{ MeV/u} \pm 0.022 \text{ MeV/u}$  with a transmission efficiency of 68% for  $^{132}\text{Sn}$  and an overall transmission efficiency of 6.8%.

The secondary target, located at the MINIBALL setup, with a thickness of 3.1 mg/cm<sup>2</sup> consisted of 99.80%-enriched  $^{206}\text{Pb}$  evaporated onto a 25  $\mu\text{g/cm}^2$  thin  $^{12}\text{C}$  supporting foil. The average intensity of the post-accelerated ion beam amounted to approx.  $3.0 \times 10^5$  ions/s, with an beam-on-target time of 127 hours.

## 5. Data analysis

The Coulomb-excitation experiment was performed with the high-resolution germanium array MINIBALL in combination with the C-REX setup (cf. Sec 3.1.6). Data were recorded with a digital data acquisition (DAQ) system consisting of Digital Gamma Finder 4C (DGF-4C), fast 32 channel multiplexer MUX-32 and peak sensing Analog-to-Digital Converter (ADC) modules. For a fast and efficient data analysis, a proper data pre-processing is necessary to perform an event-by-event analysis. Particle information from the silicon detectors (DSSSD) as well as the  $\gamma$ -ray information from MINIBALL have to be combined for particle- $\gamma$  and  $\gamma\gamma$  coincidences. This step is the so-called event building. For a appropriate event building, a calibration of all detection systems, timing cuts, addback of the HPGe cluster detectors and further adjustments are required. The following section deals with the pre-processing of the recorded data and the calibration. In the subsequent sections the final  $\gamma$ -ray spectra are generated after applying required corrections and essential analysis conditions.

### 5.1. Data acquisition and pre-processing

The data acquisition for the  $^{132}\text{Sn}$  experiment at ISOLDE, CERN was performed with the MAR<sub>a</sub>B $\mathcal{O}$ U [109] system. MAR<sub>a</sub>B $\mathcal{O}$ U is a conjunction of the front-end MBS (Multi Branch System) data readout, developed at GSI, Darmstadt [110], and the back-end framework ROOT [111, 112]. The data processing of MAR<sub>a</sub>B $\mathcal{O}$ U is illustrated in Figure 34. The MBS was used for data readout, event building and data transfer, whereas the ROOT environment provided setup configurations, run and hardware control, online/offline data visualization via histograms, data analysis and data storage. The event structure of the recorded data was passed to the ROOT framework via a macro file and processed by CINT [113] (C++ interpreter). After the environment configuration for the MBS front-end and analyzing programs were finished, the proper readout structure of the MBS and

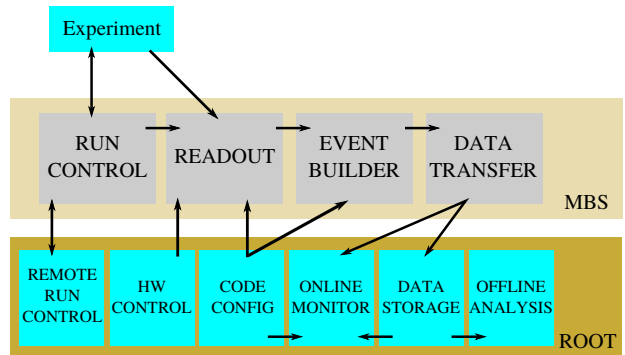


**Figure 34:** Schematic illustration of data processing of MARABOU. The arrows indicate the user programs for control and monitor the data acquisition. See text for more details.

simultaneously the usage of standard routines like histogramming, monitoring and event storage were available. The configured system was able to manage the following tasks:

1. Record of experimental data.
2. Translation of MBS events to ROOT objects.
3. Energy, position and time assignment for each event.
4. Online/Offline visualization of the physical data.
5. Storage of event data in ROOT format for following post-processing.

Further efficient data evaluation requires an adequate post-processing of data. Therefore, the energy and efficiency calibrations of the detectors are one of the essential first steps.

## 5.2. Detector calibration

### 5.2.1. DSSSD segment identification

A correlation between the 16 annular segments on the front side and the 64 strips (four quadrants with 16 strips) on the back side of the silicon detector allowed for a separation of the DSSSD in 1024 single pixels. Thus, an accurate position determination of the ions were possible, which is important for the Doppler correction. The energy and segment id were processed via mesytec MUX-32 modules. These fast 32 channel multiplexed modules incorporate preamplifier shapers and discriminators, which exhibit good timing resolution [114]. For each DSSSD quadrant two MUX-32 modules were used. All 16 segments of one side of the DSSSD quadrant were connected to one MUX-32 module. The remaining 16 channels of the MUX-32 were used for the backward DSSSD, which was not in operation during the present experiment. In total eight MUX-32 modules were used. Up to two simultaneously responding segments connected to one MUX-32 module can be identified and are designated as 1st and 2nd hit. Therefore, the incoming signal was splitted into the shaping preamplifier and the leading edge discriminator. The fast signal generated by the discriminator was analyzed by a hit decoder, which determined the address of the hit segment and generated a typical silicon signal with a characteristic amplitude for each segment. The particle energy is determined from the output signal of the preamplifier shaper. Peak sensing Analog-to-Digital Converters (ADCs) are used to digitize the incoming energy and position signals. The application of the MUX-32 modules required only 4 ADC channels for the data acquisition of the DSSSD. Fig. 35 illustrates one measured particle energy



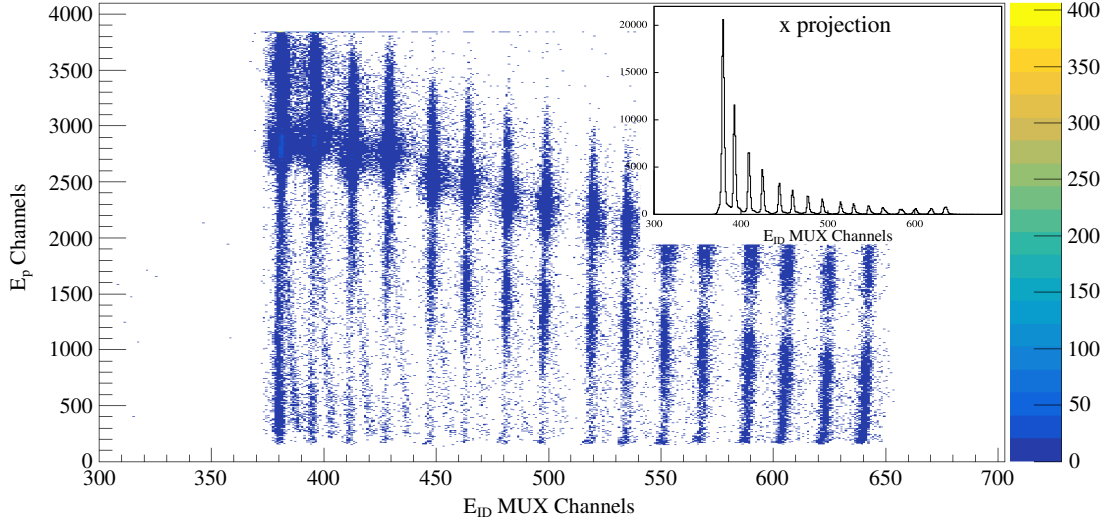


**Figure 35:** Particle energy in channels as a function of the MUX ID in channels for the front side of one DSSSD quadrant (annular segments) recorded in one run. The MUX id corresponds to the hit segment. The inset illustrates the x-projection of the two dimensional spectrum. See text for more details.

spectrum as a function of the segment id for one run.

The 16 segment ids ( $E_{ID}$  MUX channels) correspond, from left to right, to the annular segments from the innermost to the outermost rings of one DSSSD quadrant. With the x-projection of the two dimensional spectrum illustrated in the inset of Fig. 35, a separation of the segment via their ids is possible. The width of the peaks is mostly related to the difference of the grounding potential between the MUX-32 modules (close to the DSSSD) and the following ADCs located inside the data acquisition rack. In both spectra the expected Rutherford scattering dependence of the ions is observed. Moreover, in the two dimensional spectrum two distinct branches are visible, which originate from the projectile and target-like particles. The underlying kinematics are discussed in more detail in Sec. 5.4.

### 5.2.2. DSSSD energy calibration

The thickness of the DSSSD detector amounts to approx. 140  $\mu\text{m}$  [107, 108], thus, the impinging heavy ions with an maximum penetration depth of 64  $\mu\text{m}$  are detected with an efficiency of approx. 100%. Prior to the energy calibration, the detection stability as a function of time was verified to exclude non-physical shifts of the recorded data. This is illustrated for all quadrants in the left plot of Figure 36. The plot on the right demonstrates the shift of the mean value of the top DSSSD quadrant with respect to the detected peak

width. The shifting of the mean value is small compared to the peak width and mainly caused by the statistical errors during the corresponding runs and the related fit routine errors. Thus, for the time of the experiment, the peak positions of the DSSSD spectra are constant.

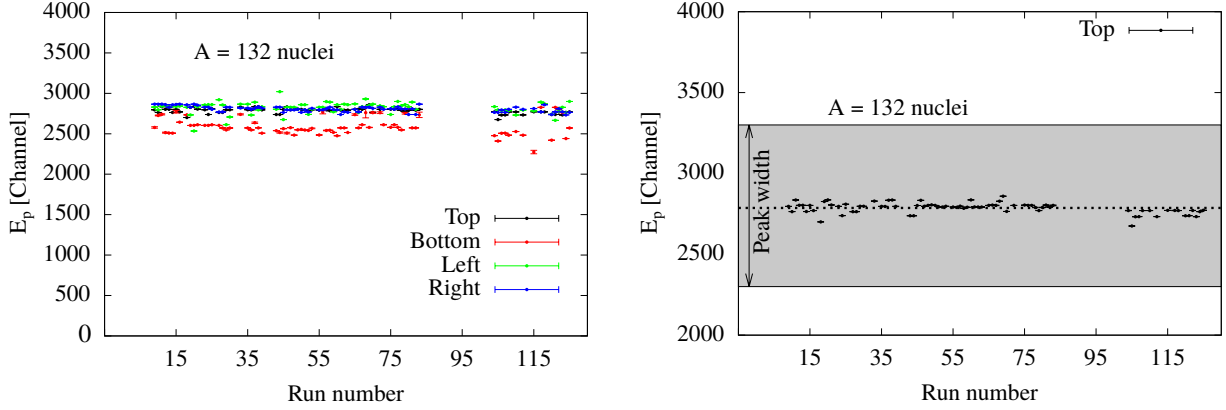


**Figure 36:** left: The mean value of the prominent peak (mass  $A = 132$ ) for each DSSSD quadrant is plotted as a function of time (Run number). The behavior is constant during the experiment and deviations originate from the automatic fit routine and the statistics. The offset of the Bottom quadrant is related to a different amplification factor. Right: Peak position of the top quadrant in relation to the typical peak width.

As aforementioned, the double-sided silicon-strip detector consisted out of four identical quadrants with 16 annular segments on the front side and 16 strips, perpendicular to the rings, on the back side. This resulted in 1024 single pixels, which were used for position sensitive detection of the particles. The particle energy was measured via the annular segment electrode on the front side.

The beam energy in the laboratory frame amounts to 726 MeV. The energy deposition in the DSSSD for projectiles after a scattering event with  $\theta_{\text{lab}} = 16^\circ - 53^\circ$  ranges between 350 MeV up to 600 MeV. For target-like nuclei the energy deposition amounts to 100 MeV up to 350 MeV for the same scattering interval. Hence, a typical calibration with an  $\alpha$ -source ( $E_{\gamma,\alpha} < 6$  MeV) is insufficient, due to the large deviations resulting from the required extrapolation. The tight time schedule at HIE-ISOLDE did not allow for a calibration with a high-energy test beam. Therefore, the DSSSD detector was calibrated by using in-beam information and data. For each individual annular segment the detected particle spectrum (cf. Fig. 37) was calibrated using the calculated kinematics of  $^{132}\text{Sn}$  on  $^{206}\text{Pb}$  at 726 MeV. The kinematics were determined with the simulation program LISE++ [115].

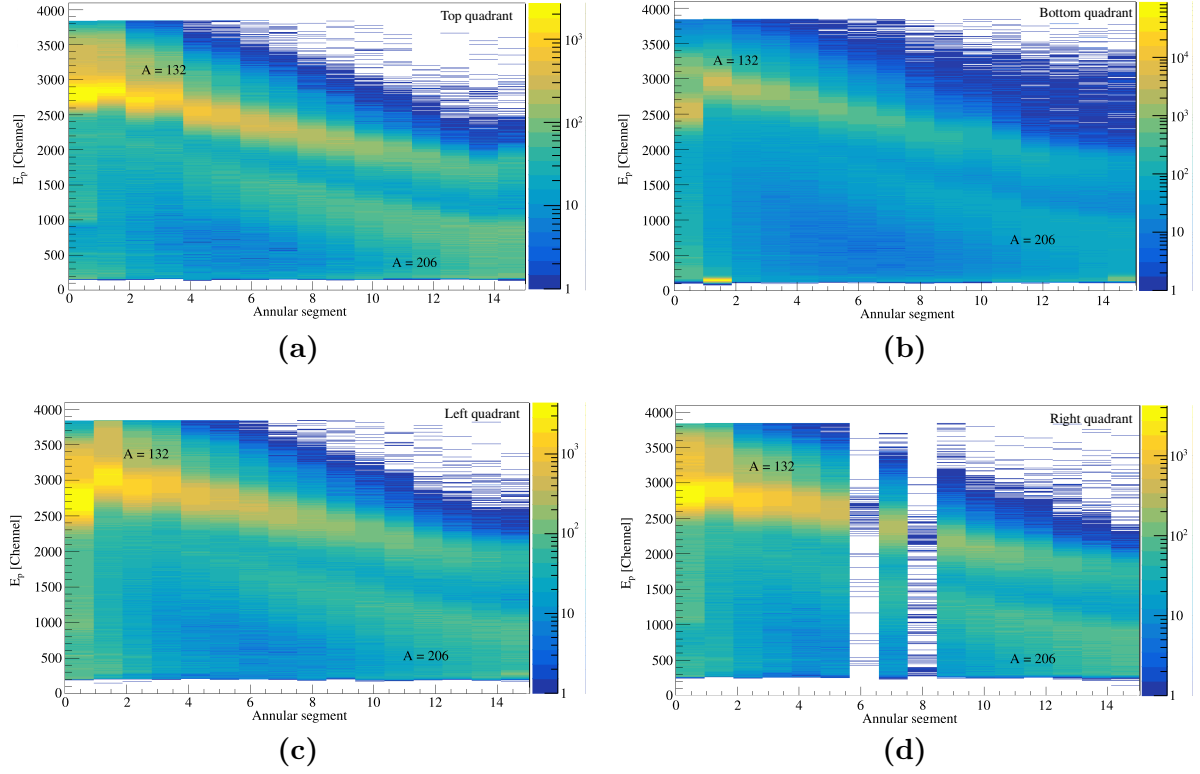


**Figure 37:** (a) - (d)Uncalibrated particle spectra for individual quadrants as a function of the annular segment in logarithmic representation. The energy is presented in channels. Projectile and target-like particles ( $A = 132$  and  $A = 206$ ) can be distinguished in the spectra.

Figure 38(a) illustrates the energy spectrum of particles detected in the first annular segment of the top quadrant after a first energy calibration. In Fig. 38(b) the calculated kinematics for the projectiles are shown, together with the calibrated peak positions of all annular segments. From the reaction kinematics, it is expected that the particle peak with the highest energy and intensity corresponds to mass  $A = 132$ . Due to the low probability for  $^{206}\text{Pb}$  scattering in the solid angle of the innermost rings, no peak for mass  $A = 206$  is visible in the innermost rings and, hence, only a two-point calibration with 0 MeV is possible. The calibration was performed via the calculated energy of particles with mass  $A = 132$  at the corresponding  $\theta$  angle at the center of the DSSSD segment and assuming that channel 0 corresponds to 0 MeV. For detection in the annular segments No. 5 and greater, a two-point calibration with  $A = 132$  and  $A = 206$  is possible. Before further comparing the two calibrations, it is essential to understand the particle spectra in detail.

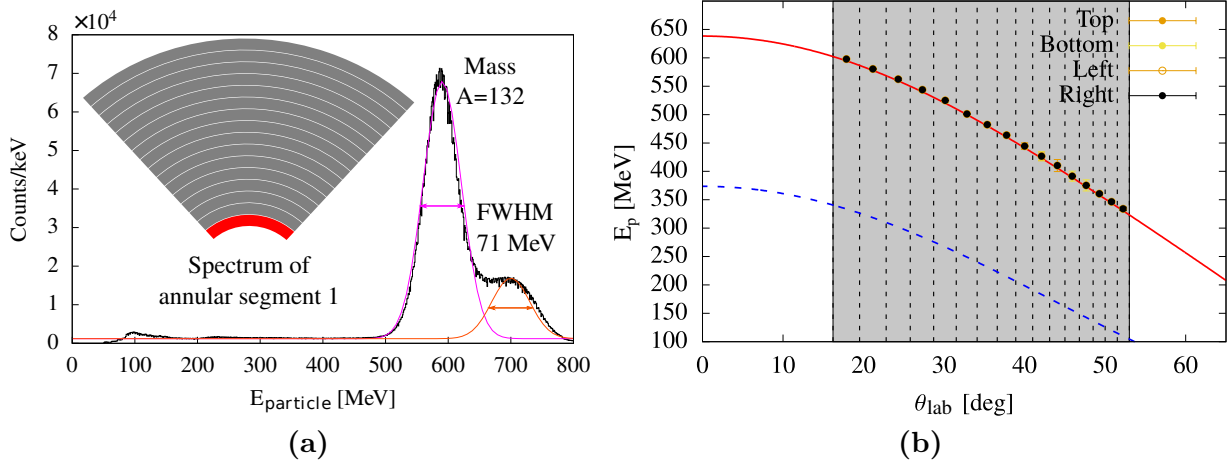


**Figure 38:** (a) The energy spectrum of particles detected in the annular segment No. 1 of the top quadrant with the statistics of all runs is shown. The double-peak structure is related to particles with mass  $A = 132$ . Both peaks show the same FWHM. For more details see text. (b) Kinematics obtained with the computer code LISE++. The red solid line represents the mass  $A = 132$  particles, whereas the blue dashed line illustrates the energy of target ( $A = 206$ ) nuclei as a function of the scattering angle.

In the spectrum illustrated in Fig. 38 (a), a second peak is emerging at the right tail of the prominent particle peak of mass  $A = 132$  at around 700 MeV. This peak arises from capacitive coupling of neighboring segments or charge sharing and corresponds to particles with mass  $A = 132$ . This becomes more evident considering two-dimensional spectra of a DSSSD pixel. Figure 39 illustrates an example of a correlation between the energy deposition in the front ring No. 1 (annular segment No. 1) and the back-side strip (strip No. 15). The spectrum can be divided in three parts:

1. The measured energy deposition at the front and back side of the pixel are equal and, hence, linear correlated.
2. Region 2 corresponds to events with full or less energy detected by the back-sided strip and full or artificially increased energy deposition in the ring segment. Two possible explanations are, a baseline shift of the electrode potential due to capacitive coupling or a large charge trapping and high charge recombination rate of particle-hole pairs. After the interaction of a particle in a highly-segmented silicon detector the resulting charge cloud can be detected in one ring at the front side and two neighboring strips at the back side. This charge sharing between two neighboring strips results in a reduced energy, measured within one strip and in the detection of a 1st and 2nd hit event. Charge sharing only occurs in events where the interaction position was close to the

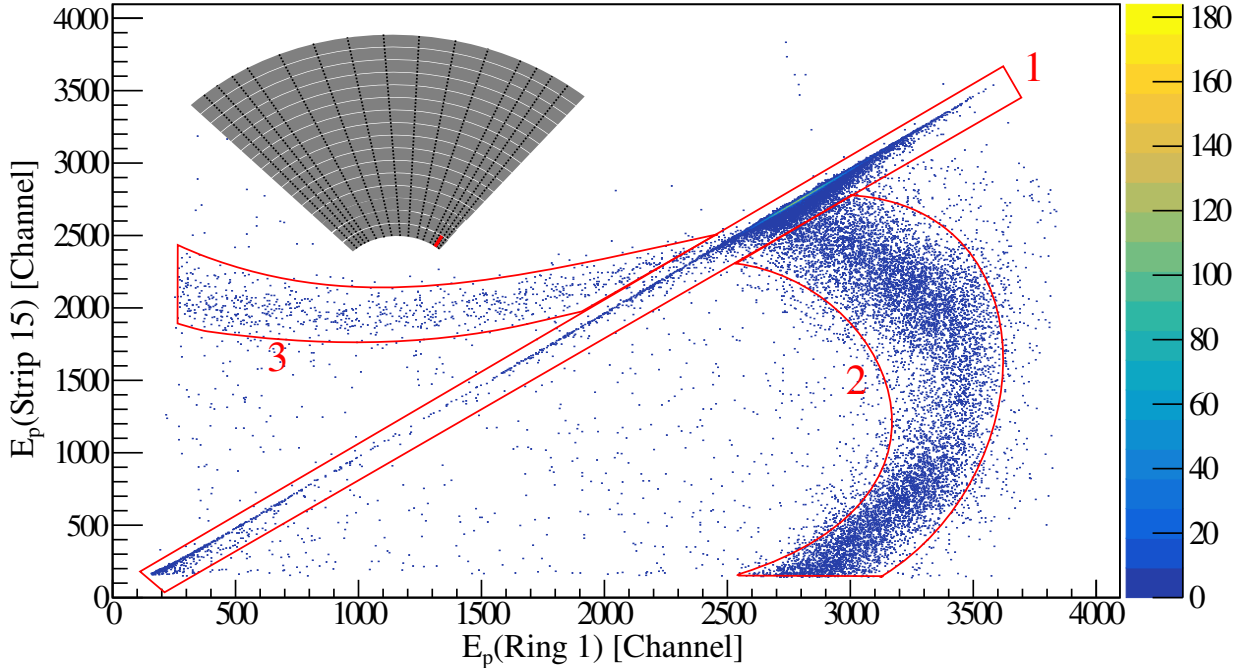


**Figure 39:** The energy correlation illustrates the detected energy with the back side strip No. 15 as a function of the energy detected with the front annular segment No. 1. This correlation spectrum represents the detected energy of the DSSSD pixel that is marked in red in the schematical inset. Three regions can be identified in the spectrum. More information are given in the text.

inter-strip region or inside the inter-strip region. The current from the neighboring pixel can possibly induce a baseline shift of the annular-segment potential, which results in an artificially higher energy deposition. This baseline shift influences the detected voltage amplitude and depends on the energy splitting between neighboring segments, as indicated by the curved structure of region 2. A similar phenomenon of baseline shifts was observed in highly segmented HPGe detectors of the AGATA and GREYINA array and discussed in more detail in References [116–119]. The impact of the described cross-talk induced by the capacitive coupling of the segments is of the order of  $10^{-3}$ , whereas the impact of the truncated mirror charges [119, 120] is larger, but both mechanism lead in general to reduced energy detection in the segments. Thus, a further capacitive coupling can potentially induce the baseline shifts, e.g. capacitive coupling of the cabling of the detector or in the subsequent electronic chain of the DSSSD. The second possible explanation is the Pulse-Height Defect (PHD) originating from charge trapping and charge recombination of the particle-hole pairs, due to the breakdown of the electric field after the creation of

a plasma by a high density of ionized particles [121, 122]. The innermost charge carriers are almost not affected by the electric field as their are shielded by the outer particle-hole pairs and, therefore, exhibit higher probability for recombination and trapping. If charge sharing occurs, the particle-hole pairs are distributed between the neighboring pixels and the probability for recombination and trapping is reduced as the charge cloud is spread over a larger area, which results in the detection of more charge carriers. However, to evaluate the exact origin it is indispensable to investigate the pulse shapes of each individual DSSSD segment and obtain more information from the induced transient signals as well as a calibration from low energies up to the beam energy (726 MeV) is required. Unfortunately, the exact origin can not be verified with the present data, but further investigation and identification is required to eliminate the source of this effect.

The projection of the two-dimensional spectrum from Fig. 39 onto the x axis results in the particle spectrum shown in Fig. 38 (a), which explains the double-peak structure.

3. : The third area exhibits a similar energy deposition pattern as 2. But a major difference is that on both sides of the DSSSD full or less energy deposition is observed. The reduced energy in the ring segments is induced by the charge sharing between neighboring annular segments at the front side. The reduced energy deposition in the strip is related to interactions in the inter-strip region of the silicon detector. Due to incomplete charge collection of negative charge carriers, caused by a positively charged layer in the inter-strip region, the detected charge is reduced. This mechanism is described in Ref. [123]. These events also belong to particles with mass  $A = 132$  and amount to 4% of the total events. In addition, a positive voltage is applied at the back side strips to bias the DSSSD. Thus, the back-side strips are equipped with coupling capacities, which could potentially compensate baseline shifts induced by capacitive coupling and, therefore, this effect is not present on the back-side strips. If this effect is induced by the increased charge trapping and charge recombination, it is predominantly related to the holes (collected at the annular segment electrode) as their trapping probability is much higher than for the electrons [124].

Two-dimensional spectra corresponding to the energy spectrum of a pixel with one ring and two connected strips feature an additional structure. This is illustrated in Figure 40 and marked as region 4. The origin of this structure is the same as for region 2. Considering that these neighboring strips are connected, the splitted charge carriers are added up to the

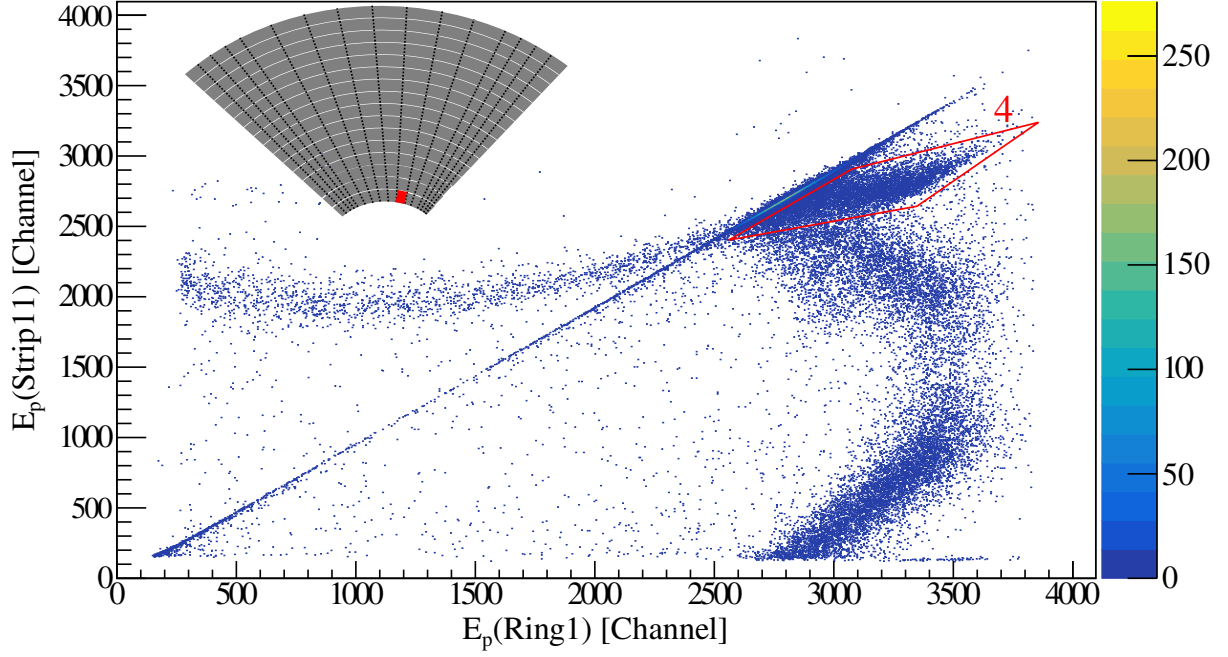


**Figure 40:** The energy correlation illustrates the detected energy with the back side strip No. 11 as a function of the energy detected with the front annular segment No. 1. The DSSSD pixel is marked in the inset. An additional region compared to Figure 39 is visible, which arises from connected neighboring strips at the back side. More information is given in the text.

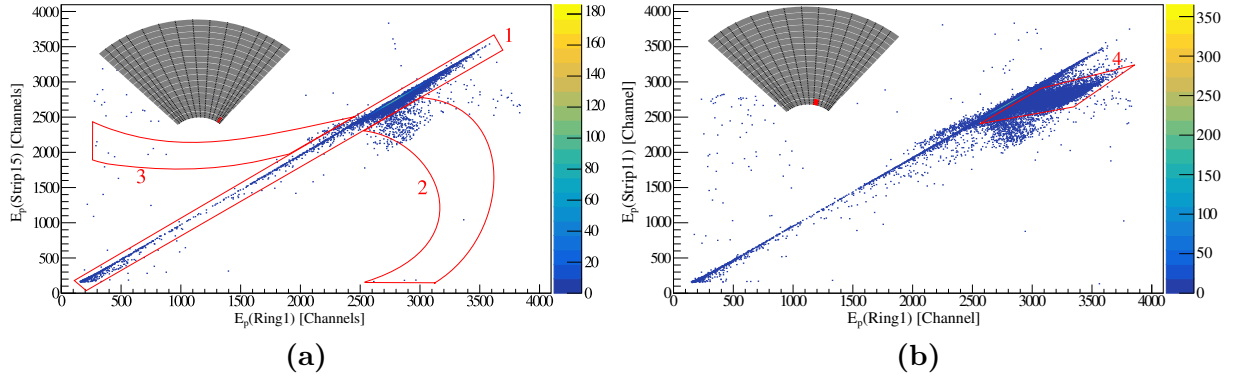


**Figure 41:** (a) Energy spectrum from Fig. 39 and (b) energy spectrum from Fig. 40 with the restriction of single-hit events in each quadrant. The additional structures in region 1 and 2 vanish with the restriction of single-hit events. For more information see text.



total charge. The presented explanations were verified by a restriction to single-hit events in each quadrant, which allows only 1st hit/single hit events in one quadrant (cf. Fig.41). Regions 2 and 3 vanish and only the linear correlation between the front side and back side of the detector remains. Structure 4 remains under the condition of single hit events, because charge sharing occurs between two strips but within a single pixel. This confirms that the additional structures in the particle spectra arise from real single-hit events, which are not fully detected in a single pixel, but in multiple pixels. The correction of these effects is quite challenging, as it has to be implemented for each pixel individually. In total 1024 different slopes, curvatures and zero-crossing points induced by the different amplification factors of the annular segments and strips have to be considered. Figure 42 illustrates the spectrum of the annular segment 1, presented in Fig. 38 (a), after implementation of a rudimentary correction algorithm. The correction algorithm distributes all events inside region 2 and 3 in a Gaussian distribution around the calculated mean energy of mass  $A = 132$  particles. The sigma of the Gaussian curve is obtained from the fit of the spectrum shown in Fig. 38 (a). Due to the correction, a sharp drop arises at the right tail of the corrected particle peak, which illustrates the potential for additional improvements.

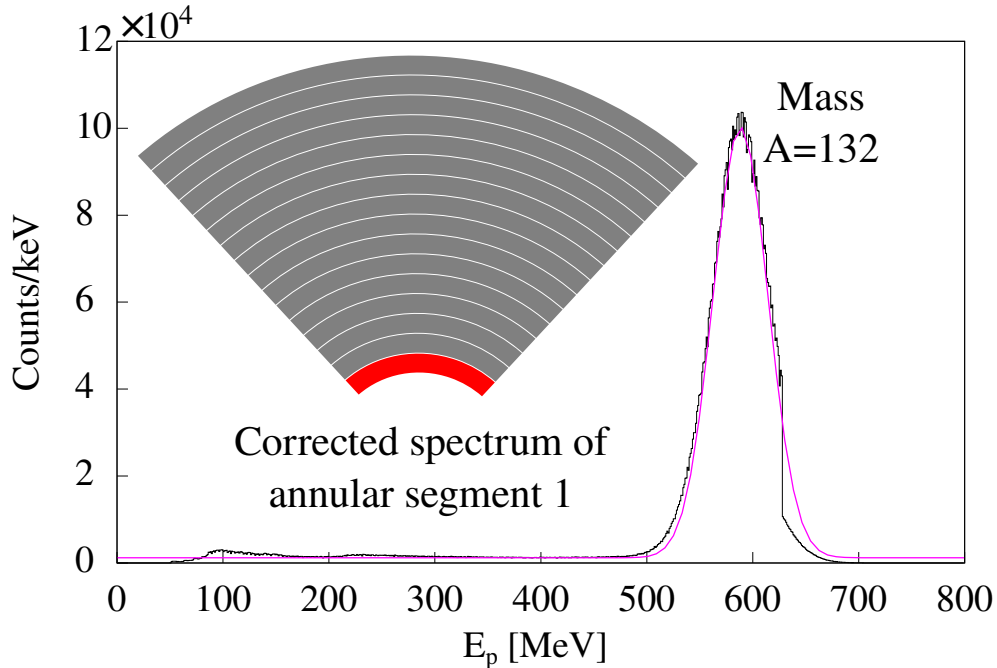


**Figure 42:** Energy spectrum of particles detected in the innermost ring after correction of the capacitive coupling effect (black curve). The sharp drop at the right tail of the peaks is caused by the correction algorithm. The magenta curve illustrates the Gaussian fit of the particle peak of mass  $A = 132$ . Find more information in the text.



Figure 43 illustrates a comparison of the final  $\gamma$ -ray spectra for projectile and target de-excitation with the aforementioned correction and the two energy calibrations. The black curve corresponds to the outcome without the capacitive coupling correction and the two-point calibration with 0 MeV. The green curve illustrates the spectrum with the two-point calibration including the  $A = 206$  mass peak for the 11 outermost rings. The red curve includes the correction for the capacitive coupling. In Fig. 43 (a) the  $2_1^+ \rightarrow 0_{g.s.}^+$  transition of  $^{206}\text{Pb}$  is illustrated with no visible improvement applying the capacitive coupling correction, as this correction does not affect the target-like particle energies. However, for the

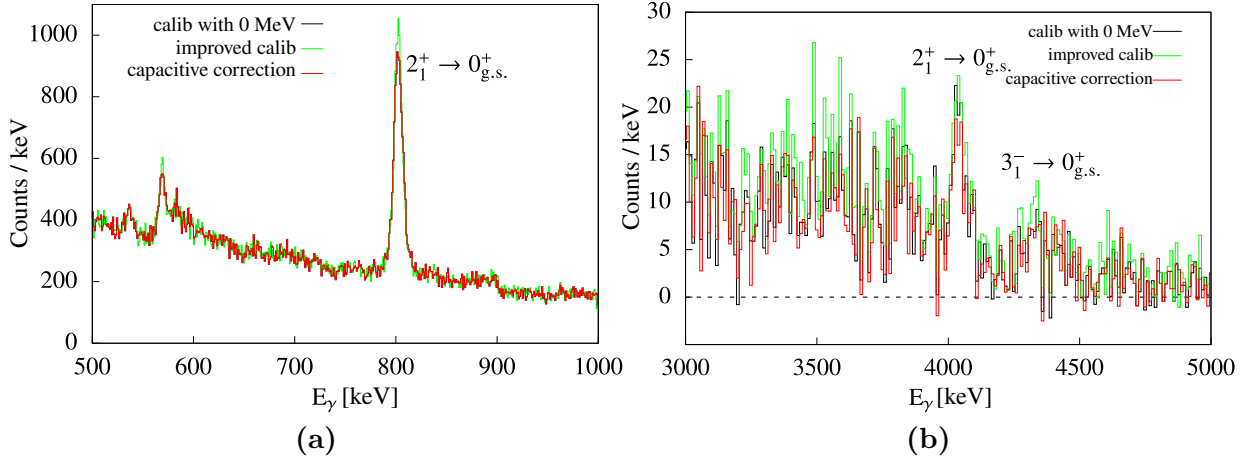


**Figure 43:** (a) The 803 keV transition of the first excited state in  $^{206}\text{Pb}$  is shown. The black curve shows the transition with the two-point calibration with 0 MeV and no capacitive correction. The green and red curves are with the improved two-point calibration and capacitive correction, respectively. (b) The  $2_1^+ \rightarrow 0_{g.s.}^+$  and  $3_1^- \rightarrow 0_{g.s.}^+$  transitions of  $^{132}\text{Sn}$  are presented. The color code is the same as before. More information can be found in the text.

$\gamma$ -ray transitions of  $^{132}\text{Sn}$  (Fig. 43 (b)) a difference between both curves is observed. The resolution after applying the capacitive coupling correction is slightly worse than without. For an improvement of the correction a more advanced algorithm is required, which considers for each pixel the slope as well as the curvature of the energy correlation in region 2 and 3. To estimate a potential benefit of this effort, the typical energy difference of the resulting  $\gamma$ -ray transition at around 4 MeV after a Doppler correction without correction of the right particle bump is calculated by

$$\Delta E_0 = E_{\text{lab}} \left( \frac{1 + \hat{\beta} \cos(\theta_{p\gamma})}{\sqrt{1 - \hat{\beta}^2}} - \frac{1 + \beta \cos(\theta_{p\gamma})}{\sqrt{1 - \beta^2}} \right), \quad (5.1)$$

where  $\theta_{p\gamma}$  is the angle between the particle and the emitted  $\gamma$  ray in the center-of-mass frame,  $\hat{\beta}$  and  $\beta$  are impact velocities of the particles. Using mean particle energies of 590 MeV and 710 MeV after and before applying the correction algorithm, respectively, the energy difference amounts to  $\Delta E_0 = 60$  keV for a  $\gamma$ -ray energy of 4 MeV. For particles detected in region 2, the corresponding  $\gamma$  rays will be Doppler corrected within a range of 120 keV around the mean energy. However, this interval is within the range of the final integration limits for the yield determination, which will be discussed later. Therefore, the detected deexcitation is included in the final yields and no additional capacitive coupling or charge loss correction and corresponding programming efforts are justified.

An improvement between the particle-energy calibrations can be observed in Figure 43 (a). The two-point calibration including the target-like particle peak results in a more accurate target-particle energy and, thus, in a better energy resolution of the  $\gamma$ -ray spectra of target-like transitions. In the analysis this two-point particle-energy calibration is used. According to this energy calibration, the innermost rings exhibit a relative energy resolution of  $> 10\%$ , originating from an irradiation damage of the detector caused by an intense  $^{110}\text{Sn}$  beam from the previous beam time.

### 5.2.3. Energy calibration of MINIBALL

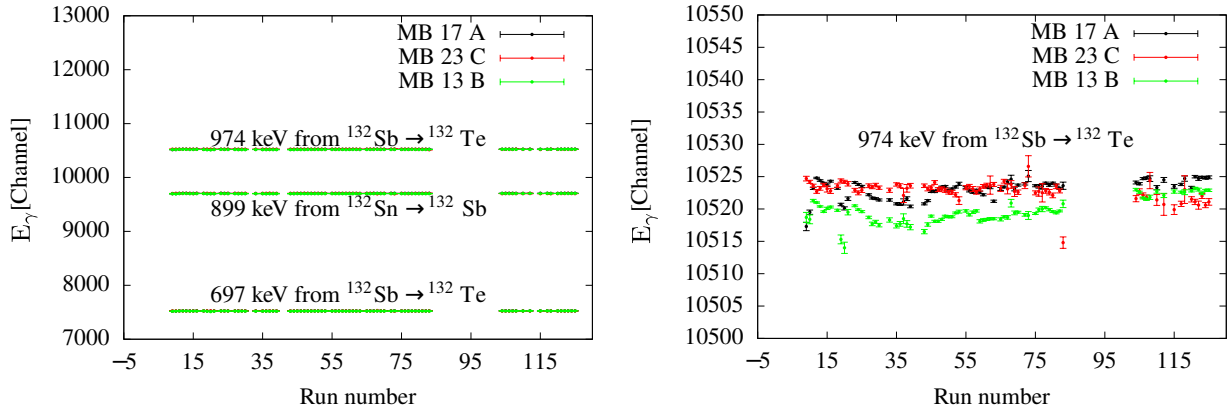


**Figure 44:** Uncalibrated  $\gamma$ -ray energy of three dominant lines from the  $\beta$ -decay as a function of time. Detected mean value of three HPGe crystals from three different MINIBALL clusters are shown with a deviation less than 0.1%. A time dependent energy shift during the experiment was excluded.

The time stability for the MINIBALL acquisition system is ensured similar to the DSSSD data. The results are illustrated in Figure 44. The dominant  $\beta$ -decay transitions of  $^{132}\text{Sn}$

and its daughter nucleus  $^{132}\text{Sb}$  were used for this verification. The highest deviation of the detected  $\gamma$ -ray energies amounts to 0.1%, which quantifies the stability for the investigated transitions. Hence, no time dependent shifts are expected for higher  $\gamma$ -ray energies around 4 MeV.

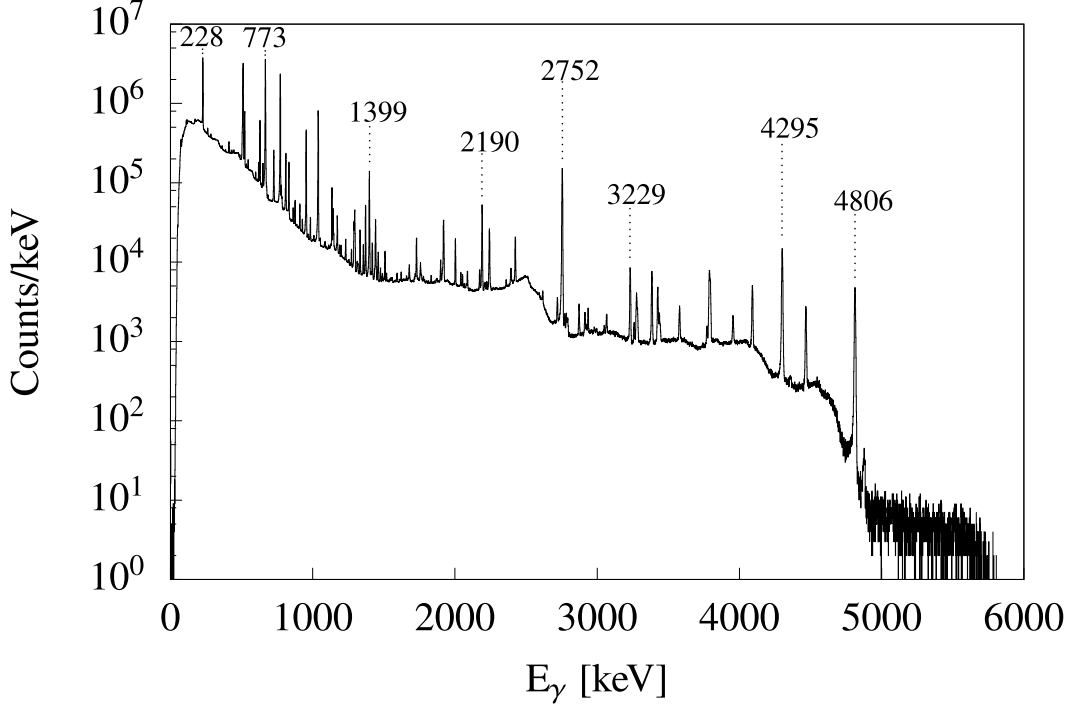


**Figure 45:**  $\gamma$ -ray spectrum of the decay of  $^{66}\text{Ga}$ . The known energies indicated were used for the energy calibration. See text for more details.

In order to obtain an accurate energy calibration and energy resolution, at high transition energies around 4 MeV of the first  $2_1^+$  and  $3_1^-$  states in doubly-magic  $^{132}\text{Sn}$ , typical calibration sources like  $^{60}\text{Co}$ ,  $^{137}\text{Ba}$  and  $^{152}\text{Eu}$  with  $\gamma$ -ray transitions below 1.5 MeV are not sufficient. For this purpose a calibration source with energies up to 4.5 MeV is required. Therefore, a radioactive source was specially produced at one of the low-energy beam lines of ISOLDE via implantation of a  $^{66}\text{Ga}$  beam into a copper foil. The  $^{66}\text{Ga}$  source was transported to the MINIBALL setup and mounted at the target position. Due to the uncertainties of the beam current plus additional activity of  $^{66}\text{Cu}$  in the beginning, the activity of the created calibration source was roughly estimated yielding approx. 1 MBq. Nonetheless, the precise activity of the source is not important for the energy calibration. The  $^{66}\text{Ga}$  source incorporates two major advantages: (i) high amount of  $\gamma$ -ray transitions with energies ranging from less than 300 keV up to 4.8 Me; (ii) well-studied relative tran-

sition intensities [125]. The recorded  $\gamma$ -ray spectrum of the decay of  $^{66}\text{Ga}$  is shown in logarithmic scale in Figure 45. Due to the wide range of transition energies up to 5 MeV, an accurate and precise energy calibration in the energy range of interest around 4 MeV is possible.

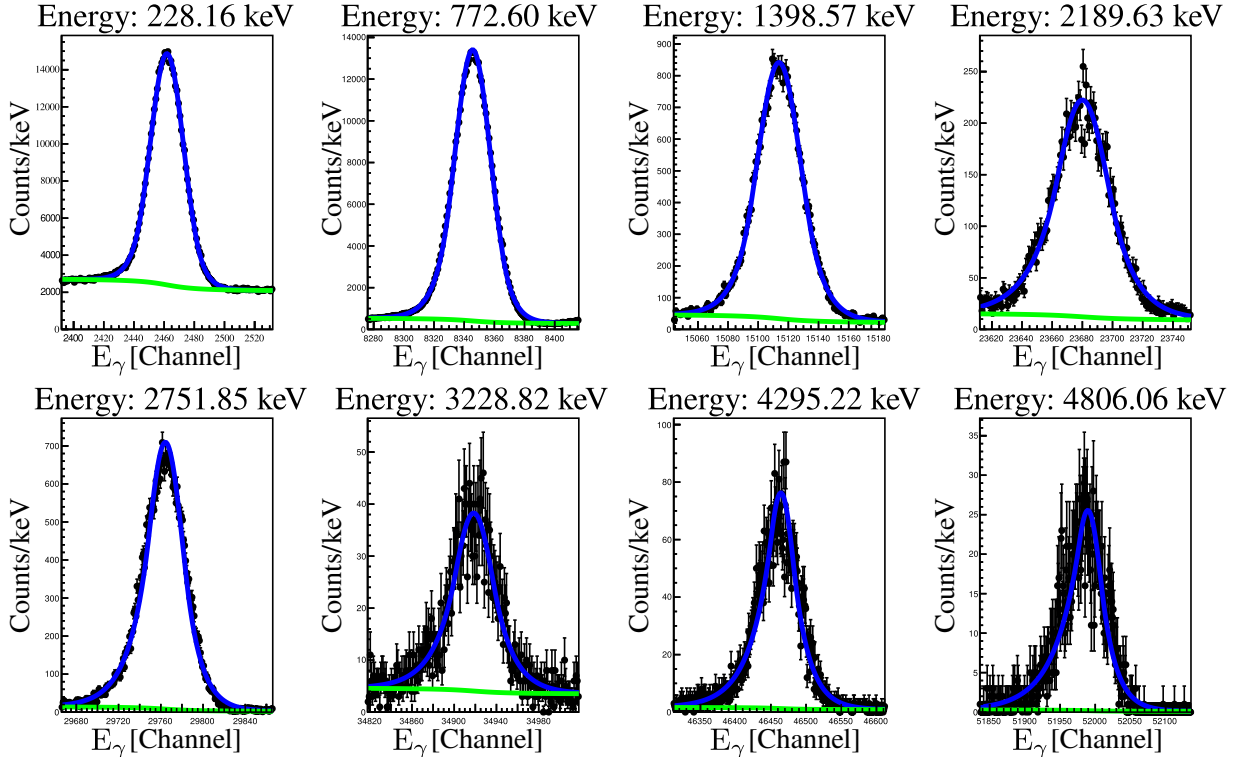


**Figure 46:** Resulting Gaussian fits to selected  $\gamma$ -ray transitions obtained with a  $^{66}\text{Ga}$  source measurement of one MINIBALL HPGe crystal. A proper energy calibration is guaranteed by sufficient statistics in each transition.

In total eight dominant transitions at 228 keV, 773 keV, 1399 keV, 2190 keV, 2752 keV, 3229 keV, 4295 keV and 4806 keV were used to obtain the energy calibration of the germanium detectors. The deposited  $\gamma$ -ray energy is detected by the core electrode of the germanium crystals. Thus, the energy calibration was performed for all 24 detectors of MINIBALL via the fit of the eight transitions in each core spectrum. For one HPGe crystal the resulting fits are presented in Figure 46. A second order polynomial was fitted to the data. The corresponding fit and the parameters are presented in Figure 47. The contribution of the quadratic term compared to the linear term is less than per mill and, thus, the non-linearity of the preamplifier and digitizer is negligible.

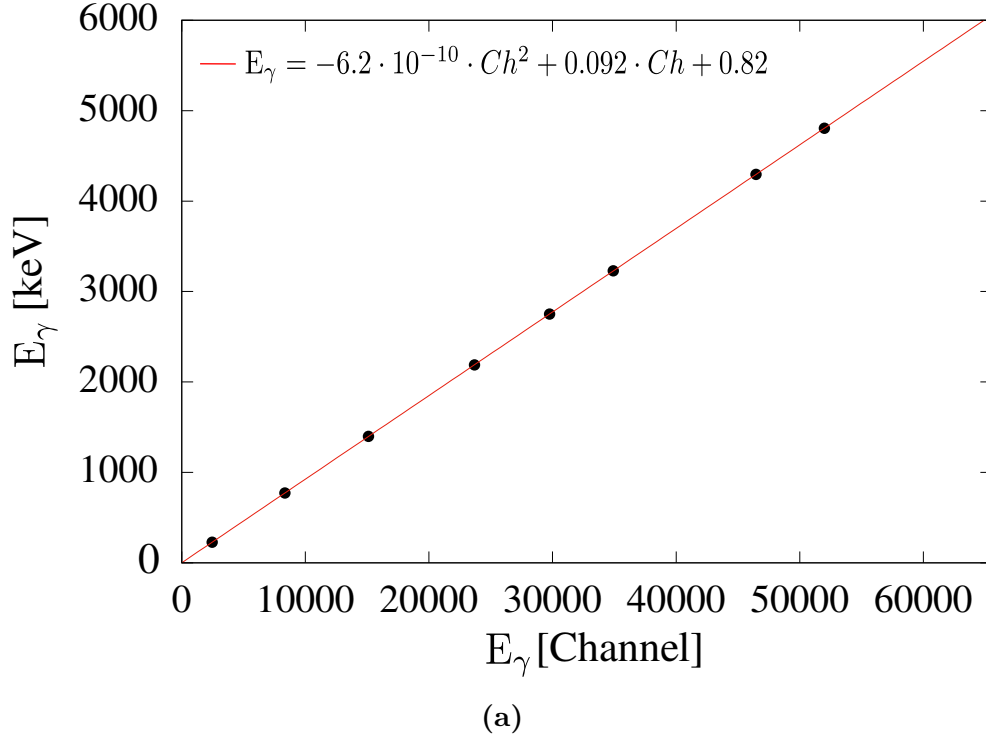


**Figure 47:** Polynomial fit to the data shown in Fig. 46. The non-linearity of the electronics for high  $\gamma$ -ray energies is almost zero ( $\approx 10^{-4}$ ).

#### 5.2.4. Efficiency calibration of MINIBALL

In addition to the energy calibration, an efficiency calibration is required and was performed with the  $^{66}\text{Ga}$  source. As mentioned before, the relative intensities of the  $\gamma$ -ray transitions following the  $\beta$  decay are known. The uncertainty of the activity of the source prevents an absolute efficiency measurement, but still allows for a precise relative efficiency calibration. To determine reduced transition strengths a relative efficiency calibration is sufficient (cf. Section 1.4). However, an additional  $^{60}\text{Co}$  source measurement at target position allowed to determine the absolute efficiency of the MINIBALL setup to 5.8(7)% at 1332 keV. The relative efficiency of the MINIBALL setup in conjunction with the C-REX chamber was determined with the  $^{66}\text{Ga}$  and  $^{152}\text{Eu}$  sources at target position. The additional  $^{152}\text{Eu}$  source was used to complement the efficiency spectrum below 228 keV. The relative efficiencies of both decays are normalized to the 832.9 keV line of the  $^{66}\text{Ga}$  decay. Figure 48 illustrates the relative efficiency of the MINIBALL spectrometer as a function of the  $\gamma$ -ray energy with 100% at 832.9 keV. The data was fitted with the following logarithmic function

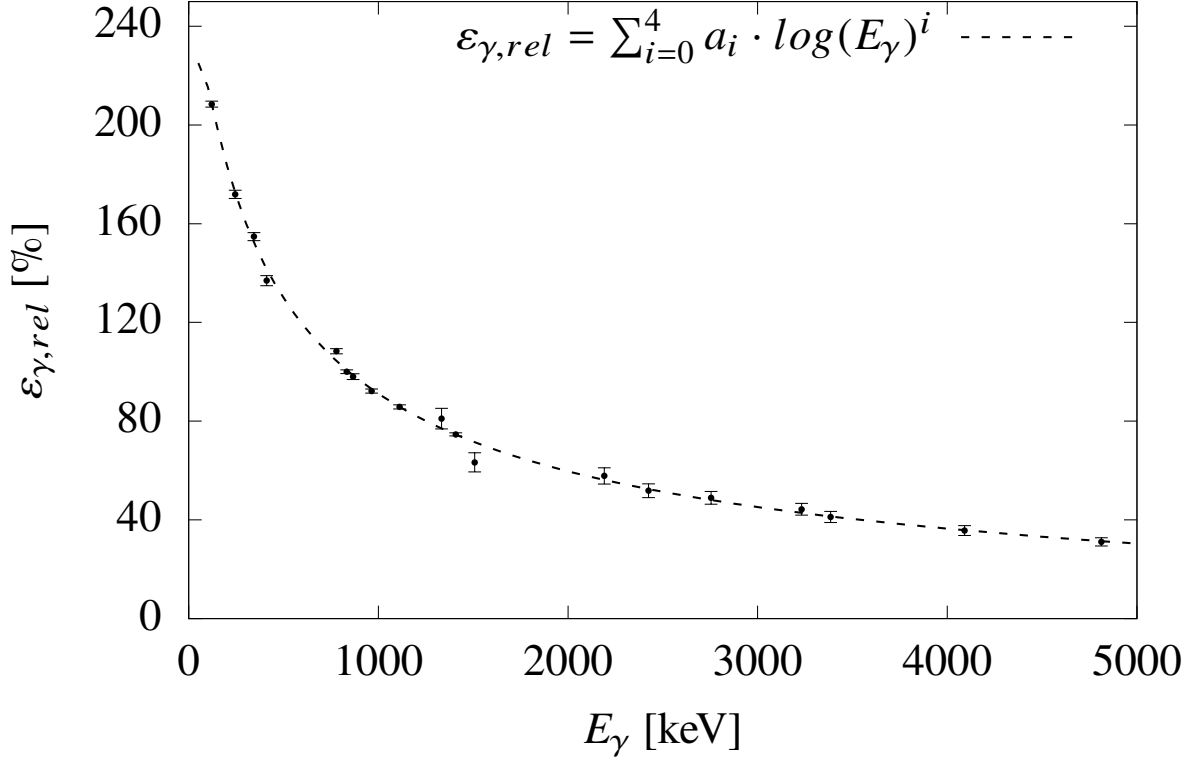


**Figure 48:** The relative efficiency of the MINIBALL array around the C-REX target chamber was measured with a  $^{66}\text{Ga}$  and a  $^{152}\text{Eu}$  source at target position. For more details see text.

$$\varepsilon_{\gamma} = \sum_i^4 a_i \cdot \log(E_{\gamma})^i, \quad (5.2)$$

with  $a_0 = -1162.5$ ,  $a_1 = 923.9$ ,  $a_2 = -213.4$ ,  $a_3 = 20.0$  and  $a_4 = -0.7$ . Normalizing this data to the absolute efficiency at 1332 keV, yields an absolute detection efficiency of 2.72(4)% at 4041 keV ( $2_1^+ \rightarrow 0_{\text{g.s.}}^+$ ) and 2.57(4)% at 4531 keV ( $3_1^- \rightarrow 0_{\text{g.s.}}^+$ ).

### 5.3. Doppler correction

In Coulomb-excitation reactions with high-energy beams, the  $\gamma$ -ray energies have to be corrected due to the Doppler effect. The experiment deals with a recoil velocity of  $\beta \sim 10\%$ . The high recoil velocity and the close configuration of the HPGe detectors, result in a large Doppler broadening of the detected  $\gamma$  rays. The 3-dimensional transversal Doppler effect

is a function of  $\beta$  and the relative emittance angle  $\theta_{p\gamma}$ . Thus, the interaction position of the  $\gamma$  ray inside the HPGe crystals and the particle position within the DSSSD have to be known precisely to perform a proper correction for this effect. The corrected  $\gamma$ -ray energy is given as

$$E_{\gamma,0} = E_{\gamma,\text{lab}} \frac{1 + \beta \cos(\theta_{p\gamma})}{\sqrt{1 - \beta^2}}, \quad (5.3)$$

where  $E_{\gamma,\text{lab}}$  is the energy measured in the laboratory frame,  $E_{\gamma,0}$  the emitted energy in the rest frame of the particle,  $\beta = v/c$  and  $\theta_{p\gamma}$  the angle between particle momentum vector and direction of emitted  $\gamma$  ray with

$$\cos(\theta_{p\gamma}) = \sin(\theta_{\text{lab},\gamma}) \sin(\theta_{\text{lab},p}) \cos(\varphi_{\text{lab},p} - \varphi_{\text{lab},\gamma}) + \cos(\theta_{\text{lab},\gamma}) \cos(\theta_{\text{lab},p}). \quad (5.4)$$

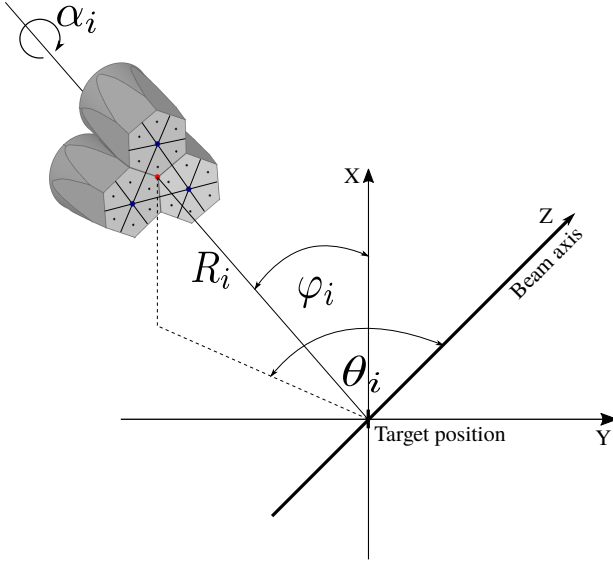


**Figure 49:** Definition of the four parameters  $R_i$ ,  $\theta_i$ ,  $\phi_i$  and  $\alpha_i$  describing the exact position of a MINIBALL triple detector (red point) relative to the target position. The blue points mark the three core positions, whereas the black dots illustrate the center of each segment.

The detected observables  $\theta_{\text{lab},\gamma}$ ,  $\phi_{\text{lab},\gamma}$  and  $\theta_{\text{lab},p}$ ,  $\phi_{\text{lab},p}$  denote the detected angles in the laboratory frame measured with the MINIBALL and DSSSD detectors, respectively.

As already mentioned in the previous section the energy information of the  $\gamma$  rays is obtained from the core signal of the HPGe crystals. This is due to the larger volume for detection and, hence, a higher probability for a complete energy deposition of the  $\gamma$  ray, which will improve the peak to background ratio. A further improvement is the add-back method, which allows to reconstruct Compton-scattered events within one MINIBALL triple cluster in a small time window and add the detected energies. To perform a proper Doppler correction a precise interaction position of the  $\gamma$  ray inside the detector volume is essential.

Especially for the presented experiment with transition energies above 4 MeV and low statistics an exact Doppler correction is important. A high position sensitivity of the MINIBALL detectors is achieved by the granularity of the six-fold MINIBALL detectors, which ensure an improved assignment of the interaction position within each HPGe.

To use the position sensitivity, each segment position relative to the target is identified by an angular-calibration measurement, employing Doppler-shifted  $\gamma$  rays after  $d(^{22}\text{Ne}, ^{23}\text{Ne})p$  and  $d(^{22}\text{Ne}, ^{23}\text{Na})n$  reactions performed in an independent stable beam experiment with  $^{22}\text{Ne}$ . The approach is the following:

1. The position of each MINIBALL triple cluster relative to the target spot can be described by a set of four parameters  $R_i$ ,  $\theta_i$ ,  $\phi_i$  and  $\alpha_i$  as shown in Fig. 49. The center of each core and segment is determined in terms of these parameter relative.

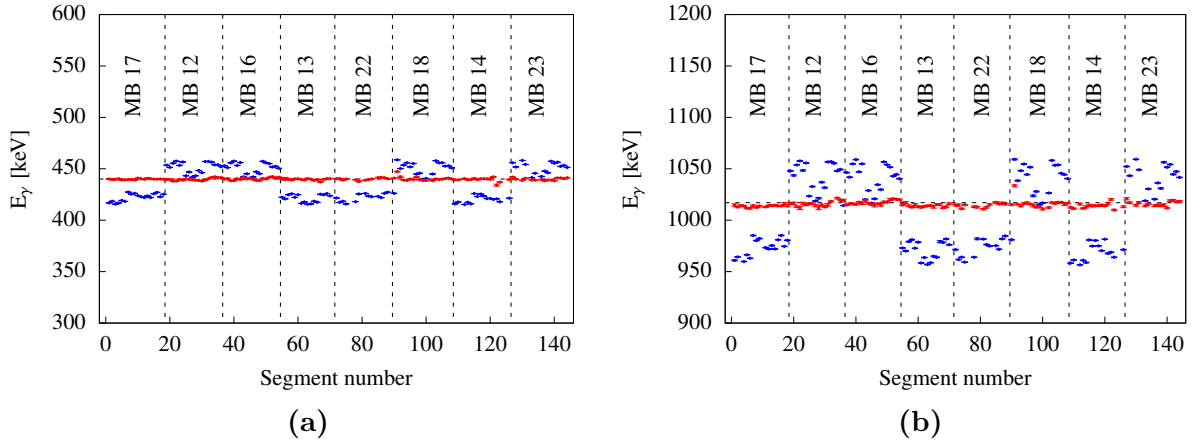


**Figure 50:** (a) Fitted mean energy of each segment before (blue) and after (red) Doppler correction for the 440-keV deexcitation of  $^{23}\text{Na}$ . (b) Energy of the 1017-keV  $\gamma$  ray from  $^{23}\text{Ne}$  detected in each segment before and after Doppler correction, similar to (a).

2. After transfer reactions, the excited  $^{23}\text{Ne}$  and  $^{23}\text{Na}$  decay in flight by emitting  $\gamma$  rays, which are recorded with a Doppler broadening in the germanium detectors. The scattering angles of the recoiling nuclei are small due to the kinematics and can be neglected. Thus, the energy shift depends on the detection position of the  $\gamma$  ray. For each segment a specific set of parameters  $R_{ij}$ ,  $\theta_{ij}$ ,  $\phi_{ij}$  and  $\alpha_{ij}$  is calculated to correct the  $\gamma$ -ray energies according to Equation 5.3. Considering the rigidity of the germanium crystals and the configuration within a triple cluster, all 18 segments ( $0 \leq j \leq 18$ ) can be used to obtain the final set of  $R_i$ ,  $\theta_i$ ,  $\phi_i$  and  $\alpha_i$  via an minimization algorithm. The results of the minimization procedure are illustrated in Figure 50 for



cluster 17. The measured core energy was combined with the angular position of the segment, which detected the 440 keV transition of the  $^{23}\text{Na}$  decay.

3. The determined coordinates of each detector segment relative to the target spot is used to perform the Doppler correction at segment level. In Figure 51 the sum of the core spectra of all 24 HPGe crystals are shown for the  $^{22}\text{Ne}$  in-beam measurement with and without Doppler correction. To verify the results from the minimization, the FWHM of the 1017 keV transition was analyzed as a function of the  $\theta_i$ ,  $\phi_i$  and  $\alpha_i$ . In Figure 52 the FWHM of the 1017 keV transition from the deexciting  $^{23}\text{Ne}$  nucleus is plotted as a function of the position parameters. Therefore, two parameters were fixed and the last one was varied. For all three parameters a global minimum can be observed and it matches almost perfectly the obtained values from the minimization procedure. The values from the minimization algorithm are presented in Table 1. The final relative energy resolution after adjusting the position parameters for the Doppler correction amounts to 1.1% at 1017 keV.

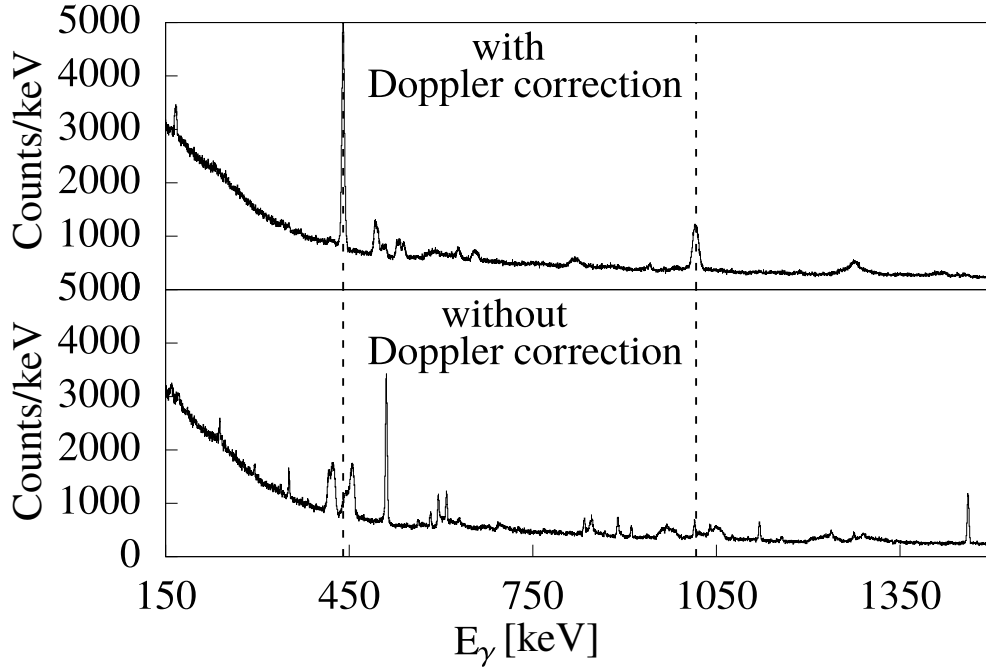


**Figure 51:**  $\gamma$ -ray spectrum after  $d(^{22}\text{Ne}, ^{23}\text{Ne})p$  and  $d(^{22}\text{Ne}, ^{23}\text{Na})n$  transfer reactions with Doppler correction (top) and without (bottom). The two expected transitions at 440 keV and 1017 keV are blurred in the uncorrected spectrum and narrow in the Doppler corrected spectrum. For the other transitions which decayed at rest, it is vice versa.

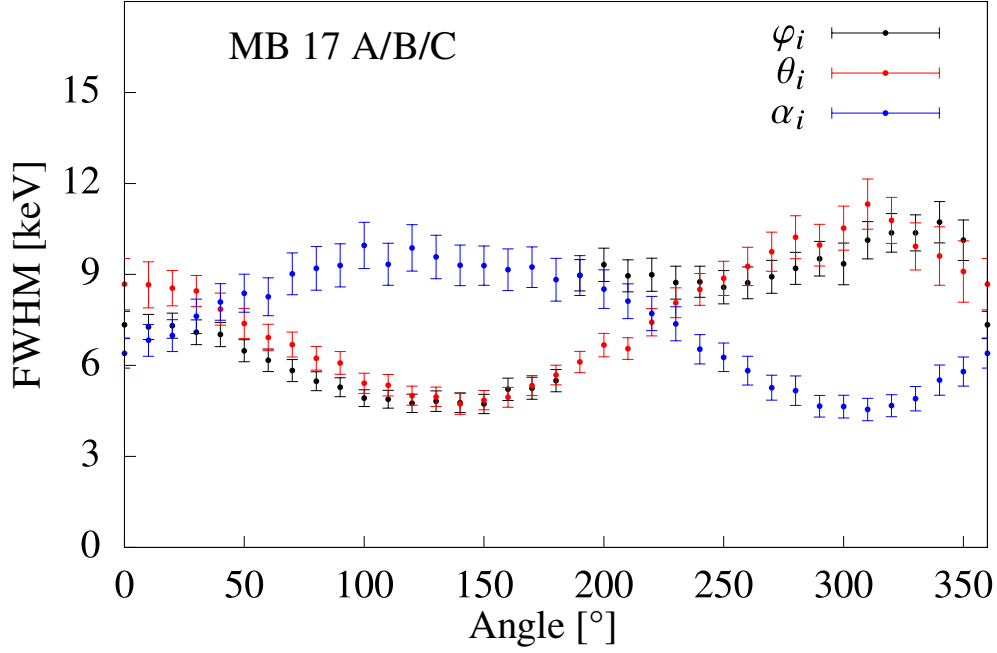


**Figure 52:** FWHM of the 1017 keV transition following the deexcitation of  $^{23}\text{Ne}$  as a function of the position parameters  $\theta_i$ ,  $\phi_i$  and  $\alpha_i$ . The plot illustrates a scan for MINIBALL triple detector 17 (MB 17). The plotted FWHM is the average of the FWHM of each crystal inside MB 17. See text for more details.

**Table 1.:** Position parameters used for the center of each MINIBALL (MB) triple cluster for the Doppler correction.

MB cluster	$R_i$ [mm]	$\theta_i$ [deg]	$\phi_i$ [deg]	$\alpha_i$ [deg]
MB 17	169.98	136.93	126.99	304.95
MB 12	154.05	57.35	51.49	163.59
MB 16	144.79	57.90	134.17	114.48
MB 13	168.39	137.71	55.68	123.76
MB 22	174.94	141.52	228.34	60.2
MB 18	156.73	55.49	222.36	1.03
MB 14	181.62	142.08	302.69	149.83
MB 23	131.2	61.9	299.4	310.9

For the identification of the particle position, the DSSSD geometry and Coulomb excitation of the  $^{206}\text{Pb}$  target were used. The scattering angle  $\theta_{\text{lab,p}}$  was calculated from the known dimensions of the detector and the distance to the target, which was  $d = 32.0(5)$  mm. An angular range for the detection of scattered particles between  $15.7^\circ$  and  $52.0^\circ$  in the laboratory frame was covered by the DSSSD. The azimuth angle  $\phi_{\text{lab,p}}$  was calibrated via the minimization of the FWHM of the target excitation.

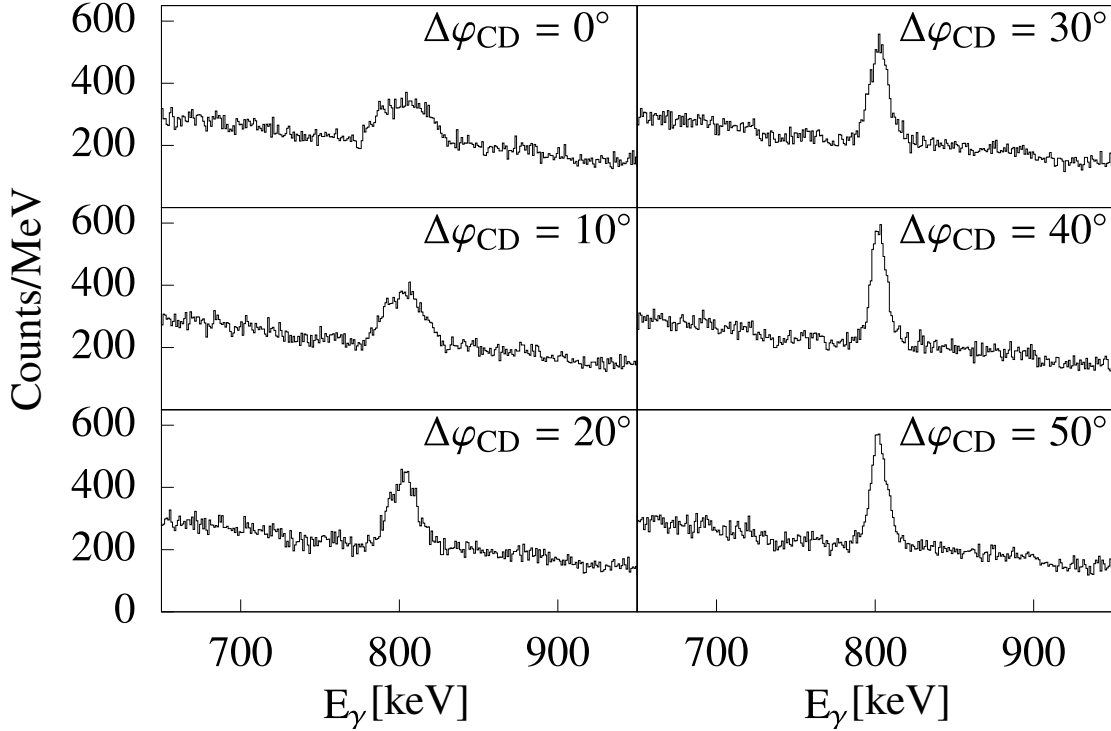


**Figure 53:** The FWHM of the target deexcitation as a function of the DSSSD azimuth angle offset. The best Doppler-correction is achieved at a rotation between  $40^\circ$  and  $50^\circ$ .

It was assumed that the first back-side strip of the top quadrant is aligned with the beam axis and corresponds to  $\phi_{\text{lab,p}} = 0$ . An additional offset  $\Delta\phi_{\text{CD}}$  was applied to minimize the FWHM of the 803 keV transition of  $^{206}\text{Pb}$  after the Coulomb-excitation reaction. Figure 53 shows the  $2_1^+ \rightarrow 0_{\text{g.s.}}^+$  transition of  $^{206}\text{Pb}$  for different  $\Delta\phi_{\text{CD}}$  offsets up to  $50^\circ$ . Larger rotations lead to more Doppler broadening again. The best lineshape, energy position and FWHM after Doppler-correction is achieved for an offset between  $\Delta\phi_{\text{CD}} = 40^\circ$  and  $\Delta\phi_{\text{CD}} = 50^\circ$ . Around this value an additional scan was performed (cf. Fig. 54), which results in an optimal rotation of  $\Delta\phi_{\text{CD}} = 45.0^\circ \pm 0.5^\circ$ . The resulting FWHM of the target excitation peak amounts to 10.5 keV or 1.3%.

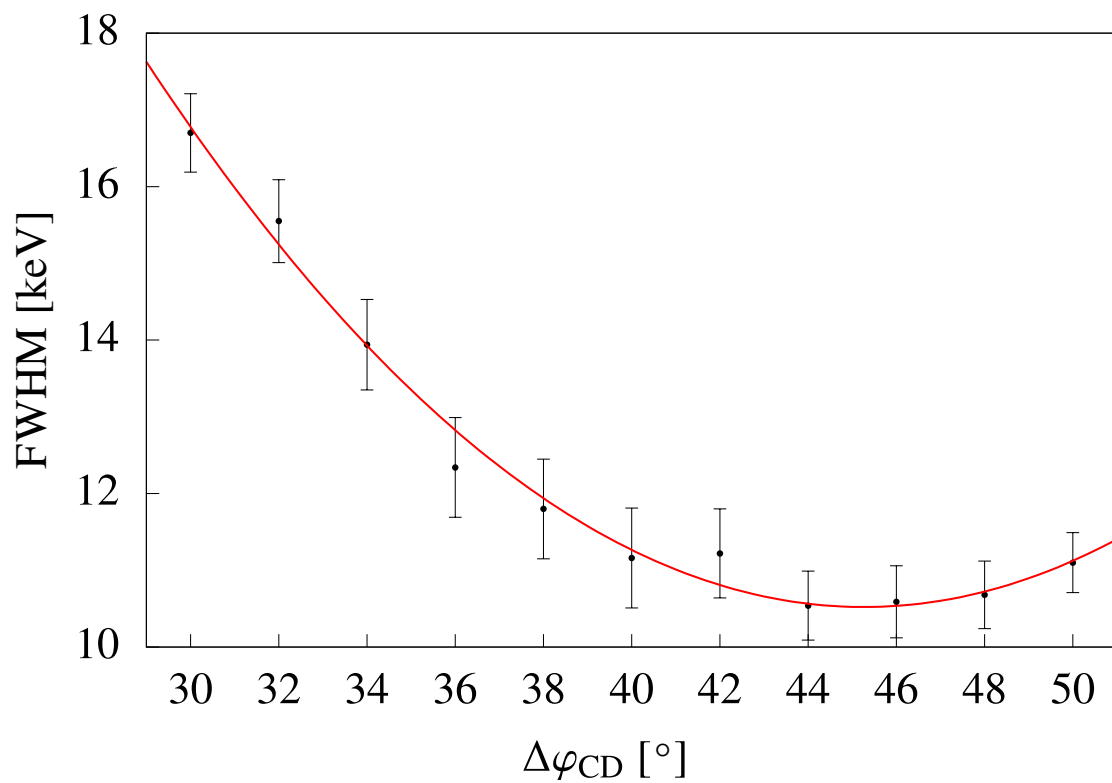


**Figure 54:** FWHM of the 803 keV transition of  $^{206}\text{Pb}$  after Doppler correction as a function of the rotation of the DSSSD detector. A minimum value of 10.5 keV is found at  $45.0(5)^\circ$ . See text for details.

## 5.4. Kinematic conditions

In Section 5.2.2, the recorded particle spectrum of all particles was shown (cf. Figure 37). Two distinct branches are visible, which correspond to projectile-like and target-like particles after scattering. Figure 55 illustrates the measured and calculated particle energy spectrum as a function of the scattering angle. Both spectra are comparable, which is the first evidence for a scattering of  $^{132}\text{Sn}$  on  $^{206}\text{Pb}$  at a beam energy of 726 MeV. The broad structure of scattered  $^{132}\text{Sn}$  ions at low scattering angles is caused by the capacitive coupling or PHD effect discussed in Section 5.2.2 plus the reduced energy resolution induced by radiation damage.

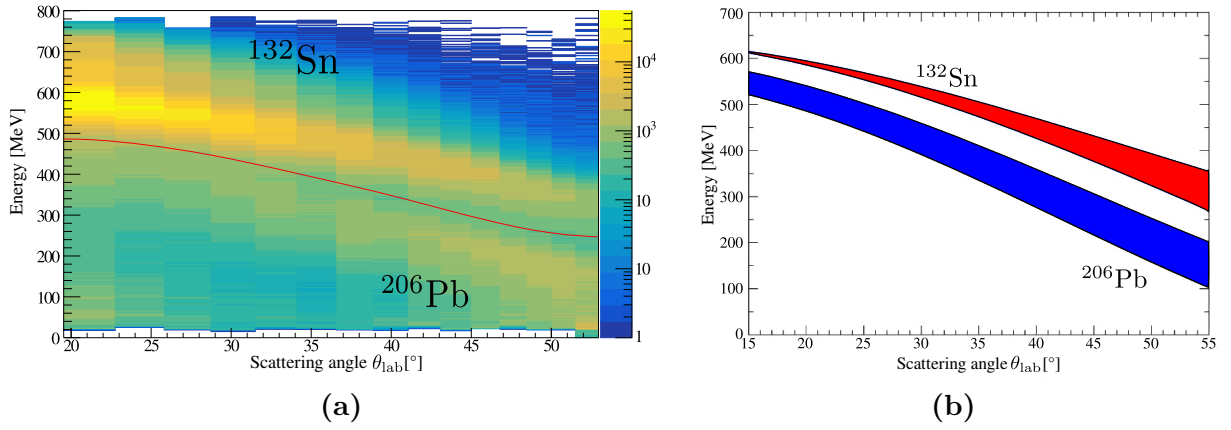


**Figure 55:** Energy DSSSD spectra as a function of the scattering angle in the center-of-mass system. (a) Experimental spectrum measured with the DSSSD detector at ISOLDE. (b) Calculated energy spectrum with the computer code LISE++. The width of the kinematic branches originate from the beam spot size, the target thickness, opening angle of the DSSSD segments and the charge sharing in the DSSSD.

As reported in Ref. [22] a minimum distance of 5 fm between the nuclear surfaces of the scattering particles is required to ensure safe Coulomb excitation (cf. Sec.1.4). To confirm the validity of this safe Coulomb criterion for the present experiment, the ratio of the measured scattering cross section and the calculated Rutherford cross section is plotted in Figure 56 as a function of the point of closest approach. The ratio is obtained via the measured number of scattered projectiles in the DSSSD. The calculated Rutherford cross section is normalized to the intensity obtained of the innermost annular segment of the DSSSD. A constant trend along unity is observed for distances larger than 4.6 fm. For smaller distances the ratio drops and indicates the contribution of the nuclear force to

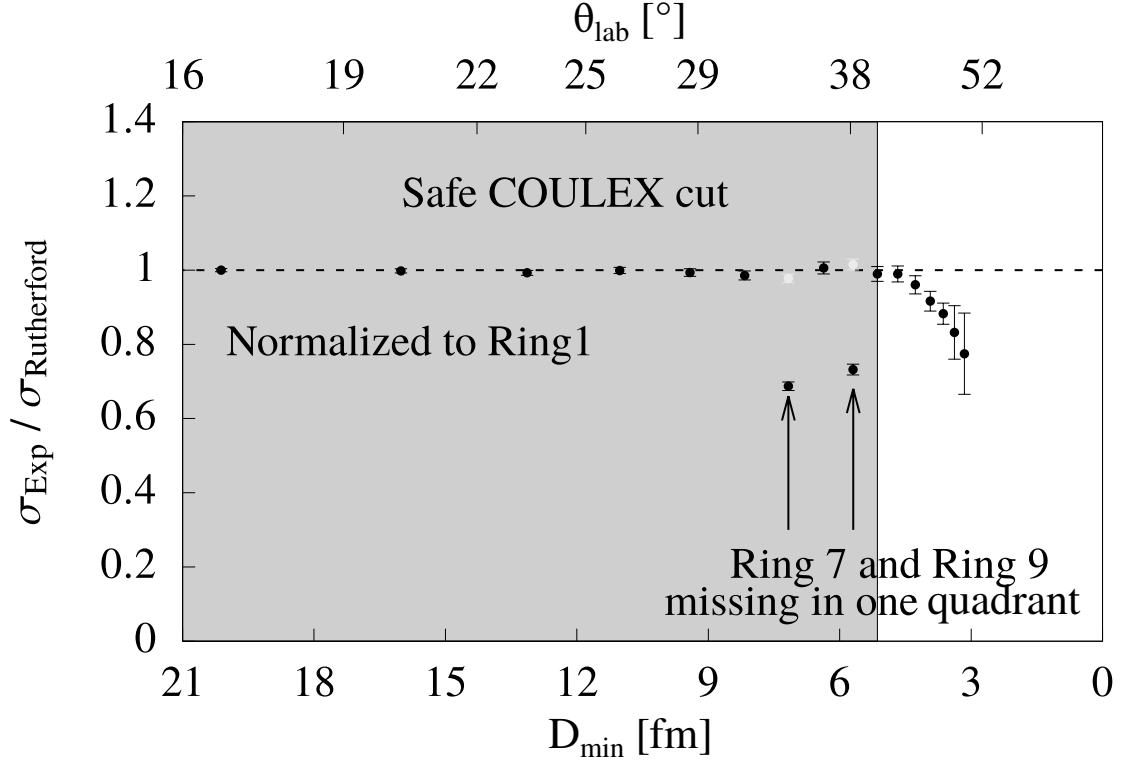


**Figure 56:** Ratio of measured and calculated Coulomb cross section for projectile particles. The value of 1 indicates a pure electromagnetic interaction between the scattering nuclei. Below 4.6 fm for the point-of-closest approach the contribution of the nuclear force is not longer negligible. Data points in white-grey denote the obtained values after the solid-angle correction for the broken rings. See text for more details.

the excitation and its impact on the scattering angle. At this point the contribution of the nuclear force is not longer negligible, consequently the assumption of safe Coulomb excitation breaks down. Thus, only scattered particles with more than 5.14 fm distance at the point of closest approach (marked by the shaded area in Figure 56) were considered to fulfill the safe Coulomb-excitation condition. The deviation of the two data points in Figure 56 is explained by the broken annular segments 7 and 9 in one DSSSD quadrant. Data points in white-grey mark the solid-angle corrected cross-section ratio for segments 7 and 9. The increasing error bars for higher scattering angles result from reduced statistics in these segments.

It is concluded that, the 5 fm criterion is well justified. Moreover, it is possible to distinguish between projectile and target-like particles, which is essential to obtain the final  $\gamma$ -ray yields. However, the separation is not trivial and will be discussed in the next chapter in detail (see Sec. 6.0.1).

## 5.5. Particle- $\gamma$ coincidence

After analysis of the particle spectra and the kinematics of the reaction, it is possible to use the momentum vector of the particles to improve the Doppler correction of the  $\gamma$ -ray spectra. In principle it is not known if the  $\gamma$ -ray was emitted by a projectile or a target-like particle. Therefore, at least two  $\gamma$ -ray spectra are generated with Doppler-correction for beam-like ( $A = 132$ ) and target-like ( $A = 206$ ) particles. The particle-cut condition for the separation between beam-like and target-like particles is illustrated by the red line in Figure 55. The information of the detected particle in combination with the direction of the  $\gamma$ -ray is used for the Doppler correction. Particle- $\gamma$  coincidences are applied to select the right  $\gamma$  transitions and to enhance the peak-to-background ratio of the resulting spectra. This is especially important for Coulomb-excitation experiments with radioactive ion beams, as the huge amount of background radiation superimpose the rare events of interest. The background radiation is due to  $\beta$ -decay of the radioactive ions implanted inside the target chamber and along the beam line as well as bremsstrahlung from the accelerator. Only prompt  $\gamma$  rays which are detected within a  $\Delta t_p = 225$  ns time window relative to a particle in the DSSSD are selected for the final  $\gamma$ -ray spectra.

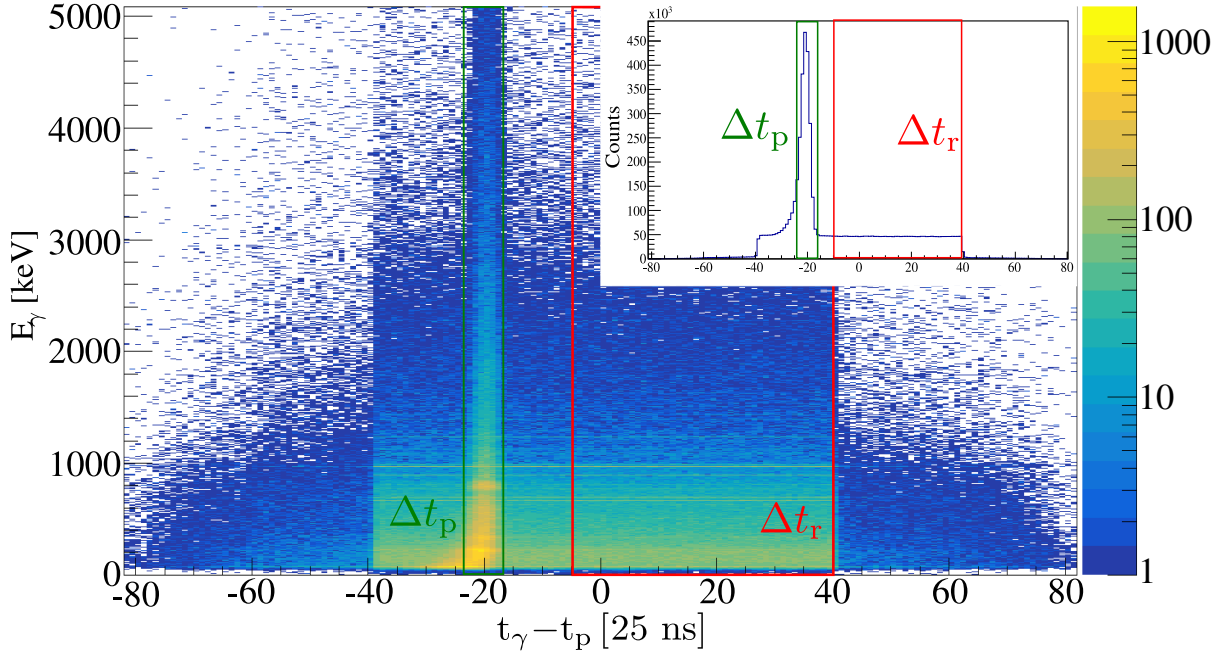


**Figure 57:**  $\gamma$ -ray energy as a function of the time correlation between detected particles and  $\gamma$  rays. Prompt and random time windows are marked, which are used to generate the final  $\gamma$ -ray spectra

The detected  $\gamma$ -ray energy in dependence of the time difference between particle and  $\gamma$  ray is shown in Figure 57. Two time windows are marked and the x-projection of the spectrum is shown as an inset. The prompt component is on top of the continuous background radiation. To eliminate the random background within the prompt time window, a background subtraction is performed using a distinct time window  $\Delta t_r$  on the continuous background. Fluctuations of the random  $\gamma$ -ray background are minimized by selecting a time window with a large width of  $\Delta t_r = 1.275 \mu\text{s}$ .

The resulting  $\gamma$ -ray spectra with a gate on detected projectile particles are illustrated in Figure 58. The low-energy part of the  $\gamma$ -ray spectrum is shown without Doppler-correction in order to illustrate the existing  $\beta$ -decay transitions prior to background subtraction. The high-energy part is shown with Doppler-correction in order to illustrate the  $\gamma$ -ray transitions of  $^{132}\text{Sn}$ . To account for the larger random time window, the background spectrum is multiplied by a factor of  $m = 225/1275$  before the subtraction. The final  $\gamma$ -ray spectra for beam-like and target-like particles are particularly clean from background radiation and mostly contain transitions caused by Coulomb excitation. A detailed discussion of the observed transition lines in the final  $\gamma$ -ray spectra is given in the following sections.

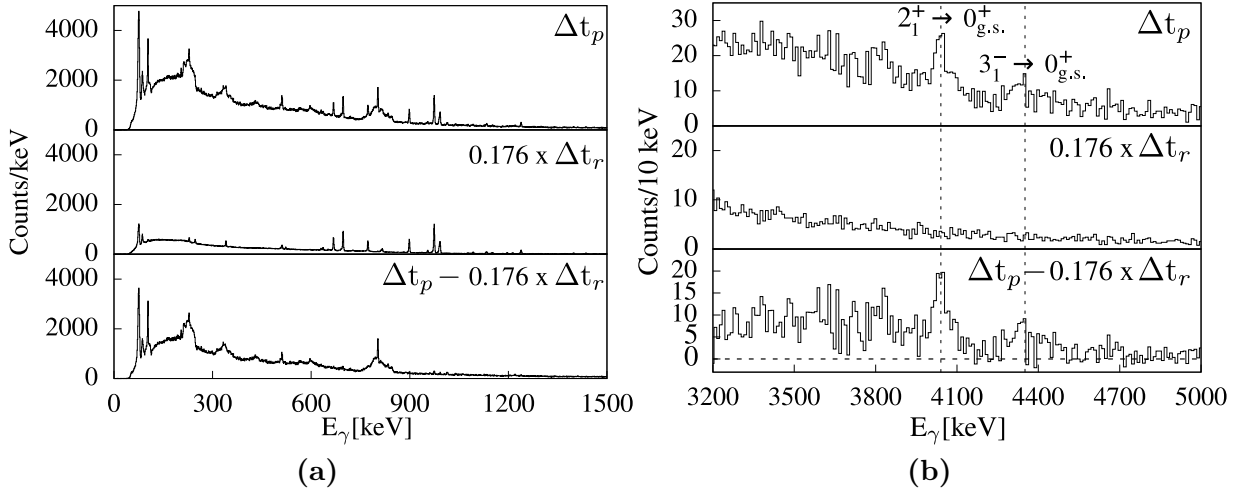


**Figure 58:** (a) Final  $\gamma$ -ray spectrum for  $^{132}\text{Sn}$  projectiles without Doppler-correction before ( $\Delta t_p$ ) and after ( $\Delta t_p - 0.176 \cdot \Delta t_r$ ) background ( $\Delta t_r$ ) subtraction for the low-energy part. (b) Same as in (a) for the high-energy part, but with Doppler-correction. See text for more details.



## 5.6. Beam composition

<sup>132</sup> Ba	<sup>133</sup> Ba	<sup>134</sup> Ba	<sup>135</sup> Ba	<sup>136</sup> Ba	<sup>137</sup> Ba	<sup>138</sup> Ba	<sup>139</sup> Ba
<sup>131</sup> Cs	<sup>132</sup> Cs	<sup>133</sup> Cs	<sup>134</sup> Cs	<sup>135</sup> Cs	<sup>136</sup> Cs	<sup>137</sup> Cs	<sup>138</sup> Cs
<sup>130</sup> Xe	<sup>131</sup> Xe	<sup>132</sup> Xe	<sup>133</sup> Xe	<sup>134</sup> Xe	<sup>135</sup> Xe	<sup>136</sup> Xe	<sup>137</sup> Xe
<sup>129</sup> I	<sup>130</sup> I	<sup>131</sup> I	<sup>132</sup> I	<sup>133</sup> I	<sup>134</sup> I	<sup>135</sup> I	<sup>136</sup> I
<sup>128</sup> Te	<sup>129</sup> Te	<sup>130</sup> Te	<sup>131</sup> Te	<sup>132</sup> Te	<sup>133</sup> Te	<sup>134</sup> Te	<sup>135</sup> Te
<sup>127</sup> Sb	<sup>128</sup> Sb	<sup>129</sup> Sb	<sup>130</sup> Sb	<sup>131</sup> Sb	<sup>132</sup> Sb	<sup>133</sup> Sb	<sup>134</sup> Sb
<sup>126</sup> Sn	<sup>127</sup> Sn	<sup>128</sup> Sn	<sup>129</sup> Sn	<sup>130</sup> Sn	<sup>131</sup> Sn	<sup>132</sup> Sn	<sup>133</sup> Sn
<sup>125</sup> In	<sup>126</sup> In	<sup>127</sup> In	<sup>128</sup> In	<sup>129</sup> In	<sup>130</sup> In	<sup>131</sup> In	<sup>132</sup> In
<sup>124</sup> Cd	<sup>125</sup> Cd	<sup>126</sup> Cd	<sup>127</sup> Cd	<sup>128</sup> Cd	<sup>129</sup> Cd	<sup>130</sup> Cd	<sup>131</sup> Cd

**Figure 59:** Nuclei along the isobaric  $A = 132$  chain that potentially contribute to the beam composition of the experiment are marked with red squares.

Due to the high vacuum specifications of the newly installed cryomodules of the HIE-ISOLDE linear accelerator, the installation of an additional detection system at MINIBALL, e.g. an ionization chamber, to measure the beam composition directly was not possible. Potential beam contaminations are possible along the isobaric  $A = 132$  chain, since the mass separators are only selective to the mass-over-charge ratio (cf. Fig. 59). As the primary ISOLDE beam is extracted as a singly-charged molecular beam of  $^{132}\text{Sn}^{34}\text{S}$ , contaminations are also possible from ions with mass  $A = 166$ . The transport from REXTRAP to REXEBIS is managed by an electrostatic steerer, thus, no  $A/q$  separation is possible at that stage. Mass  $A = 132$  ions were charge breed in REXEBIS for 194 ms and extracted with charge state  $q = 31^+$ , which results in an

$A/q = 4.258$ . For potential mass  $A = 166$  ions reaching REXEBIS a feasible charge breeding to charge state  $q = 39^+$  yields a similar mass-over-charge ratio of  $A/q = 4.256$ . All highly charged ions with  $A/q \simeq 4.26$  were injected into the REXLINAC with an extraction time of 200  $\mu\text{s}$ . The deduced total beam intensity at the MINIBALL setup amounted to  $3 \times 10^5$  ions/s.

### $\beta$ -decay investigation

A first step to determine the beam composition is the identification of all transition lines of the  $\beta$ -decay spectrum. Figure 60 presents the recorded  $\gamma$ -ray spectrum of the random background radiation mainly caused by  $\beta$ -delayed  $\gamma$  transitions. The observed transition energies and the corresponding  $\beta$ -decays are listed in Table 2. All observed transitions are assigned to the decays of  $^{132}\text{Sn} \rightarrow ^{132}\text{Sb}$ ,  $^{132}\text{Sb} \rightarrow ^{132}\text{Te}$ ,  $^{132}\text{Te} \rightarrow ^{132}\text{I}$ ,  $^{132}\text{I} \rightarrow ^{132}\text{Xe}$ .

**Table 2.:** Observed  $\gamma$ -ray transition energies following the corresponding  $\beta$ -decay.

$E_\gamma$	$\beta$ -decay	$E_\gamma$	$\beta$ -decay	$E_\gamma$	$\beta$ -decay
75 keV	XR $k\alpha 1$ $^{206}\text{Pb}$	1092 keV	$^{132}\text{Sb} \rightarrow ^{132}\text{Te}$	2051 keV	$^{132}\text{I} \rightarrow ^{132}\text{Xe}$
86 keV	$^{132}\text{Sn} \rightarrow ^{132}\text{Sb}$	1133 keV	$^{132}\text{Sb} \rightarrow ^{132}\text{Te}$	2115 keV	$^{132}\text{Sb} \rightarrow ^{132}\text{Te}$
103 keV	$^{132}\text{Sb} \rightarrow ^{132}\text{Te}$	1151 keV	$^{132}\text{Sb} \rightarrow ^{132}\text{Te}$	2126 keV	$^{132}\text{Sb} \rightarrow ^{132}\text{Te}$
228 keV	$^{132}\text{Te} \rightarrow ^{132}\text{I}$	1182 keV	$^{132}\text{Sb} \rightarrow ^{132}\text{Te}$	2197 keV	$^{132}\text{Sb} \rightarrow ^{132}\text{Te}$
246 keV	$^{132}\text{Sn} \rightarrow ^{132}\text{Sb}$	1196 keV	$^{132}\text{Sb} \rightarrow ^{132}\text{Te}$	2221 keV	$^{132}\text{Sb} \rightarrow ^{132}\text{Te}$
276 keV	$^{132}\text{Sb} \rightarrow ^{132}\text{Te}$	1213 keV	$^{132}\text{Sb} \rightarrow ^{132}\text{Te}$	2248 keV	$^{132}\text{Sb} \rightarrow ^{132}\text{Te}$
339 keV	$^{132}\text{Sn} \rightarrow ^{132}\text{Sb}$	1237 keV	$^{132}\text{Sn} \rightarrow ^{132}\text{Sb}$	2280 keV	$^{132}\text{Sb} \rightarrow ^{132}\text{Te}$
353 keV	$^{132}\text{Sb} \rightarrow ^{132}\text{Te}$	1274 keV	$^{132}\text{Sb} \rightarrow ^{132}\text{Te}$	2362 keV	$^{132}\text{Sb} \rightarrow ^{132}\text{Te}$
382 keV	$^{132}\text{Sb} \rightarrow ^{132}\text{Te}$	1289 keV	$^{132}\text{I} \rightarrow ^{132}\text{Xe}$	2383 keV	$^{132}\text{Sb} \rightarrow ^{132}\text{Te}$
436 keV	$^{132}\text{Sb} \rightarrow ^{132}\text{Te}$	1295 keV	$^{132}\text{I} \rightarrow ^{132}\text{Xe}$	2413 keV	$^{132}\text{Sb} \rightarrow ^{132}\text{Te}$
505 keV	$^{132}\text{I} \rightarrow ^{132}\text{Xe}$	1300 keV	$^{132}\text{Sb} \rightarrow ^{132}\text{Te}$	2477 keV	$^{132}\text{Sb} \rightarrow ^{132}\text{Te}$
511 keV		1372 keV	$^{132}\text{I} \rightarrow ^{132}\text{Xe}$	2514 keV	$^{132}\text{Sb} \rightarrow ^{132}\text{Te}$
521 keV	$^{132}\text{I} \rightarrow ^{132}\text{Xe}$	1389 keV	$^{132}\text{Sb} \rightarrow ^{132}\text{Te}$	2586 keV	$^{132}\text{Sb} \rightarrow ^{132}\text{Te}$
529 keV	$^{132}\text{Sn} \rightarrow ^{132}\text{Sb}$	1398 keV	$^{132}\text{I} \rightarrow ^{132}\text{Xe}$	2614 keV	$^{208}\text{Tl} \rightarrow ^{208}\text{Pb}$
549 keV	$^{132}\text{Sn} \rightarrow ^{132}\text{Sb}$	1435 keV	$^{132}\text{Sb} \rightarrow ^{132}\text{Te}$	2633 keV	$^{132}\text{Sb} \rightarrow ^{132}\text{Te}$
629 keV	$^{132}\text{I} \rightarrow ^{132}\text{Xe}$	1442 keV	$^{132}\text{I} \rightarrow ^{132}\text{Xe}$	2665 keV	$^{132}\text{Sb} \rightarrow ^{132}\text{Te}$
635 keV	$^{132}\text{Sb} \rightarrow ^{132}\text{Te}$	1460 keV	$^{40}\text{K} \rightarrow ^{40}\text{Ar}$	2710 keV	$^{132}\text{Sb} \rightarrow ^{132}\text{Te}$
651 keV	$^{132}\text{Sn} \rightarrow ^{132}\text{Sb}$	1512 keV	$^{132}\text{Sb} \rightarrow ^{132}\text{Te}$	2762 keV	$^{132}\text{Sb} \rightarrow ^{132}\text{Te}$
667 keV	$^{132}\text{I} \rightarrow ^{132}\text{Xe}$	1540 keV	$^{132}\text{I} \rightarrow ^{132}\text{Xe}$	2800 keV	$^{132}\text{Sb} \rightarrow ^{132}\text{Te}$
690 keV	$^{132}\text{Sb} \rightarrow ^{132}\text{Te}$	1574 keV	$^{132}\text{Sb} \rightarrow ^{132}\text{Te}$	2829 keV	$^{132}\text{Sb} \rightarrow ^{132}\text{Te}$
696 keV	$^{132}\text{Sb} \rightarrow ^{132}\text{Te}$	1633 keV	$^{132}\text{Sb} \rightarrow ^{132}\text{Te}$	2911 keV	$^{132}\text{Sb} \rightarrow ^{132}\text{Te}$
727 keV	$^{132}\text{I} \rightarrow ^{132}\text{Xe}$	1643 keV	$^{132}\text{Sb} \rightarrow ^{132}\text{Te}$	2920 keV	$^{132}\text{Sb} \rightarrow ^{132}\text{Te}$
771 keV	$^{132}\text{I} \rightarrow ^{132}\text{Xe}$	1786 keV	$^{132}\text{Sb} \rightarrow ^{132}\text{Te}$	3052 keV	$^{132}\text{Sb} \rightarrow ^{132}\text{Te}$
813 keV	$^{132}\text{Sb} \rightarrow ^{132}\text{Te}$	1840 keV	$^{132}\text{Sn} \rightarrow ^{132}\text{Sb}$	3329 keV	$^{132}\text{Sb} \rightarrow ^{132}\text{Te}$
815 keV	$^{132}\text{Sb} \rightarrow ^{132}\text{Te}$	1854 keV	$^{132}\text{Sb} \rightarrow ^{132}\text{Te}$	3350 keV	$^{132}\text{Sb} \rightarrow ^{132}\text{Te}$
899 keV	$^{132}\text{Sn} \rightarrow ^{132}\text{Sb}$	1920 keV	$^{132}\text{I} \rightarrow ^{132}\text{Xe}$	3407 keV	$^{132}\text{Sb} \rightarrow ^{132}\text{Te}$
953 keV	$^{132}\text{I} \rightarrow ^{132}\text{Xe}$	2002 keV	$^{132}\text{I} \rightarrow ^{132}\text{Xe}$	3460 keV	$^{132}\text{Sb} \rightarrow ^{132}\text{Te}$
974 keV	$^{132}\text{Sb} \rightarrow ^{132}\text{Te}$	2018 keV	$^{132}\text{Sb} \rightarrow ^{132}\text{Te}$	3558 keV	$^{132}\text{Sb} \rightarrow ^{132}\text{Te}$
991 keV	$^{132}\text{Sn} \rightarrow ^{132}\text{Sb}$	2040 keV	$^{132}\text{Sb} \rightarrow ^{132}\text{Te}$	3611 keV	$^{132}\text{Sb} \rightarrow ^{132}\text{Te}$
1078 keV	$^{132}\text{Sn} \rightarrow ^{132}\text{Sb}$				

In addition, the observed potassium decay  $^{40}\text{K} \rightarrow ^{40}\text{Ar}$  indicates that transitions with intensities down to the natural background radiation are identified. No transitions corresponding to the decay of  $^{132}\text{In}$  and  $^{132}\text{Cs}$  are present in the  $\beta$ -decay spectrum. This is expected, as these nuclei should not form a molecular compound with sulfur, due to their atomic properties. The same argument is valid for the stable noble gas  $^{132}\text{Xe}$ . Remaining possible contaminations along the isobaric chain of  $A = 132$  are  $^{132}\text{Sb}$ ,  $^{132}\text{Te}$ ,  $^{132}\text{I}$  and

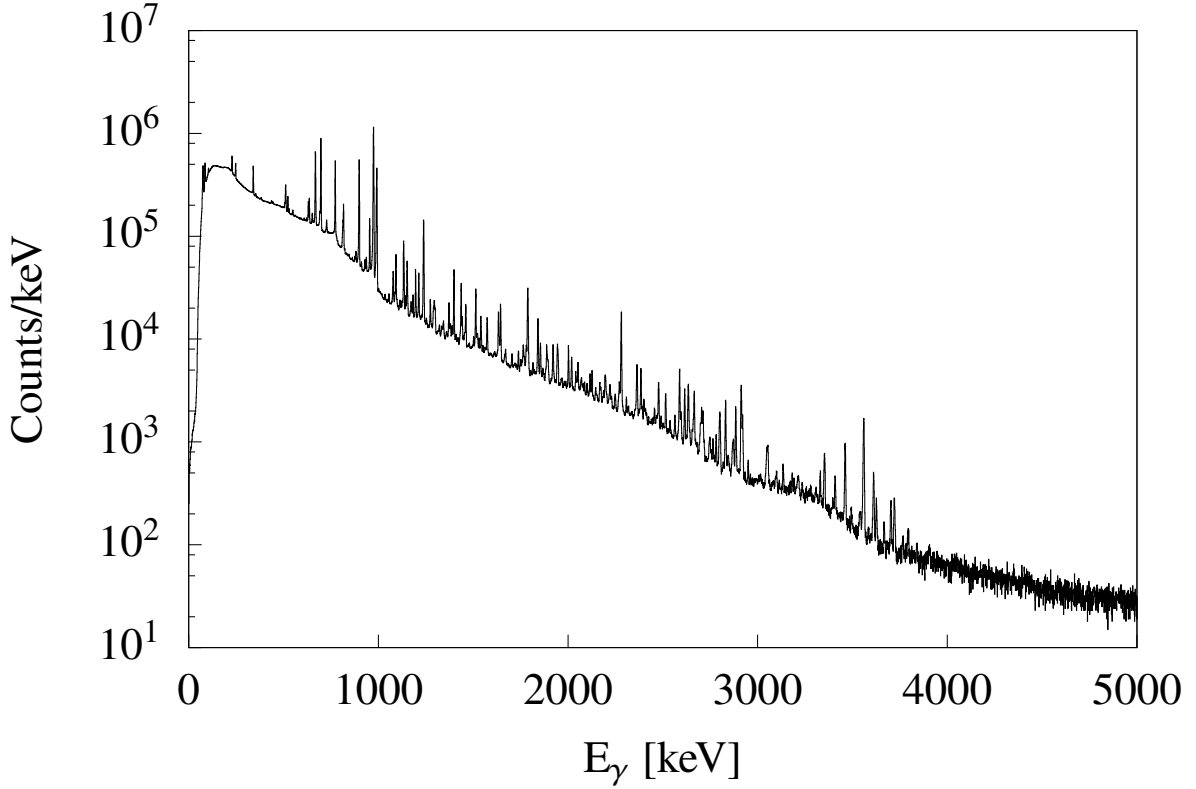


**Figure 60:** Detected random  $\beta$ -decay spectrum.  $\gamma$ -ray transitions with energies up to almost 4 MeV are observed.

$^{132}\text{Ba}$ . The amount of  $^{132}\text{Te}$  and  $^{132}\text{I}$  is investigated via ratios of  $\beta$ -decay transitions of mother and daughter nuclei as a function of time. For the determination of the time dependent  $\beta$ -decay ratios, i.e.  $^{132}\text{Sn} \rightarrow ^{132}\text{Sb}/^{132}\text{Sb} \rightarrow ^{132}\text{Te}$  and  $^{132}\text{Te} \rightarrow ^{132}\text{I}/^{132}\text{I} \rightarrow ^{132}\text{Xe}$ , the dominant transitions at 899 keV ( $^{132}\text{Sn} \rightarrow ^{132}\text{Sb}$ ), 974 keV ( $^{132}\text{Sb} \rightarrow ^{132}\text{Te}$ ), 228 keV ( $^{132}\text{Te} \rightarrow ^{132}\text{I}$ ) and 667 keV ( $^{132}\text{I} \rightarrow ^{132}\text{Xe}$ ) were used. Figure 61 illustrates the measured ratios as a function of the run number (total time = 127 hours). After the drop of both ratio curves at the beginning of the beam time, an equilibrium is reached and a constant ratio value is measured, which indicate a minor amount of Te and I in the beam.

The lack of data between run 85 up to 102 for the decay ratio of  $^{132}\text{Sn}$  and  $^{132}\text{Sb}$  is a result of an 8 hour beam stop. During these 8 hours, a ten minute implantation measurement was performed to determine the ratio of  $^{132}\text{Sn}$  and  $^{132}\text{Sb}$  in the beam (cf. Sec 5.6). The decay of  $^{132}\text{Te}$  and  $^{132}\text{I}$  with much longer half-lives is still observed and stays constant during the beam stop. After returning to the experimental setup and starting the in-beam measurement, an increase of the  $^{132}\text{Te} \rightarrow ^{132}\text{I}/^{132}\text{I} \rightarrow ^{132}\text{Xe}$  ratio is observed. Considering

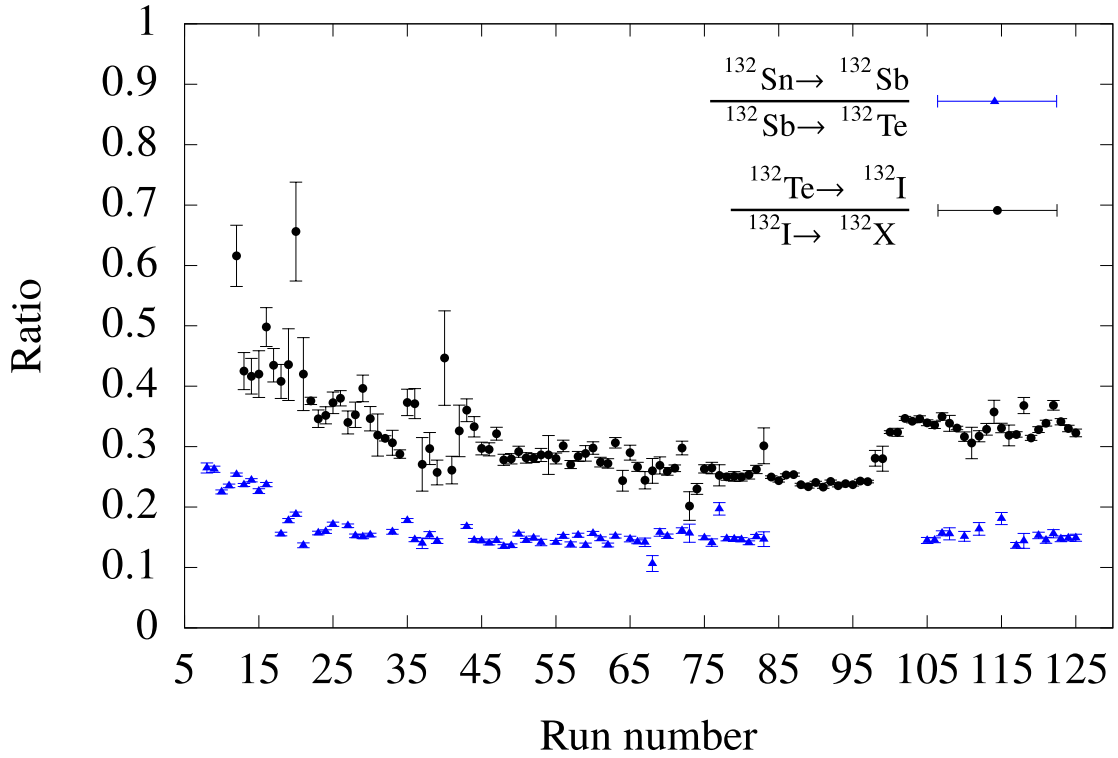


**Figure 61:** Time-dependent intensity ratios of  $\gamma$ -ray transitions following the respective  $\beta$  decays. See text for more details.

the much larger half-life of  $^{132}\text{Te}$  of 3.2 d compared to 2.3 h for  $^{132}\text{I}$ , an increase of the calculated ratio is only possible with no or a negligible amount of iodine in the beam. Further confirmation of the absence of  $^{132}\text{I}$ ,  $^{132}\text{Te}$  and  $^{132}\text{Cs}$  as a part of the beam composition is achieved by the projectile gated  $\gamma$ -ray spectrum obtained after Coulomb excitation, where no  $\gamma$  lines from these isotopes are found.

### Beam-like $\gamma$ -ray spectrum

In Figure 62(a) the beam-like gated  $\gamma$ -ray spectrum with Doppler correction for mass  $A = 132$  and background subtraction is shown up to 1000 keV. No other transition lines are present between 1000 keV up to 4 MeV.

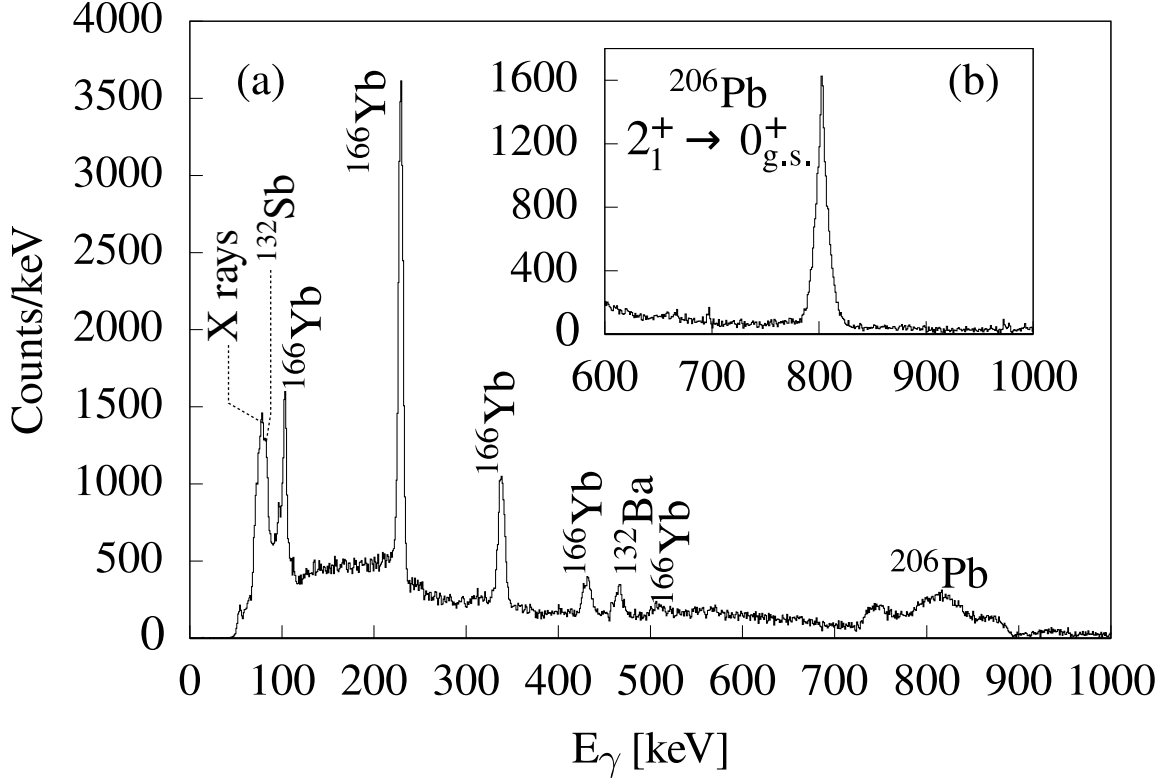


**Figure 62:** Final low-energy  $\gamma$ -ray spectrum with a gate on beam-like particles after Doppler correction for  $A = 132$  including background subtraction. All transitions are identified. For more details see text.

All transitions are identified and are caused by deexcitation of  $^{166}\text{Yb}$ ,  $^{132}\text{Ba}$  and  $^{206}\text{Pb}$  after Coulomb excitation. Therefore,  $^{132}\text{Te}$ ,  $^{132}\text{I}$  and  $^{132}\text{Xe}$  are excluded as part of the beam composition, as the transitions strengths of the dominant transitions are known [64] and the expected  $\gamma$ -ray intensity after Coulomb excitation can be calculated. No lines from  $^{132}\text{Te}$ ,  $^{132}\text{I}$ ,  $^{132}\text{Cs}$  and  $^{132}\text{Xe}$  are observed in the  $\gamma$ -ray spectrum. Thus, the final beam composition is composed of  $^{166}\text{Yb}$ ,  $^{132}\text{Ba}$ ,  $^{132}\text{Sn}$  and  $^{132}\text{Sb}$ . Figure 62 (b) shows the beam-like gated  $\gamma$ -ray spectrum Doppler-corrected for target nuclei, which presents the target deexcitation  $2_1^+ \rightarrow 0_{\text{g.s.}}^+$  at 803 keV. This proves the correctness of the performed reaction and ensures the normalization to the target excitation of the reduced transitions strength

of  $^{132}\text{Sn}$ , as described in Section 1.4. The peak shape of the target deexcitation is influenced by the kinematic reconstruction of the target scattering angle from the measured direction of the scattered projectile. In addition, uncertainties like the size of the beam spot and straggling in the target material impact the peak shape.

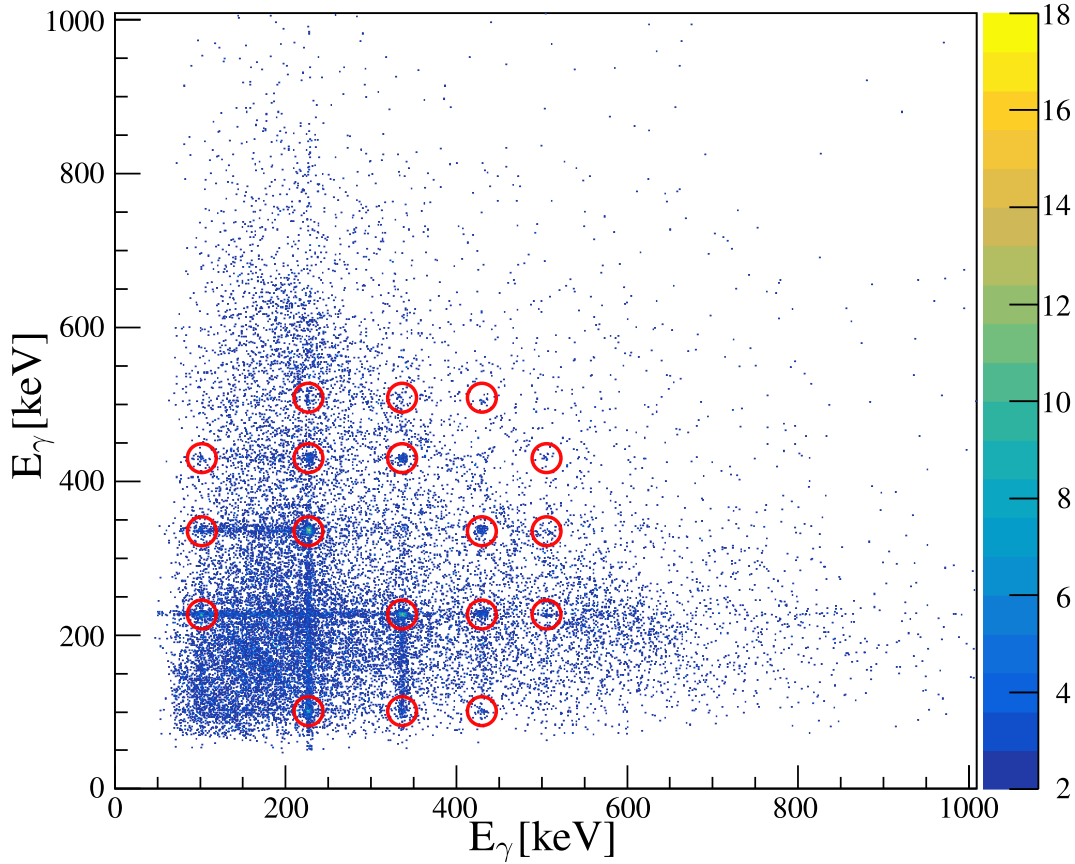


**Figure 63:**  $\gamma\gamma$  coincidences matrix for beam-like prompt  $\gamma$  rays. Yrast-band transitions of  $^{166}\text{Yb}$  are marked.

The Yrast-band transitions of  $^{166}\text{Yb}$  at 102 keV, 227 keV, 337 keV, 430 keV and 506 keV are assigned via mutual  $\gamma\gamma$  coincidences, which can be seen in Figure 63. Furthermore, gating on the 430 keV transition results in the coincidence spectrum shown in Figure 64. The feeding transition at 506 keV as well as the depopulating transitions at 102 keV, 227 keV, and 337 keV can be observed and verify unambiguously the multi-step Coulomb excitation of the Yrast band of  $^{166}\text{Yb}$  up to the  $10^+$  state. The 464 keV line is not in coincidence with any of the transitions of  $^{166}\text{Yb}$  listed above and, thus, does not belong to the Yrast band of  $^{166}\text{Yb}$ . Instead it was assigned to the  $2_1^+$  excited state of  $^{132}\text{Ba}$ . For both nuclei  $^{132}\text{Ba}$  and  $^{166}\text{Yb}$  the transition strengths of the observed transitions are known [64, 126]. Hence, the

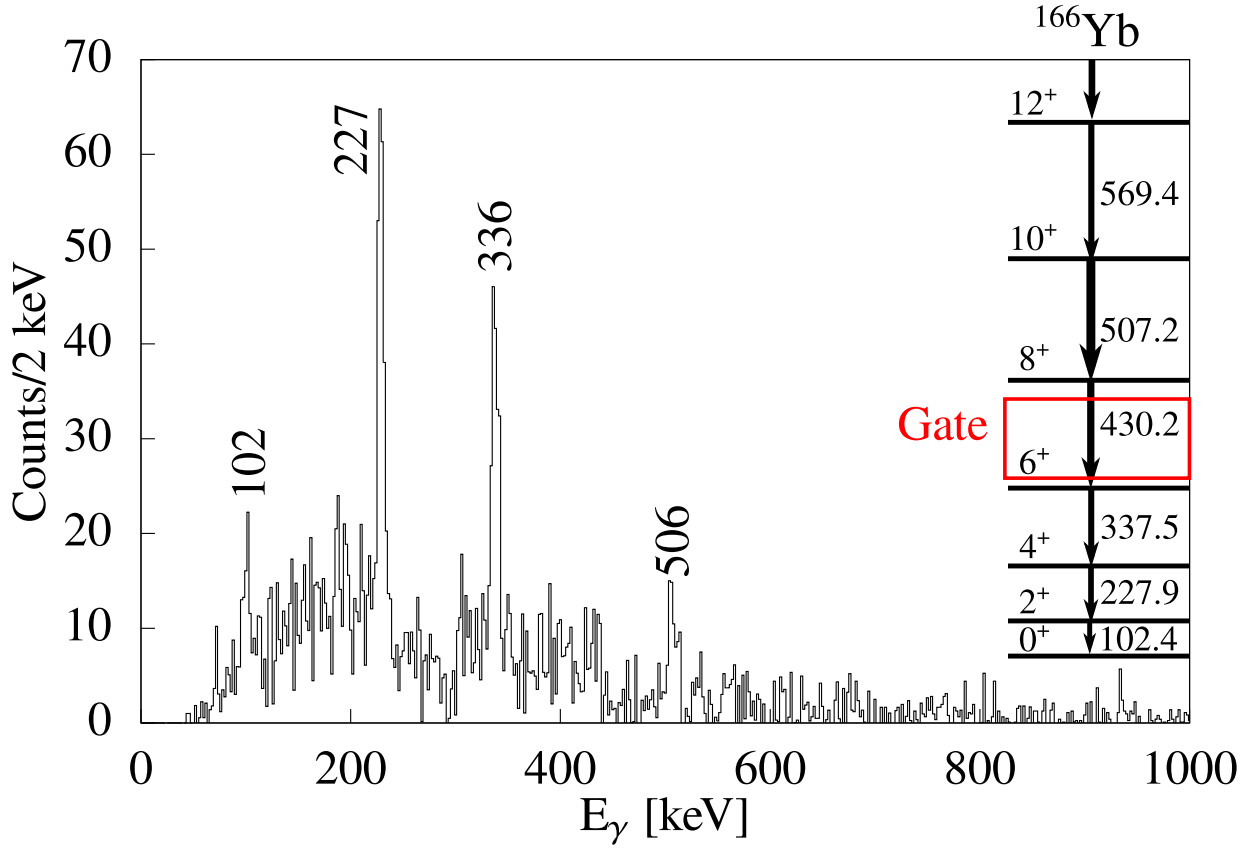


**Figure 64:**  $\gamma\gamma$  coincidences with a gate set on the  $6^+ \rightarrow 4^+$  transition of  $^{166}\text{Yb}$  at 430 keV. The feeding transition as well as the depopulating transitions are observed.

amount of target excitation induced by  $^{166}\text{Yb}$  and  $^{132}\text{Ba}$  is determined and is accounted for in the analysis.

The Doppler broadened  $K_\alpha$  X-ray line at 74 keV and the  $K_\beta$  X-ray transitions between 84 keV and 88 keV of  $^{206}\text{Pb}$  are present at the low-energy spectrum. Transitions of  $^{132}\text{Sb}$  are not visible in the projectile gated  $\gamma$ -ray spectrum, as their respective excitation probabilities are too small [64] and the half-life of the first excited state at 85.5 keV amounts to approx. 15 ns. Thus, the first excited state of  $^{132}\text{Sb}$  is Doppler broadened after the Doppler correction in the spectrum of Fig. 62. In the corresponding  $\gamma$ -ray spectrum without Doppler correction this transition line is visible. The evidence for  $^{132}\text{Sn}$  in the beam is illustrated in the beam-like gated, Doppler-corrected and background-subtracted  $\gamma$ -ray spectrum in Figure 65. The  $\gamma$ -ray decay of the first two excited states, i.e.  $2_1^+$  at 4041 keV and the  $3_1^-$  at 4351 keV, are observed at the known energies, which are known from previous  $\beta$ -decay

studies [127–129]. After Doppler correction, the FWHM of both peaks amounts to 63 keV and allows for a distinction of both transition lines from the background fluctuation. The fluctuations are caused by the background subtraction and low statistics.

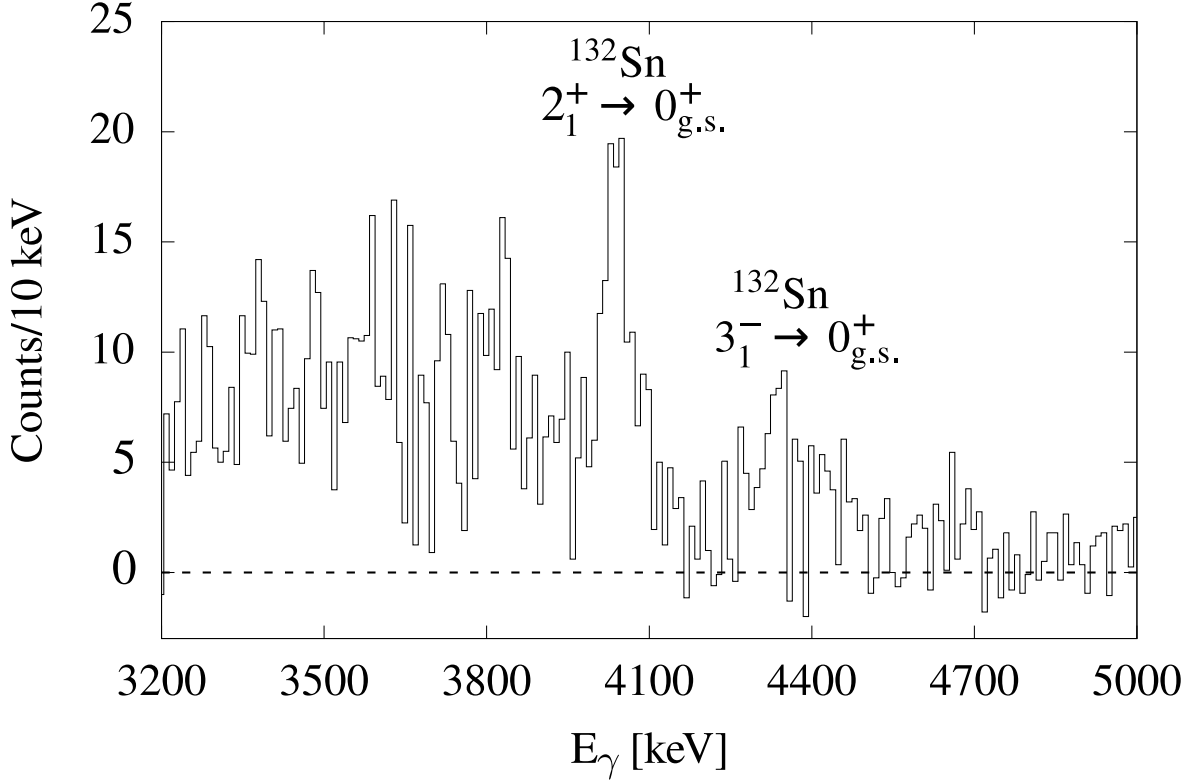


**Figure 65:** Final high-energy  $\gamma$ -ray spectrum employing a particle gate on scattered  $A = 132$  nuclei and respective Doppler correction. The background is subtracted.  $\gamma$ -ray transitions depopulating the first two excited state of  $^{132}\text{Sn}$  are observed.

### Implantation measurement

The remaining task is to calculate the amount of  $^{132}\text{Sb}$  relative to  $^{132}\text{Sn}$  in the beam, in order to deduce the amount of target excitation induced by  $^{132}\text{Sn}$ . This is required for the proper normalization of the measured transition strength. The intensity ratio  $R_{\text{Sb/Sn}} = ^{132}\text{Sb}/^{132}\text{Sn}$  in the beam was determined via a dedicated implantation measurement. Therefore, the beam was implanted into a 2 mm thick aluminum foil at the target position to ensure a complete stopping of the ions. To allow the  $^{132}\text{Sn}$  and  $^{132}\text{Sb}$  isotopes to decay away completely inside the MINIBALL setup, the RIB was stopped 30 minutes prior to the



implantation measurement. This time period is sufficient for the relatively short-lived nuclei  $^{132}\text{Sn}$  ( $T_{1/2} = 40$  s) and  $^{132}\text{Sb}$  ( $T_{1/2} = 4$  min). For the measurement the beam gate was opened for exactly 737 seconds, before closing it again. Hence, the observed  $\beta$ -decays originating from  $^{132}\text{Sn}$  and  $^{132}\text{Sb}$  are entirely induced by the implanted nuclei from this short in-beam period. A schematic drawing of the measured activity of both nuclei in arbitrary units is shown in Figure 66, to illustrate the procedure. At the time of the beam-gate closure the amount of  $^{132}\text{Sn}$  nuclei is given by  $N_{\text{Sn}}^m$  and for  $^{132}\text{Sb}$  by  $N_{\text{Sb}}^m$ . The data acquisition continued for 65 s before the run was stopped automatically. However, the statistics are sufficient to perform the determination of the relative ratio  $R_{\text{Sb/Sn}}$  within this run. For the calculation, two time intervals, the implantation  $t_0$  to  $t_c$  and the following decay  $t_c$  to  $t_f$  are investigated independently (see Figure 66 for the definition of the different times).

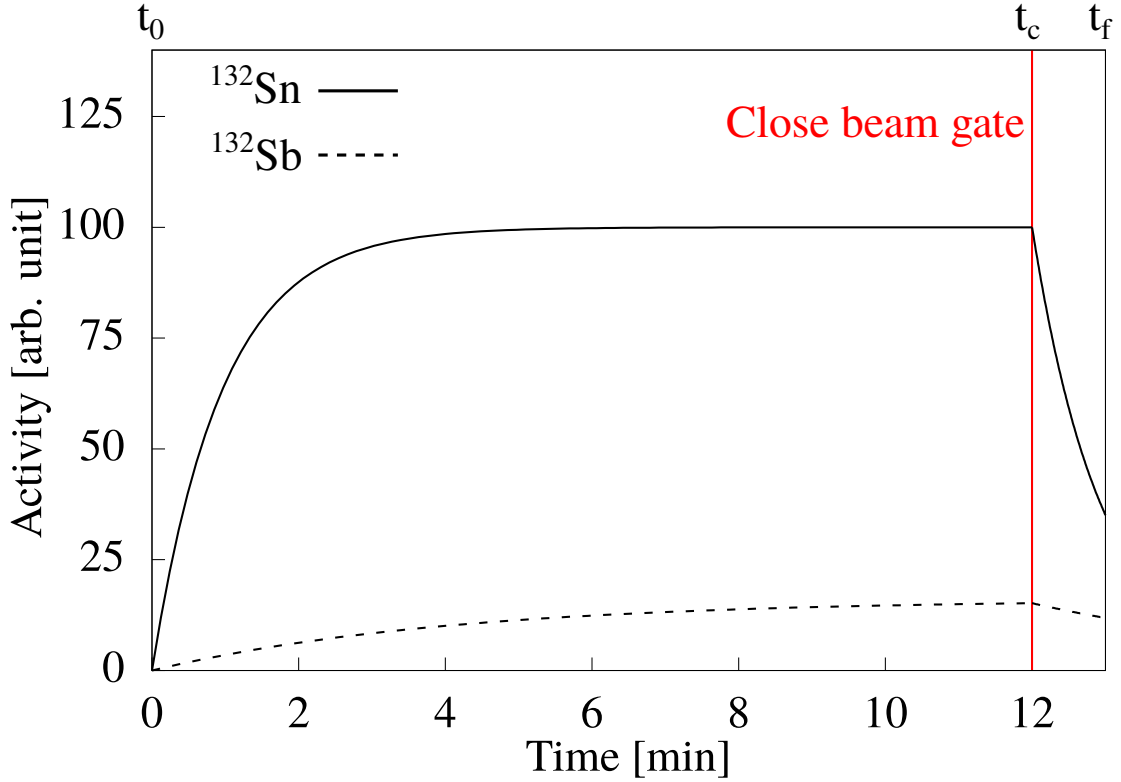


**Figure 66:** Calculated activity as a function of time for  $^{132}\text{Sn}$  and  $^{132}\text{Sb}$ .  $t_0$  denotes the point of the beam-gate opening,  $t_c$  the time of the beam-gate closure and  $t_f$  the end of the current run. For more information see text.

The amount of tin  $N(t)_{\text{Sn}}$  and antimony  $N(t)_{\text{Sb}}$  as a function of time, after the beam gate closure, are given by:

$$\frac{dN(t)_{Sn}}{dt} = -\lambda_{Sn}N(t)_{Sn} \quad (5.5)$$

$$\frac{dN(t)_{Sb}}{dt} = -\lambda_{Sb}N(t)_{Sb} + \lambda_{Sn}N(t)_{Sn}. \quad (5.6)$$

Substituting the ansatz

$$N(t)_i = \alpha_i e^{-\lambda_i t} \quad (5.7)$$

with the boundary condition  $N(t_c = 0)_{Sn} = N_{Sn}^m$  and  $N(t_c = 0)_{Sb} = N_{Sb}^m$  immediately yields

$$N(t)_{Sn} = N_{Sn}^m e^{-\lambda_{Sn} t} \quad (5.8)$$

and

$$N(t)_{Sb}^h = N_{Sb}^m e^{-\lambda_{Sb} t}. \quad (5.9)$$

The final solution of the inhomogeneous differential equation 5.6 is a composition of the homogeneous solution in Eq. 5.9 and a inhomogeneous solution. The inhomogeneous part is solved by variation of the constant for Eq. 5.7 with

$$N(t)_{Sb}^I = \alpha(t) e^{-\lambda_{Sb} t}. \quad (5.10)$$

This yields, after substituting equation 5.10 in equation 5.6,

$$\alpha(t)_{Sb} e^{-\lambda_{Sb} t} - \lambda_{Sb} \alpha(t)_{Sb} e^{-\lambda_{Sb} t} + \lambda_{Sb} \alpha(t)_{Sb} e^{-\lambda_{Sb} t} - \lambda_{Sn} N_{Sn}^m e^{-\lambda_{Sn} t} = 0, \quad (5.11)$$

which can be integrated to

$$\alpha(t)_{Sb} = \frac{\lambda_{Sn}}{(\lambda_{Sn} - \lambda_{Sb})} N_{Sn}^m e^{-(\lambda_{Sn} - \lambda_{Sb})t} + C \quad (5.12)$$

and finally results in

$$N(t)_{Sb} = N(t)_{Sb}^h + N(t)_{Sb}^I = N_{Sb}^m e^{-\lambda_{Sb}t} - \frac{\lambda_{Sn}}{(\lambda_{Sn} - \lambda_{Sb})} N_{Sn}^m (e^{-\lambda_{Sn}t} - e^{-\lambda_{Sb}t}). \quad (5.13)$$

For this, the boundary condition  $N(t_c = 0)_{Sb} = N_{Sb}^m$  was used.

Calculating the activity for each isotope with

$$A(t)_i = -\frac{dN(t)_i}{dt} \quad (5.14)$$

ends up in the following equations for the activity of  $^{132}\text{Sn}$  and  $^{132}\text{Sb}$ :

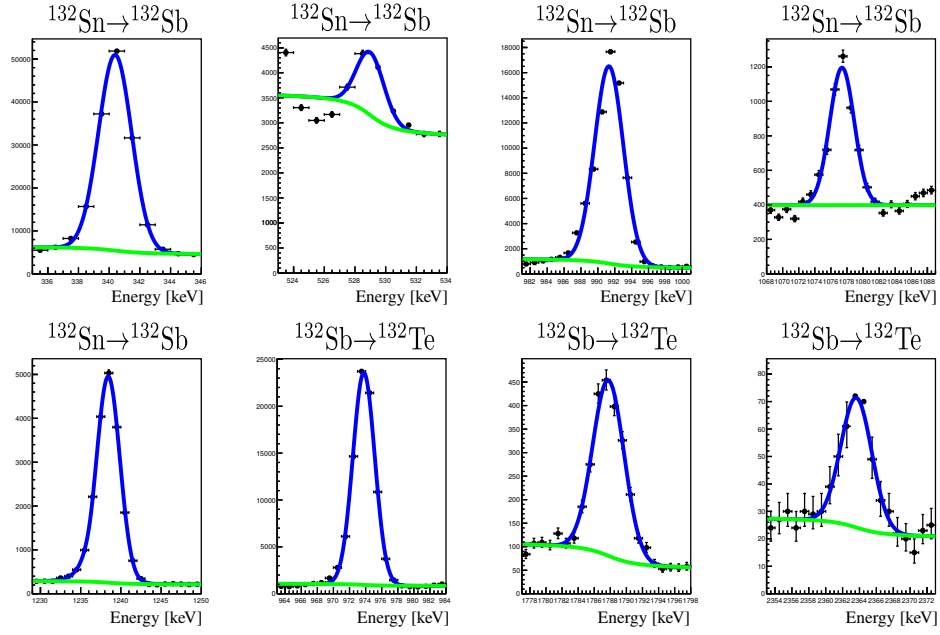
$$A(t)_{Sn} = \lambda_{Sn} N_{Sn}^m e^{-\lambda_{Sn}t} \quad (5.15)$$

$$A(t)_{Sb} = \lambda_{Sb} N_{Sb}^m e^{-\lambda_{Sb}t} - \frac{\lambda_{Sn}}{(\lambda_{Sn} - \lambda_{Sb})} N_{Sn}^m (\lambda_{Sn} e^{-\lambda_{Sn}t} - \lambda_{Sb} e^{-\lambda_{Sb}t}). \quad (5.16)$$

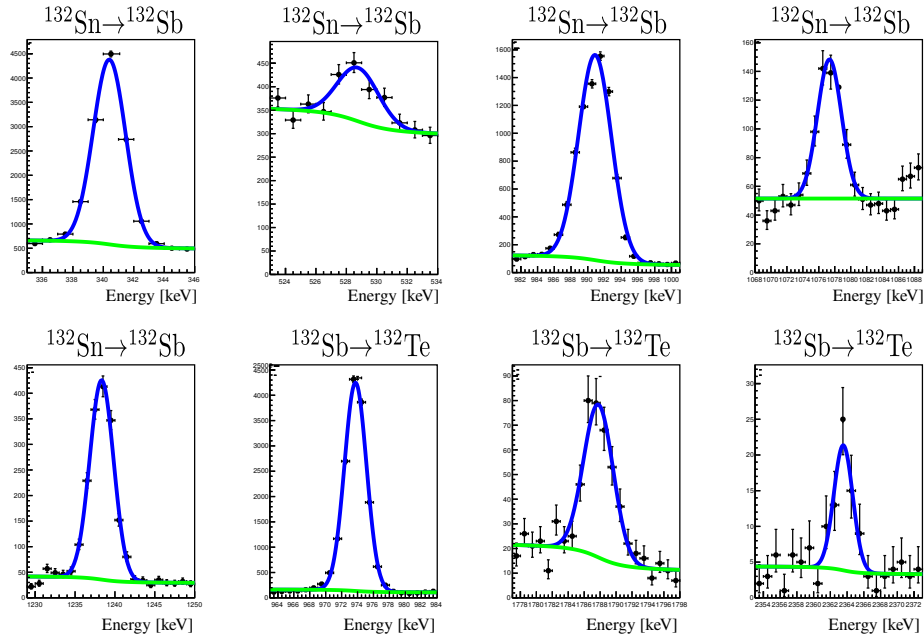
The integral of  $A(t)_{Sn}$  and  $A(t)_{Sb}$ , from the time of the beam gate closure  $t_c$  to the end of the run  $t_f$ , is equal to the amount of  $^{132}\text{Sn}$  and  $^{132}\text{Sb}$  nuclei decayed during this time interval, respectively.  $\gamma$ -ray spectra including data of this time period are used to determine the amount of decayed  $^{132}\text{Sn}$  and  $^{132}\text{Sb}$  nuclei. The total amount of  $\beta$ -decays originating from  $^{132}\text{Sn}$  are determined from the intensities of the transition lines at 340.5 keV, 529.1 keV, 992.7 keV, 1078.3 keV and 1239.6 keV, whereas the total decay of  $^{132}\text{Sb}$  is calculated from the intensities of the 974.1 keV, 1787.6 keV and 2363.5 keV transitions. The resulting fits of these transition lines are shown in Figure 67 and the corresponding yields in Table 3. The amount of  $^{132}\text{Sn}$  ( $N_{Sn}^m$ ) and  $^{132}\text{Sb}$  ( $N_{Sb}^m$ ) nuclei, at the time of the beam closure, amounts to

$$N_{Sn}^m = -\frac{\int_{t_c=0}^{t_f} A(t)_{Sn} dt}{(e^{-\lambda_{Sn}t} - 1)} \quad (5.17)$$

$$N_{Sb}^m = -\frac{\int_{t_c=0}^{t_f} A(t)_{Sb} dt}{(e^{-\lambda_{Sb}t} - 1)} + \frac{\lambda_{Sn}}{(\lambda_{Sn} - \lambda_{Sb})} N_{Sn}^m \left( \frac{e^{-\lambda_{Sn}t} - e^{-\lambda_{Sb}t}}{e^{-\lambda_{Sb}t} - 1} \right). \quad (5.18)$$



(a) Implantation



(b) Decay

**Figure 67:** (a) Gaussian fits of the transition lines of  $^{132}\text{Sn}$  and  $^{132}\text{Sb}$  to determine the amount of decays during the implantation time. (b) same as for (a) but for the decay time period. See text for more information

**Table 3.:** Obtained efficiency corrected intensities for the decay of  $^{132}\text{Sn}$  and  $^{132}\text{Sb}$  nuclei during the decay and implantation time interval. For each nucleus the total amount of the decays is given by the sum of the obtained intensities.

$E_\gamma$ [keV]	$\beta$ -decay	Intensity			
		Implantation		Decay	
		N	$\Delta N$	N	$\Delta N$
340.5	$^{132}\text{Sn} \rightarrow ^{132}\text{Sb}$	78239	280	6459	80
529.1	$^{132}\text{Sn} \rightarrow ^{132}\text{Sb}$	2347	48	307	18
992.7	$^{132}\text{Sn} \rightarrow ^{132}\text{Sb}$	72306	269	7836	89
1078.3	$^{132}\text{Sn} \rightarrow ^{132}\text{Sb}$	3337	58	390	20
1239.6	$^{132}\text{Sn} \rightarrow ^{132}\text{Sb}$	21437	146	1785	42
974.1	$^{132}\text{Sb} \rightarrow ^{132}\text{Te}$	81072	284	14976	122
1787.6	$^{132}\text{Sb} \rightarrow ^{132}\text{Te}$	2844	53	450	21
2363.5	$^{132}\text{Sb} \rightarrow ^{132}\text{Te}$	424	21	96	10

For the implantation time interval from  $t_0 = 0$  to the time of the beam gate closure  $t_c \neq 0$  (737 s),  $N_{Sn}^m$  and  $N_{Sb}^m$  is expressed by

$$N_{Sn}^m = N_{Sn}^{Beam} \Delta t - \int_{t_0}^{t_c} A(t)_{Sn} dt \quad (5.19)$$

$$N_{Sb}^m = N_{Sb}^{Beam} \Delta t - \int_{t_0}^{t_c} A(t)_{Sb} dt + \int_{t_0}^{t_c} A(t)_{Sn} dt, \quad (5.20)$$

with  $\Delta t = t_c - t_0$ . The integral of the activities of  $^{132}\text{Sn}$  and  $^{132}\text{Sb}$  nuclei can be determined from the obtained values in Table 3. From Eq. 5.19 and 5.20 the ratio  $R_{Sb/Sn}$  is given by

$$R_{Sb/Sn} = \frac{N_{Sb}^{Beam}}{N_{Sn}^{Beam}} = \frac{N_{Sb}^m + \int_{t_0=0}^{t_c} A(t)_{Sb} dt - \int_{t_0=0}^{t_c} A(t)_{Sn} dt}{N_{Sn}^m + \int_{t_0=0}^{t_c} A(t)_{Sn} dt}. \quad (5.21)$$

Finally the ratio of  $^{132}\text{Sb}$  relative to  $^{132}\text{Sn}$  amounts to  $R_{Sb/Sn} = 0.164(14)$ , which equals a beam composition of 85.9%  $^{132}\text{Sn}$  and 14.1%  $^{132}\text{Sb}$ .

## 6. Results

The goal of the experiment is to investigate the collective properties, in particular the  $2_1^+$  and  $3_1^-$  states of  $^{132}\text{Sn}$ , via their ground-state transitions. The following sections presents the achieved results.

### 6.0.1. Selection of projectile and target-like nuclei

In the analysis it is required to separate projectile ( $A = 132$ ) and target-like ( $A = 206$ ) particles, as safe Coulomb excitation is only ensured up to a scattering angle of  $\sim 42^\circ$  in the laboratory frame. Target-like particles detected in the forward DSSSD correspond to unsafe Coulomb excitation events and may include nuclear interactions, which would corrupt the analysis. The distinction between beam-like and target-like particles is difficult, due to the poor energy resolution of the innermost DSSSD segments.

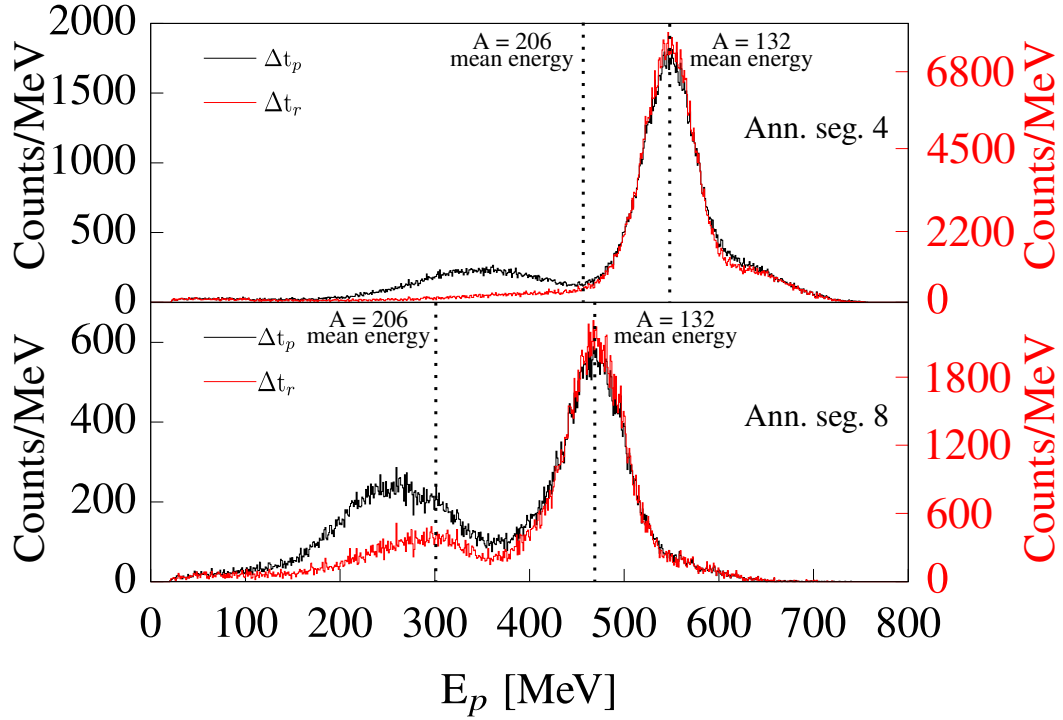


**Figure 68:** Particle energy spectrum of annular segments 4 (top) and 8 (bottom) recorded with the DSSSD. The black curve illustrates the particle spectrum in coincidence with prompt  $\gamma$  rays ( $\Delta t_p$ ), whereas the red curve illustrate the particle spectrum for particle- $\gamma$  coincidences within the random time window ( $\Delta t_r$ ). The calculated mean energies of beam-like and target-like particles after Rutherford scattering are marked with the dashed lines. See text for details.

In Figure 68 two particle spectra of annular segment 4 and 8 in coincidence with  $\gamma$  rays are shown. The black curve illustrates the recorded particle spectrum with coincident  $\gamma$  rays within the prompt time window ( $\Delta t_p$ ), whereas the red curve is in coincidence with random  $\gamma$  rays ( $\Delta t_r$ ). As  $\Delta t_r$  is five times  $\Delta t_p$ , the count rate for the random particles is higher. Even in the eighth annular segment (counting from the innermost segment to the outermost), target-like and beam-like particles can not be separated completely, although the two kinematic branches diverge with larger scattering angles. Particles in coincidence with random  $\gamma$  rays reproduce the Rutherford kinematics calculated with LISE++, while the particles within the prompt time window include an additional peak structure. Below the mean particle energy of  $^{206}\text{Pb}$  at 445 MeV in the annular segment 4 and 300 MeV in annular segment 8, an additional peak arise. This new peak structure is only present in the particle spectra within the prompt time window (black curve). Thus, the target-like component is superimposed by particles in coincidence with prompt  $\gamma$  rays and with 30 to 60 MeV less energy. This is also illustrated in Figure 69, where much more particles are

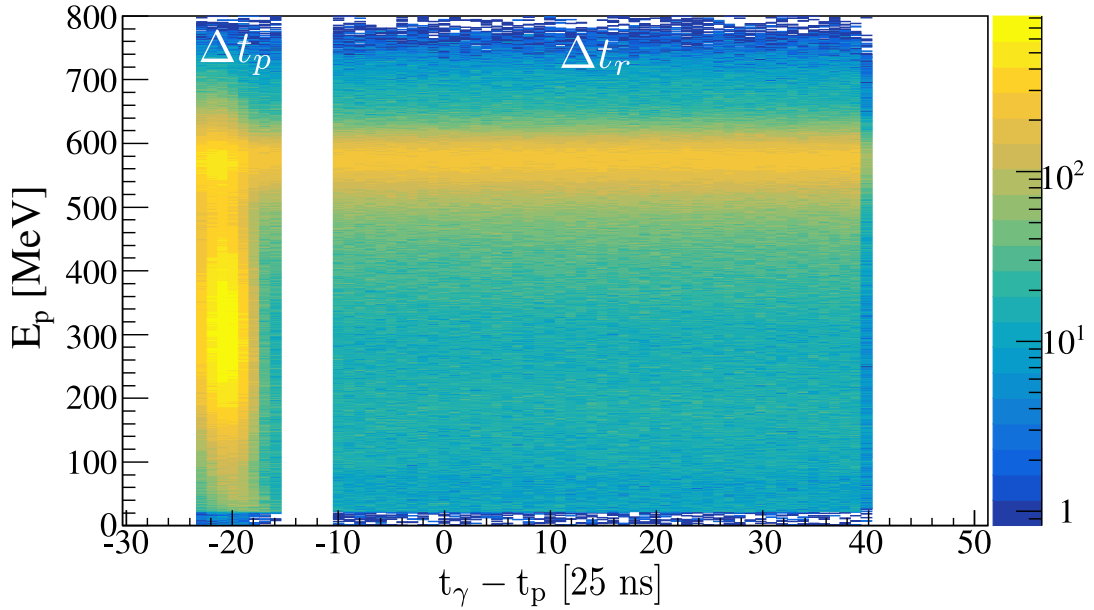


**Figure 69:** Particle energy as a function of the particle- $\gamma$  time differences within the prompt and random time windows for the ten innermost annular DSSSD segments. The structure within  $\Delta t_p$  and  $\Delta t_r$  is different especially for particle energies below 400 MeV. See text for more details.

observed between 200 MeV up to 400 MeV in the prompt coincidence window, whereas this component does not occur in the random time window.

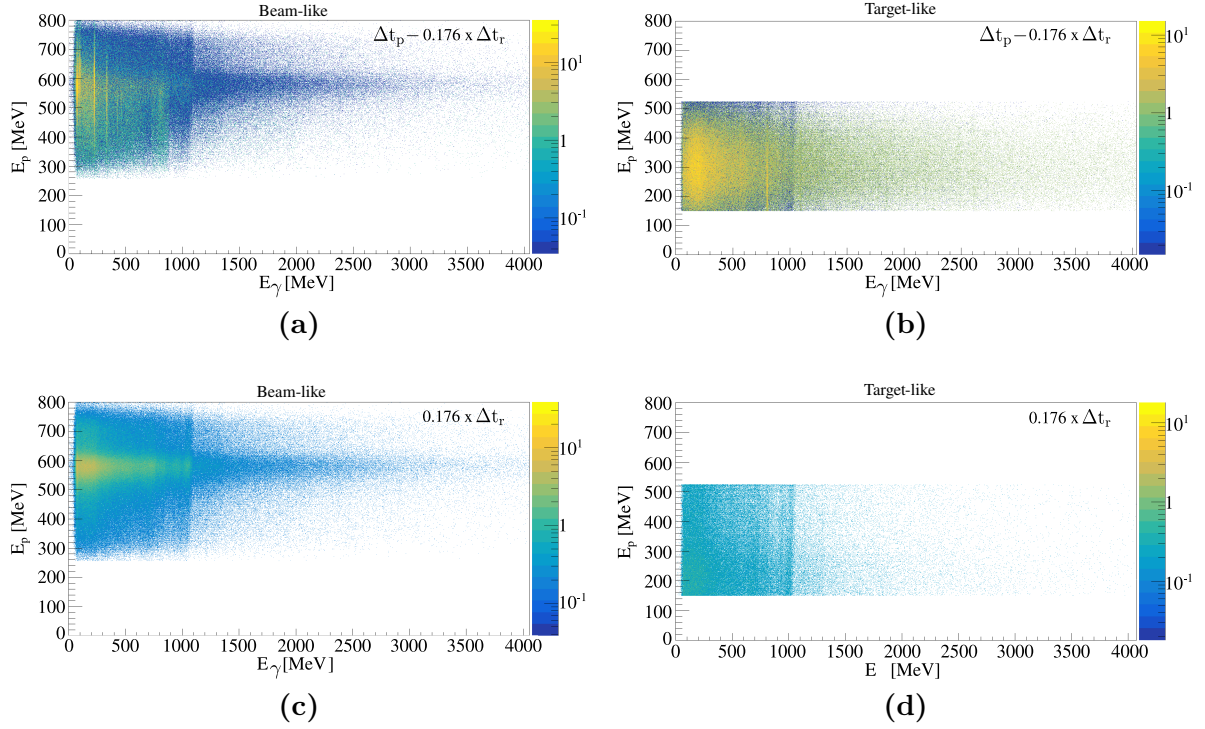


**Figure 70:** (a) Beam-like particle energy spectrum in correlation with prompt  $\gamma$ -rays as a function of the  $\gamma$ -ray energy. The spectrum is restricted to the ten innermost DSSSD rings. (b) same as in (a), but for target-like particles. (c) and (d) are similar to (a) and (b), respectively, but in coincidence with random  $\gamma$ -rays. More information can be found in the text.

The corresponding Doppler-corrected prompt  $\gamma$ -ray energies to the particles from Figure 69 are plotted in Figure 70 (a) and (b) for beam-like and target-like particles, respectively. Figure 70 (c) and (d) illustrate the Doppler-corrected random  $\gamma$ -ray energies in coincidence with beam-like (c) and target-like (d) particles. The beam-like and target-like selection is achieved by a first energy cut, which was illustrated in Figure 55 (a) and correspond to the valley between the two particle peaks of the black curve in Figure 68. The cutoff energy at 150 MeV is imposed to avoid random coincidences from the noise of the DSSSD detectors. In the range of the new particle structure for target-like particles much more  $\gamma$  rays are observed in the prompt time window than in the random time window.

The projection of Figure 70 (b) onto the x axis yields the  $\gamma$ -ray spectrum illustrated in Figure 71. Two sharp transitions stemming from  $^{206}\text{Pb}$ , i.e.  $2_1^+ \rightarrow 0_{\text{g.s.}}^+$  at 803 keV,  $3_1^+ \rightarrow 2_1^+$  at 537 keV and two transitions from  $^{207}\text{Pb}$ , i.e.  $5/2_1^- \rightarrow 1/2_{\text{g.s.}}^+$  at 570 keV and  $9/2_2^+ \rightarrow 13/2_1^+$  at 1094 keV are observed on a high background-like structure. The inset



of Figure 71 illustrates the target-like gated  $\gamma$ -ray spectrum with Doppler-correction for beam-like particles. Transitions at 331 keV and 1221 keV are observed which belong to ground-state transitions in  $^{131}\text{Sn}$  and  $^{130}\text{Sn}$ , respectively. Furthermore, transitions from  $^{166}\text{Yb}$  at 227 keV, 337 keV, 430 keV and 506 keV are observed, which originate from the excitation of the beam-like component under large scattering angles (unsafe).

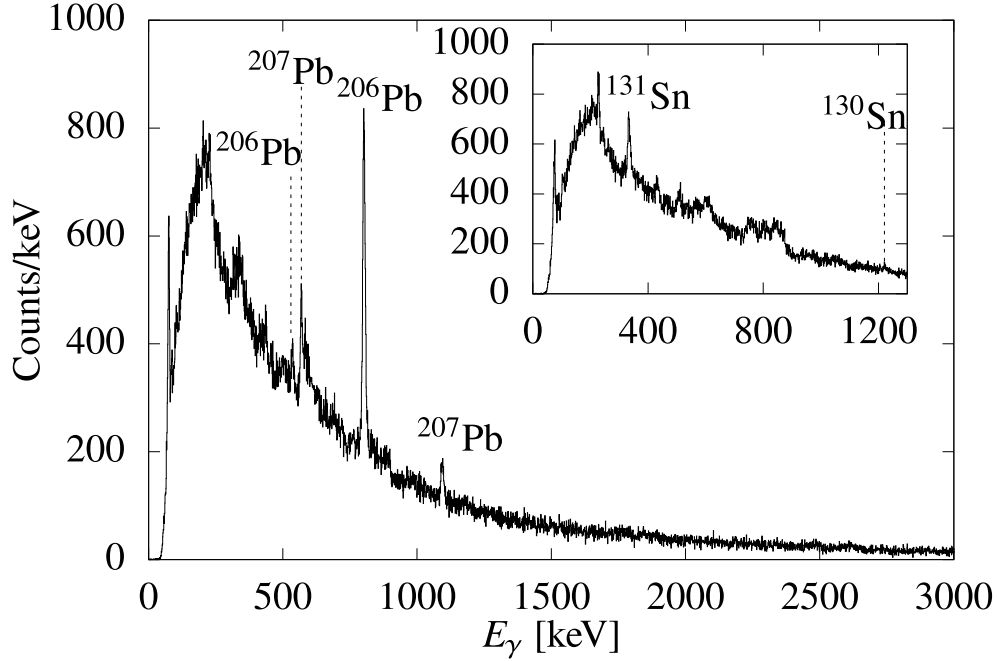


**Figure 71:** Target-like particle-gated  $\gamma$ -ray spectrum Doppler-corrected for target-like particles. The inset shows the target-like particle-gated  $\gamma$ -ray spectrum Doppler-corrected for beam-like particles. Both spectra are background subtracted. The observed  $\gamma$ -ray transitions correspond to beam and target nuclei as well as the neutron transfer products. See text for more information.

Additional evidence for transfer reactions is obtained by the Doppler-uncorrected  $\gamma$ -ray spectrum illustrated in Figure 72. The spectrum shows transitions which most likely stem from  $^{204}\text{Hg}$  at 691 keV and 436 keV,  $^{205}\text{Tl}$  at 204 keV,  $^{206}\text{Tl}$  at 265 keV, 304 keV, 330 keV,  $^{72}\text{Ge}$  at 834 keV,  $^{74}\text{Ge}$  at 596 keV and  $^{27}\text{Al}$  at 844 keV, 1014 keV, 2212 keV. Especially, transitions of  $^{72,74}\text{Ge}$  can only occur as a side product during or after transfer reactions where neutrons are generated from highly excited reaction products and excite the HPGe detection material. Free neutrons emerging from possible transfer reactions of lead into thallium or mercury can also induce the aluminum excitations. This gives rise to the assumption that the new particle peak corresponds to transfer reaction products. A refined investigation is not possible with the present data. However, for the normalization

of the transition strength the amount of the target excitation is obtained from the beam-like gated spectrum after Doppler-correction for target-like particles. This  $\gamma$ -ray spectrum is free of possible transfer products, as the distance between the nuclear surfaces is within the safe Coulomb-excitation range and does not allow for transfer reactions at all.

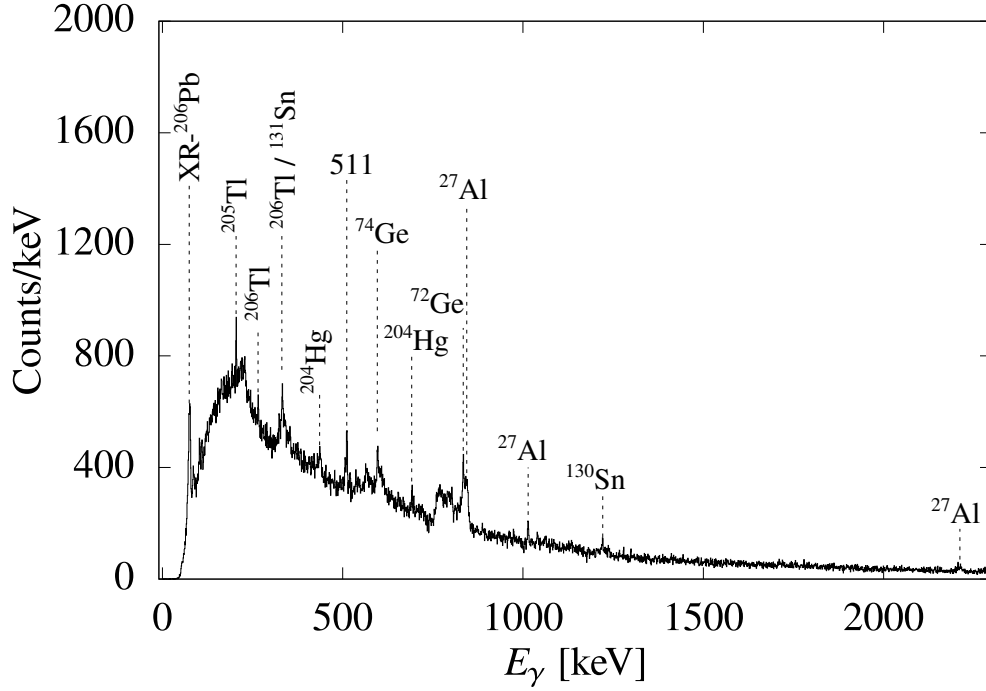


**Figure 72:**  $\gamma$ -ray spectrum gated on prompt target-like particles without Doppler-correction. Sharp transitions are observed, which can be associated to  $^{205,206}\text{Tl}$ ,  $^{204}\text{Hg}$ ,  $^{72,74}\text{Ge}$  and  $^{27}\text{Al}$  transitions. More information is given in the text.

On account of this, a clean separation between beam-like and target-like particles has to be achieved to guarantee a pure safe Coulomb-excitation spectrum for a proper normalization to the target excitation. The background subtracted  $\gamma$ -ray spectrum from Figure 73 was generated via gating on beam-like particles and performing Doppler correction for mass  $A = 132$ . The safe Coulomb-excitation criterion was implemented by including only the 10 innermost DSSSD rings ( $\theta_{\text{c.m.}} = 26.5^\circ - 68.2^\circ$ ). The yields were obtained by a  $5\sigma$  integral around the mean energy of the  $2_1^+ \rightarrow 0_{\text{g.s.}}^+$  and  $3_1^- \rightarrow 0_{\text{g.s.}}^+$  transition of  $^{132}\text{Sn}$  and amount to  $70 \pm 12$  counts and  $28 \pm 8$  counts, respectively. As discussed, within the applied particle cut the beam- and target-like components are not completely separated. For this reason, the contribution of the unsafe excitation were investigated in more detail.

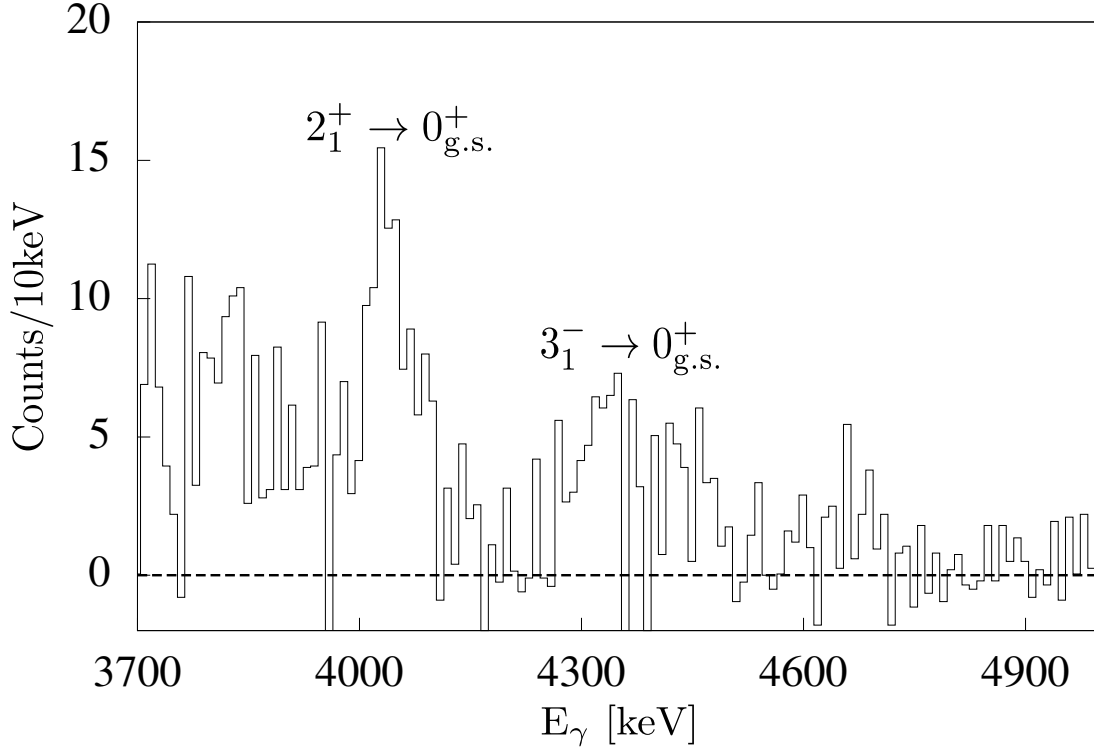


**Figure 73:** (a) Prompt beam-like gated  $\gamma$ -ray spectrum with background subtraction and Doppler-correction for mass  $A = 132$ . Only the ten innermost DSSSD rings were used to ensure safe Coulomb excitation. The two ground-state transitions of  $^{132}\text{Sn}$  at 4041 keV and 4351 keV are observed at the right energies.

### Particle cuts

To assure a clean particle separation and correct yield determination of the  $^{132}\text{Sn}$  and  $^{206}\text{Pb}$  transitions, several analysis conditions were applied. Figure 74 illustrates the applied cut criteria, as an example the particle spectrum of annular segment eight is depicted.

Similar to Figure 68, the black curve shows the detected particles within the prompt  $\gamma$ -ray time window and the red curve shows particles in coincidence with random  $\gamma$  rays. The transfer reaction channel superimpose the target-like particles in coincidence with prompt  $\gamma$  rays and, therefore, the proper cut conditions are applied considering the random particle spectra with predominantly Rutherford scattered events. To assure a pure projectile gated  $\gamma$ -ray spectrum, particle- $\gamma$  coincidences are selected for each annular DSSSD segment with particle energies equal to or greater than the mean energy of the mass  $A = 132$  peak (see Figure 74 (a) beam-like component). The remaining particles are treated as target-

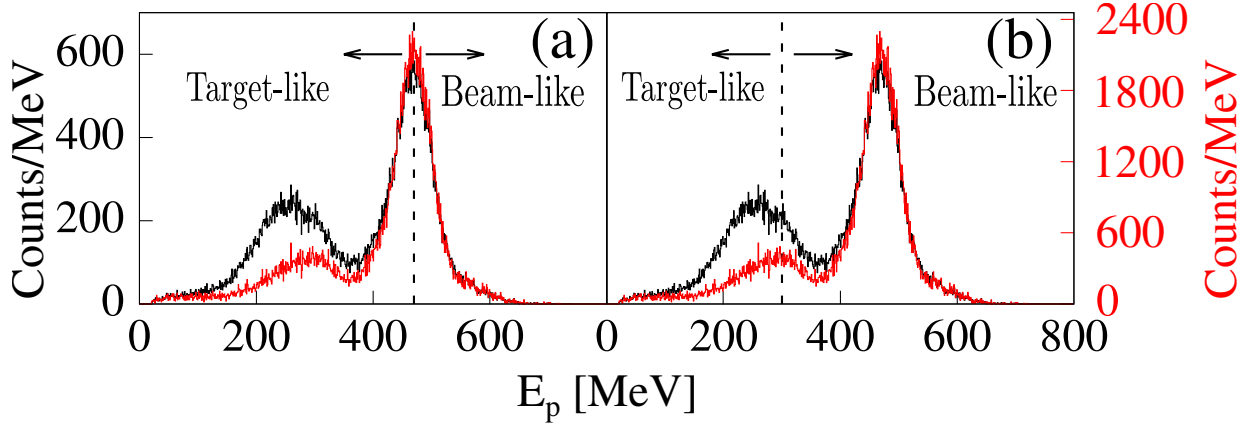


**Figure 74:** Applied particle cuts for particle- $\gamma$  coincidences: (a)  $\gamma$  rays in coincidence with beam-like particles are selected via particle energies above the mean energy of the mass  $A = 132$  peak. For coincidences with target-like particles energies below the mean value are used. (b) same as for (a), but the separation is performed with the mean energy of the mass  $A = 206$  peak. See text for more information.

like. Likewise, the background subtracted target-like gated  $\gamma$ -ray spectrum with Doppler-correction for mass  $A = 206$  is generated with the particle separation cut from Figure 74 (b). The background subtracted  $\gamma$ -ray spectra with Doppler-correction for either projectile gated or target-like gated particles are illustrated in Figure 75 (a) and (b), respectively. Considering the peak symmetry, both  $\gamma$ -ray spectra comprise half of the total excitation and are only in coincidence with either beam-like or target-like particles. The target-like  $\gamma$ -ray spectrum generated with the cut condition from Fig. 74 (a) and the beam-like  $\gamma$ -ray spectrum generated from 74 (b) are not used for further analysis, as they include a mixture of beam-like and target-like particles. The deexcitation of  $^{132}\text{Sn}$  with respect to the  $2_1^+ \rightarrow 0_{g.s.}^+$  transition amounts to  $36 \pm 8$  counts, while for the  $3_1^- \rightarrow 0_{g.s.}^+$  deexcitation the yield amounts to  $9 \pm 3$  counts. The target deexcitation corresponding to unsafe scattering angles is determined to  $3743 \pm 97$  counts for the  $2_1^+ \rightarrow 0_{g.s.}^+$  transition in  $^{206}\text{Pb}$ .

The intensity for the  $2_1^+ \rightarrow 0_{g.s.}^+$  transition agrees within the errors nicely with the full intensity of  $70 \pm 12$ . This indicates that the impact from the overlap of the two particle peaks is well understood and negligible for this transition. For the  $3_1^- \rightarrow 0_{g.s.}^+$  transition the yield with a clean separation between projectile and target-like particles is smaller than the full value, but still matches within the errors. To determine the target excitation induced within the safe Coulomb excitation range, the unsafe target excitation determined above has to be subtracted from the total target excitation. For the total target excitation all

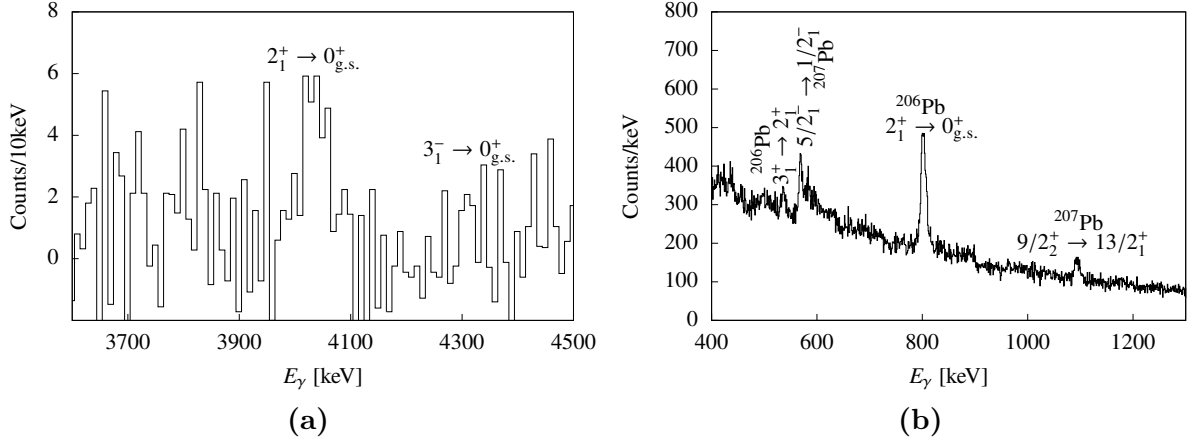


**Figure 75:** (a) Generated  $\gamma$ -ray spectrum in coincidence only with pure beam-like particles. (b) same as for (a) with the exception that particle- $\gamma$  coincidences are selected with target-like particles.

particles are treated either as projectiles or target-like particles with Doppler correction for both mass numbers. The corresponding  $\gamma$ -ray spectra are illustrated in Figure 76 for both cases.

The intensity of the target deexcitation, which comprises Doppler corrected and uncorrected contributions, yields the total amount of the target excitation  $N_{\text{tot}}^{\text{Pb}}$  with

$$N_{\text{tot}}^{\text{Pb}} = N_{\text{t}}^{\text{Pb}} + N_{\text{p}}^{\text{Pb}}. \quad (6.1)$$

In equation 6.1,  $N_{\text{t}}^{\text{Pb}}$  denotes the detected  $^{206}\text{Pb}$  deexcitation induced under large (unsafe) scattering angles, whereas  $N_{\text{p}}^{\text{Pb}}$  is the target deexcitation in coincidence with beam-like particles detected in the DSSSD detector (safe). The total amount of the deexcitation of  $^{206}\text{Pb}$  is determined via the average of the four generated  $\gamma$ -ray spectra from Fig. 76 and amounts to  $25255 \pm 605$  counts.  $N_{\text{t}}^{\text{Pb}}$  is two times the yield obtained from the  $\gamma$ -ray spectrum illustrated in Figure 75 (b) with  $N_{\text{t}}^{\text{Pb}} = 7494 \pm 194$ . Thus, the amount of the detected safe target deexcitation is given by

$$N_{\text{p}}^{\text{Pb}} = N_{\text{tot}}^{\text{Pb}} - N_{\text{t}}^{\text{Pb}}, \quad (6.2)$$

and equals  $N_{\text{p}}^{\text{Pb}} = 17739 \pm 620$ .

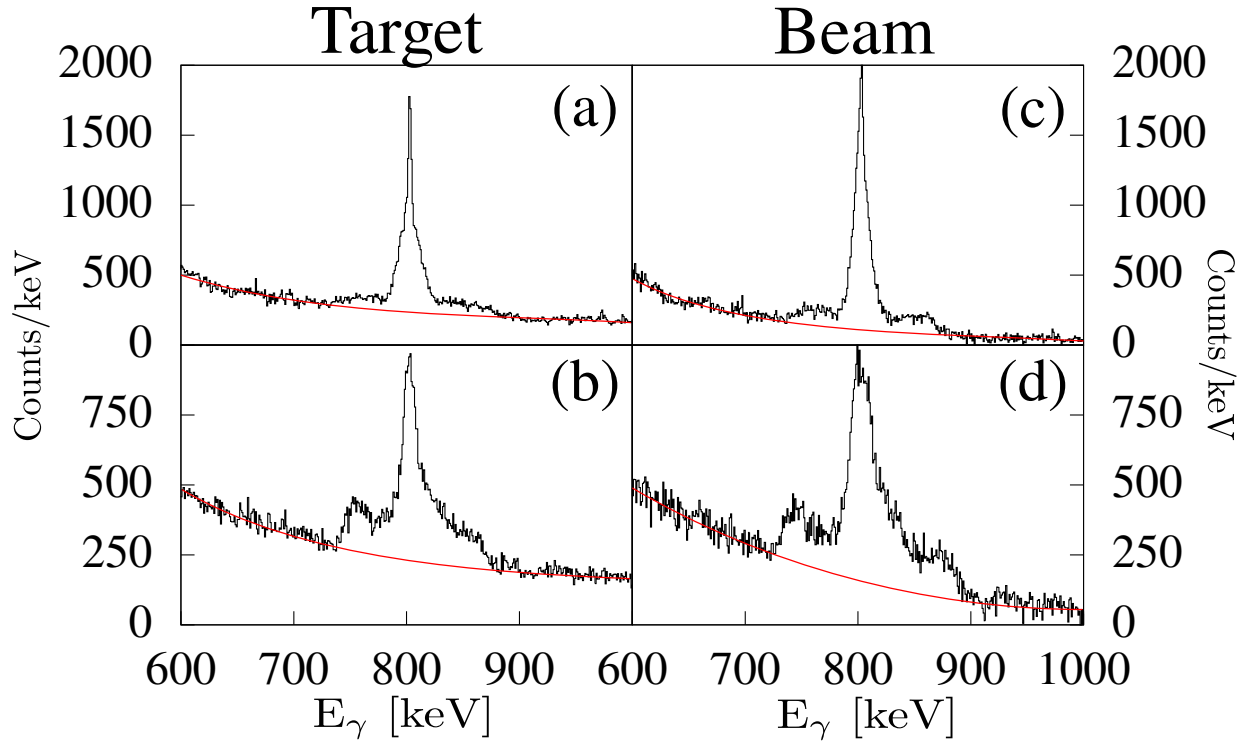


**Figure 76:**  $\gamma$ -ray spectra with the total detected target excitation. The red line illustrates the fitted background. (a) and (b) show  $\gamma$ -ray spectra treating all particles as target-like with Doppler correction for mass  $A = 206$  and kinematic reconstruction for mass  $A = 132$ , respectively. (c) and (d) illustrate similar  $\gamma$ -ray spectra as in (a) and (b), but treating all particles as beam-like and performing the Doppler correction for mass  $A = 132$  and  $A = 206$ , respectively. For more details see text.

### 6.0.2. Yield calculation

The yields of the  $^{132}\text{Sn}$  deexcitation were already determined in the previous section and amount to  $70 \pm 12$  and  $18 \pm 5$  for the  $2_1^+ \rightarrow 0_{\text{g.s.}}^+$  and  $3_1^- \rightarrow 0_{\text{g.s.}}^+$  deexcitation, respectively. To perform the normalization of the transition strengths with the coupled-channel code GOSIA2, the target excitation only induced by  $^{132}\text{Sn}$  is required. The above calculated  $N_p^{\text{Pb}}$  target deexcitation includes the safe Coulomb excitation induced by  $^{132}\text{Ba}$ ,  $^{132}\text{Sb}$ ,  $^{132}\text{Sn}$ ,  $^{166}\text{Yb}$  beam components. The unsafe excitation from  $^{166}\text{Yb}$ ,  $^{132}\text{Ba}$ ,  $^{132}\text{Sb}$  and  $^{132}\text{Sn}$  beam particles are detected with similar energies inside the DSSSD, whereas the beam-like as well as the target-like particle energies of  $^{166}\text{Yb}$  are higher compared to mass  $A = 132$  particles. The kinematics are illustrated in Figure 77.

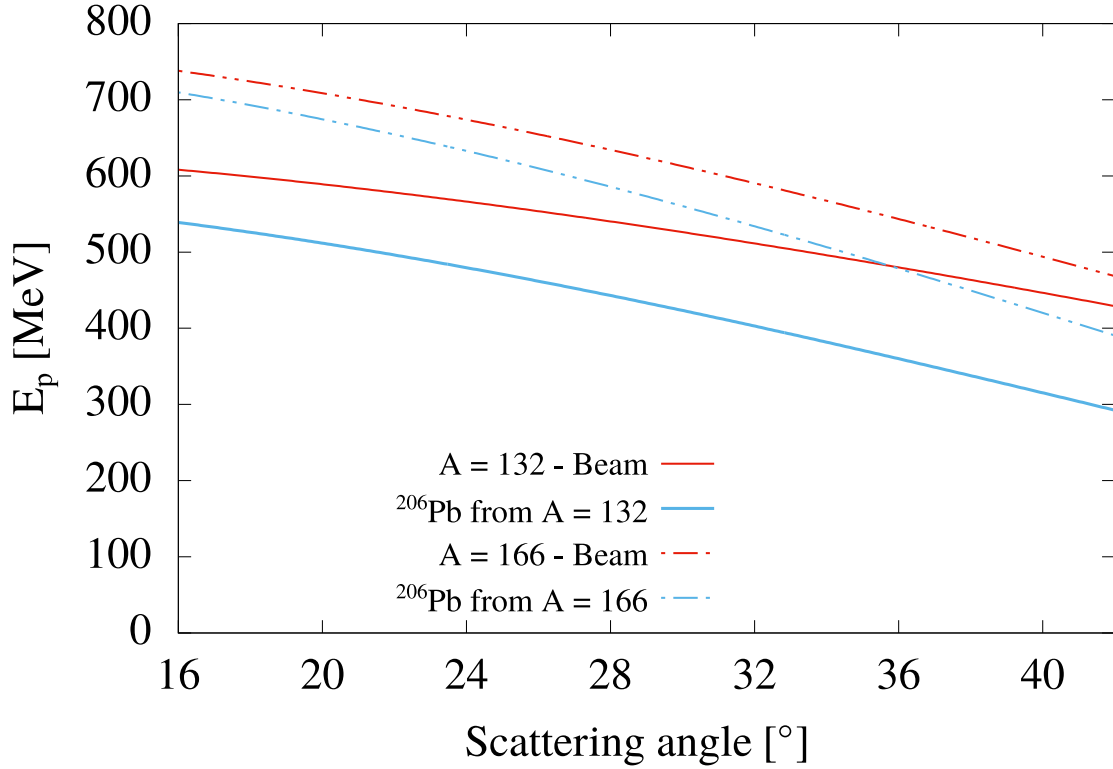


**Figure 77:** Calculated particle energies as a function of the scattering angle in the laboratory frame. The LISE++ output for  $^{132}\text{Sn}$  and  $^{166}\text{Yb}$  is shown in red, whereas the scattered lead particle energies are shown in blue.

The total amount of the detected deexcitation of  $^{132}\text{Ba}$  after safe Coulomb excitation and the total amount of the  $^{166}\text{Yb}$  deexcitation is determined from the  $\gamma$ -ray spectrum (cf. Fig. 62) with the particle cut including the complete mass  $A = 132$  peak from

**Table 4.:** Determined excitation cross sections for  $^{132}\text{Ba}$  and  $^{166}\text{Yb}$  on  $^{206}\text{Pb}$  corresponding to the observed  $\gamma$ -ray transitions.

	$I_i \rightarrow I_f$	$\sigma(N)$ [b]	$I_i \rightarrow I_f$	$\sigma(^{206}\text{Pb})$ [b]
$^{132}\text{Ba}$	$0_{\text{g.s.}}^+ \rightarrow 2_1^+$	14.56	$0_{\text{g.s.}}^+ \rightarrow 2_1^+$	0.82
$^{166}\text{Yb}$	$2_1^+ \rightarrow 4_1^+$	10.95	$0_{\text{g.s.}}^+ \rightarrow 2_1^+$	1.10
	$4_1^+ \rightarrow 6_1^+$	4.79	$0_{\text{g.s.}}^+ \rightarrow 2_1^+$	1.10
	$6_1^+ \rightarrow 8_1^+$	1.94	$0_{\text{g.s.}}^+ \rightarrow 2_1^+$	1.10
	$8_1^+ \rightarrow 10_1^+$	0.89	$0_{\text{g.s.}}^+ \rightarrow 2_1^+$	1.10

Figure 55 (a) presented in Section 5.4. The intensity of the deexcitation of  $^{132}\text{Ba}$  amounts to  $1920 \pm 150$ . For the yrast-band transitions of  $^{166}\text{Yb}$  the determined intensities are  $15589 \pm 147$  for  $4_1^+ \rightarrow 2_1^+$ ,  $5055 \pm 99$  for  $6_1^+ \rightarrow 4_1^+$ ,  $1428 \pm 76$  for  $8_1^+ \rightarrow 6_1^+$  and  $331 \pm 60$  for  $10_1^+ \rightarrow 8_1^+$ . The cross sections for all transitions were determined via CLX [28, 29], with the known transition strengths, the target thickness and the beam energy. The cross sections for all transitions are summarized in Table 4. Therewith, it is possible to calculate the total amount of the target deexcitation induced by  $^{132}\text{Ba}$  and  $^{166}\text{Yb}$  with the known cross sections and equations 1.33 and 1.34.

$$N_{\text{p}}^{\text{Pb}}(^{132}\text{Ba}) = N_{^{132}\text{Ba}} \frac{\sigma(^{206}\text{Pb})}{\sigma(^{132}\text{Ba})} \frac{\varepsilon(^{206}\text{Pb})}{\varepsilon(^{132}\text{Ba})} \quad (6.3)$$

and

$$N_{\text{p}}^{\text{Pb}}(^{166}\text{Yb}) = N_{^{166}\text{Yb}} \frac{\sigma(^{206}\text{Pb})}{\sigma(^{166}\text{Yb})} \frac{\varepsilon(^{206}\text{Pb})}{\varepsilon(^{166}\text{Yb})}, \quad (6.4)$$

where  $\sigma(N)$  is the cross section and  $\varepsilon(N)$  the detection efficiency of the HPGe detectors for the corresponding transition energy. Employing equation 6.3 and 6.4, the amount of the detected target deexcitation induced by  $^{132}\text{Ba}$  yields  $41 \pm 6$  counts and by  $^{166}\text{Yb}$  yields  $739_{-370}^{+28}$  counts. The large error corresponding to the target deexcitation induced by  $^{166}\text{Yb}$  originate from the fact that the peak intensities for the yrast-band transitions observed in the  $\gamma$ -ray spectrum are from safe (beam-like particles) and unsafe (target-like particles) Coulomb excitation. This implies, a part of the excitation could potentially stem from nuclear interactions. However, R. H. Spear *et al.* showed in Ref. [130] that the probability for the excitation of the  $2_1^+$  state of  $^{206}\text{Pb}$  decreases with decreasing impact parameter. As the precise nuclear-force cross section is not known due to potential nuclear Coulomb interference for large scattering angles, an upper limit can be calculated using the approach that the probability for both excitation mechanisms is equal. Therefore, the error of 50%



---

arise in the uncertainties. The total amount  $N_p^{\text{Pb}}$  is a composition of the target deexcitation induced by the different beam components

$$N_p^{\text{Pb}} = N_p^{\text{Pb}}(^{132}\text{Sn}) + N_p^{\text{Pb}}(^{132}\text{Sb}) + N_p^{\text{Pb}}(^{132}\text{Ba}) + N_p^{\text{Pb}}(^{166}\text{Yb}). \quad (6.5)$$

Subtracting the intensities induced by  $^{132}\text{Ba}$  and  $^{166}\text{Yb}$  yields  $N_p^{\text{Pb}}(^{132}\text{Sn}) + N_p^{\text{Pb}}(^{132}\text{Sb}) = 16959 \pm 721$ , which is the total detected target deexcitation induced by  $^{132}\text{Sn}$  and  $^{132}\text{Sb}$ . In Section 5.6 the ratio of both nuclei in the beam was determined and, hence, it is possible to calculate the amount of the target deexcitation induced by  $^{132}\text{Sn}$ . Considering the Coulomb excitation cross sections for the  $2_1^+$  excitation of  $^{206}\text{Pb}$  via  $^{132}\text{Sn}$  ( $\sigma(^{132}\text{Sn}) = 0.910\text{b}$ ) and  $^{132}\text{Sb}$  ( $\sigma(^{132}\text{Sb}) = 0.897\text{b}$ ), the final number caused by  $^{132}\text{Sn}$  is  $N_p^{\text{Pb}}(^{132}\text{Sn}) = 14777 \pm 622$  counts.

### Reduced transition strength

All yields, which are needed to determine the  $2_1^+ \rightarrow 0_{\text{g.s.}}^+$  and  $3_1^- \rightarrow 0_{\text{g.s.}}^+$  transitions of  $^{132}\text{Sn}$ , are at this point available. The coupled-channels code GOSIA2 [23–25] is able to extract electromagnetic matrix elements by a least-square fit to a Coulomb-excitation dataset utilizing these matrix elements as free variables. Hence, the coupled-channels system of differential equations describing electromagnetic excitations is determined in an fast and efficient way. The determined yields, i.e.  $2_1^+ \rightarrow 0_{\text{g.s.}}^+$ ,  $3_1^- \rightarrow 0_{\text{g.s.}}^+$  of  $^{132}\text{Sn}$  and  $2_1^+ \rightarrow 0_{\text{g.s.}}^+$  of  $^{206}\text{Pb}$  are used as data points. The level scheme shown in Figure 78 (a) as an inset, is implemented in the input file of GOSIA2 to adjust the calculation of the excitation and deexcitation to the case of  $^{132}\text{Sn}$ . The  $4_1^+$  state, which was not observed in the experiment, is a buffer state representative for all higher excited state in  $^{132}\text{Sn}$  to ensure a proper excitation and deexcitation mechanism by avoiding unphysical population and feeding of the underlying levels. Further data points for the least-square fit, are two branching ratio of  $^{132}\text{Sn}$  i.e.  $3_1^- \rightarrow 2_1^+ / 3_1^- \rightarrow 0_{\text{g.s.}}^+$  and  $4_1^+ \rightarrow 3_1^- / 4_1^+ \rightarrow 2_1^+$  known from  $\beta$ -decay measurements of  $^{132}\text{In}$  [129]. The branching ratio of the  $4_1^+$  level into the ground state is not included in the calculation as an E4 transition would be required, but the deexcitation via an E4 transition is negligible and not implemented in GOSIA2 [23]. The well studied reduced transition matrix element of the target excitation  $\mathfrak{M}(E2; 2_1^+ \rightarrow 0_{\text{g.s.}}^+) = 0.3178(47)\text{eb}$  [131] is an additional data point for the  $\chi^2$  minimization and in addition used for the normalization of the transition strength of  $^{132}\text{Sn}$  relative to the target excitation of  $^{206}\text{Pb}$ . Thus, in total six data points are used for the minimization with GOSIA2.

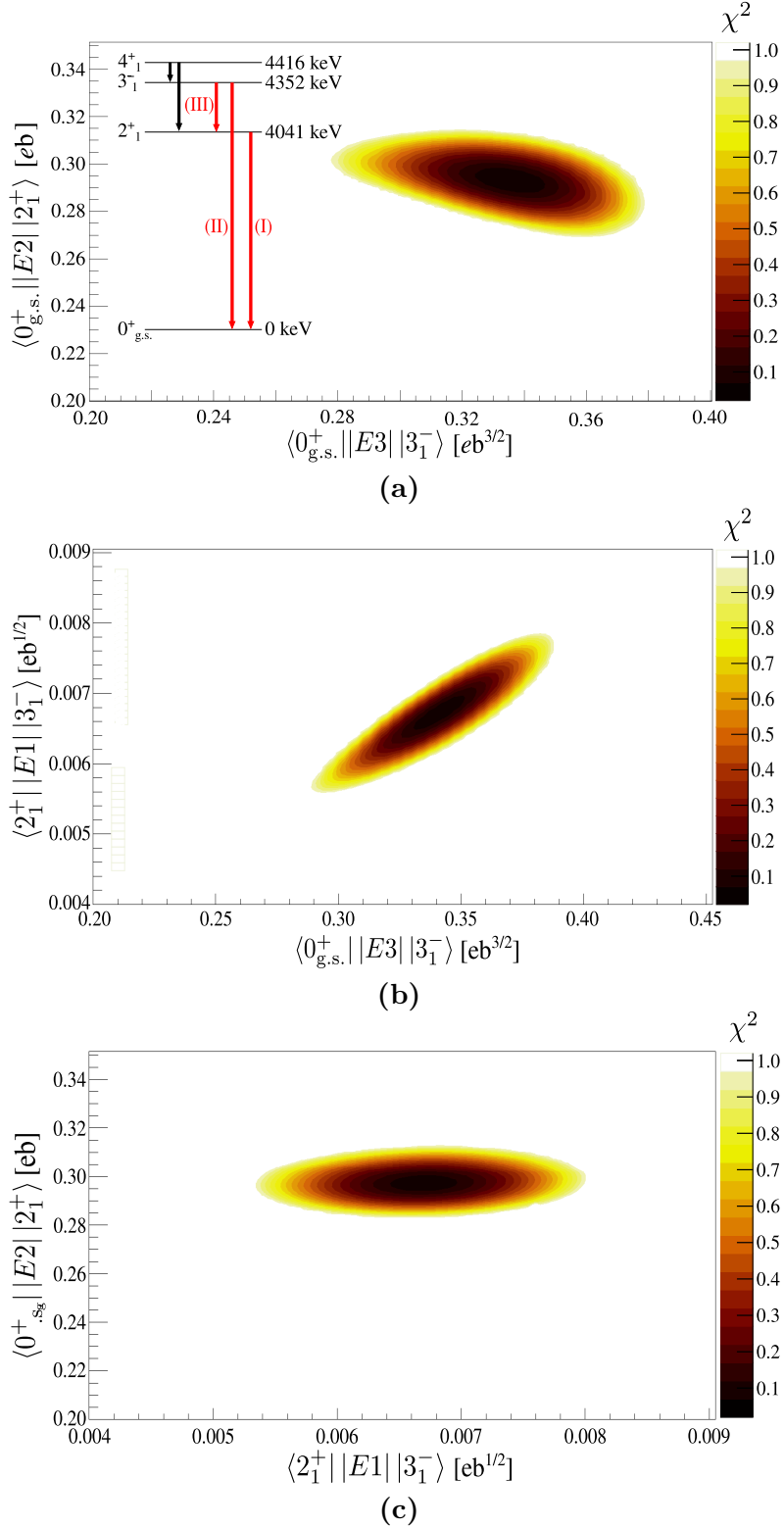


**Figure 78:** Projections of the 3-dimensional contour plot of the  $\chi^2$ -surface scans normalized to the  $^{206}\text{Pb}$  target excitation. (a)  $\chi^2$  values obtained within the  $1\sigma$  range as a function of the (I) and (II) transitions. The inset shows the implemented level scheme used for the calculation. (b) and (c) shows the global  $\chi^2$ -surface minimum as a function of (III) and either (II) or (I) transition, respectively. More information can be found in the text.

The  $\chi^2$ -surface calculated with GOSIA2 is, in the present case of the doubly-magic  $^{132}\text{Sn}$ , 3-dimensional. For the visualization of the  $\chi^2$  surface two transitions were fixed, whereas the remaining one was minimized by GOSIA2. The data is normalized to the excitation of a  $3.1 \text{ mg/cm}^2$  thick  $^{206}\text{Pb}$  target irradiated with  $^{132}\text{Sn}$  at  $5.5 \text{ MeV/u}$  beam energy. The quadrupole moments were set to zero, which is justified by the spherical structure of the doubly-magic nucleus. A global minimum was obtained for all hypersurfaces and is presented within the  $1\sigma$  range ( $\chi^2 \leq \chi^2_{\min} + 1$ ) in Figure 78. All calculations are in good agreement and yield one unique set of reduced matrix elements describing the transition strengths. The final reduced transition strengths are  $B(E2 \uparrow; 0_{\text{g.s.}}^+ \rightarrow 2_1^+) = 0.0869 \pm 0.019 \text{ } e^2\text{b}^2$ ,  $B(E3 \uparrow; 0_{\text{g.s.}}^+ \rightarrow 3_1^-) = 0.11 \pm 0.035 \text{ } e^2\text{b}^3$  and  $B(E1 \uparrow; 2_1^+ \rightarrow 3_1^-) = (9.05 \pm 3.04) \times 10^{-6} \text{ } e^2\text{b}$ . These values are summarized in Table 5 and compared to prior determined values.

**Table 5.:** Reduced transition strengths for  $^{132}\text{Sn}$  determined in this work and from previous measurements.

$E_f$ [keV]	$E_\gamma$ [keV]	$I_i \rightarrow I_f$	This work		Previous
			B(E $\lambda$ ) [ $e^2\text{b}^\lambda$ ]	B(E $\lambda$ ) [W.u.]	B(E $\lambda$ ) [W.u.]
4041.2	4041.2	$0_{\text{g.s.}}^+ \rightarrow 2_1^+$	0.087(19)	4.4(9)	7.0(3) [30, 43] 5.5(15) [44]
4351.94	4351.94	$0_{\text{g.s.}}^+ \rightarrow 3_1^-$	0.11(4)	15.2(48)	$>7.1$ [129]
	310.7	$2_1^+ \rightarrow 3_1^-$	$9.1(31) \times 10^{-6}$	$4.2(13) \times 10^{-4}$	$> 1.7 \cdot 10^{-4}$ [129]

The  $B(E2)$  value determined within this work shows a reduced quadrupole transition strength compared to the previous Coulomb excitation of  $^{132}\text{Sn}$  at ORNL. However, within the error of approx. 40% the preliminary value agrees with the new findings. The higher quadrupole strength and the large error of the ORNL measurement can be explained by the poor energy resolution of the used  $\text{BaF}_2$  array and the lack of the efficiency calibration. The better energy resolution of the MINIBALL spectrometer and the high energy of the  $^{132}\text{Sn}$  beam delivered by HIE-ISOLDE, allowed to reduce the error to approx. 20% and exhibit reduced quadrupole strength. However, compared to the neighbor isotopes  $^{130,134}\text{Sn}$ , the

quadrupole strength of  $^{132}\text{Sn}$  is increased and, therefore, indicate an larger collectivity.  $B(E1)$  and  $B(E3)$  values were determined in this work for the first time and are consistent with previous determined lower limits. The errors for the  $B(E3)$  and  $B(E1)$  values are approx. 30%. The  $B(E3)$  value of about 15 W.u. fits nicely the trend of  $B(E3)$  values along the isotopic chain of tin with values between 10 W.u. and 30 W.u. and suggests a collective behavior (cf. Sec. 2.1 and Fig. 14).

Due to the low statistics the experiment is not sensitive to the quadrupole moment. However, Fig. 79 illustrates the calculated  $\chi^2$ -surface of the  $E2$  transition as a function of the spectroscopic quadrupole moment. Thus, if the first excited state of the doubly-magic  $^{132}\text{Sn}$  would deviate from a spherical structure, the transition strength could change depending whether the nucleus is prolate deformed ( $Q > 0$ ) or oblate deformed ( $Q < 0$ ). However, state-of-the-art theoretical calculations confirm the spherical structure for this nucleus and, therefore, a vanishing quadrupole moment (cf. Sec. 7).

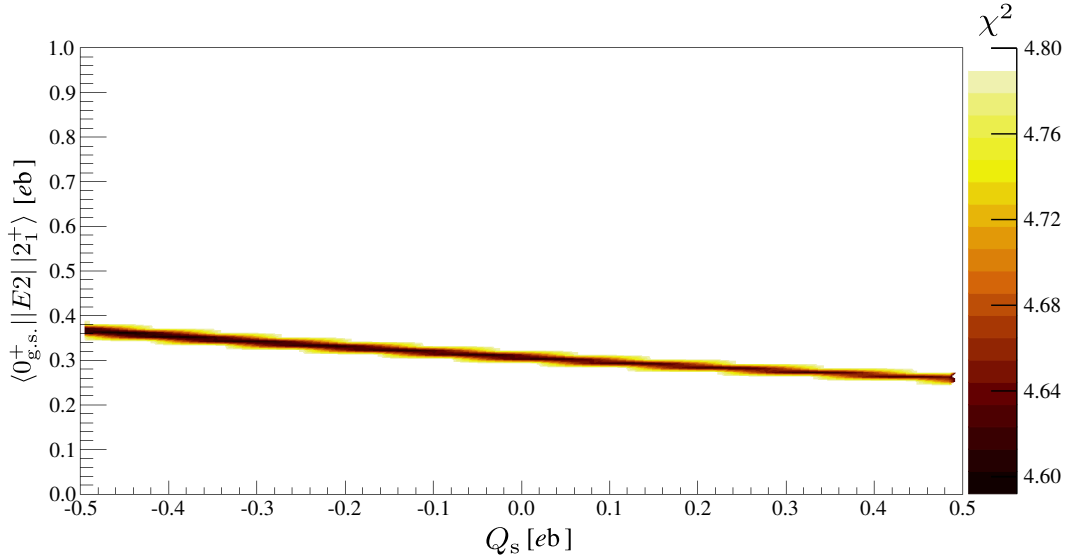


**Figure 79:** Reduced matrix element of the  $2_1^+ \rightarrow 0_{g.s.}^+$  transitions as a function of the spectroscopic quadrupole moment. The dependency of the transition matrix element is quite flat with respect to the different quadrupole moments. Negative values of  $Q$  describe a oblate deformation, whereas positive  $Q$  values indicate a prolate shape.

## 7. Comparison with theoretical results

The measured  $B(E\lambda)$  values as well as the established energy level scheme for the doubly-magic  $^{132}\text{Sn}$  are compared with results from state-of-the-art large-scale shell-model calculation (LSSM), Monte-Carlo shell-model calculation (MCSM), Relativistic Random Phase Approximation calculation (RRPA) and Random Phase Approximation calculation (RPA). The latter two calculations are utilized within the Relativistic Quasiparticle-Vibration Coupling (RQVC) and Hybrid Configuration Mixing model (HCM) to determine properties of odd-mass nuclei, respectively.

### 7.1. Theoretical models

#### 7.1.1. Relativistic Quasiparticle-vibration coupling

Self-Consistent Mean Field (SCMF) models describe atomic nuclei as independent particles moving in an average potential, created by the interplay of the individual particles. These models allow the calculation of many-body systems and predict essential properties of nuclei like masses, radii and deformation. Similar to the Density Functional Theory (DFT) for atomic electrons, the determination of single-particle properties with static SCMF models is not possible without additional modifications. However, for single-particle properties in odd mass nuclei dynamic correlations, between single-particle states and collective vibrations of closed shell nuclei (“core”), are of major importance. Collective vibrations are the most dominant contribution for low-lying states in spherical nuclei. Characteristics like the nuclear giant resonance or the fragmentation of the single-particle strength are not predictable within the framework of static SCMF models. Thus, a modification from a static density to a many-body theory including dynamic correlations is required. This is done by the Particle-Vibration Coupling model (PVC) [132]. The PVC model improves the energy as well as the wave function predictions of excited states for spherical odd-mass nuclei [133–135]. For the relativistic quasiparticle-vibration coupling model, developed in Ref. [136], collective properties of even-even nuclei were determined via Relativistic Quasiparticle Random Phase Approximation (RQRPA) calculations. The determined core-excitation properties, which are an essential part for the PVC model, are presented in Ref. [133] along the tin chain and in particular for the doubly-magic  $^{132}\text{Sn}$  nucleus.

### 7.1.2. Hybrid configuration mixing model

A different extension of the PVC model is the Hybrid Configuration Mixing model (HCM) presented in Ref. [137]. To account for the fact that nucleons outside closed shells can exhibit either particle-like character or manifest properties that correspond to the coupling of particle and core vibrations, the model incorporates particle states that arise from Random Phase Approximation (RPA) calculations. RPA calculations are a proper way to describe nuclear collective motion. These RPA states are implemented via mean-field solutions of the Skyrme Hamiltonian and the residual interactions [137]. Core excitations for the doubly-magic  $^{132}\text{Sn}$  were calculated to determine  $^{133}\text{Sb}$  properties within the HCM model [41]. The RPA calculations including the Skyrme interactions are performed as stated in Ref. [138]. The applied model space allow to fulfill the appropriate Energy-Weighted Sum Rules: all hole states of  $^{132}\text{Sn}$  and particle states up to a maximum energy cutoff of 120 MeV were included, discretized in a spherical box of 20 fm. However, while the results for giant resonances only depend on bulk properties of the Skyrme force, e.g. effective mass, those for the low-lying excitations are quite sensitive to the details of the levels close to the Fermi surface. For the detailed theoretical formalism see Ref. [137, 138].

### 7.1.3. Shell-model calculation based on $^{110}\text{Zr}$

New large-scale shell-model calculations were performed including the model space spanned by  $0h_{11/2}$ ,  $1f_{7/2}$ ,  $0h_{9/2}$ ,  $1f_{5/2}$ ,  $2p_{3/2}$ ,  $2p_{1/2}$  orbitals for neutrons, and  $0g_{9/2}$ ,  $0g_{7/2}$ ,  $1d_{5/2}$ ,  $1d_{3/2}$ ,  $2s_{1/2}$  orbitals for protons above the inert core of  $^{110}\text{Zr}$  [139]. Realistic interactions derived from the CD-Bonn potential were used. These interactions were renormalized by the  $V_{low-k}$  approach and adjusted to the model space by many-body perturbation theory including Q-box folded diagrams up to second order [140]. Monopole adjustments yield the experimentally determined single-particle energies for  $^{133}\text{Sb}$  and  $^{133}\text{Sn}$ . Further adjustments, corresponding to proton-proton ( $\pi\pi$ ) and neutron-proton ( $\nu\pi$ ) monopole matrix elements, allow to obtain single-particle energies for  $N = 82$  and  $N = 83$  isotones [139, 141]. Employing particle-hole (ph) excitations from  $\nu h_{11/2}$  and  $\pi g_{9/2}$  orbits, consequently demand the usage of  $^{110}\text{Zr}$  as an inert core. During this step the neutron gap of  $^{132}\text{Sn}$  and the proton gap of  $^{120}\text{Sn}$  were fixed, in addition to the prior mentioned properties. The calculations of  $^{132}\text{Sn}$  require to take np-nh excitations from the  $\nu 0h_{11/2}$  and  $\pi 0g_{9/2}$  orbitals into account. The diagonalization of the Hamiltonian with the dimension of  $2 \times 10^{19}$  in the case of  $^{132}\text{Sn}$  is only feasible with the truncation of 7p7h excitations. The diagonalization was performed

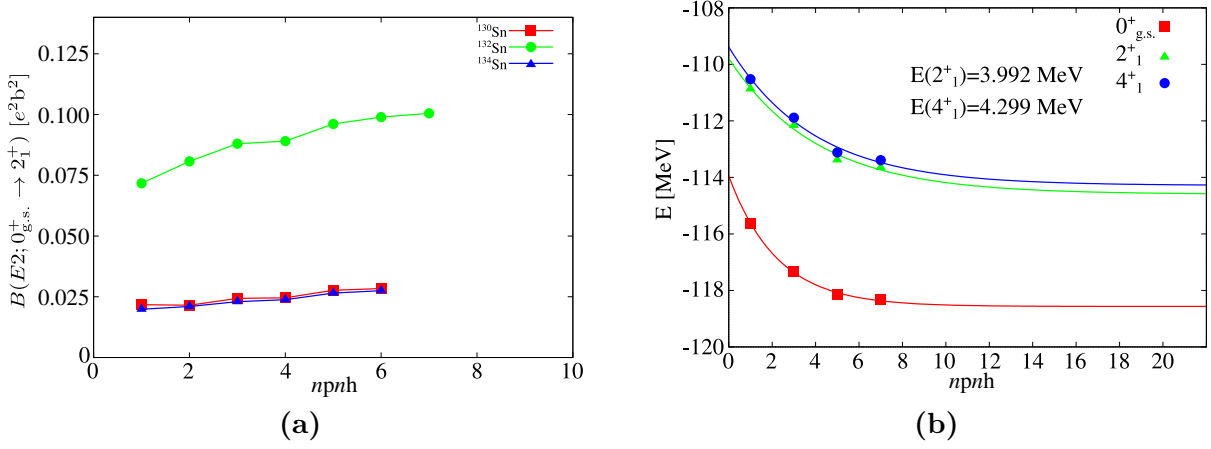


**Figure 80:** (a) Large-scale shell-model calculations for the  $B(E2)$  transition decay of the doubly-magic  $^{132}\text{Sn}$  and the two 2p and 2h neighbor isotopes  $^{130,134}\text{Sn}$ . (b) Calculated level binding energies for the  $2_1^+$  and  $4_1^+$  states within the large-scale shell-model framework. In both cases a convergence is achieved at 7p7h excitations. See text for more details. Figures adapted from private communication Ref. [145].

by N. Houda from the Université de Strasbourg with the ANTOINE shell-model code [142, 143] within the m-scheme. Effective charges  $e_\pi = 1.68 e$  and  $e_\nu = 0.41 e$  were used. The 7p7h excitation limitation ensures the convergence of the  $B(E2)$  values shown in Figure 80 (a) with  $B(E2; 0_{g.s.}^+ \rightarrow 2_1^+) = 0.1 e^2b^2$ . In Figure 80 (b) the calculated results for the level energies, i.e.  $E(2_1^+) = 3992 \text{ keV}$  and  $E(4_1^+) = 4229 \text{ keV}$ , are presented. Further sensitive tests of the effective interaction of the shell-model calculation are obtained by comparison with the neighboring isotopes  $^{130,134}\text{Sn}$ . The calculated  $B(E2; 0_{g.s.}^+ \rightarrow 2_1^+)$  strengths from the LSSM calculation yield 0.028 and 0.027  $e^2b^2$  for  $^{130}\text{Sn}$  and  $^{134}\text{Sn}$ , respectively. This is in good agreement with the experimental values yielding 0.023(5) and 0.029(5)  $e^2b^2$  [144]. These values demonstrate the locally increased quadrupole strength in doubly-magic  $^{132}\text{Sn}$ .

#### 7.1.4. Monte Carlo shell-model calculation

The advanced Monte Carlo Shell Model (MCSM) [146, 147] was used to calculate nuclear shapes along the even tin isotopes between  $N = 50$  and  $N = 88$ . The discrepancy between the expected general seniority description along the Sn isotopic chain for the  $B(E2)$  values and experimentally determined transitions strength along tin isotopes, require further clarification [148].

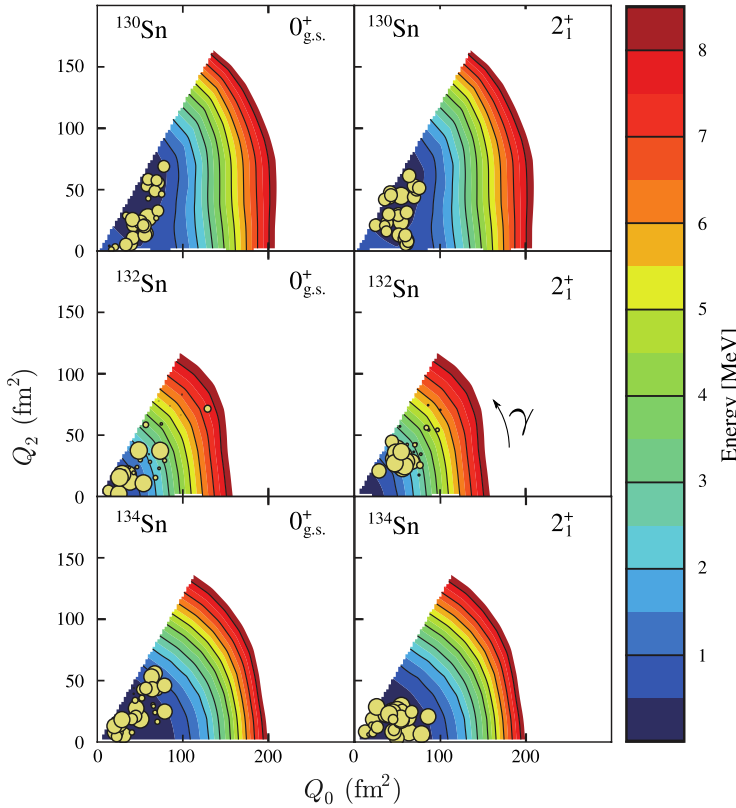


**Figure 81:** T-plot of the ground-state and first excited  $2_1^+$  states of  $^{130,132,134}\text{Sn}$  determined with the MCSM. Figure adapted from Ref. [149].

The MCSM calculations use a large model space spanned by  $1g_{9/2}$ ,  $2d_{5/2,3/2}$ ,  $3s_{1/2}$ ,  $1h_{11/2}$ ,  $2f_{7/2}$  and  $3p_{3/2}$  orbitals for protons and neutrons. This large model space corresponds to a maximum dimension of  $7.5 \times 10^{23}$ , which is not solvable with conventional shell-model techniques. The Hamiltonian applied in the calculation is once fixed via modifications of the Two Body Matrix Elements (TBME) and remains unchanged for all calculations. The adjustments do not include the properties of the  $^{132}\text{Sn}$  nucleus. For further details see Ref. [148]. The advanced MCSM calculations facilitate to determine the properties of even- $N$  ( $N = 50 - 88$ ) tin isotopes with no truncations with respect

to the occupation number of the included orbitals. In particular the  $2_1^+$  and  $4_1^+$  states were calculated, which were accessible within the present model space and computational power. The effective charges are  $e_\nu = 0.75 e$  and  $e_\pi = 1.25 e$  and were fixed by a global fit to  $^{104-134}\text{Sn}$ , while the calculations were done for  $^{132}\text{Sn}$ . The average of the isoscalar effective charges was kept to be 1.0 in the fit. The free parameter is the isovector charge.

The nuclear structures along isotopic chains can be visualized by the so-called T-plot using the MCSM. The nuclear shape of the doubly-magic  $^{132}\text{Sn}$  was calculated for the ground-state and the first excited state. The results illustrated in the T-plot [150, 151] of Figure 81, emphasize a spherical shape of the ground state of  $^{132}\text{Sn}$  with a more pronounced minimum compared to  $^{130,134}\text{Sn}$ . A superposition of  $J^\pi$  projected MCSM basis vectors represents the shell-model eigenstate. The basis vectors are deformed Slater determinants, characterized by the intrinsic quadrupole moments,  $Q_0$  and  $Q_2$ . These values are indicated by circles in the T-plot on top of the Potential Energy Surface (PES) for the shell-model Hamiltonian.



For details see Ref. [151]. A small deformation of  $^{130}\text{Sn}$  tends to exhibit an oblate character, whereas for  $^{134}\text{Sn}$  a spherical shape with dynamic prolate deformation is predicted. The T-plot is spread outwards to a similar extent among the  $0_{\text{g.s.}}^+$  states of  $^{130,132,134}\text{Sn}$  due to pairing correlations. The weak oblate deformation of the  $2_1^+$  state of  $^{132}\text{Sn}$  is only of dynamic character and can be deduced from the deformation parameter  $\beta$ , which can be calculated to first order with the intrinsic quadrupole moment  $Q_0 \approx 50 \text{ efm}^2$  from Fig. 81 via

$$\beta = \frac{\sqrt{5\pi}}{3} \frac{Q_0}{ZR_0^2}, \quad (7.1)$$

with  $R_0$  the nuclear radius and  $Z$  the proton number [152]. This corresponds to  $\beta = 0.03$ , which indicates for  $\gamma = 0$  a spherical nucleus. To account for  $\gamma \neq 0$  the deformation of the nucleus along his three axis is calculated with

$$\Delta R_i = R_0 \sqrt{\frac{5}{4\pi}} \beta \cos\left(\gamma - \frac{2\pi}{3}\kappa\right), \kappa = 1, 2, 3. \quad (7.2)$$

Substituting the values of  $\beta = 0.03$  and  $\gamma = 60^\circ$  in Eq. 7.2 [152] yields a maximum deformation of 3% along one axis, which stress the spherical structure of the first excited state of  $^{132}\text{Sn}$  and justify the fixation of the quadrupole moments to zero of the GOSIA2 calculation. Thus, the predictions from Figure 81 indicate that the doubly-magic character is restricted to the  $^{132}\text{Sn}$  nucleus. The quality of the MCSM calculations and the effective interactions are illustrated and described in more detail in Ref. [148]. The calculation is able to describe the properties along the isotopic tin chain, especially the local decrease of the  $B(E2)$  around  $N = 64$  and the increased bump around  $N = 58$ . In addition, the  $B(E2)$  value of the doubly-magic  $^{132}\text{Sn}$  is predicted in excellent agreement with the value determined in this work.

## 7.2. Comparison

The theoretically determined values for energies and reduced transition strength are summarized for the different models in Figure 82. The ground state ( $0_{\text{g.s.}}^+$ ) of the doubly-magic  $^{132}\text{Sn}$  is predominantly composed of the spherical  $\pi g_{9/2}^{10} \otimes \nu h_{11/2}^{12}$  configuration. The occupation numbers of protons and neutrons predicted by the LSSM calculation are 0.28 and 0.22, respectively. The MCSM calculations state even smaller occupation numbers with 0.09 for protons and 0.13 for neutrons. The excitation energy of the first excited state of  $^{132}\text{Sn}$  is quite well reproduced by all theoretical models (see Fig. 82(a)). The best agreement is

achieved by the LSSM based on the  $^{110}\text{Zr}$  core with 3992 keV and the RPA calculation using the Skyrme SkM\* interaction [153, 154] with 4060 keV. The energy obtained with RRPA calculations amounts to 4300 keV and the MCSM yields 4390 keV. The  $B(E2)$  values obtained from the LSSM, MCSM and RRPA calculations are in good agreement within the error bars with the experimentally determined value, whereas the RPA predictions overestimates the transition strength shown in Fig. 82(b). The value predicted by the MCSM calculation of  $B(E2; 0_{\text{g.s.}}^+ \rightarrow 2_1^+) = 0.085 e^2 \text{b}^2$  fits exactly the experimentally determined value. The outcome of the LSSM based on  $^{110}\text{Zr}$  and RRPA calculations are equal and result in a value of  $B(E2; 0_{\text{g.s.}}^+ \rightarrow 2_1^+) = 0.1 e^2 \text{b}^2$ . Both shell-model calculations describe the  $2_1^+$  wave functions predominantly by the 1p1h excitation from the  $\nu h_{11/2}$  to the  $\nu f_{7/2}$  orbit. The neutron occupation number of the  $\nu f_{7/2}$  orbit calculated with the LSSM is 0.92, whereas the MCSM calculation predict an occupation number of 1.04 for neutrons in the  $\nu f_{7/2}$  orbit. Proton excitations from the  $\pi g_{9/2} d_{5/2}^1$  orbital amount to a fraction of about 13% of the total wave function in the LSSM, corresponding to an occupation number of 0.21 for the  $\pi d_{5/2}$  orbital. Two proton excitations ( $\pi g_{9/2} g_{7/2}^2$ ) contribute with 5% to the total wave function, which results in 0.18 protons in the  $g_{7/2}$  orbital. In total, the proton contribution amount so approx 19%. The MCSM predicts an occupation number of 0.03 for the  $\pi g_{7/2}$  orbit and 0.07 for the  $\pi g_{5/2}$  orbit. Even the proton occupation numbers are small, the contribution to the  $\Delta j = \Delta l = 2$  transition of the total  $E2$  matrix element is approx. 17% and, thus, the proton excitation across the  $Z = 50$  shell gap is not negligible for the doubly-magic  $^{132}\text{Sn}$  nucleus. The wave function contributions obtained with the LSSM calculation are illustrated in Figure 83 for the three even-even  $^{130,132,134}\text{Sn}$  nuclei. This comparison clarify that the proton contribution is increased almost by a factor two for  $^{132}\text{Sn}$  compared to the neighboring  $^{130,134}\text{Sn}$  isotopes.

A larger proton contribution is predicted by the RPA calculation, where the excitation of the  $2_1^+$  state is composed out of a 56%  $\nu h_{11/2}^{-1} f_{7/2}$ , 19%  $\pi g_{9/2}^{-1} d_{5/2}$  and 14%  $\nu g_{9/2}^{-1} g_{7/2}$  configuration. This enhanced proton contribution of about 33% results in an increased  $B(E2)$  value, as mentioned in Ref. [53, 55, 155]. Thus, the overestimation of approx. 60% of the  $B(E2)$  value, independent of the Skyrme interaction, can be explained by the enhanced proton contribution. For the RRPA calculation no information on the wave function decomposition is available.

The  $B(E3)$  value could not be determined within the SM calculations, as the configuration could not be achieved within the utilized model space. The determined level energy with the MCSM calculation within the applies model space of  $E(3_1^-) = 4.985$  keV is too high,

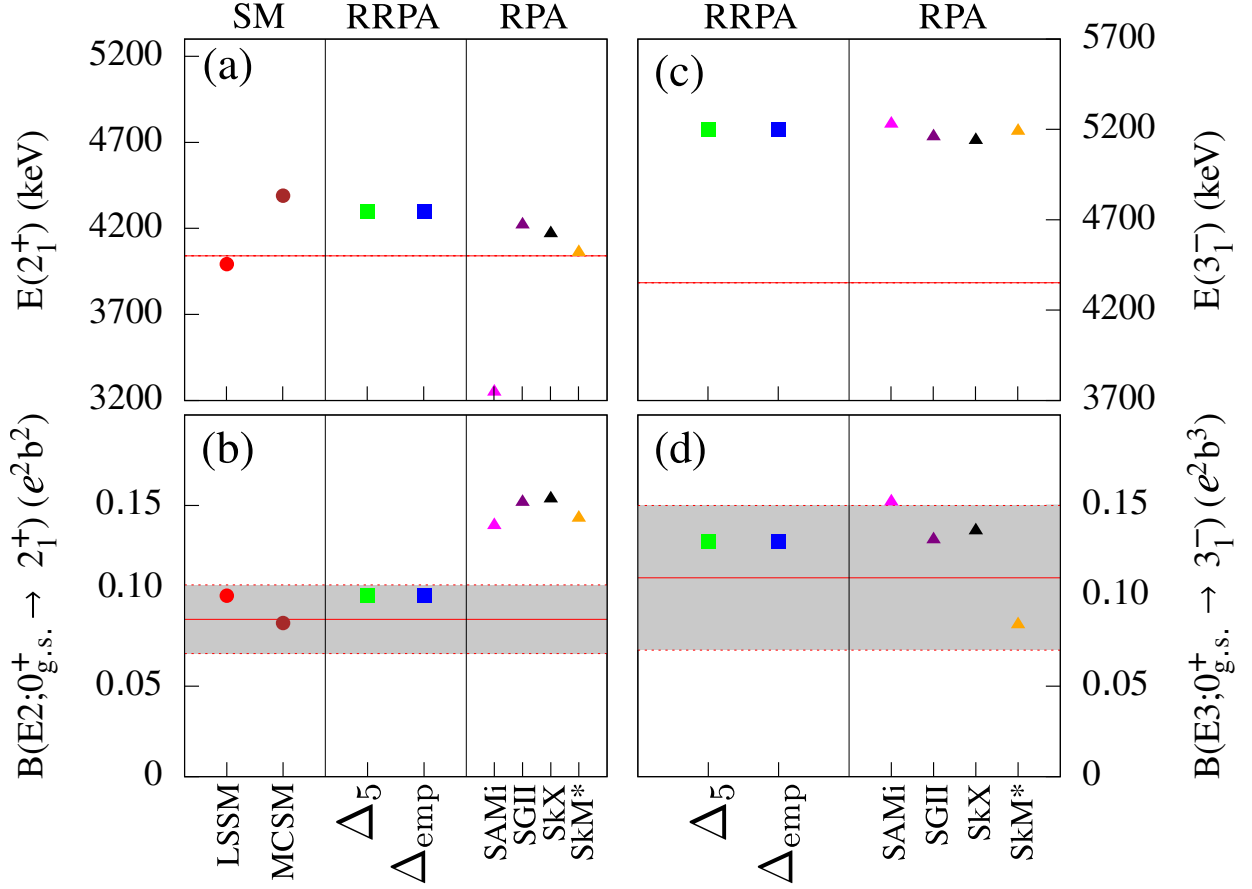


**Figure 82:** (a)-(d) Theoretical data of the reduced transition strength and level energies for the first excited  $2_1^+$  and  $3_1^-$  states in the doubly-magic  $^{132}\text{Sn}$  nucleus. LSSM and MCSM represent shell model calculations,  $\Delta_5$  and  $\Delta_{\text{emp}}$  are RRPA calculations with different shell gaps for the contribution nucleon orbits. SAMi, SGII, SkX and SkM\* denote different Skyrme interactions used for the Hamiltonian in RPA calculations. Experimental values for the  $B(E\lambda)$  values are marked with the red line and the errors are indicated by the grey area between the red dashed lines. The level energies are taken from Ref. [64], whereas the  $B(E\lambda)$  values were determined in this work. For more information see text.

whereas the respective  $B(E3) = 0.039 e^2 b^2$  value is too small. Both deviations can be addressed to the missing proton excitations from the missing  $fp$  orbitals into the  $sdg$  orbitals, as the  $fp$  orbitals are not included in the applied model space. The predictions from RRPA and RPA calculations, independent of the used Skyrme interactions and pairing gaps, are in very good agreement with the experimentally achieved  $B(E3)$  value. All calculated values are within the experimentally determined error of  $\sim 30\%$ . This excitation is predominantly described by a  $1p1h$  neutron excitation within the RPA calculation ( $\nu s_{1/2}^1 f_{7/2}$

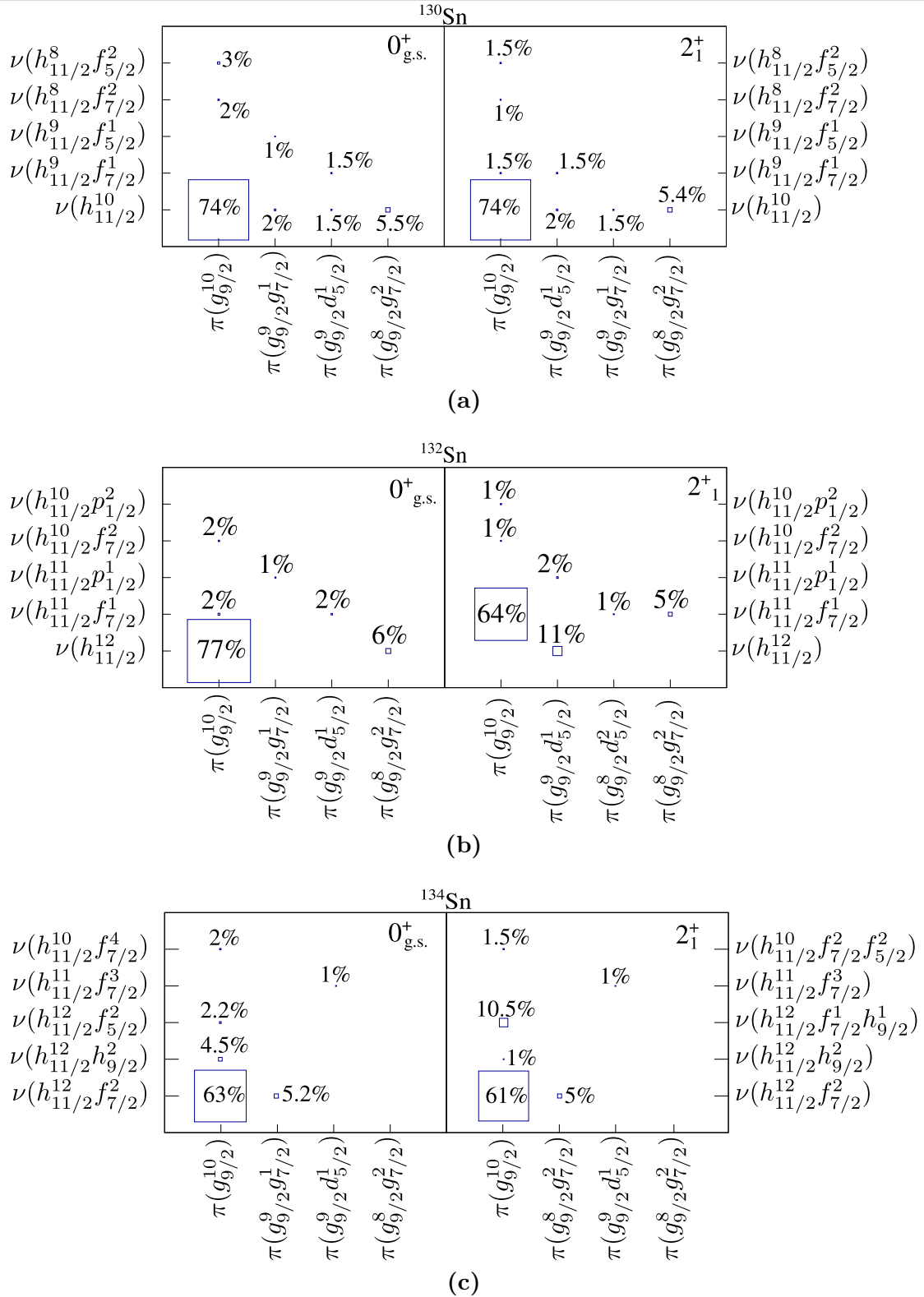


**Figure 83:** Large-scale shell-model calculated wave function decomposition for the ground ( $0_{\text{g.s.}}^+$ ) and first ( $2_1^+$ ) excited state of (a)  $^{130}\text{Sn}$ , (b)  $^{132}\text{Sn}$  and (c)  $^{134}\text{Sn}$ . The calculations were performed with the shell-model code ANTOINE within the m-scheme (based onto a  $^{110}\text{Zr}$  core). For more information see Section 7.1.3. Data taken from [145].

(40%),  $\nu d_{3/2}^3 f_{7/2}$  (12%)). The proton contribution amounts to around 12% mainly originating from the  $\pi p_{1/2}^1 g_{7/2}$  orbitals. The predictions for the excitation energy, obtained by both models, overestimates the experimentally determined energy between 800 keV up to 900 keV.

In addition, the large-scale shell-models calculate the properties of the  $4_1^+$  state. The LSSM and MCSM calculations yield  $E(4_1^+) = 4.30$  MeV and 4.66 MeV, respectively, which agrees nicely with the experimental value of 4.416 MeV. Figure 84 illustrates the calculated wave function decomposition of the  $4_1^+$  state obtained from the LSSM calculation. The wave function of the  $4_1^+$  state is mainly characterized by the  $1p1h$  neutron  $\pi g_{9/2}^{10} \otimes \nu h_{11/2}^{11} f_{7/2}^1$ . It can be recognized that, the amount of the proton contribution of the  $4_1^+$  state resembles more the ground state than the  $2_1^+$  state (cf. Fig. 83 (b)). Thus, the proton excitations  $\pi g_{9/2}^{-1} d_{5/2}$  are significantly reduced, resulting in lower average occupation numbers of 0.10 and 0.03 of the  $\pi d_{5/2}$  orbit for the LSSM and MCSM calculations, respectively. The corresponding transition strengths are  $B(E2; 2_1^+ \rightarrow 4_1^+) = 0.00107 e^2 b^2$  determined with LSSM and  $0.00219 e^2 b^2$  obtained with the MCSM calculation. The MCSM result agrees very good with the experimentally known value of  $0.00288 e^2 b^2$  [129]. The observed branching ratio of the  $4_1^+$  state shows that the  $E4$  transition amounts almost to 17% relative to the  $E2$  transition [129]. The increased  $E4$  transition is possibly the result of the preferred proton rearrangement into the ground-state configuration rather than into the  $2_1^+$  configuration, due to the higher resemblance of the  $4_1^+$  state and the ground state. Moreover, the isomeric lifetime of approx. 4 ns of the  $4_1^+$  can also be attributed to the proton configuration and the small transition energy of 375 keV compared to the ground-state transition of 4416 keV.

The collectivity reflected by the excitation energies of the  $2_1^+$  and  $4_1^+$  states and their  $B(E2)$  values are well reproduced. Even the dominant contribution is caused by the  $1p1h$  neutron excitation across the  $N = 82$  shell gap, the contribution of the proton excitation to the total transition strengths is crucial to reproduce the experimental values in  $^{132}\text{Sn}$ . A change from oblate to prolate oscillations of the first excited  $2_1^+$  state across the doubly-magic configuration is deduced from MCSM results (see Fig. 81). Besides the  $E2$  transition strengths also the  $B(E3)$  value is well reproduced by RPA and RRPA results.

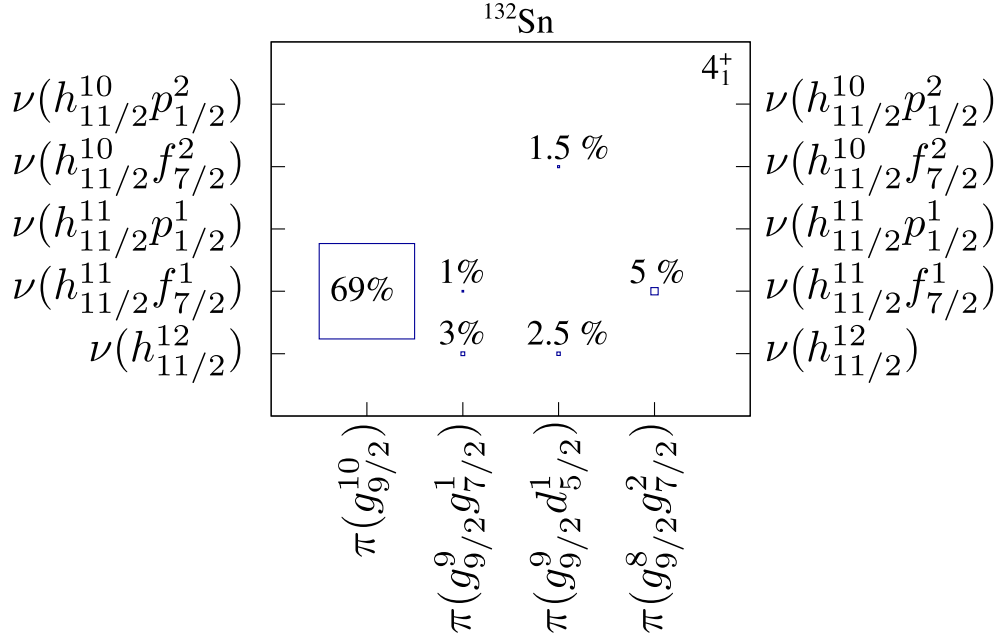


**Figure 84:** Wave function decomposition of the  $4_1^+$  state of  $^{132}\text{Sn}$ . The amount of proton configuration resembles the ground-state of  $^{132}\text{Sn}$ . See text for more information. Data taken from [145].

### 7.3. Summary and Outlook

In this work the Coulomb excitation of the radioactive and exotic doubly-magic  $^{132}\text{Sn}$  was conducted. In particular, the quadrupole and octupole collectivity were studied via the excitation of the first  $2_1^+$  and  $3_1^-$  states. Compared to preliminary  $B(E2)$  values, which were obtained via a Coulomb excitation of  $^{132}\text{Sn}$  at ORNL, the present analysis points to a reduced collectivity of the first excited state in  $^{132}\text{Sn}$ . In addition, state-of-the-art large-scale shell-model calculations, RRPA and RPA models were compared to the experimentally determined results. A good agreement for the first excited state of  $^{132}\text{Sn}$  is observed between the LSSM calculations and the experimental outcome. Thus, the theoretical predicted increase of the collectivity of the excited state in the doubly-magic  $^{132}\text{Sn}$  nucleus is observed and endorses the findings.

Furthermore, the experimental findings support the RRPA and RPA predictions concerning the  $B(E3)$  transition strength. Considering the large-scale shell-model calculations, no  $B(E3)$  value could be predicted as this configuration require the inclusion of the proton fp shells below  $Z = 82$ . However, due to the continuous development of advanced SM calculation and increasing computational power, the calculation of the octupole collectivity

will be accessible and yield further information about the collective properties of  $^{132}\text{Sn}$

The interest for the doubly-magic  $^{132}\text{Sn}$  and his vicinity remains unbroken, as these nuclei are of major importance for theoretical models and predictions e.g. for the astrophysical r-process. Therefore, properties like single particle energies, masses, binding energies or collective properties are essential. A variety of ongoing and future experiments for example at HIE-ISOLDE and MINIBALL are addressing this question.

The collectivity of the doubly-magic  $^{132}\text{Sn}$  was presented in this work. Upcoming Coulomb-excitation studies dealing with the collectivity of tin nuclei beyond the shell closure at  $N = 82$  to even more neutron-rich isotope are aimed for in the proposal [156]. The analysis of collectivity in the north-east region (away from  $Z = 50$  and  $N = 82$  shell closure) with respect to  $^{132}\text{Sn}$  were measured recently and data evaluation is ongoing [157]. A different approach compared to Coulomb excitation is the fast-timing spectroscopy at HIE-ISOLDE and Isolde Decay Station (IDS). The experiment proposed in Ref. [158] intends to investigate single-particle energies in  $^{130,131,133,134}\text{Sn}$  and will examine the nucleon-nucleon interactions in this mass region. For these challenging experiments the new HIE-ISOLDE facility provides an excellent basis and offers with the upcoming upgrades new and important physics opportunities for future measurement investigations.





## **Part II.**

### **Development of escape-suppression shields for the MINIBALL spectrometer**



## 8. Introduction

State-of-the-art radioactive-beam facilities like ISOLDE at CERN [70–72] and the continuous development of high-performance and high-efficient  $\gamma$ -ray spectrometers allow to study the properties of rare radioactive isotopes far from stability. The investigation of properties of exotic nuclei far from stability is important to shed light, e.g. on astrophysical processes like the waiting points during the r- and p-process path.

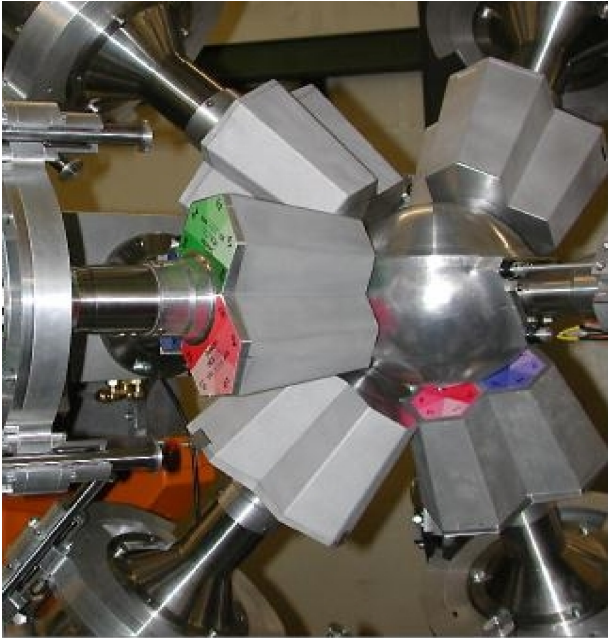


**Figure 85:** MINIBALL spectrometer arranged around the COULEX target chamber at Cologne 2004.

The high-detection efficiency of modern  $\gamma$ -ray spectrometers is achieved via multi-detector arrays, which are able to cover a large solid angle. In the mid 80's  $\gamma$ -ray spectrometer like OSIRIS in Germany, TESSA3 in the UK and NORDBALL in Denmark could reach detection efficiencies up to 1% [159]. During the 1990's the next generation of  $4\pi$  detector arrays started operating. EUROBALL [160] in Europe and GAMMASPHERE [161] in the United States, reaching detection efficiencies of about 10%. These detector systems facilitated the analysis of fusion-evaporation experiments by the detection of resolvable  $\gamma$ -ray cascades after the deexcitation of highly excited states in heavy nuclei.

The first segmented  $\gamma$ -ray spectrometer is the MINIBALL detector array [106, 162], which is operating most of the time at the ISOLDE facility at CERN. The MINIBALL spectrometer, which was described in Section 3.1.6, consists out of eight triple cluster detectors typically arranged as close as possible around the experimental target chamber. This ensures for the limited amount of active detection volume the highest possible detection efficiency (see Figure 85), whereas the six-fold segmentation preserves a good position sensitivity [103]. Since the start of MINIBALL the  $\gamma$ -ray spectrometer was predominantly used in experiments with low  $\gamma$ -ray multiplicities ( $M_\gamma \leq 3$ ). Nevertheless, it was constructed to cope with higher  $\gamma$ -ray multiplicities [103, 162]. Additional detectors are required to assure a high single-hit probability and reduce Compton-scattered  $\gamma$  rays between individ-

ual triple clusters. Figure 86 illustrates a  $\gamma\gamma$ -coincidence matrix between two MINIBALL triple cluster detectors. Horizontal and vertical lines correspond to fully absorbed  $\gamma$ -rays within one triple cluster. The diagonal lines represent Compton-scattered events between these two detectors. Potential peaks within the Compton background can be hidden and, thus, it is desirable to eliminate the Compton background from the  $\gamma$ -ray spectra.

Escape-Suppression Shields (ESS) will improve the Peak-to-Total (P/T) ratio (see Section 9.1) of the recorded  $\gamma$ -ray spectra by rejecting actively the Compton background. For the MINIBALL spectrometer a detailed Monte-Carlo study was performed, employing the computer code GEANT4 [164, 165] to determine the ideal geometry for the additional detectors [166]. The supplementary detectors are scintillation counters made out of bismuth germanium oxide (BGO). This compound material is characterized by a high density of  $7.13 \text{ g/cm}^3$  and a high  $Z$  to enhance the detection efficiency. Furthermore, their fast detection signals are highly suitable for fast veto coincident signals. The first prototype of the MINIBALL ESS was developed in collaboration with the Institut de Physique Nucléaire (IPN) at Orsay. First performance results of the Compton-suppression shield are presented as well as the comparison with theoretical calculations obtained with GEANT4.

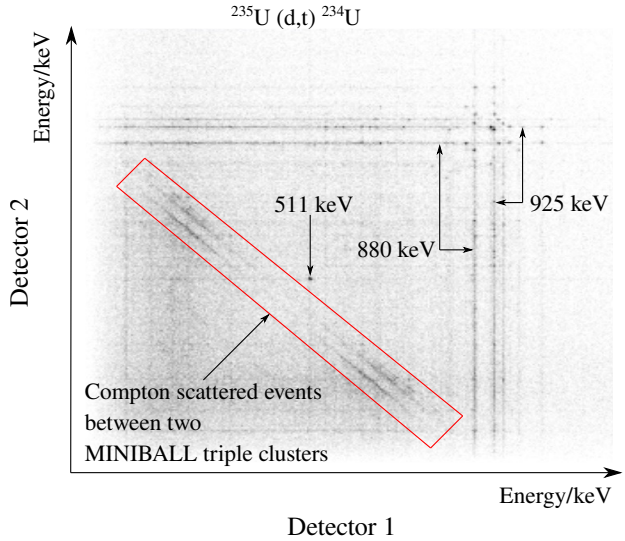


**Figure 86:**  $\gamma\gamma$ -matrix recorded with two MINIBALL triple cluster detectors 2004 at Cologne after  $^{235}\text{U}(\text{d,t})^{234}\text{U}$  reaction. Adapted from ref. [163]

## 9. Geant4 simulations

As contemporary physics experiments increase in complexity and costs, it is desirable to predict very detailed the properties of future experimental setups. Especially during the development of large and complex detection systems a simulated efficiency response and other quantities minimize the development costs. Also in fields like target development, detector geometry and beam energy estimation this type of simulations are of major importance. The fine tuning of these systems via simulations allow to improve the efficiency and quality of upcoming experiments in a very efficient manner. Therefore, the GEometry AND Tracking (GEANT4) computer code was developed at CERN. The code is able to determine the interactions of particles in matter based on the Monte-Carlo formalism. The computer code is written in C++ and delivers a huge amount of programmed packages, which are continuously updated with latest verified physics data. This allows simulations and predictions from simplest geometries and phenomena up to complex experimental setup, e.g. the detector response of the LHC experiments at CERN.

### 9.1. MINIBALL escape-suppression shield

The first step towards the development of an ESS detector system for the MINIBALL spectrometer, was to create a realistic as possible computer simulation to predict the detector performance. This allows in the most efficient way to determine the ideal detector geometry and obtain a first impression of the expected results for the final geometry. The performance of a combined detector system of MINIBALL and a Compton-suppression shield is characterized by two quantities. The first one is the detection efficiency of the shielded MINIBALL spectrometer. Including additional detectors in the MINIBALL setup will reduce the detection efficiency by a necessary larger detector-target distance. On the other hand, an increasing  $\gamma$ -ray multiplicity for example caused by increasing beam energies will result in a reduced peak-to-total ratio. The peak-to-total ratio describes the peak intensity relative to the total amount of counts in a  $\gamma$ -ray spectrum. It is therefore, a direct measure for the  $\gamma$ -ray spectra quality. In the case of a  $^{60}\text{Co}$  source measurement, the peak-to-total ratio is calculated by the integral of both transition peaks at 1173 keV and 1332 keV relative to the total amount of detected  $\gamma$  rays. Both quantities, detection efficiency and peak-to-total ratio, are used for benchmarking the escape-suppression detector design. The crucial point is that both quantities cannot be optimized simultaneously. Thus, GEANT4 simulations are required to determine a detector geometry with

a reasonable balance between the detection efficiency and peak-to-total ratio, suitable for future experiments. A variety of simulations were performed with different BGO detector thicknesses, lengths and shapes. The elaborated results as well as a precise description of the simulations can be found in Ref. [166]. In the following the final outcome of the GEANT4 study will be presented.

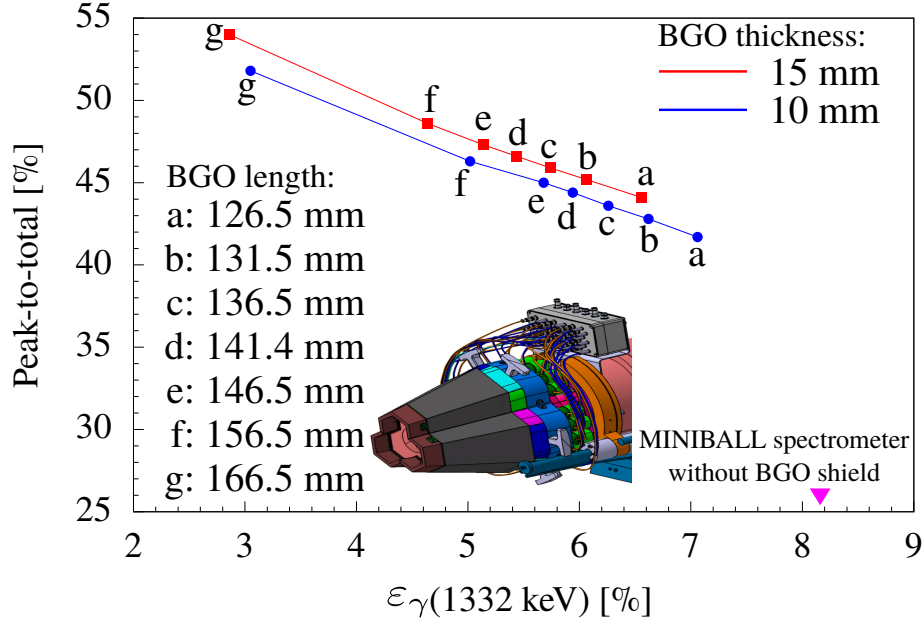


**Figure 87:** Peak-to-total as a function of the detection efficiency for the complete MINIBALL spectrometer obtained with the GEANT4 simulation using a  $^{60}\text{Co}$  source. The simulated setup is similar to the one shown in Fig. 85, but additional BGO detectors are implemented around the MINIBALL triple clusters. The inset shows one CAD drawing of an ancillary BGO detector (black) surrounding one MINIBALL triple cluster. Further, the heavy-met (dark red), the fixation (orange and blue) and the photomultiplier tubes (green) are shown. More details can be found in the text.

The simulation included the complete MINIBALL spectrometer surrounding the COULEX target chamber, shown in Figure 85. The detector-target distance with the final ESS detectors amounts to 12 cm (without BGO shields a detector-target distance of 8 cm is achieved). All GEANT4 simulations were performed with a  $^{60}\text{Co}$  source placed at the center of the target chamber. The first goal was to reproduce the experimentally measured peak-to-total and detection efficiency. Both values were measured 2008 at CERN with the MINIBALL spectrometer [106]. From calibration measurements with a  $^{60}\text{Co}$  source a peak-to-total of 25% and an detection efficiency of 7.8% for the 1332 keV transition were determined. The simulation predicts a peak-to-total ratio of 26% and an efficiency

of 8.2%. Both measured values are slightly overestimated by the simulation. However, the deviations are  $\leq 5\%$  and, thus, the simulation is reliable in a confidence level of 95% for simulations with  $^{60}\text{Co}$ .

For the best coverage of the MINIBALL triple detectors, the BGO crystal shapes were adapted to the shape of the MINIBALL endcap (compare inset in Figure 87). In a first step the peak-to-total ratio was investigated as a function of the BGO crystal thickness. The simulations predicted a saturation of the peak-to-total ratio around 15 mm BGO crystal thickness, for  $\gamma$ -ray energies up to 3 MeV. As a comparison: the EUROBALL BGO Compton-suppression shield is made of tapered BGO crystals with thicknesses between 3 mm and 20 mm [160]. This is an other proof for the reliability of the simulation. In contrast to the EUROBALL Compton-suppression shield, which operates at 43 cm distance between detector and target, the MINIBALL Compton-suppression shield geometry is limited by the compact detector setup. Therefore, a compromise between the BGO crystal shape (thickness and length) and the reduction of the efficiency had to be elaborated. Figure 87 presents the final results obtained with the GEANT4 simulations incorporating the full MINIBALL setup. The data points represent 10 mm and 15 mm thick BGO Compton-suppression shields with 3 cm heavy-met (passive shielding to avoid direct irradiation from the source) in front of the ESS detectors. The allegation in mm describes the length of the BGO Compton-suppression shield. The biggest improvement of the peak-to-total ratio is achieved by applying a BGO shield with the length of the MINIBALL endcap of 126.5 mm. The increase in the P/T ratio with increasing BGO length is less than 6% along with a decrease of a factor of 2 for the detection efficiency. Furthermore, the improvement gained with 5 mm thicker BGO crystals is around 2% for the peak-to-total, but at the same time the detection efficiency is reduced by 11% compared to the 10 mm thick crystals. Therefore, the final geometry was chosen to be tapered. The crystals are 10 mm thick at the front side and 20 mm thick at the back side. This is possible as the MINIBALL detectors are arranged around a spherical geometry and, hence, the space at the back side of the detectors is not the limiting factor. The ESS geometry accomplish, according to the simulation, an peak-to-total of 44% and a detection efficiency of 7.2% with respect to the 1332 keV transition.

## 10. Escape-suppression shield prototype

Based on this Compton-suppression shield geometry for the MINIBALL spectrometer, a first prototype was built in collaboration with the IPN at Orsay. The described geometry and response study with the computer code GEANT4 and the determination of the final escape-suppression shield geometry was performed at Cologne. The hardware development and assembly was done at the IPN in Orsay. To examine the performance of the BGO prototype, the escape-suppression shield was combined with a MINIBALL triple cluster detector and tested in a dedicated detector test laboratory at the IKP in Cologne (see Section 11) as part of this thesis project.

### 10.1. Escape-suppression shield design

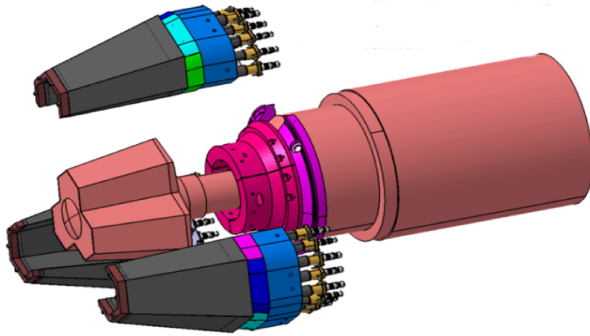


**Figure 88:** CAD drawing of one MINIBALL triple cluster with three BGO subsystems. Figure from [167].

One ESS for one MINIBALL triple cluster comprises three identical and separate removable subsystems (see Figure 88). This additional BGO detector will increase the weight of one MINIBALL triple cluster by 21 kg, as it will be mounted onto the triple cluster. One BGO subsystem is composed out of four different BGO crystal geometries and will be assembled around the MINIBALL endcap of one HPGe detector. All crystal geometries have the same tapered shape described before. Each BGO crystal

is wrapped independently in a reflector foil to avoid photon loss. In addition a second layer of carbon-fiber is wrapped around the BGO crystals to avoid damages of the material and assure optical shielding. The following sections describe the BGO components and manufacturing process in more detail.

#### 10.1.1. BGO crystals

Escape-suppression shields require a high photo fraction for  $\gamma$ -ray absorption. Hence, a high  $Z$  and dense ( $7.13 \text{ g/cm}^3$ ) material like bismuth germanate (BGO) is a reasonable solution. BGO Compton-suppression shields were already used in various experimental setups, e.g. in combination with the EUROBALL spectrometer [160]. The possibility to



machine this material in various shapes, geometries and the easy handling (no hermetic sealing needed) makes it very advantageous for these kind of applications. Furthermore, the fast decay constant of  $\approx 300$  ns suits the detector material for fast-veto coincidence setups. The light yield is between 8 and 10 photons per keV, within a wavelength range of 320 – 640 nm and the maximum intensity around 480 nm. The rather poor energy resolution of about 20% at 662 keV, compared to HPGe detectors, is accepted for the purpose to reject the Compton-scattered  $\gamma$  rays. Time resolution and detection efficiency are the desired and more important quantities. For the MINIBALL triple cluster detectors four different BGO crystal shapes are required to build one BGO subsystem. Figure 89 illustrates the shape and geometry of the MINIBALL endcap, to which the BGO crystals has to be adjusted in order to coat the HPGe crystals. Due to the symmetry of the triple endcap of the HPGe detectors four different BGO crystal shapes are needed (cf. Figure 89 Left).

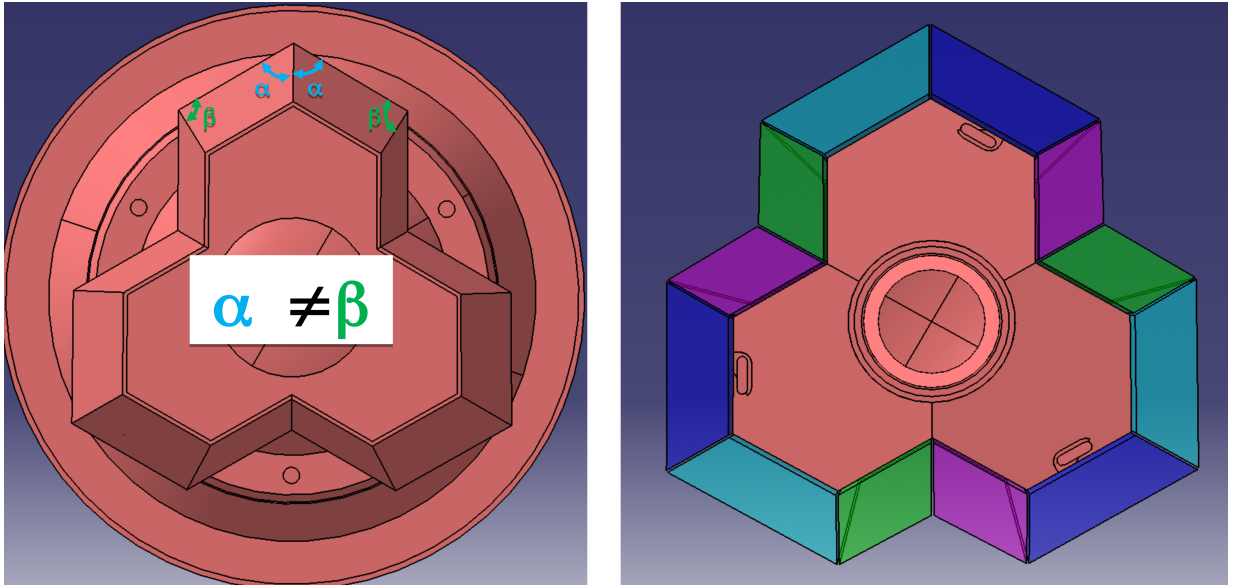


**Figure 89:** Left: CAD drawing illustrating the MINIBALL endcap geometry. Right: Back side look at a MINIBALL cryostat with BGO shields surrounding the endcap. Equal BGO shapes are color coded. See text for further information.

In Figure 90 (a) and (b) one set of four bare BGO crystals for one BGO sub-system is shown. The manufacturing of the crystals was done by SCIONIX and delivered to the laboratories in Orsay.

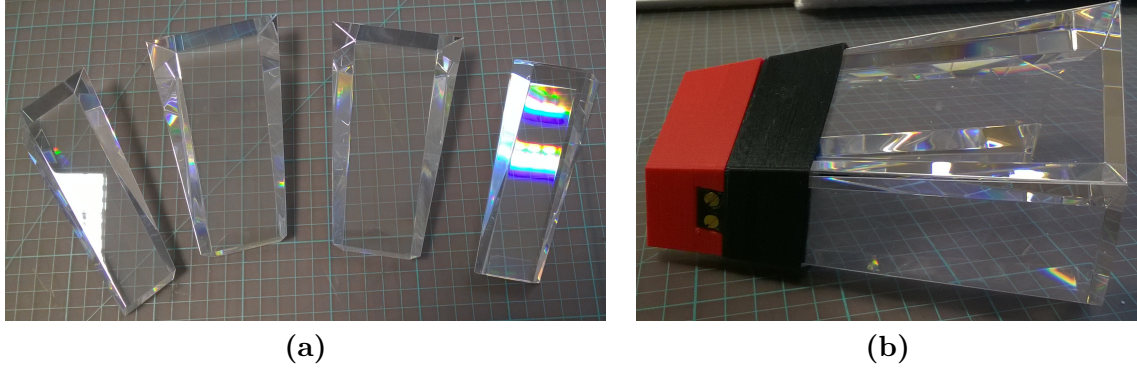


**Figure 90:** (a) Four different BGO crystals are required for one BGO sub-system as delivered by SCIONIX. (b) BGO crystals arranged in the shape of one BGO sub-system for illustration.

### 10.1.2. BGO housing

The emission of photons after deexcitation of the BGO material is an isotropic process. To avoid a huge photon loss, the bare BGO crystals have to be surrounded with a reflective material to guarantee a high reflection of the crystal surface. This procedure improves the properties of the detection system by increasing the detection probability of the photomultiplier tubes (PMTs), which is important as the PMTs can only cover a small area of the BGO crystals. Without the wrapping, the energy resolution as well as the detection efficiency would suffer tremendously. The BGO crystals are wrapped in VM2000 foil. This reflection foil is a metal-free multi-layered polymeric film, which reflects 98% of visible light [168, 169]. Figure 91 shows the process of the wrapping. Each BGO crystal is almost completely enclosed in the VM2000 foil, only openings for the PMT connections are left open (Fig. 91 (b)). A second layer, the so-called BGO housing, is coating the BGO crystals to shield them from external optical light and to protect the material from damages. The requirements for this material are:

1. High optical shielding to avoid any external irradiation with optical light.
2. Low absorption and attenuation characteristics to enable a low energy threshold for  $\gamma$  rays.

After material studies performed in Orsay, specially manufactured carbon-fiber was selected as a solution. The BGO housing was produced with a thickness of 0.4 mm and a weight of 0.6 kg per crystal. Mechanical test in combination with bending simulations predicted a

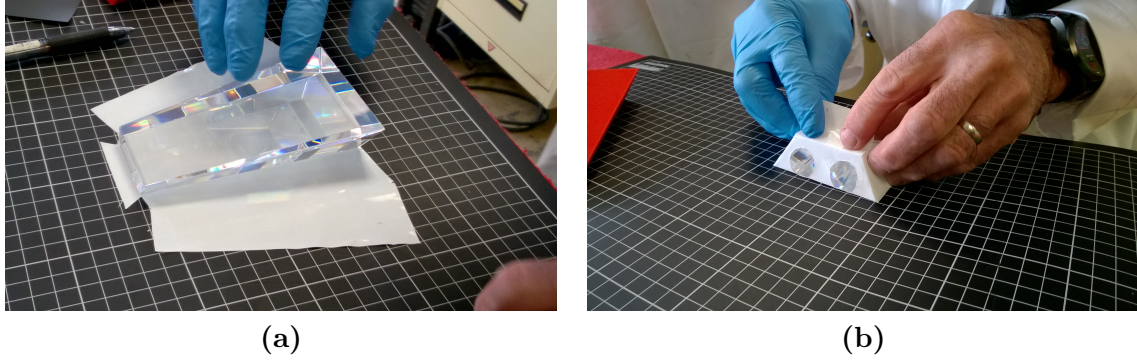


**Figure 91:** The bare BGO crystals are wrapped first with VM2000 foil to guarantee a high photon detection after a  $\gamma$ -ray interaction in the BGO. See text for more details.

bending of less than 130  $\mu\text{m}$  for the final experimental setup. For the specific shape of the BGO crystals, the carbon-fiber material had to be formed in a custom-build procedure. The carbon-fiber was heated in an oven and carefully pressed in the particular shape with dedicated equipment, as seen in Figure 92 (a) and (b). Remaining slots were optically shielded with an isolating black tape, to ensure no external optical irradiation.

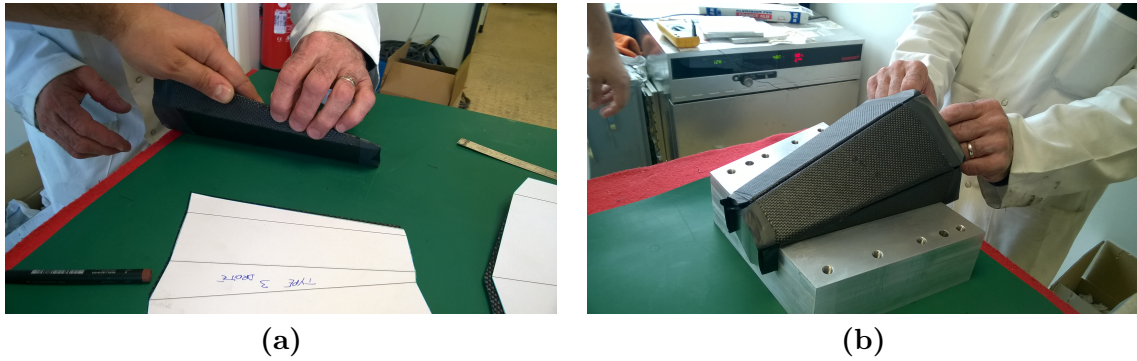


**Figure 92:** (a) and (b) show the forming of the carbon-fiber housing for the BGO Compton-suppression shield as part of the production process.

### 10.1.3. Photomultipliers for the escape-suppression shield

The optical photons produced by the BGO crystals are converted into electrons and are consecutively amplified by the connected photomultipliers to generate detectable charge signals. The higher the coverage of the crystal by the PMTs, the better the detection efficiency and also the energy resolution. However, an important point is the limited space avail-

able at the end of the MINIBALL triple cluster HPGe detectors and the cryostat housing, which restricts the potential size of possible PMTs for the readout. Measurements in Orsay showed, that an adequate choice of the PMTs are the Hamamatsu R3478 photomultipliers with a round shape and a diameter of 19 mm. These PMTs comprise 8 dynode stages with a gain factor of  $1.7 \times 10^6$  for electrons and operate up to a voltage of 1800 V. The accepted wavelengths are between 300 nm and 650 nm with a maximum efficiency at 420 nm. This corresponds to the wavelengths emitted by the BGO crystal which are between 320 nm up to 640 nm with an maximum intensity at 480 nm. The rise and transit times of the PMT are 1.3 ns and 14 ns, respectively. The dark current rate (noise) of the PMT is typically around 10 nA, which is low compared to the typical anode current of 0.1 mA [170]. Attention has also be paid on the voltage-divider circuit of the PMTs, as the selected resistors have to be adapted to the fast-veto coincidence circuit. For the present setup and PMTs a fast response circuit is implemented. Figure 93 illustrates the used elements for the PMT circuit. Resistor R14 and capacity C4 build a lowpass filter inside the High-Voltage (HV) line to reduce noise pickup and, hence, increase the signal sensitivity. A high linear characteristic is achieved by using a tapered voltage-divider circuit instead of a normal voltage-divider. A detailed description of voltage-divider circuits and their applications is given in [171].

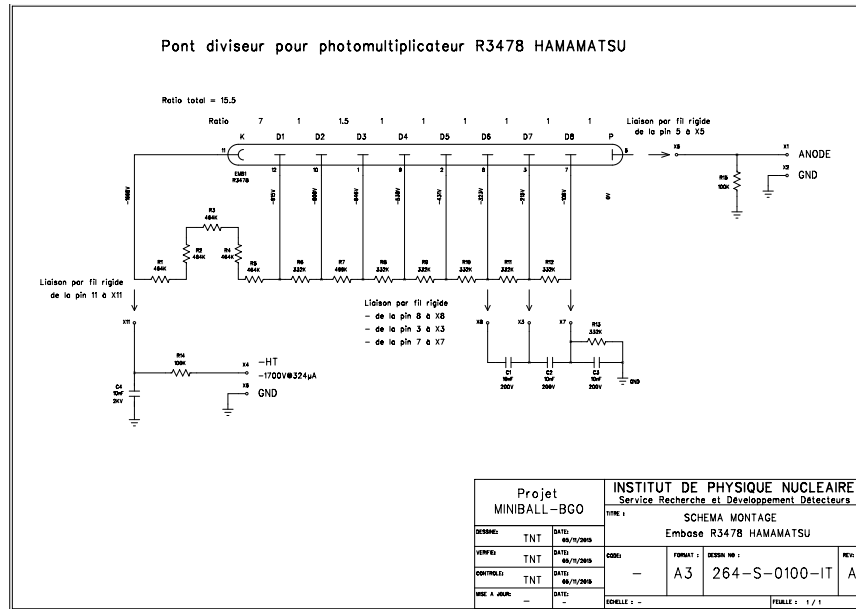


**Figure 93:** Photomultiplier voltage-divider circuit outlay used for the Hamamatsu R3478 PMTs. Taken from [168].

Another critical aspect is the optical connection between the photomultipliers and the BGO crystals. A good optical contact has to be assured to prohibit photon losses and not to decrease the detection efficiency of the ESS detectors. In the present case, specially produced “soft silicon cookies” were employed to ensure a good optical connection [168]. Therefore, two slightly viscous liquids (BLUESIL RTV 141 A and B) are mixed in a special treatment with a specific ratio for curing silicon elastomer. The dielectric properties of the material are:



**Figure 94:** Home made (at Orsay) “soft silicon cookies” used as optical connection between photomultiplier and BGO crystals. See text for more details. Figure from [168]

1. Dielectric strength, 20 kV/mm
2. Dielectric constant at 1 kHz 2.7
3. Dielectric dissipation factor at 1 kHz  $1 \cdot 10^{-3}$
4. Volume resistivity,  $1 \cdot 10^{15} \Omega/cm$ .

This kind of optical coupling was developed and used in the Auger Surface Detector for many years [168] and, thus, is a reliable technique. The final “soft silicon cookies” are illustrated in Figure 94. To shield the PMTs from external irradiation of optical light, aluminum housings are produced (see Figure 95). A magnetic shielding is not required, as the PMT tubes are small (19 mm diameter) and the magnitude of the earth magnetic field will not influence the charge collection. For the final experimental setup for example at a radioactive ion beam facility this aspect has to be verified.

#### 10.1.4. Mechanics holding structure of ESS detectors

To assemble the ESS detector system together with the MINIBALL triple clusters, an additional holding structure is required. The extra weight of about 21 kg originating from the Compton-suppression shield per MINIBALL triple cluster, is a crucial point. In addition the high flexibility offered by the MINIBALL spectrometer has to be preserved. Thus, each Compton-suppression shield will be mounted onto each MINIBALL triple cluster via an intermediate ring. Figure 95 illustrates the intermediate ring with one mounted BGO subsystem.



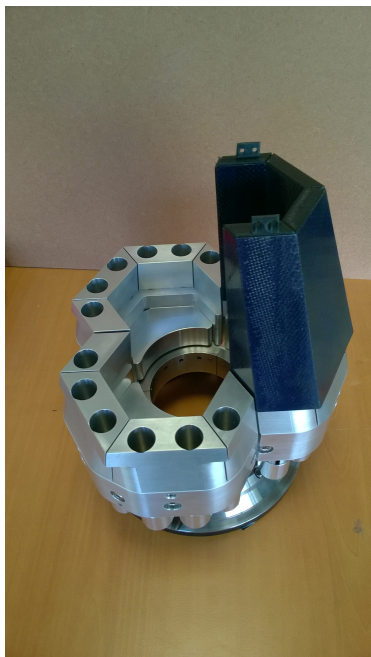
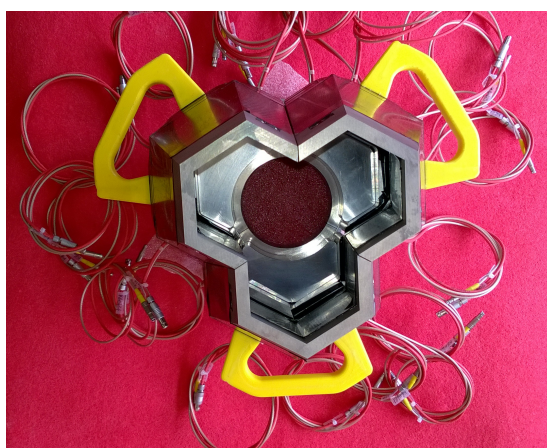


**Figure 95:** BGO fixation ring together with one BGO sub-system mounted and the aluminum PMT slots.

This allows to include the combined detection system in the MINIBALL frame (see Figure 31). Reinforcement studies at Orsay investigated the possible bending of the mechanical parts, considering the additional weight. Independent from the position of the BGO detector system, the bending will be less than 1 mm. This deflection is within the specification for the mechanical stability of the system and the experimental setup. The fully equipped and assembled BGO Compton-suppression prototype is illustrated in Figure 96 (a) and (b). Three BGO sub-systems, each including four BGO crystals and six PMTs, are mounted onto the intermediate ring. In front of the BGO crystals the heavy-met is installed. The yellow handles are used during the mounting procedure and are removed afterwards.



(a)



(b)

**Figure 96:** (a) and (b) assembled BGO prototype of the MINIBALL spectrometer.

## 10.2. Experimental setup

To assure a meaningful comparison between measurement and the Monte-Carlo GEANT4 simulations, the MINIBALL triple cluster detector together with the mounted BGO Compton-suppression shield was placed inside a scanning table with an adjustable detector-source distance (12 cm). The setup is illustrated in Figure 97. For the coincidence logic, three signals from each germanium core and three PMT signals from each BGO subsystem are used. The following sections deal with the signal processing and gives a description of the Pixie-16 data acquisition system.

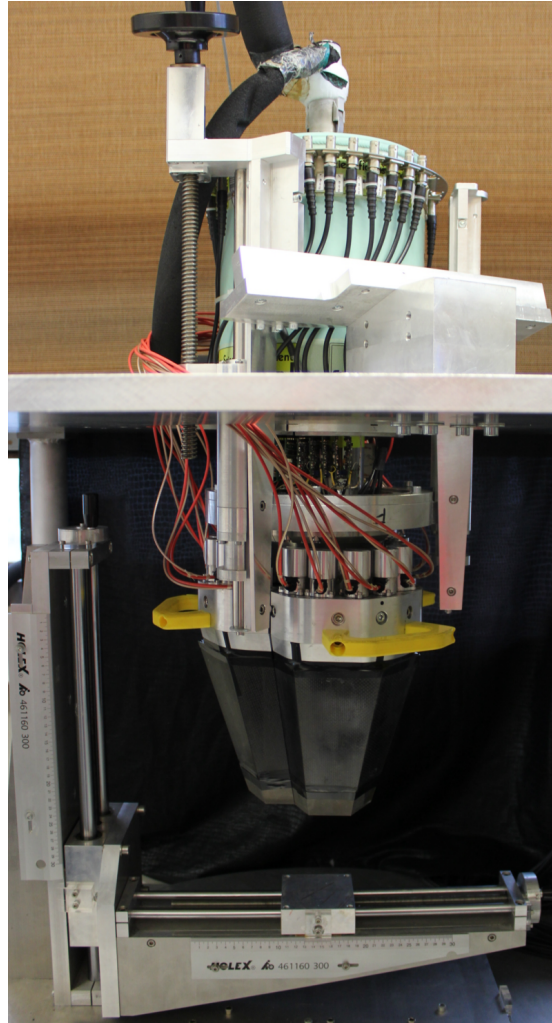


**Figure 97:** Prototype measurement setup at Cologne. The detector system is placed inside a scanning table to assure the right distances.

### 10.2.1. BGO signal processing

In total 18 Hamamatsu R3478 PMTs are used to obtain the output of the BGO crystals. For each subsystem six PMTs are used. For the sake of simplicity and no need for 18 individual veto signals, the PMTs from each subsystem are merged to produce a common veto signal. Photomultipliers in one subsystem are supplied by one HV module. Thus, all PMTs in one subsystem are operated at the same voltage, which can result in different amplification factors (cf. 98). This is mostly related to the manufacturing process and the deviations in the material properties.

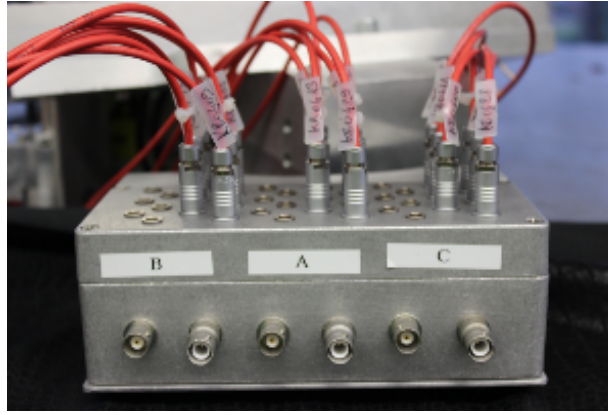


**Figure 98:** High-voltage supply box for the BGO prototype. The red HV cables for each sub-system are connected to one HV line. The signal outputs are processed in a different way. See text for more details.

However, it is preferable to adjust the gain factor (gain matching) for each PMT individually. Because a very good alignment of the amplification factors for each PMT, allows for a very low energy threshold of the BGO subsystem and causes an increased detection efficiency. For this purpose an additional alignment box was designed at IKP Cologne to adjust the single signals. The alignment box consists out of three independent inverting operational amplifiers with adjustable resistors for the six input channels. In this way each channel can be amplified individually and added to the merged signal. The circuit diagram in Figure 99 (a) illustrates one unit of the alignment box (99 (b)). The voltage output of the alignment box is given by:

$$-U_a = U_K \quad \text{with} \quad U_K = (I_{P1} + I_{P2} + I_{P3} + I_{P4} + I_{P5} + I_{P6}) \cdot R_K, \quad (10.1)$$

where  $I_{P1-P6}$  is the current from each PMT given by  $U_{e1-e6}/R_{1-6}$ . The resistance of the



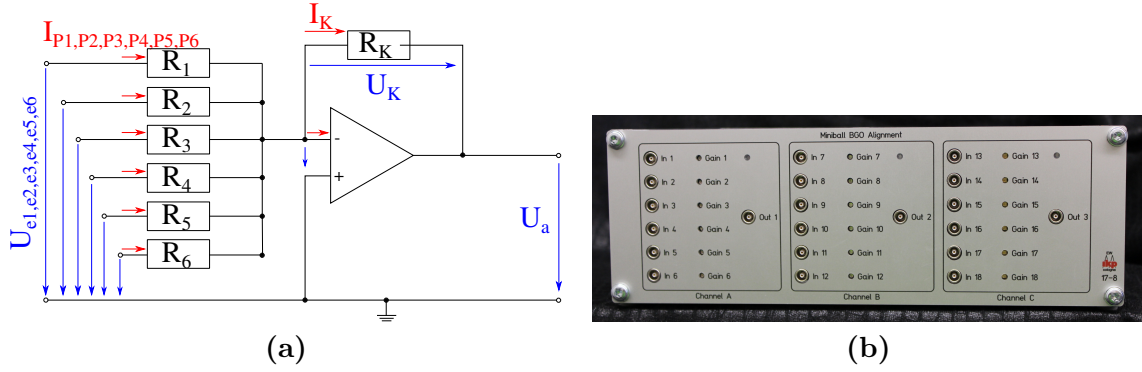


**Figure 99:** (a) Circuit diagram for one unit of the BGO alignment box. (b) BGO alignment box with three output and 18 input channels. For each input channel the resistances can be adjusted via the potentiometer (Gain) and, thus, a proper gain matching can be achieved.

six input channels can be adjusted via the installed potentiometer  $R_i$  with  $i \in [1, 6]$ . It has to be taken into account, that the merged/added signals has to be within the input range of the digital electronics. In order to obtain signals with no ringing (voltage oscillation due to reflections), an impedance converter is implemented, which modifies the signal shape to a rise time of 400 ns and a fall time of 2.5  $\mu$ s. This impedance conversion allow the signal transmission from the high resistance PMT output (kOhm) to an 50 Ohm input impedance of the digital electronics. The resulting time structure is still applicable for the fast-veto logic of the Compton-suppression system.

The impact of the additional alignment box is shown in Figure 100 (a) and (b). Both spectra are recorded with an analog MultiChannel Analyzer (MCA) and a  $^{137}\text{Cs}$  source. The source is irradiating directly one BGO subsystem. All crystals of one subsystem are measured without any gain matching (a) and with gain matching (b). The comparison illustrates that after the gain matching the energy resolution of the merged full energy peak is improved (Figure 101). Typically energy resolution is not important for Compton-suppression shields, as only a veto signal is required. However, the peak broadening can reduce the detection efficiency by a necessary high trigger threshold (energy threshold) of the Compton-suppression shield. If the amplification factor for one or more BGO crystals is higher than for the rest, the corresponding noise level can lead to a necessary high trigger threshold for the merged signal to avoid a huge amount of false coincidences. If the amplification factor is too low for single crystals, the merged signal will have a decreased detection efficiency due to the too high trigger threshold for these BGO crystals. Both cases will reduce the final peak-to-total ratio. In the present example shown in Figure 100, the

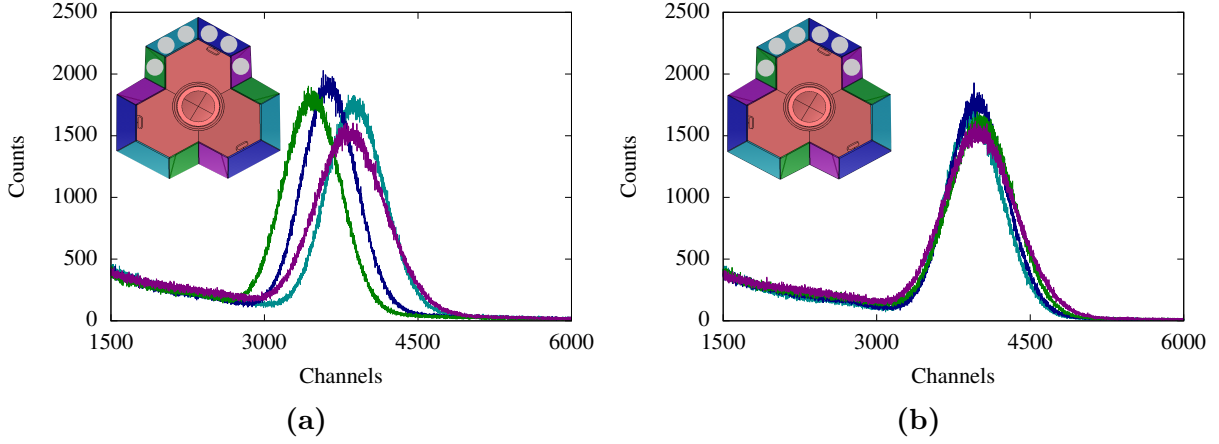


**Figure 100:**  $^{137}\text{Cs}$  source measurement with one BGO subsystem. (a) Results without gain adjustment and (b) after the amplification factors were adjusted. The color code of the spectrum corresponds to the color code of the BGO crystals arranged around an MINIBALL triple (back side view). The grey circles mark the PMT positions on each crystal.

energy resolution were improved and, thus, the energy threshold could be lowered below 20 keV. Figure 101 (Right) illustrates that after gain matching the X-ray from  $^{137}\text{Ba}$  is fully present in the recorded  $\gamma$ -ray spectrum, whereas without gain matching the left tail of the peak is cut off by the threshold. A lower threshold is limited by the electronic noise. Thus, the detection efficiency is enhanced for the gain matched setup. In general, this effect can dramatically downgrade the performance of an ESS system.

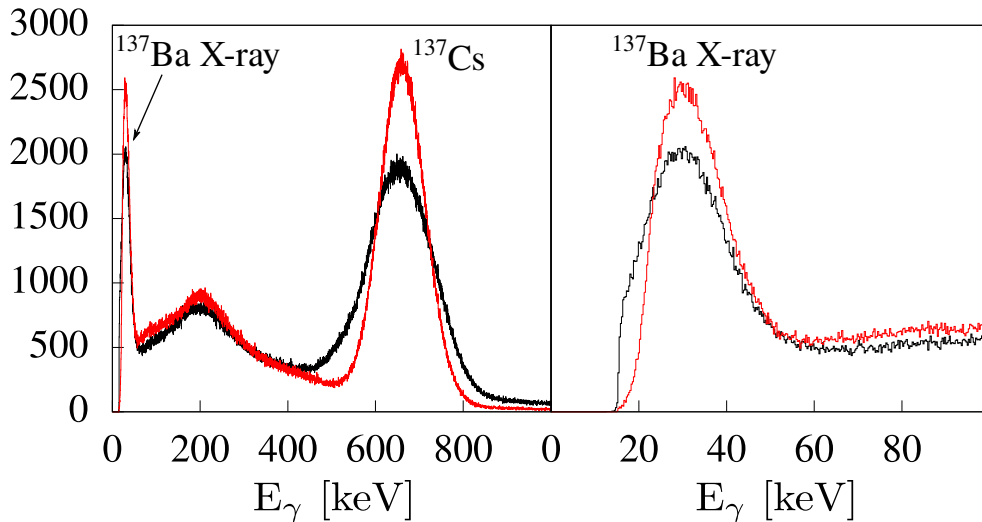


**Figure 101:**  $^{137}\text{Cs}$  source measurements recorded with a merged BGO subsystem signals, before (black) and after (red) gain matching.

The alignment box was specially produced to improve the performance of the new BGO prototype. For a final experimental setup the alignment and impedance conversion will be managed in a different way, as it is inconvenient to employ an alignment box for each ESS detector. The final solution will depend on the used electronics. However, the current study illustrated the need for individual HV supplies to power each single PMT in order to perform the gain matching.

### 10.2.2. Electronics

The six signals, three from the HPGe crystals and three from each BGO sub-system, are recorded with digital electronics, i.e. Digital Gamma Finder (DGF) Pixie-16 modules from XIA<sup>TM</sup>. These modules offer a 100 MHz sampling rate by using 12 bit analog-to-digital converter (ADC), which correspond to a 10 ns sampling rate. The four on-board Field-Programmable Gate Arrays (FPGAs) per module ensure the data acquisition of up to 16 simultaneously incoming unshaped analog preamplifier signals and record for each channel the energy, time and waveform information needed for the data analysis. The data acquisition is managed by a UNIX-based computer, linked to the PXI/PCI bridge controller from National Instruments<sup>TM</sup>, which allows for a 109 MB/s bandwidth connection between the PXI chassis and the computer. A detailed description of the Pixie-16 readout and trigger logic is available in reference [172].

The implemented firmware of the Pixie-16 modules allows to operate this detection system in two ways. The first one is a “free run” mode, which treats all signals individually and generate a trigger for each input signal. For each event detected in either the HPGe channel or BGO channel the time and energy information is stored within a buffer and later is written to disk. The second operational mode is the “coincidence mode”, which uses the HPGe crystals as a valid trigger. Accordingly, if a trigger is injected by the HPGe crystals all remaining channels are simultaneously written into the buffer within a time window of 1.2  $\mu$ s before (0.6  $\mu$ s) and after (0.6  $\mu$ s) the HPGe trigger. The timestamp corresponding to the triggering HPGe crystal is assigned to all channels. For this operational mode two Pixie-16 modules are required as one is set as the trigger module and a second one only for readout. This mode allows to focus on significant events and minimize the dead time of the recording system by limiting the count rate to the HPGe crystals. The Compton-suppression is consecutively performed by a sorting algorithm as a function of the proper conditions for energy and time information.

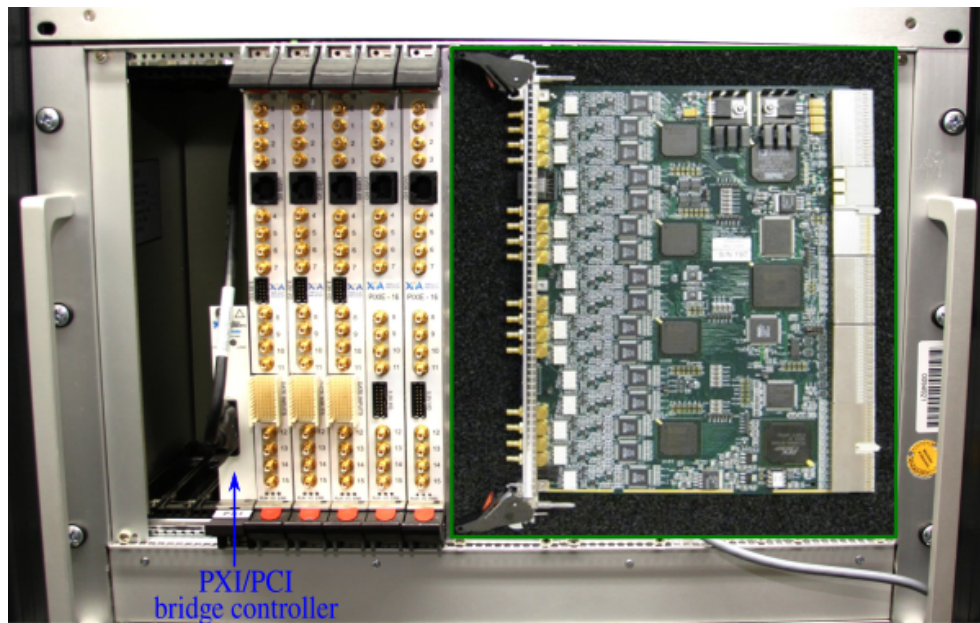


**Figure 102:** Pixie-16 modules of the electronic setup within the Pixie chassis. On the left side the connection module to the computer system is placed. The inset illustrates a side view of one Pixie-16 module.

## 11. Performance measurements with the ESS prototype

### 11.1. Escape-suppression shield

As a first step, all properties of the stand-alone BGO shield were measured. The optical shielding, energy resolution and noise level were investigated, as these properties are indicators for the quality of the crystal homogeneity, surface reflection grade and optical connection of the PMTs. The quality of the optical shielding was inspected by illuminating the BGO shield from outside with a light source (LED flashlight). No effect was observed neither on the count rates nor on the resulting  $^{137}\text{Cs}$  spectra. The energy resolution and the

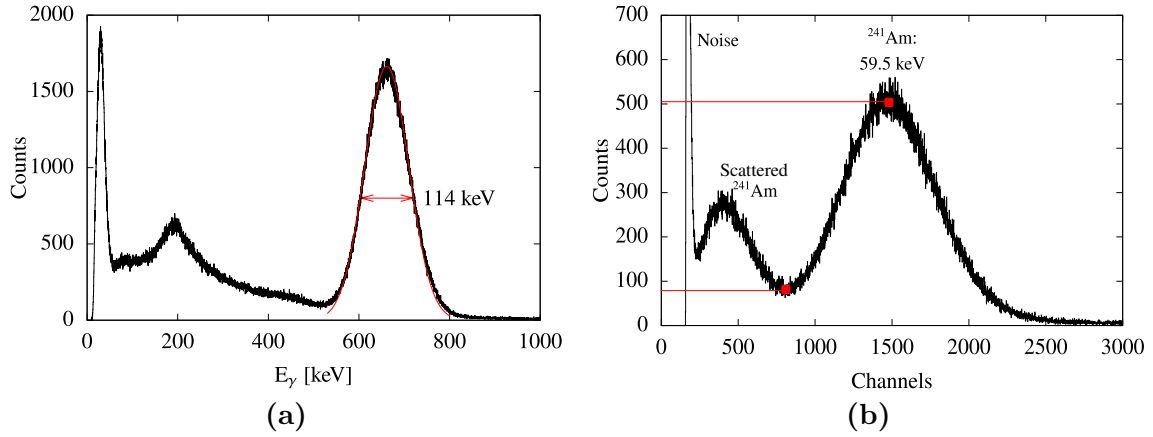


**Figure 103:** (a)  $^{137}\text{Cs}$   $\gamma$ -ray spectrum measured with one BGO crystals covered by two PMTs. The relative energy resolution at 662 keV amounts to 17.3%. (b)  $^{241}\text{Am}$  spectrum measured with a crystal equipped with one PMT. The peak-to-valley ratio amounts to 6.4. The used peak maximum and valley minimum are marked with the red squares. See text for information.

noise level were inspected with  $^{137}\text{Cs}$  and  $^{241}\text{Am}$  source measurements, respectively. For the evaluation of the noise level, the peak-to-valley ratio (peak height / valley minimum) of the 59.5 keV transition of  $^{241}\text{Am}$  was determined. It has to be taken into account, that the noise is mainly caused by the PMTs and, hence, crystals equipped with two PMTs will exhibit a lower peak-to-valley ratio than crystals with one PMT. Moreover, the peak-to-valley ratio depends on the detector-source distance, the source intensity and the background radiation. Comparison to specifications or prior measurements is only meaningful under equal measuring conditions [173]. The energy resolution was investigated for the 662 keV transition of  $^{137}\text{Cs}$ . Unlike for the peak-to-valley ratio, a larger crystal coverage yields an

enhanced energy resolution. The  $\gamma$ -ray spectra were recorded for all 12 BGO crystals via the alignment box, a main amplifier followed by a MCA. In Figure 103 examples of two spectra are illustrated, which were measured with one BGO crystal equipped with two PMTs. The relative energy resolutions and peak-to-valley ratios for the BGO crystals are summarized in Table 6. The X-ray energy at 32.4 keV, measured with the  $^{137}\text{Cs}$  source, can be observed above the noise level for all BGO crystals. Thus, the low-energy threshold is very low around 20 keV. The crystal homogeneity and surface reflection grade quality were tested by collimated source measurements with  $^{137}\text{Cs}$ . The energy resolution was measured as a function of the irradiation position. The energy resolution for crystal A2 varied between 16.1% irradiating close to the PMTs up to 19.4% by an irradiation at the opposite side of the PMTs. This indicates a good reflection quality and crystal homogeneity.

**Table 6.:** Relative energy resolution and peak-to-valley for all BGO crystals

Crystal	# PMT	$\Delta E$ at 662 keV [%]	Peak-to-valley
A1	1	19.3	6.4
A2	2	17.3	3.4
A3	2	16.9	3.1
A4	1	18.3	6.1
B1	1	19.0	6.7
B2	2	16.6	2.9
B3	2	17.5	3.6
B4	1	18.9	6.5
C1	1	19.1	5.9
C2	2	17.5	3.6
C3	2	17.1	3.1
C4	1	18.7	6.4

To classify the results obtained for the energy resolution and the noise level, both quantities are compared to values achieved with the EUROBALL BGO system. The peak-to-valley ratios measured with the EUROBALL BGO are between 18 and 34 [173]. However, these results are strongly dependent on the measuring setup and background and, thus, a comparison is not feasible due to the different parameters of both detector systems. Relative energy resolutions benchmarked with the EUROBALL BGO shield are between 16% and 23% [173]. As mentioned before, the deviation of the determined values is originating from the different BGO crystal shapes and the crystal coverage by the PMTs. The MINIBALL BGO shield prototype exhibit similar energy resolution values like the escape-suppression shield operating successfully for many year with the EUROBALL spectrometer. In addition a low-energy threshold of around 20 keV is achieved, which demonstrates the low noise level of the system.

---

## 11.2. MINIBALL escape-suppression detector

For the first performance tests of the combined detection systems, the measurements were done with a  $^{60}\text{Co}$  source with a detector-source distance of 12 cm. The peak-to-total ratio was measured with two different data acquisition modes, the “coincidence mode” and the free run mode.

### 11.2.1. Coincidence mode

In the coincidence mode data is only recorded, if a trigger is caused after a signal is recorded by one of the three HPGe crystals. Subsequently all channels, within the time range of 600 ns before and 600 ns after the trigger signal, are simultaneously stored in the buffer. Thus, only relevant events are recorded and events with no interaction in the germanium detectors are ignored. The advantage of this technique is the reduced data size and shorter dead time of the data acquisition system, due to the restricted BGO count rate. The custom firmware assigns one timestamp, generated by the triggering channel, to all channels within this event. As only one timestamp is available for all channels within the time window of  $\pm 0.6 \mu\text{s}$  (one event), this data acquisition technique prohibits a time correlation within this generated event, which could potentially increase the rate of random coincidences.

To minimize the rate of random coincidences a low-intensity  $^{60}\text{Co}$  source (3.87(12) kBq) was used. The amount of random coincidences is given by,

$$N_{\text{coin}}^{\text{random}} = 2\Delta t_{\text{rec}} N_{\text{HPGe}} N_{\text{BGO}}, \quad (11.1)$$

with the coincidence window  $\Delta t_{\text{rec}}$  [174].  $N_{\text{HPGe}}$  and  $N_{\text{BGO}}$  are the count rates of the MINIBALL and ESS detector, respectively. The count rate of the MINIBALL triple cluster detector was around 800 Hz, whereas the count rate of the BGO shield amounted to 2 kHz. The coincidence window was limited by the custom firmware to  $\pm 0.6 \mu\text{s}$ . The amount of random coincidences were less than 0.5%, which is negligible. Figure 104 (black) presents the measured  $^{60}\text{Co}$  spectrum after add-back. For the add-back routine coincident  $\gamma$  rays within one triple cluster detector within a prompt time window are assumed to originate from one Compton-scattered  $\gamma$  ray between the germanium detectors and are added up.

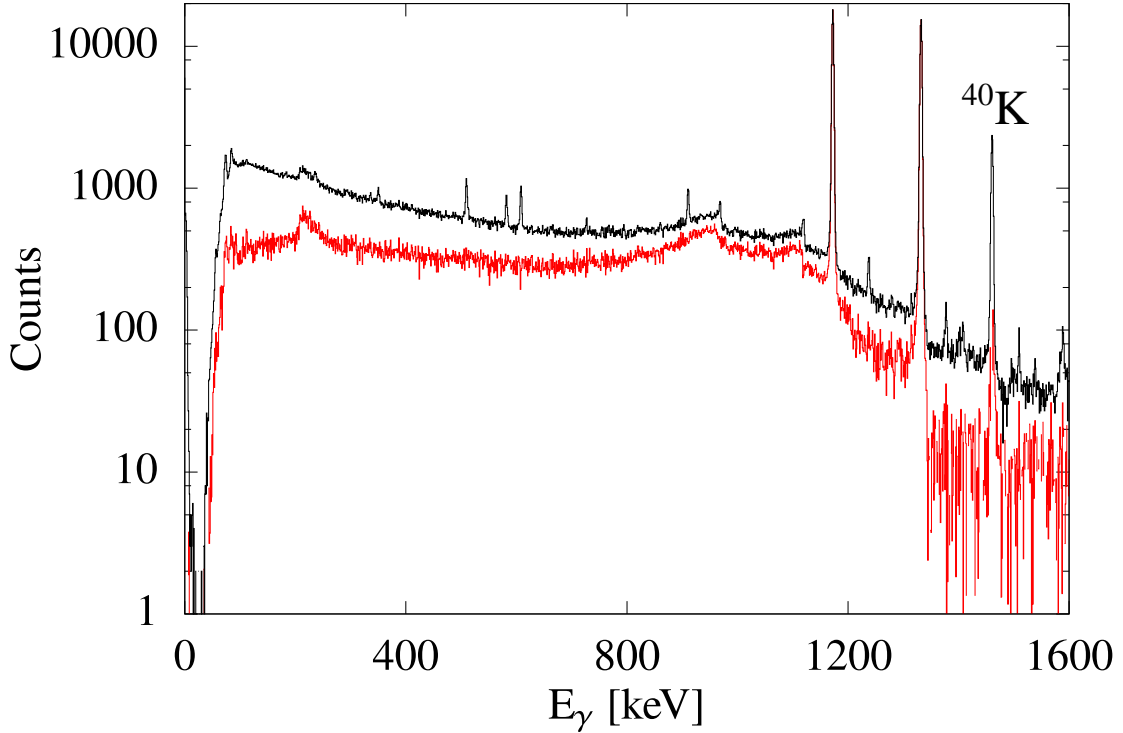


**Figure 104:** Source measurement with the prototype escape-suppression detector. The black curve illustrates the measured  $\gamma$ -ray spectrum without background subtraction and without Compton suppression. The red curve shows the recorded  $\gamma$ -ray spectrum without Compton-suppression but with background subtraction.

Due to the low intensity of the  $^{60}\text{Co}$  source and the fact that the GEANT4 simulation does not include background radiation, a background subtraction is required to obtain a comparable spectrum with the simulation. The background subtracted  $\gamma$ -ray spectrum without Compton-suppression is shown in Fig. 104 (red curve). The peak-to-total ratio with mounted BGO shield and without Compton-suppression amounts to 26.3%.

The functionality of the combined escape-suppression detection system is verified via correlations between the germanium detectors and the BGO shield. The  $\gamma\gamma$  matrix presented in Figure 105 (b) illustrates the energy deposition in the MINIBALL triple cluster detector as a function of the detected energy in the BGO shield (BGO energy uncalibrated). Diagonal lines correspond to Compton-scattered  $\gamma$ -rays between both detectors.



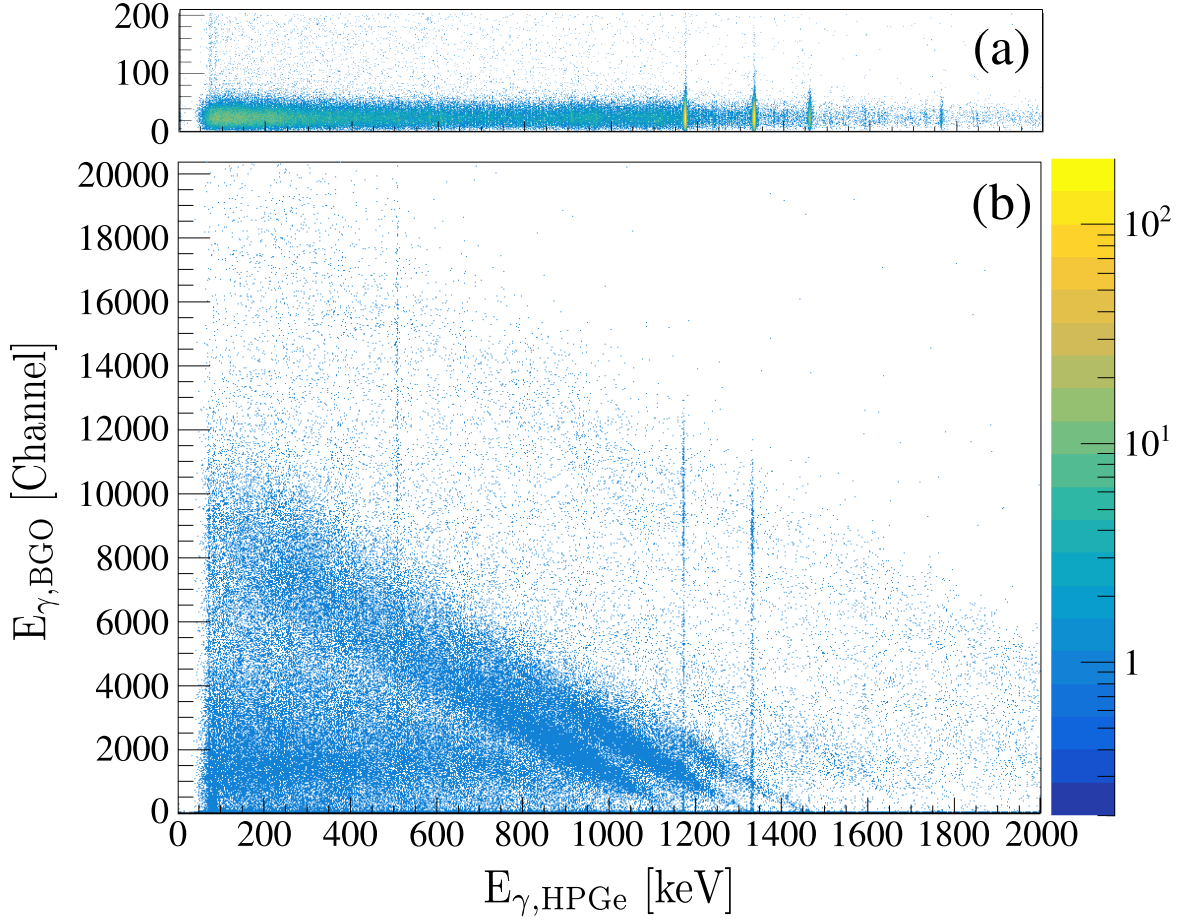


**Figure 105:** (a) Zoom in spectrum (b) up to BGO channel 200 to visualize events in the germanium, which will not be vetoed by the BGO Compton suppression. (b) Energy correlation spectrum between the MINIBALL germanium and the BGO crystals.

The broadening of the diagonal lines is caused by the different energy resolutions of both systems. Vertical lines originate from random and real coincidences of the emitted  $\gamma$  rays. In the present case the calculated amount of random coincidences is small. Therefore, the vertical lines are originating from the source multiplicity of  $M_\gamma = 2$ . One  $\gamma$  ray is fully detected in the MINIBALL triple detector, whereas the second  $\gamma$  ray is completely or partially detected in the BGO crystals. The heavy-met is not optimized for detector-source distances of 12 cm and, hence, allow a direct irradiation of the BGO shield. This was verified via collimated  $^{60}\text{Co}$  source measurements with a comparable count rate in both detectors. The  $\gamma\gamma$  matrix of the collimated measurement is presented in Figure 106. The diagonal lines as well as the vertical 511 keV (background) line are still present in the two dimensional spectrum, whereas the vertical lines of  $^{60}\text{Co}$  disappear. Due to the

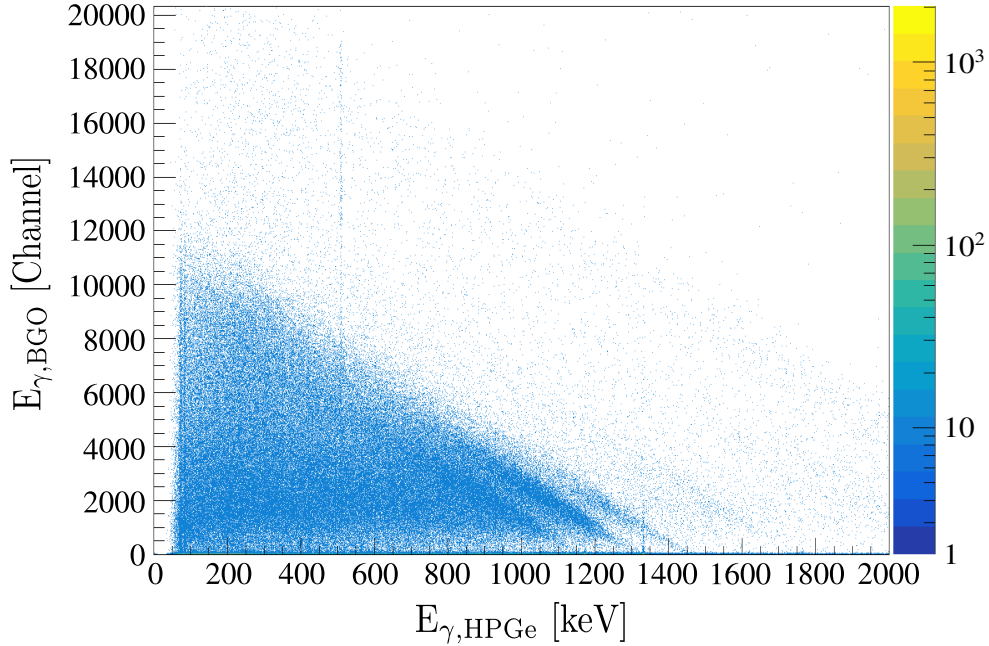


**Figure 106:** Energy correlation spectrum, recorded with a collimated  $^{60}\text{Co}$  between the MINIBALL germanium crystals with add-back and the ancillary BGO crystals. More details can be found in the text.

collimation of the source the amount of real coincidences were reduced, by decreasing the solid angle for both  $\gamma$  rays reaching the detectors. Furthermore, only one germanium crystal was irradiated by the collimation measurement. This implies, if both  $\gamma$  rays reach the MINIBALL triple cluster the detected energy in the germanium can vary between the full energy of each  $\gamma$  ray up to the sum of both  $\gamma$ -ray energies. Moreover, a direct irradiation of the BGO crystals is not possible. This confirms that the true coincidences arise from the source multiplicity and cannot be rejected by Compton-suppression.

The remaining part of the two dimensional spectrum arise from random coincidences and Compton-scattered  $\gamma$  rays which are not fully absorbed in the BGO crystals. These components can be eliminated from the spectrum via the Compton-suppression algorithm. Events which are not detected by the BGO shield are composed out of two contributions and illustrated in Figure 105 (a). The first one are events which are Compton scattered in the HPGe crystals and escape the germanium at the unshielded sides of the triple cluster. The second contribution are events with full energy deposition in the triple cluster, either  $\gamma$  rays from the source or from background radiation. These events will not be affected by the Compton-suppression. If the BGO channel number is greater 100, which correspond

to an energy deposition of  $> 20$  keV in the BGO crystals, the corresponding event is rejected from the HPGe  $\gamma$ -ray spectrum. Events with less than 20 keV energy deposition in the BGO shield are not rejected. This procedure improves the peak-to-total ratio by eliminating a large amount of Compton-scattered  $\gamma$  rays leaving the HPGe crystals and contributing to the Compton background in the  $\gamma$ -ray spectrum of the HPGe detectors.

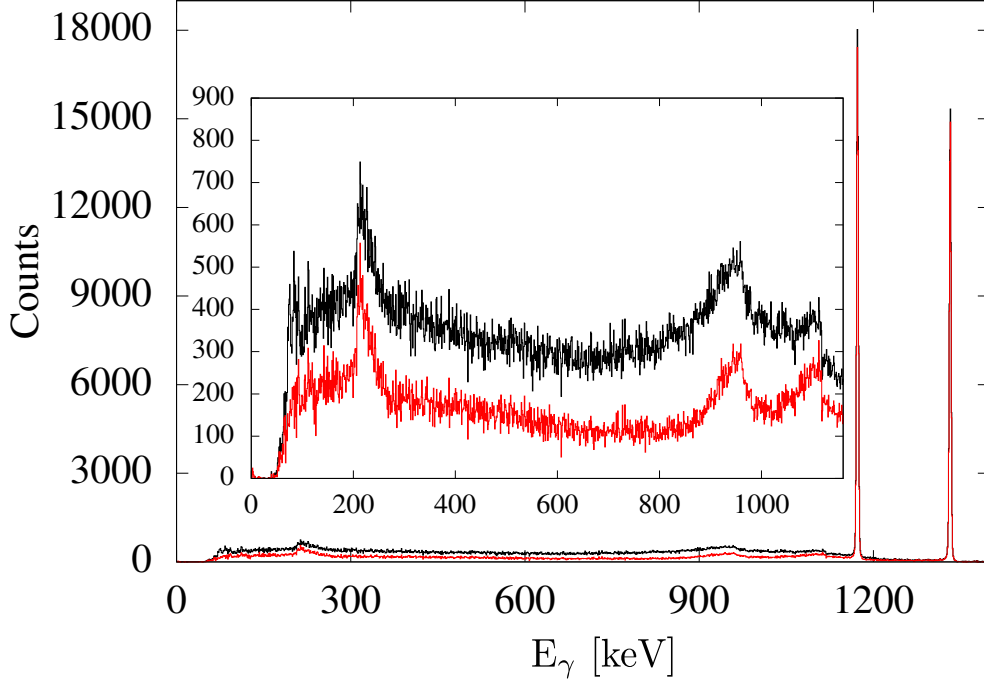


**Figure 107:**  $\gamma$ -ray spectrum without (black) and with (red) Compton suppression. The inset shows the Compton continuum of the same spectrum.

The final  $\gamma$ -ray spectra in add-back mode before (black) and after (red) the BGO veto are illustrated in Figure 107. The resulting peak-to-total ratio after background subtraction and Compton suppression amounts to 40.9(1)%.

### 11.2.2. Free run mode

The second approach for the determination of the peak-to-total ratio is the free run mode, which operates with the identical setup and source as before. The only difference is the new implemented firmware, which facilitate triggering for each channel independently. Each channel will generate an own trigger and store the recorded information immediately in the buffer. The downside is the higher BGO count rate which will result in a large amount of unnecessary data that is written to disk. The advantage is the possibility of time correlations between single detectors. For the optimization of the sorting and veto

algorithm a pre-processing (event building) of the recorded data is performed. Hits in HPGe and BGO channels within a time window of 1.2  $\mu\text{s}$  are combined and are part of one event.

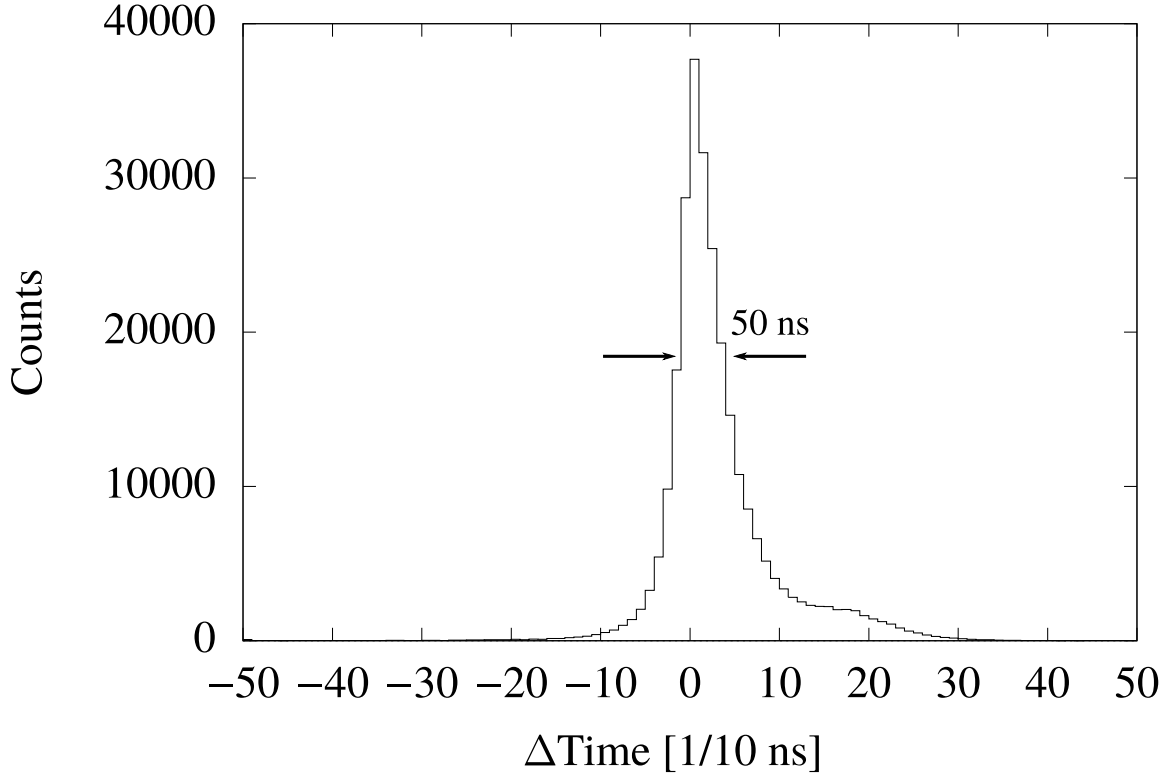


**Figure 108:** Time difference spectrum between one HPGe crystal and the surrounding BGO sub-system. The time is shown in tics with 10 ns per tic.

Time correlation spectra between each HPGe crystal and each BGO subsystem are created. Figure 108 illustrates the time correlation between one HPGe crystal and the surrounding BGO subsystem. Timestamps are generated by a Leading Edge Trigger (LET), as no Constant Fraction Discriminator (CFD) is available for the Pixie-16 modules as part of the firmware. The time resolution originates predominantly from the walk effect, the energy dependence of the timing signal for a LET, in both detection systems. On one hand the walk is induced by the rising edge of the germanium crystals, which strongly depends on the interaction position within the HPGe material [106]. On the other hand, the leading edge trigger generates a walk in both systems induced by different pulse amplitudes (energy deposition). However, a prompt peak around 10 ns with a time resolution of 50 ns can be observed. The peak structure contains a right tail and plateau. This right plateau is caused by the walk and jitter effect of the leading edge trigger for low-energy events detected inside

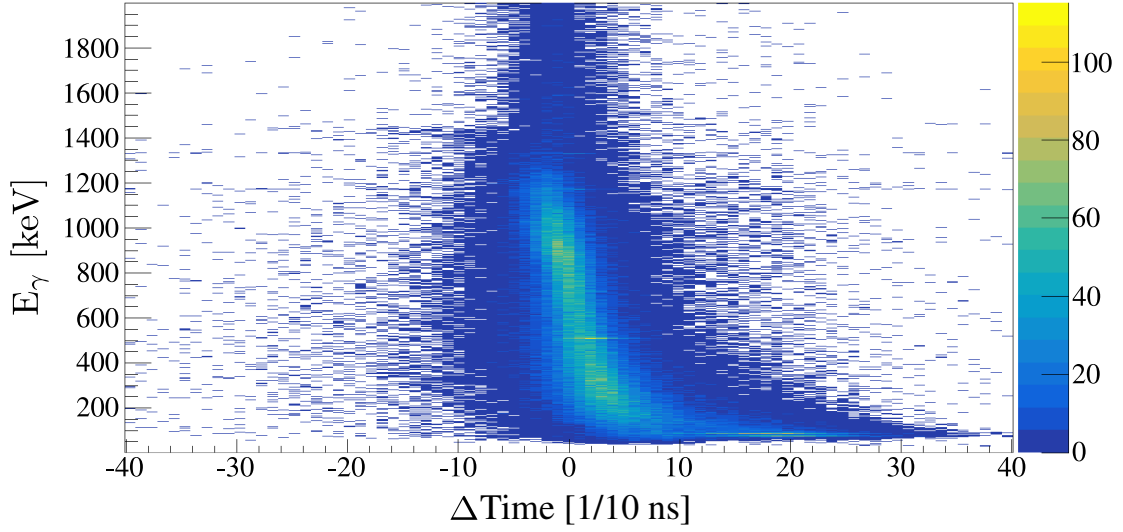


**Figure 109:**  $\gamma$ -ray energy detected in one germanium crystal as a function of the time difference between the one germanium time signal and BGO time signal.

the germanium crystals. This is illustrated in Figure 109, where the germanium energy is plotted as a function of the time difference between the germanium and BGO crystal. A shift to larger time differences is observed for low-energy events in the germanium detector. The small pulse amplitudes of the low-energy signals are later detected by the leading edge trigger and, therefore, cause a bigger time difference between BGO and germanium crystals.

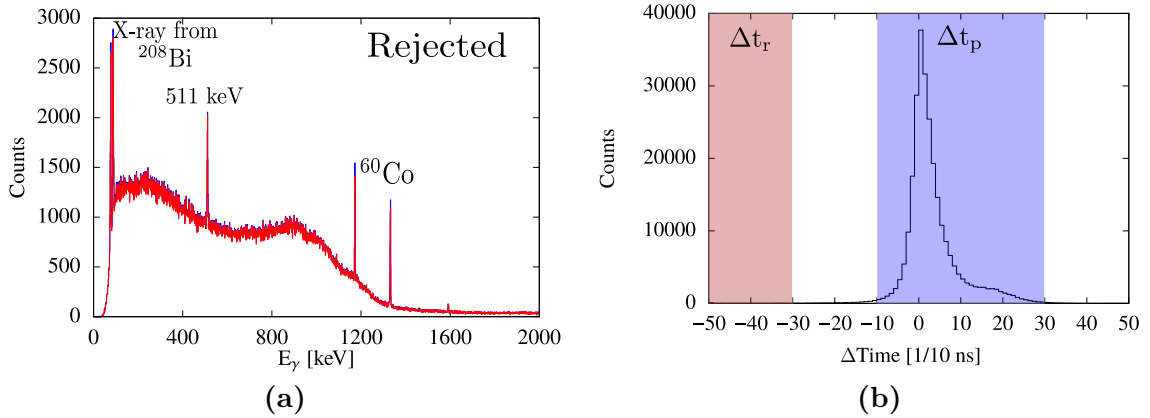


**Figure 110:** (a) Rejected  $\gamma$ -ray spectrum after Compton suppression without restrictive timing cuts (blue) and with  $\Delta t_p - 2\Delta t_r$  (red). (b) Applied prompt  $\Delta t_p$  and random  $\Delta t_r$  time windows for timing in (a).

To verify the impact of random coincidences, the rejected  $\gamma$ -ray spectrum (spectrum of rejected  $\gamma$  rays) without any timing conditions is compared with a prompt minus random

rejected  $\gamma$ -ray spectrum. The result is illustrated in Figure 110. The two  $^{60}\text{Co}$  peaks in the rejected spectrum are caused by real coincidences originating from the source multiplicity and can not be reduced by timing cuts. In the present measurement random coincidences are very rare and have no influence on the resulting peak-to-total ratio, as the count rates in both detectors are low. Nevertheless, in future experiments where typical count rates of 5-10 kHz in the germanium crystals are expected, timing will be an important tool to optimize the Compton suppression.

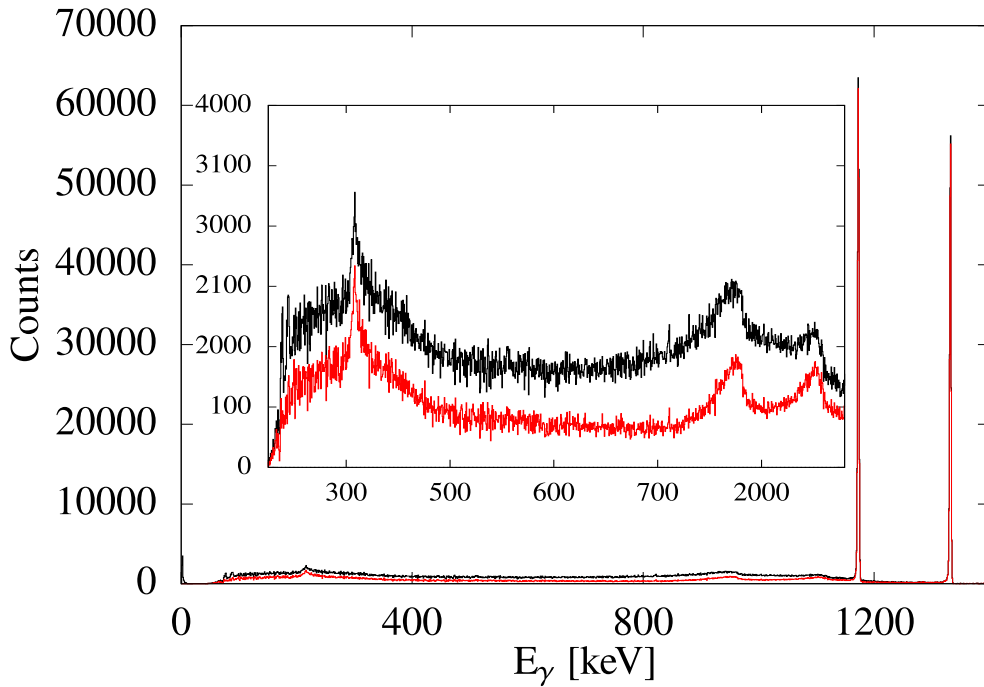


**Figure 111:** Final  $\gamma$ -ray spectra before (black) and after (red) Compton suppression in free run mode.

The final  $\gamma$ -ray spectra for the HPGe crystals in the add-back mode are presented in Figure 111. The obtained peak-to-total ratio amounts to 25.9(1)% before and 39.2(1)% after the Compton suppression.

### 11.3. Summary and Outlook

The investigation of the stand-alone Compton-suppression shield yielded a comparable performance (energy resolution) as the EUROBALL escape-suppression shield. This demonstrates that the crystal quality as well as the complete detector properties are adapted for fast-veto escape-suppression of MINIBALL. For the investigation of the MINIBALL BGO prototype a special gain alignment box was constructed in cooperation with the mechanical workshop of the IPK Cologne, to assure proper signal processing and improve the BGO efficiency. Results of GEANT4 simulations with a  $^{60}\text{Co}$  source at a detector-source distance of 12 cm and no background radiation yielded a peak-to-total value of 44%. The results from Paragraph 11 are close to reproduce the simulated values. The experimental peak-to-total values were 39.2% and 40.9% for two different measuring modes. This is in reasonable agreement with the expected value obtained by the simulation. The small deviations can be explained by the missing details of the GEANT4 simulation, e.g. the energy threshold for the escape-suppression detector, the missing BGO crystal housing, the deviation between the simulated and manufactured ESS geometry or the missing laboratory equipment (scattering volume, PMTs). In addition, it seems that the GEANT4 simulation underestimates the real coincidences originating from the source multiplicity. However, the achieved result for the peak-to-total value is an improvement of almost a factor of 1.6. Thus, the new escape-suppression detector system provides a clear improvement for future experiments with nuclear reactions in combination with higher  $\gamma$ -ray multiplicities. On one hand, the peak-to-total ratio is improved by a logic fast-veto. On the other hand, contributions from background radiation is reduced by shielding the MINIBALL HPGe triple detectors from outside radiation. Thus, the prototype performance is satisfactory and ready for series production after a successful funding approval.





## Bibliography

- [1] Otto Haxel; J. Hans D. Jensen; Hans E. Suess. “On the ‘Magic Numbers’ in Nuclear Structure.” In: *Phys. Rev.* 75 (11 June 1949), pp. 1766–1766 (cit. on pp. 11, 15).
- [2] Maria G. Mayer. “On Closed Shells in Nuclei.” In: *Phys. Rev.* 74 (3 Aug. 1948), pp. 235–239 (cit. on pp. 11, 15).
- [3] Meng Wang; G. Audi; F.G. Kondev; W.J. Huang; S. Naimi; Xing Xu. “The AME2016 atomic mass evaluation (II). Tables, graphs and references.” In: *Chinese Phys. C* 41.3 (2017), p. 030003 (cit. on pp. 12, 18).
- [4] B. Pritychenko; M. Birch; B. Singh; M. Horoi. “Tables of E2 transition probabilities from the first states in even–even nuclei.” In: *At. Data. Nucl. Data Tables* 107 (2016), pp. 1–139 (cit. on pp. 13, 22, 35, 37).
- [5] M. Moinester; J. P. Schiffer; W. P. Alford. “Multipole Analysis of Particle-Particle or Particle-Hole Multiplets.” In: *Phys. Rev.* 185 (4 Sept. 1969), pp. 1598–1598 (cit. on p. 15).
- [6] O. Sorlin; M.-G. Porquet. “Nuclear magic numbers: New features far from stability.” In: *Prog. Part. Nucl. Phys.* 61.2 (2008), pp. 602–673 (cit. on pp. 15, 34–36).
- [7] Takaharu Otsuka; Michio Honma; Daisuke Abe. “Effects of Spin-Isospin-Interactions on Nuclear Collective Motion.” In: *Nucl. Phys. A* 788.1 (2007). Proceedings of the 2nd International Conference on Collective Motion in Nuclei under Extreme Conditions, pp. 3–11 (cit. on p. 15).
- [8] Maria Goeppert Mayer. “Nuclear Configurations in the Spin-Orbit Coupling Model. I. Empirical Evidence.” In: *Phys. Rev.* 78 (1 Apr. 1950), pp. 16–21 (cit. on p. 15).
- [9] R.F. Casten. *Nuclear Structure from a Simple Perspective*. Oxford University Press, New York Oxford, 1990 (cit. on pp. 16, 20–21, 24–25).
- [10] Takaharu Otsuka; Rintaro Fujimoto; Yutaka Utsuno; B. Alex Brown; Michio Honma; Takahiro Mizusaki. “Magic Numbers in Exotic Nuclei and Spin-Isospin Properties of the  $NN$  Interaction.” In: *Phys. Rev. Lett.* 87 (8 Aug. 2001), p. 082502 (cit. on p. 15).
- [11] T. Otsuka; Y. Utsuno; R. Fujimoto; B.A. Brown; M. Honma; T. Mizusaki. “Frontiers and challenges of nuclear shell model.” In: *Eur. Phys. J. A* 13.1 (2002), pp. 69–74 (cit. on p. 15).

- [12] T. Otsuka; Y. Utsuno; R. Fujimoto; B.A. Brown; M. Honma; T. Mizusaki. “Frontiers and challenges of nuclear shell model.” In: *Eur. Phys. J. A* 15.1 (2002), pp. 151–155 (cit. on p. 15).
- [13] R. Kanungo; C. Nociforo; A. Prochazka; T. Aumann; D. Boutin; D. Cortina-Gil; B. Davids; M. Diakaki; F. Farinon; H. Geissel; R. Gernhäuser; J. Gerl; R. Janik; B. Jonson; B. Kindler; R. Knöbel; R. Krücken; M. Lantz; H. Lenske; Y. Litvinov; B. Lommel; K. Mahata; P. Maierbeck; A. Musumarra; T. Nilsson; T. Otsuka; C. Perro; C. Scheidenberger; B. Sitar; P. Strmen; B. Sun; I. Szarka; I. Tanihata; Y. Utsuno; H. Weick; M. Winkler. “One-Neutron Removal Measurement Reveals  $^{24}\text{O}$  as a New Doubly Magic Nucleus.” In: *Phys. Rev. Lett.* 102 (15 Apr. 2009), p. 152501 (cit. on p. 15).
- [14] N.J. Stone. “Table of nuclear electric quadrupole moments.” In: *At. Data. Nucl. Data Tables* 111 (2016), pp. 1–28 (cit. on p. 19).
- [15] A. Ozawa; T. Kobayashi; T. Suzuki; K. Yoshida; I. Tanihata. “New Magic Number,  $N = 16$ , near the Neutron Drip Line.” In: *Phys. Rev. Lett.* 84 (24 June 2000), pp. 5493–5495 (cit. on p. 19).
- [16] Rituparna Kanungo; I Tanihata; A Ozawa. “Observation of new neutron and proton magic numbers.” In: *Phys. Lett. B* 528.1 (2002), pp. 58–64 (cit. on p. 19).
- [17] R. Kanungo. “Shell closures in the  $N$  and  $Z = 40 - 60$  region for neutron and proton-rich nuclei.” In: *Phys. Lett. B* 649.1 (2007), pp. 31–34 (cit. on p. 19).
- [18] K. Alder; A. Bohr; T. Huus; B. Mottelson; A. Winther. “Study of Nuclear Structure by Electromagnetic Excitation with Accelerated Ions.” In: *Rev. Mod. Phys.* 28 (4 Oct. 1956), pp. 432–542 (cit. on pp. 20, 22–24, 27–28).
- [19] K. Alder; A. Winther. *Electromagnetic Excitation - Theorie of Coulomb Excitation with Heavy Ions*. North-Holland Publishing Company, Amsterdam Oxford, 1975 (cit. on pp. 20, 24, 28).
- [20] W.D. Hamilton. *The Electromagnetic Interaction in Nuclear Spectroscopy*. North-Holland Publishing Company, Amsterdam Oxford, 1975 (cit. on pp. 20, 22).
- [21] W. Nörenberg; H.A. Weidenmüller. *Introduction to the Theory of Heavy-ion Collisions*. Springer-Verlag, Berlin Heidelberg GmbH, 1976 (cit. on pp. 20, 25–26, 28).
- [22] D. Cline. “Nuclear Shapes Studied by Coulomb Excitation.” In: *Ann. Rev. Nucl. Part. Sci.* 36.1 (1986), pp. 683–716 (cit. on pp. 20, 30, 39, 87).

- 
- [23] D. Cline; T. Czosnyka; A.B. Hayes; P. Napiorkowski; N. Warr; C.Y. Wu. GOSIA user manual for simulation and analysis of Coulomb excitation experiments. Rochester, NY, US, 2012. 304 pp. January 25, 2012 (cit. on pp. 23, 31, 115).
- [24] M. Zielińska; L. P. Gaffney; K. Wrzosek-Lipska; E. Clément; T. Grahn; N. Kesteloot; P. Napiorkowski; J. Pakarinen; P. Van Duppen; N. Warr. “Analysis methods of safe Coulomb-excitation experiments with radioactive ion beams using the GOSIA code.” In: *Eur. Phys. J. A* 52.4 (Apr. 2016), p. 99 (cit. on pp. 23, 31, 115).
- [25] T. Czosnyka; D. Cline; C.Y. Wu. In: *Bull. Am. Phys. Soc.* 28 (1983), p. 745 (cit. on pp. 23, 31, 115).
- [26] M. Born; V. Fock. “Beweis des Adiabatsatzes.” In: *Zeitschrift für Physik* 51.3 (Mar. 1928), pp. 165–180 (cit. on p. 25).
- [27] K. Alder; F. Roesel; R. Morf. “Second-order quantum-mechanical theory of Coulomb excitation.” In: *Nuclear Physics A* 186.3 (1972), pp. 449–474 (cit. on p. 28).
- [28] H. Ower. “High Spin States of  $^{232}\text{Th}$ ,  $^{234}\text{U}$  and  $^{236}\text{U}$ .” PhD thesis. J.W. Goethe-University of Frankfurt a.M., 1980, unpublished (cit. on pp. 31, 114).
- [29] H. Ower; J. Gerl; H. Scheit. Multiple Coulomb Excitation Program CLX. computer code (cit. on pp. 31, 114).
- [30] J.R. Beene; R.L. Varner; C. Baktash; A. Galindo-Uribarri; C.J. Gross; J. Gomez del Campo; M.L. Halbert; P.A. Hausladen; Y. Larochelle; J.F. Liang; J. Mas; P.E. Mueller; E. Padilla-Rodal; D.C. Radford; D. Shapira; D.W. Stracener; J.-P. Urrego-Blanco; C.-H. Yu. “Coulomb excitation studies of  $^{132,134}\text{Sn}$ .” In: *Nucl. Phys. A* 746 (2004). Proceedings of the Sixth International Conference on Radioactive Nuclear Beams (RNB6), pp. 471–474 (cit. on pp. 32, 117).
- [31] L Satpathy; R C Nayak. “Study of nuclei in the drip-line regions.” In: *J. Phys. G* 24.8 (1998), p. 1527 (cit. on p. 32).
- [32] G. Audi; F.G. Kondev; Meng Wang; W.J. Huang; S. Naimi. “The NUBASE2016 evaluation of nuclear properties.” In: *Chinese Phys. C* 41.3 (2017), p. 030001 (cit. on p. 32).
- [33] E. Margaret Burbidge; G. R. Burbidge; William A. Fowler; F. Hoyle. “Synthesis of the Elements in Stars.” In: *Rev. Mod. Phys.* 29 (4 Oct. 1957), pp. 547–650 (cit. on p. 32).
-

- [34] Friedrich-Karl Thielemann; Karl-Ludwig Kratz; Bernd Pfeiffer; Thomas Rauscher; Laura van Wormer; Michael C. Wiescher. “Astrophysics and nuclei far from stability.” In: *Nucl. Phys. A* 570.1 (1994), pp. 329–343 (cit. on p. 33).
- [35] Katharina Lodders. “Solar System Abundances and Condensation Temperatures of the Elements.” In: *Astrophys. J.* 591.2 (2003), p. 1220 (cit. on p. 33).
- [36] I. Dillmann; K.-L. Kratz; A. Wöhr; O. Arndt; B. A. Brown; P. Hoff; M. Hjorth-Jensen; U. Köster; A. N. Ostrowski; B. Pfeiffer; D. Seweryniak; J. Shergur; W. B. Walters. “ $N = 82$  shell quenching of classical  $r$ -process ‘waiting-point’ nucleus  $^{130}\text{Cd}$ .” In: *Phys. Rev. Lett.* 91 (16 Oct. 2003), p. 162503 (cit. on p. 33).
- [37] K. -L. Kratz; B. Pfeiffer; O. Arndt; S. Hennrich; A. Wöhr; t. ISOLDE/IS333; IS393 Collaborations. “ $r$ -process isotopes in the  $^{132}\text{Sn}$  region.” In: *Eur. Phys. J. A* 25.1 (Sept. 2005), pp. 633–638 (cit. on p. 33).
- [38] K. L. Jones; A. S. Adekola; D. W. Bardayan; J. C. Blackmon; K. Y. Chae; K. A. Chipps; J. A. Cizewski; L. Erikson; C. Harlin; R. Hatarik; R. Kapler; R. L. Kozub; J. F. Liang; R. Livesay; Z. Ma; B. H. Moazen; C. D. Nesaraja; F. M. Nunes; S. D. Pain; N. P. Patterson; D. Shapira; J. F. Shriner; M. S. Smith; T. P. Swan; J. S. Thomas. “The magic nature of  $^{132}\text{Sn}$  explored through the single-particle states of  $^{133}\text{Sn}$ .” In: *Nature* 465.7297 (May 2010), pp. 454–457 (cit. on pp. 34, 36).
- [39] R. L. Kozub; G. Arbanas; A. S. Adekola; D. W. Bardayan; J. C. Blackmon; K. Y. Chae; K. A. Chipps; J. A. Cizewski; L. Erikson; R. Hatarik; W. R. Hix; K. L. Jones; W. Krolas; J. F. Liang; Z. Ma; C. Matei; B. H. Moazen; C. D. Nesaraja; S. D. Pain; D. Shapira; J. F. Shriner; M. S. Smith; T. P. Swan. “Neutron Single Particle Structure in  $^{131}\text{Sn}$  and Direct Neutron Capture Cross Sections.” In: *Phys. Rev. Lett.* 109 (17 Oct. 2012), p. 172501 (cit. on p. 34).
- [40] M. Gorska; L. Caceres; H. Grawe; M. Pfützner; A. Jungclaus; S. Pietri; E. Werner-Malento; Z. Podolyak; P.H. Regan; D. Rudolph; P. Detistov; S. Lalkovski; V. Modamio; J. Walker; T. Beck; P. Bednarczyk; P. Doornenbal; H. Geissel; J. Gerl; J. Grebosz; R. Hoischen; I. Kojouharov; N. Kurz; W. Prokopowicz; H. Schaffner; H. Weick; H.-J. Wollersheim; K. Andgren; J. Benlliure; G. Benzoni; A.M. Bruce; E. Casarejos; B. Cederwall; F.C. L. Crespi; B. Hadinia; M. Hellström; G. Ilie; A. Khaplanov; M. Kmiecik; R. Kumar; A. Maj; S. Mandal; F. Montes; S. Myalski; G.S. Simpson; S.J. Steer; S. Tashenov; O. Wieland; Zs. Dombradi; P. Reiter; D. Sohler. “Evolution of the  $N = 82$  shell gap below  $^{132}\text{Sn}$  inferred from core excited states in  $^{131}\text{In}$ .” In: *Phys. Lett. B* 672.4 (2009), pp. 313–316 (cit. on p. 34).
- [41] G. Bocchi; S. Leoni; B. Fornal; G. Colo; P.F. Bortignon; S. Bottoni; A. Bracco; C. Michelagnoli; D. Bazzacco; A. Blanc; G. de France; M. Jentschel; U. Köster; P. Mutti; J.-M. Regis; G. Simpson; T. Soldner; C.A. Ur; W. Urban; L.M. Fraile;

- R. Lozeva; B. Belvito; G. Benzoni; A. Bruce; R. Carroll; N. Cieplicka-Orynczak; F.C.L. Crespi; F. Didierjean; J. Jolie; W. Korten; T. Kröll; S. Lalkovski; H. Mach; N. Marginean; B. Melon; D. Mengoni; B. Million; A. Nannini; D. Napoli; B. Olaizola; V. Pazy; Zs. Podolyak; P.H. Regan; N. Saed-Samii; B. Szpak; V. Vedia. “The mutable nature of particle-core excitations with spin in the one-valence-proton nucleus  $^{133}\text{Sb}$ .” In: *Phys. Lett. B* 760 (2016), pp. 273–278 (cit. on pp. 34, 120).
- [42] A. Banu; J. Gerl; C. Fahlander; M. Górska; H. Grawe; T. R. Saito; H.-J. Wollersheim; E. Caurier; T. Engeland; A. Gniady; M. Hjorth-Jensen; F. Nowacki; T. Beck; F. Becker; P. Bednarczyk; M. A. Bentley; A. Bürger; F. Cristancho; G. de Angelis; Zs. Dombrádi; P. Doornenbal; H. Geissel; J. Grebosz; G. Hammond; M. Hellström; J. Jolie; I. Kojouharov; N. Kurz; R. Lozeva; S. Mandal; N. Marginean; S. Muralithar; J. Nyberg; J. Pochodzalla; W. Prokopowicz; P. Reiter; D. Rudolph; C. Rusu; N. Saito; H. Schaffner; D. Sohler; H. Weick; C. Wheldon; M. Winkler. “ $^{108}\text{Sn}$  studied with intermediate-energy Coulomb excitation.” In: *Phys. Rev. C* 72 (6 Dec. 2005), p. 061305 (cit. on pp. 35–36).
- [43] D.C. Radford; C. Baktash; C.J. Barton; J. Batchelder; J.R. Beene; C.R. Bingham; M.A. Caprio; M. Danchev; B. Fuentes; A. Galindo-Uribarri; J. Gomez del Campo; C.J. Gross; M.L. Halbert; D.J. Hartley; P. Hausladen; J.K. Hwang; W. Krolas; Y. Larochele; J.F. Liang; P.E. Mueller; E. Padilla; J. Pavan; A. Piechaczek; D. Shapira; D.W. Stracener; R.L. Varner; A. Woehr; C.-H. Yu; N.V. Zamfir. “Coulomb excitation and transfer reactions with rare neutron-rich isotopes.” In: *Nucl. Phys. A* 752 (2005). Proceedings of the 22nd International Nuclear Physics Conference (Part 2), pp. 264–272 (cit. on pp. 35–36, 39–40, 117).
- [44] Varner, R. L.; Beene, J. R.; Baktash, C.; Galindo-Uribarri, A.; Gross, C. J.; Gomez del Campo, J.; Halbert, M. L.; Hausladen, P. A.; Larochele, Y.; Liang, J. F.; Mas, J.; Mueller, P. E.; Padilla-Rodal, E.; Radford, D. C.; Shapira, D.; Stracener, D. W.; Urrego-Blanco, J. -P.; Yu, C. -H. “Coulomb excitation measurements of transition strengths in the isotopes  $^{132}, ^{134}\text{Sn}$ .” In: *Eur. Phys. J. A* 25 (2005), pp. 391–394 (cit. on pp. 35, 39–40, 117).
- [45] S. Shlomo; I. Talmi. “Shell-model hamiltonians with generalized seniority eigenstates.” In: *Nucl. Phys. A* 198.1 (1972), pp. 81–108 (cit. on p. 35).
- [46] Igal Talmi. “Generalized seniority and structure of semi-magic nuclei.” In: *Nucl. Phys. A* 172.1 (1971), pp. 1–24 (cit. on p. 35).
- [47] C. Vaman; C. Andreoiu; D. Bazin; A. Becerril; B. A. Brown; C. M. Campbell; A. Chester; J. M. Cook; D. C. Dinca; A. Gade; D. Galaviz; T. Glasmacher; M. Hjorth-Jensen; M. Horoi; D. Miller; V. Moeller; W. F. Mueller; A. Schiller; K. Starosta; A. Stolz; J. R. Terry; A. Volya; V. Zelevinsky; H. Zwahlen. “ $Z = 50$  Shell Gap

- near  $^{100}\text{Sn}$  from Intermediate-Energy Coulomb Excitation in Even-Mass  $^{106-112}\text{Sn}$  Isotopes.” In: *Phys. Rev. Lett.* 99 (16 Oct. 2007), p. 162501 (cit. on p. 36).
- [48] J. Cederkäll; A. Ekström; C. Fahlander; A. M. Hurst; M. Hjorth-Jensen; F. Ames; A. Banu; P. A. Butler; T. Davinson; U. Datta Pramanik; J. Eberth; S. Franchoo; G. Georgiev; M. Górska; D. Habs; M. Huyse; O. Ivanov; J. Iwanicki; O. Kester; U. Köster; B. A. Marsh; O. Niedermaier; T. Nilsson; P. Reiter; H. Scheit; D. Schwalm; T. Sieber; G. Sletten; I. Stefanescu; J. Van de Walle; P. Van Duppen; N. Warr; D. Weisshaar; F. Wenander. “Sub-Barrier Coulomb Excitation of  $^{110}\text{Sn}$  and Its Implications for the  $^{100}\text{Sn}$  Shell Closure.” In: *Phys. Rev. Lett.* 98 (17 Apr. 2007), p. 172501 (cit. on p. 36).
- [49] J. N. Orce; S. N. Choudry; B. Crider; E. Elhami; S. Mukhopadhyay; M. Scheck; M. T. McEllistrem; S. W. Yates. “ $2_1^+ \rightarrow 0_1^+$  transition strengths in Sn nuclei.” In: *Phys. Rev. C* 76 (2 Aug. 2007), p. 021302 (cit. on p. 36).
- [50] N.-G. Jonsson; A. Bäcklin; J. Kantele; R. Julin; M. Luontama; A. Passoja. “Collective states in even Sn nuclei.” In: *Nucl. Phys. A* 371.2 (1981), pp. 333–348 (cit. on p. 36).
- [51] J. M. Allmond; A. E. Stuchbery; J. R. Beene; A. Galindo-Uribarri; J. F. Liang; E. Padilla-Rodal; D. C. Radford; R. L. Varner; A. Ayres; J. C. Batchelder; A. Bey; C. R. Bingham; M. E. Howard; K. L. Jones; B. Manning; P. E. Mueller; C. D. Nesaraja; S. D. Pain; W. A. Peters; A. Ratkiewicz; K. T. Schmitt; D. Shapira; M. S. Smith; N. J. Stone; D. W. Stracener; C.-H. Yu. “Double-Magic Nature of  $^{132}\text{Sn}$  and  $^{208}\text{Pb}$  through Lifetime and Cross-Section Measurements.” In: *Phys. Rev. Lett.* 112 (17 Apr. 2014), p. 172701 (cit. on p. 36).
- [52] W. J. Vermeer; M. T. Esat; J. A. Kuehner; R. H. Spear; A. M. Baxter; S. Hinds. “Coulomb Excitation of the 2.615 MeV ( $3^-$ ) and 4.086 MeV ( $2^+$ ) States of  $^{208}\text{Pb}$ .” In: *Aust. J. Phys.* 37 (1984), p. 123 (cit. on p. 36).
- [53] A. Ansari. “Study of the lowest  $2^+$  excitations and B(E2) transition strengths in relativistic QRPA for Sn-, and Pb-isotopes.” In: *Phys. Lett. B* 623.1 (2005), pp. 37–42 (cit. on pp. 36, 124).
- [54] B. G. Carlsson; J. Toivanen; A. Pastore. “Collective vibrational states within the fast iterative quasiparticle random-phase approximation method.” In: *Phys. Rev. C* 86 (1 July 2012), p. 014307 (cit. on p. 36).
- [55] J. Terasaki; J. Engel; W. Nazarewicz; M. Stoitsov. “Anomalous behavior of  $2^+$  excitations around  $^{132}\text{Sn}$ .” In: *Phys. Rev. C* 66 (5 Nov. 2002), p. 054313 (cit. on pp. 36, 124).

- 
- [56] M Grinberg; T K Dinh; C Protochristov; I Penev; C Stoyanov; W Andrejtscheff. “Level structure and transition probabilities in  $^{140}\text{Ce}$ .” In: *J. Phys. G* 19.8 (1993), p. 1179 (cit. on p. 38).
- [57] O. Hansen; O. Nathan. “Excitation of collective optupole states in the Pd-Sm region.” In: *Nucl. Phys.* 42 (1963), pp. 197–220 (cit. on p. 38).
- [58] P. Kleinheinz; M. Ogawa; R. Broda; P. J. Daly; D. Haenni; H. Beuscher; A. Kleinrahm. “Properties of the  $3^-$  First Excited State in the Doubly Closed Shell Nucleus  $^{146}\text{Gd}$ .” In: *Z.Phys.* A286 (1978), p. 27 (cit. on p. 38).
- [59] S.M. Burnett; A.M. Baxter; S. Hinds; F. Pribac; R.H. Spear; W.J. Vermeer. “A measurement of  $B(E3;0^+ \rightarrow 3_1^-)$  and some E2 transition probabilities in  $^{132,134,136,138}\text{Ba}$  using Coulomb excitation.” In: *Nucl. Phys. A* 432.2 (1985), pp. 514–524 (cit. on p. 38).
- [60] R.A. Gatenby; E.L. Johnson; E.M. Baum; S.W. Yates; D. Wang; J.R. Vanhoy; M.T. McEllistrem; T. Belgia; B. Fazekas; G. Molnar. “Decay properties and lifetimes of states in  $^{144}\text{Sm}$  from  $(n, n'\gamma)$  reaction studies.” In: *Nucl. Phys. A* 560.2 (1993), pp. 633–663 (cit. on p. 38).
- [61] P Van Duppen; K Riisager. “Physics with REX-ISOLDE: from experiment to facility.” In: *J. Phys. G* 38.2 (2011), p. 024005 (cit. on pp. 42, 51).
- [62] ISOLDE YIELD DATABASE. URL: [http://test-isolde-yields.web.cern.ch/test-isolde-yields/query\\_tgt.htm](http://test-isolde-yields.web.cern.ch/test-isolde-yields/query_tgt.htm) (visited on 02/13/2018) (cit. on p. 43).
- [63] H. J. Kluge. ISOLDE User’s Guide. CERN 86–05, 1986 (cit. on p. 43).
- [64] Yu. Khazov; A.A. Rodionov; S. Sakharov; Balraj Singh. “Nuclear Data Sheets for  $A = 132$ .” In: *Nucl. Data Sheets* 104.3 (2005), pp. 497–790 (cit. on pp. 42, 95–97, 125).
- [65] P. Gregers Hansen. “Chapter 9 - The SC: ISOLDE and Nuclear Structure.” In: *History of CERN*. Ed. by John Krige. Vol. 3. History of CERN. North-Holland, 1996, pp. 327–413 (cit. on pp. 43, 45).
- [66] Otto Mogens Kofoed-Hansen. “The birth of on-line isotope separation.” In: *3rd International Conference on Nuclei Far from Stability* (1976) (cit. on p. 43).
- [67] B. Jonson; A. Richter. “More than three decades of ISOLDE physics.” In: *Hyperfine Interact.* 129.1 (Dec. 2000), pp. 1–22 (cit. on pp. 43, 50).
-

- [68] Y. Kadi; Y. Blumenfeld; W. V. Delsolaro; M. A. Fraser; M. Huyse; A. P. Koufidou; J. A. Rodriguez; F. Wenander. “Post-accelerated beams at ISOLDE.” In: *J. Phys. G* 44.8 (2017), p. 084003 (cit. on pp. 44, 50–51, 53, 56–58).
- [69] ISOLDE HALL. ISOLDE-layout.ppt. URL: <http://isolde.web.cern.ch/isolde-logos-layouts-and-templates> (visited on 02/13/2018) (cit. on pp. 44, 49).
- [70] M. J. G. Borge; B. Jonson. “ISOLDE past, present and future.” In: *J. Phys. G* 44.4 (2017), p. 044011 (cit. on pp. 44, 51, 56, 133).
- [71] M. J. G. Borge; K. Riisager. “HIE-ISOLDE, the project and the physics opportunities.” In: *Eur. Phys. J. A* 52.11 (Nov. 2016), p. 334 (cit. on pp. 44, 51, 56–57, 133).
- [72] E. Kugler. “The ISOLDE facility.” In: *Hyperfine Interact.* 129.1 (2000), pp. 23–42 (cit. on pp. 45, 49–50, 64, 133).
- [73] Christoph Seiffert; Thierry Stora; Thorsten Kröll. “Production of radioactive molecular beams for CERN-ISOLDE.” Presented 04 Feb 2015. PhD thesis. Dec. 2014 (cit. on p. 45).
- [74] ISOLDE TARGET. URL: <http://isolde.web.cern.ch/targets-and-separators> (visited on 02/13/2018) (cit. on p. 45).
- [75] U. Köster; O. Arndt; E. Bouquerel; V.N. Fedoseyev; H. Frånberg; A. Joinet; C. Jost; I.S.K. Kerkines; R. Kirchner. “Progress in ISOL target-ion source systems.” In: *Nucl. Instrum. Methods Phys. Research Section B: Beam Interactions with Materials and Atoms* 266.19 (2008). Proceedings of the XVth International Conference on Electromagnetic Isotope Separators and Techniques Related to their Applications, pp. 4229–4239 (cit. on pp. 46–48).
- [76] A.H.M. Evensen; R. Catherall; P. Drumm; P. Van Duppen; O.C. Jonsson; E. Kugler; J. Lettry; O. Tengblad; V. Tikhonov; H.L. Ravn. “Release and yields from thorium and uranium targets irradiated with a pulsed proton beam.” In: *Nucl. Instrum. Methods Phys. Research Section B: Beam Interactions with Materials and Atoms* 126.1 (1997). International Conference on Electromagnetic Isotope Separators and Techniques Related to Their Applications, pp. 160–165 (cit. on p. 46).
- [77] David R. LIDE. HANDBOOK of CHEMISTRY and PHYSICS. 84th EDITION. CRC PRESS (cit. on p. 46).
- [78] J. A. Lettry. “Review of ion-source developments for radioactive ion-beam facilities.” In: *Proceedings of the 1999 Particle Accelerator Conference*. Vol. 1. New York, 1999, pp. 92–96 (cit. on p. 47).



- [79] V.I. Mishin; V.N. Fedoseyev; H.-J. Kluge; V.S. Letokhov; H.L. Ravn; F. Scheerer; Y. Shirakabe; S. Sundell; O. Tengblad. “Chemically selective laser ion-source for the CERN-ISOLDE on-line mass separator facility.” In: *Nucl. Instrum. Methods Phys. Research Section B: Beam Interactions with Materials and Atoms* 73.4 (1993), pp. 550–560 (cit. on p. 47).
- [80] U. Köster. “Ausbeuten und Spektroskopie radioaktiver Isotope bei LOHENGRIN und ISOLDE.” PhD thesis. TU Munich, 2000 (cit. on pp. 47–48).
- [81] D.W Stracener. “Status of radioactive ion beams at the HRIBF.” In: *Nucl. Instrum. Methods Phys. Research Section B: Beam Interactions with Materials and Atoms* 204.Supplement C (2003). 14th International Conference on Electromagnetic Isotope Separators and Techniques Related to their Applications, pp. 42–47 (cit. on p. 48).
- [82] L. Penescu. PhD thesis. Universitatea Politehnica Bucharest, 2009 (cit. on p. 48).
- [83] Thierry Stora. “Radioactive Ion Sources.” In: *CAS-CERN Accelerator School: Ion Sources - Proceedings* (Apr. 2014) (cit. on p. 48).
- [84] L. Penescu; R. Catherall; J. Lettry; T. Stora. “Development of high efficiency Versatile Arc Discharge Ion Source at CERN ISOLDE.” In: *Rev. Sci. Instrum.* 81.2 (2010), 02A906 (cit. on p. 48).
- [85] P. Schmidt; F. Ames; G. Bollen; O. Forstner; G. Huber; M. Oinonen; J. Zimmer. “Bunching and cooling of radioactive ions with REXTRAP.” In: *Nucl. Phys. A* 701.1 (2002). 5th International Conference on Radioactive Nuclear Beams, pp. 550–556 (cit. on pp. 51–52).
- [86] REX-ISOLDE, REXTRAP. URL: <http://rex-isolde.web.cern.ch/rextrap> (visited on 10/13/2017) (cit. on p. 52).
- [87] A. Gustafsson; A. Herlert; F. Wenander. “Mass-selective operation with REXTRAP.” In: *Nucl. Instrum. Methods Phys. Research Section A: Accelerators, Spectrometers, Detectors and Associated Equipment* 626.Supplement C (2011), pp. 8–15 (cit. on pp. 51–52).
- [88] F. Ames; G. Bollen; P. Delahaye; O. Forstner; G. Huber; O. Kester; K. Reisinger; P. Schmidt. “Cooling of radioactive ions with the Penning trap REXTRAP.” In: *Nucl. Instrum. Methods Phys. Research Section A: Accelerators, Spectrometers, Detectors and Associated Equipment* 538.1 (2005), pp. 17–32 (cit. on p. 51).

- [89] F Wenander; B Jonson; L Liljeby; G H Nyman. REXEBIS the Electron Beam Ion Source for the REX-ISOLDE project. Tech. rep. CERN-OPEN-2000-320. Geneva: CERN, Dec. 1998 (cit. on pp. 52–54).
- [90] B.H. Wolf; J. Cederkäll; O. Forstner; F. Wenander; F. Ames; K. Reisinger; L. Liljeby; Ö. Skeppstedt; B. Jonson; G. Nyman. “First radioactive ions charge bred in REXEBIS at the REX-ISOLDE accelerator.” In: *Nucl. Instrum. Methods Phys. Research Section B: Beam Interactions with Materials and Atoms* 204, Supplement C (2003). 14th International Conference on Electromagnetic Isotope Separators and Techniques Related to their Applications, pp. 428–432 (cit. on p. 53).
- [91] F Wenander. “Charge breeding of radioactive ions with EBIS and EBIT.” In: *J. Instrum.* 5.10 (2010), p. C10004 (cit. on pp. 53–54).
- [92] REX-ISOLDE, REXEBIS. URL: <http://rex-isolde.web.cern.ch/rexebis> (visited on 10/13/2017) (cit. on p. 53).
- [93] REX-ISOLDE, MASS-SEPARATOR. URL: <http://rex-isolde.web.cern.ch/mass-separator> (visited on 10/13/2017) (cit. on p. 54).
- [94] R. Rao; O. Kester; T. Sieber; D. Habs; K. Rudolph. “Beam optics design of the REX-ISOLDE q/m-separator.” In: *Nucl. Instrum. Methods Phys. Research Section A: Accelerators, Spectrometers, Detectors and Associated Equipment* 427.1 (1999), pp. 170–176 (cit. on p. 54).
- [95] R. von Hahn; M. Grieser; D. Habs; E. Jaeschke; C.-M. Kleffner; J. Liebmam; S. Papureanu; R. Repnow; D. Schwalm; M. Stampfer. “Development of seven-gap resonators for the Heidelberg high current injector.” In: *Nucl. Instrum. Methods Phys. Research Section A: Accelerators, Spectrometers, Detectors and Associated Equipment* 328.1 (1993), pp. 270–274 (cit. on p. 55).
- [96] REX-ISOLDE, REXLINAC. URL: <http://rex-isolde.web.cern.ch/rfq>, <http://rex-isolde.web.cern.ch/buncher>, <http://rex-isolde.web.cern.ch/ihs>, <http://rex-isolde.web.cern.ch/7gaps>, <http://rex-isolde.web.cern.ch/9-gap-ih> (visited on 10/13/2017) (cit. on p. 55).
- [97] D. Habs; O. Kester; T. Sieber; H. Bongers; S. Emhofer; P. Reiter; P.G. Thierolf; G. Bollen; J. Aystö; O. Forstner; H. Ravn; T. Nilsson; M. Oinonen; H. Simon; J. Cederkäll; F. Ames; P. Schmidt; G. Huber; L. Liljeby; O. Skeppstedt; K.G. Rensfelt; F. Wenander; B. Jonson; G. Nyman; R. von Hahn; H. Podlech; R. Repnow; C. Gund; D. Schwalm; A. Schempp; K.-U. Kühnel; C. Welsch; U. Ratzinger; G. Walter; A. Huck; K. Kruglov; M. Huyse; P. Van den Bergh; P. Van Duppen; L. Weissman; A.C. Shotter; A.N. Ostrowski; T. Davinson; P.J. Woods; J. Cub; A. Richter; G.

- Schrieder. “The REX-ISOLDE project.” In: *Hyperfine Interact.* 129.1 (Dec. 2000), pp. 43–66 (cit. on p. 55).
- [98] HIE-ISOLDE, HIELINAC. URL: <http://rex-isolde.web.cern.ch/sc-linac> (visited on 10/13/2017) (cit. on p. 57).
- [99] HIE-ISOLDE. URL: <https://hie-isolde-project.web.cern.ch/> (visited on 10/13/2017) (cit. on p. 57).
- [100] M. J. G Borge. private communication. 2017 (cit. on p. 57).
- [101] M. A. Fraser; R. M. Jones; M. Pasini. “Beam dynamics design studies of a superconducting radioactive ion beam postaccelerator.” In: *Phys. Rev. ST Accel. Beams* 14 (2 Feb. 2011), p. 020102 (cit. on p. 56).
- [102] Klaus Hanke et al. “The LHC Injectors Upgrade (LIU) Project at CERN: Proton Injector Chain.” In: *Proceedings, 8th International Particle Accelerator Conference (IPAC 2017): Copenhagen, Denmark, May 14-19, 2017*. 2017, WEPVA036 (cit. on p. 58).
- [103] J. Eberth; G. Pascovici; H.G. Thomas; N. Warr; D. Weisshaar; D. Habs; P. Reiter; P. Thirolf; D. Schwalm; C. Gund; H. Scheit; M. Lauer; P. Van Duppen; S. Franchoo; M. Huyse; R.M. Lieder; W. Gast; J. Gerl; K.P. Lieb. “MINIBALL A Ge detector array for radioactive ion beam facilities.” In: *Prog. Part. Nucl. Phys.* 46.1 (2001), pp. 389–398 (cit. on pp. 60–61, 133).
- [104] N. Warr. Private Communication. University of Cologne, 2018 (cit. on pp. 60, 63).
- [105] Revamped HIE-ISOLDE serves experiments. CERN COURIER. published online, <http://cerncourier.com/cws/article/cern/69612>. Aug. 2017 (cit. on p. 60).
- [106] N. Warr; J. Van de Walle; M. Albers; F. Ames; B. Bastin; C. Bauer; V. Bildstein; A. Blazhev; S. Bönig; N. Bree; B. Bruyneel; P. A. Butler; J. Cederkäll; E. Clément; T. E. Cocolios; T. Davinson; H. De Witte; P. Delahaye; D. D. DiJulio; J. Diriken; J. Eberth; A. Ekström; J. Elseviers; S. Emhofer; D. V. Fedorov; V. N. Fedosseev; S. Franchoo; C. Fransen; L. P. Gaffney; J. Gerl; G. Georgiev; R. Gernhäuser; T. Grahm; D. Habs; H. Hess; A. M. Hurst; M. Huyse; O. Ivanov; J. Iwanicki; D. G. Jenkins; J. Jolie; N. Kesteloot; O. Kester; U. Köster; M. Krauth; T. Kröll; R. Krücken; M. Lauer; J. Leske; K. P. Lieb; R. Lutter; L. Maier; B. A. Marsh; D. Mücher; M. Münch; O. Niedermaier; J. Pakarinen; M. Pantea; G. Pascovici; N. Patronis; D. Pauwels; A. Petts; N. Pietralla; R. Raabe; E. Rapisarda; P. Reiter; A. Richter; O. Schaile; M. Scheck; H. Scheit; G. Schrieder; D. Schwalm; M. Seidlitz; M. Seliverstov; T. Sieber; H. Simon; K. -H. Speidel; C. Stahl; I. Stefanescu; P. G. Thirolf; H. -G. Thomas; M. Thürauf; P. Van Duppen; D. Voulot; R. Wadsworth; G. Walter; D. Weißhaar;

- F. Wenander; A. Wiens; K. Wimmer; B. H. Wolf; P. J. Woods; K. Wrzosek-Lipska; K. O. Zell. “The Miniball spectrometer.” In: *Eur. Phys. J. A* 49.3 (Mar. 2013), p. 40 (cit. on pp. 61–62, 133, 136, 158).
- [107] Bildstein, Vinzenz; Gernhäuser, Roman; Kröll, Thorsten; Krücken, Reiner; Wimmer, Kathrin; Van Duppen, Piet; Huyse, Mark; Patronis, Nikolas; Raabe, Riccardo; T-REX Collaboration. “T-REX - A new setup for transfer experiments at REX-ISOLDE.” In: *Eur. Phys. J. A* 48.6 (2012), p. 85 (cit. on pp. 61–62, 67).
- [108] A.N Ostrowski; S. Cherubini; T. Davinson; D. Groombridge; A.M. Laird; A. Musumarra; A. Ninane; A. di Pietro; A.C. Shotter; P.J Woods. “CD: A double sided silicon strip detector for radioactive nuclear beam experiments.” In: *Nucl. Instrum. Methods Phys. Research Section A: Accelerators, Spectrometers, Detectors and Associated Equipment* 480.2 (2002), pp. 448–455 (cit. on pp. 62, 67).
- [109] R. Lutter; O. Schaile; K. Schoffel; K. Steinberger; P. Thirolf; C. Broude. “MARaBOOU-A MBS and ROOT based online/offline utility.” In: *IEEE Transactions on Nuclear Science - IEEE TRANS NUCL SCI* 47 (Feb. 1999), pp. 363–366 (cit. on p. 65).
- [110] H.G. Essel; N Kurz. “The general purpose data acquisition system MBS.” In: 47 (May 2000), pp. 337–339 (cit. on p. 65).
- [111] Rene Brun; Fons Rademakers. “ROOT — An object oriented data analysis framework.” In: *Nucl. Instrum. Methods Phys. Research Section A: Accelerators, Spectrometers, Detectors and Associated Equipment* 389.1 (1997). New Computing Techniques in Physics Research V, pp. 81–86 (cit. on p. 65).
- [112] I. Antcheva; M. Ballintijn; B. Bellenot; M. Biskup; R. Brun; N. Buncic; Ph. Canal; D. Casadei; O. Couet; V. Fine; L. Franco; G. Ganis; A. Gheata; D. Gonzalez Maline; M. Goto; J. Iwaszkiewicz; A. Kreshuk; D. Marcos Segura; R. Maunder; L. Moneta; A. Naumann; E. Offermann; V. Onuchin; S. Panacek; F. Rademakers; P. Russo; M. Tadel. “ROOT — A C++ framework for petabyte data storage, statistical analysis and visualization.” In: *Computer Physics Communications* 180.12 (2009). 40 YEARS OF CPC: A celebratory issue focused on quality software for high performance, grid and novel computing architectures, pp. 2499–2512 (cit. on p. 65).
- [113] M. Goto. C++ Interpreter - CINT. CQ publishing, 1995 (cit. on p. 65).
- [114] Mesytec. MUX-16/32/64. published online, <https://www.mesytec.com/products/datasheets/MUX-16.pdf>. Data sheet V2.4 01. Apr. 2018 (cit. on p. 66).
- [115] O.B. Tarasov; D. Bazin. “LISE++: Exotic beam production with fragment separators and their design.” In: *Nucl. Instrum. Methods Phys. Research Section B: Beam*

- Interactions with Materials and Atoms* 376.Supplement C (2016). Proceedings of the XVIIth International Conference on Electromagnetic Isotope Separators and Related Topics (EMIS2015), Grand Rapids, MI, U.S.A., 11-15 May 2015, pp. 185–187 (cit. on p. 68).
- [116] Bart Bruyneel; Peter Reiter; Gheorghe Pascovici. “Characterization of large volume HPGe detectors. Part I: Electron and hole mobility parameterization.” In: *Nucl. Instrum. Methods Phys. Research Section A: Accelerators, Spectrometers, Detectors and Associated Equipment* 569.3 (2006), pp. 764–773 (cit. on p. 71).
- [117] Bart Bruyneel; Peter Reiter; Gheorghe Pascovici. “Characterization of large volume HPGe detectors. Part II: Experimental results.” In: *Nucl. Instrum. Methods Phys. Research Section A: Accelerators, Spectrometers, Detectors and Associated Equipment* 569.3 (2006), pp. 774–789 (cit. on p. 71).
- [118] B. Bruyneel. “Characterization of Segmented Large Volume, High Purity Germanium Detectors.” PhD thesis. University of Cologne, 2006 (cit. on p. 71).
- [119] M. Descovich; I.Y. Lee; P.N. Luke; R.M. Clark; M. Cromaz; M.A. Deleplanque; R.M. Diamond; P. Fallon; A.O. Macchiavelli; E. Rodriguez-Vieitez; F.S. Stephens; D. Ward. “Effects of neutron damage on the performance of large volume segmented germanium detectors.” In: *Nuclear Instruments and Methods in Physics Research Section A: Accelerators, Spectrometers, Detectors and Associated Equipment* 545.1 (2005), pp. 199–209 (cit. on p. 71).
- [120] I. Abt; L. Garbini; C. Gooch; S. Irlbeck; X. Liu; M. Palermo; O. Schulz. “Alpha-event and surface characterisation in segmented true-coaxial HPGe detectors.” In: *Nuclear Instruments and Methods in Physics Research Section A: Accelerators, Spectrometers, Detectors and Associated Equipment* 858 (2017), pp. 80–89 (cit. on p. 71).
- [121] G. L. Miller; W. M. Gidson; P. F. Donovan. “Semiconductor Particle Detectors.” In: *Annual Review of Nuclear Science* 12.1 (1962), pp. 189–220 (cit. on p. 72).
- [122] B.D. Wilkins; M.J. Fluss; S.B. Kaufman; C.E. Gross; E.P. Steinberg. “Pulse-height defects for heavy ions in a silicon surface-barrier detector.” In: *Nuclear Instruments and Methods* 92.3 (1971), pp. 381–391 (cit. on p. 72).
- [123] L. Grassi; J. Forneris; D. Torresi; L. Acosta; A. Di Pietro; P. Figuera; M. Fisichella; V. Grilj; M. Jakšić; M. Lattuada; T. Mijatović; M. Milin; L. Prepolec; N. Skukan; N. Soić; V. Tokić; M. Uroić. “Study of the inter-strip gap effects on the response of Double Sided Silicon Strip Detectors using proton micro-beams.” In: *Nucl. Instrum. Methods Phys. Research Section A: Accelerators, Spectrometers, Detectors and Associated Equipment* 767.Supplement C (2014), pp. 99–111 (cit. on p. 72).

- [124] G Kramberger; V Cindro; I Mandić; M Mikuž; M Zavrtanik. “Effective trapping time of electrons and holes in different silicon materials irradiated with neutrons, protons and pions.” In: *Nuclear Instruments and Methods in Physics Research Section A: Accelerators, Spectrometers, Detectors and Associated Equipment* 481.1 (2002), pp. 297–305 (cit. on p. 72).
- [125] E. Browne; J.K. Tuli. “Nuclear Data Sheets for  $A = 66$ .” In: *Nuclear Data Sheets* 111.4 (2010), pp. 1093–1209 (cit. on p. 78).
- [126] C. M. Baglin. “Nuclear Data Sheets for  $A = 166$ .” In: *Nucl. Data Sheets* 109.5 (2008), pp. 1103–1382 (cit. on p. 96).
- [127] P. Bhattacharyya; P. J. Daly; C. T. Zhang; Z. W. Grabowski; S. K. Saha; R. Broda; B. Fornal; I. Ahmad; D. Seweryniak; I. Wiedenhöver; M. P. Carpenter; R. V. F. Janssens; T. L. Khoo; T. Lauritsen; C. J. Lister; P. Reiter; J. Blomqvist. “Magic Nucleus  $^{132}\text{Sn}$  and Its One-Neutron-Hole Neighbor  $^{131}\text{Sn}$ .” In: *Phys. Rev. Lett.* 87 (6 July 2001), p. 062502 (cit. on p. 98).
- [128] T. Björnstad; M.J.G. Borge; J. Blomqvist; R.D. Von Dincklage; G.T. Ewan; P. Hoff; B. Jonson; K. Kawade; A. Kerek; O. Klepper; G. Lövhöiden; S. Mattsson; G. Nyman; H.L. Ravn; G. Rudstam; K. Sistemich; O. Tengblad. “The doubly closed shell nucleus  $^{132}_{50}\text{Sn}_{82}$ .” In: *Nucl. Phys. A* 453.3 (1986), pp. 463–485 (cit. on p. 98).
- [129] B. Fogelberg; M. Hellström; D. Jerrestam; H. Mach; J. Blomqvist; A. Kerek; L. O. Norlin; J. P. Omtvedt. “Detailed Spectroscopy of the Doubly Closed Shell Nucleus  $^{132}\text{Sn}$  : First Observation of Octupole Collectivity.” In: *Phys. Rev. Lett.* 73 (18 Oct. 1994), pp. 2413–2416 (cit. on pp. 98, 115, 117, 127).
- [130] R.H. Spear; T.H. Zabel; D.C. Kean; A.M.R. Joye; A.M. Baxter; M.P. Fewell; S. Hinds. “Systematics of coulomb-nuclear interference: Implications for reliable measurement of the reorientation effect.” In: *Phys. Lett. B* 76.5 (1978), pp. 559–561 (cit. on p. 114).
- [131] F. G. Kondev. “Nuclear Data Sheets for  $A = 206$ .” In: *Nucl. Data Sheets* 109.6 (2008), pp. 1527–1654 (cit. on p. 115).
- [132] Gianluca Colò; Pier Francesco Bortignon; Hiroyuki Sagawa; Kassem Moghrabi; Marcella Grasso; Nguyen Van Giai. “Microscopic theory of particle-vibration coupling.” In: *J. Phys.: Conference Series* 321.1 (2011), p. 012018 (cit. on p. 119).
- [133] A. V. Afanasjev; E. Litvinova. “Impact of collective vibrations on quasiparticle states of open-shell odd-mass nuclei and possible interference with the tensor force.” In: *Phys. Rev. C* 92 (4 Oct. 2015), p. 044317 (cit. on p. 119).

- 
- [134] Li-Gang Cao; G. Colò; H. Sagawa; P. F. Bortignon. “Properties of single-particle states in a fully self-consistent particle-vibration coupling approach.” In: *Phys. Rev. C* 89 (4 Apr. 2014), p. 044314 (cit. on p. 119).
- [135] E. V. Litvinova; A. V. Afanasjev. “Dynamics of nuclear single-particle structure in covariant theory of particle-vibration coupling: From light to superheavy nuclei.” In: *Phys. Rev. C* 84 (1 July 2011), p. 014305 (cit. on p. 119).
- [136] Elena Litvinova. “Quasiparticle-vibration coupling in a relativistic framework: Shell structure of  $Z = 120$  isotopes.” In: *Phys. Rev. C* 85 (2 Feb. 2012), p. 021303 (cit. on p. 119).
- [137] G. Colò; P. F. Bortignon; G. Bocchi. “Hybrid configuration mixing model for odd nuclei.” In: *Phys. Rev. C* 95 (3 Mar. 2017), p. 034303 (cit. on p. 120).
- [138] Gianluca Coló; Ligang Cao; Nguyen Van Giai; Luigi Capelli. “Self-consistent RPA calculations with Skyrme-type interactions.” In: *Computer Physics Communications* 184.1 (2013), pp. 142–161 (cit. on p. 120).
- [139] H. Naidja; F. Nowacki; K. Sieja. “Spectroscopic properties of neutron rich nuclei beyond  $^{132}\text{Sn}$  and seniority mixing.” In: *J. Phys.: Conference Series* 580.1 (2015), p. 012030 (cit. on p. 120).
- [140] Morten Hjorth-Jensen; Thomas T.S. Kuo; Eivind Osnes. “Realistic effective interactions for nuclear systems.” In: *Physics Reports* 261.3 (1995), pp. 125–270 (cit. on p. 120).
- [141] G. Simpson G. S. and Gey; A. Jungclaus; J. Taprogge; S. Nishimura; K. Sieja; P. Doornenbal; G. Lorusso; P.-A. Söderström; T. Sumikama; Z. Y. Xu; H. Baba; F. Browne; N. Fukuda; N. Inabe; T. Isobe; H. S. Jung; D. Kameda; G. D. Kim; Y.-K. Kim; I. Kojouharov; T. Kubo; N. Kurz; Y. K. Kwon; Z. Li; H. Sakurai; H. Schaffner; Y. Shimizu; H. Suzuki; H. Takeda; Z. Vajta; H. Watanabe; J. Wu; A. Yagi; K. Yoshinaga; S. Bönig; J.-M. Daugas; F. Drouet; R. Gernhäuser; S. Ilieva; T. Kröll; A. Montaner-Pizá; K. Moschner; D. Mücher; H. Naidja; H. Nishibata; F. Nowacki; A. Odahara; R. Orlandi; K. Steiger; A. Wendt. “Yrast  $6^+$  Seniority Isomers of  $^{136,138}\text{Sn}$ .” In: *Phys. Rev. Lett.* 113 (13 Sept. 2014), p. 132502 (cit. on p. 120).
- [142] E. Caurier; G. Martinez-Pinedo; F. Nowacki; A. Poves; A. P. Zuker. “The shell model as a unified view of nuclear structure.” In: *Rev. Mod. Phys.* 77 (2 June 2005), pp. 427–488 (cit. on p. 121).
- [143] E. Caurier; F. Nowacki. “Present status of shell model techniques\*.” In: *Acta Phys. Polonica* 30 (3 1999), pp. 705–714 (cit. on p. 121).
-

- [144] D.C. Radford; C. Baktash; J.R. Beene; B. Fuentes; A. Galindo-Uribarri; J. Gomez del Campo; C.J. Gross; M.L. Halbert; Y. Larochele; T.A. Lewis; J.F. Liang; J. Mas; P.E. Mueller; E. Padilla; D. Shapira; D.W. Stracener; R.L. Varner; C.-H. Yu; C.J. Barton; M.A. Caprio; D.J. Hartley; N.V. Zamfir. “Nuclear structure studies with heavy neutron-rich RIBS at the HRIBF.” In: *Nuclear Physics A* 746 (2004). Proceedings of the Sixth International Conference on Radioactive Nuclear Beams (RNB6), pp. 83–89 (cit. on p. 121).
- [145] N. Houda. Private Communication. Université de Strasbourg, 2018 (cit. on pp. 121, 126, 128).
- [146] T. Otsuka; M. Honma; T. Mizusaki; N. Shimizu; Y. Utsuno. “Monte Carlo shell model for atomic nuclei.” In: *Prog. Part. Nucl. Phys.* 47.1 (2001), pp. 319–400 (cit. on p. 121).
- [147] Noritaka Shimizu; Takashi Abe; Yusuke Tsunoda; Yutaka Utsuno; Tooru Yoshida; Takahiro Mizusaki; Michio Honma; Takaharu Otsuka. “New-generation Monte Carlo shell model for the K computer era.” In: *Progress of Theoretical and Experimental Physics* 2012.1 (2012), 01A205 (cit. on p. 121).
- [148] T. Togashi; Y. Tsunoda; T. Otsuka; N. Shimizu; M. Honma. “Novel shape evolution in Sn isotopes from magic numbers 50 to 82.” In: *Phys. Rev. Lett.* (2018). to be published (cit. on pp. 121–123).
- [149] T. Otsuka. Private Communication. Department of Physics, University of Tokyo, 2018 (cit. on p. 122).
- [150] Tomoaki Togashi; Yusuke Tsunoda; Takaharu Otsuka; Noritaka Shimizu. “Quantum Phase Transition in the Shape of Zr isotopes.” In: *Phys. Rev. Lett.* 117 (17 Oct. 2016), p. 172502 (cit. on p. 122).
- [151] Yusuke Tsunoda; Takaharu Otsuka; Noritaka Shimizu; Michio Honma; Yutaka Utsuno. “Novel shape evolution in exotic Ni isotopes and configuration-dependent shell structure.” In: *Phys. Rev. C* 89 (3 Mar. 2014), p. 031301 (cit. on pp. 122–123).
- [152] P. Ring; P. Schuck. *The Nuclear Many-Body Problem*. Springer-Verlag, New York, 1980 (cit. on p. 123).
- [153] J.R. Stone; P.-G. Reinhard. “The Skyrme interaction in finite nuclei and nuclear matter.” In: *Prog. Part. Nucl. Phys.* 58.2 (2007), pp. 587–657 (cit. on p. 124).



- 
- [154] M. Dutra; O. Lourenco; J. S. Sa Martins; A. Delfino; J. R. Stone; P. D. Stevenson. “Skyrme interaction and nuclear matter constraints.” In: *Phys. Rev. C* 85 (3 Mar. 2012), p. 035201 (cit. on p. 124).
- [155] A. Ansari; P. Ring. “Lowest lying  $2^+$  and  $3^-$  vibrational states in Pb, Sn, and Ni isotopes in relativistic quasiparticle random-phase approximation.” In: *Phys. Rev. C* 74 (5 Nov. 2006), p. 054313 (cit. on p. 124).
- [156] T.Kröll et al. Evolution of quadrupole and octupole collectivity north-east of  $^{132}\text{Sn}$ : the even Te and Xe isotopes. Proposal to the INTFC, Cern. unpublished. Oct. 2012 (cit. on p. 129).
- [157] T.Kröll et al. Coulomb Excitation of Neutron-rich  $^{134,136}\text{Sn}$  isotopes. Proposal to the INTFC, Cern. unpublished. Oct. 2012 (cit. on p. 129).
- [158] L.M. Fraile et al. Gamma and fast-timing spectroscopy of doubly magic  $^{132}\text{Sn}$  and its one- and two-neutron particle/hole neighbours. Proposal to the INTFC, Cern. unpublished. Oct. 2015 (cit. on p. 129).
- [159] P.J. Twin. “Observation of a Discrete-Line Superdeformed Band up to 60h  $^{152}\text{Dy}$ .” In: *Phys. Rev. Lett.* 54, 811-814 (1986) (cit. on p. 133).
- [160] J. Simpson. “The Euroball Spectrometer.” English. In: *Zeitschrift für Physik A Hadrons and Nuclei* 358.2 (1997), pp. 139–143 (cit. on pp. 133, 137–138).
- [161] A. Deleplanque. Gammasphere: A National Gamma-ray Facility ; Preliminary Proposal. Lawrence Berkeley Laboratory, 1988 (cit. on p. 133).
- [162] N. Warr; J. Eberth; G. Pascovici; H. G. Thomas; D. Weißhaar. “MINIBALL: The first gamma-ray spectrometer using segmented, encapsulated germanium detectors for studies with radioactive beams.” In: *Eur. Phys. J. A* 20.1 (Apr. 2003), pp. 65–66 (cit. on p. 133).
- [163] Tanja Striepling. “ $\gamma$ -spektroskopische Untersuchung von  $^{236}\text{U}$ .” Diploma Thesis. Albertus-Magnus Platz, Cologne, Germany: University of Cologne, 2005 (cit. on p. 134).
- [164] S. Agostinelli; J. Allison; K. Amako; J. Apostolakis; H. Araujo; P. Arce; M. Asai; D. Axen; S. Banerjee; G. Barrant; F. Behner; L. Bellagamba; J. Boudreau; L. Broglia; A. Brunengo; H. Burkhardt; S. Chauvie; J. Chuma; R. Chytrcek; G. Cooperman; G. Cosmo; P. Degtyarenko; A. Dell’Acqua; G. Depaola; D. Dietrich; R. Enami; A. Feliciello; C. Ferguson; H. Fesefeldt; G. Folger; F. Foppiano; A. Forti; S. Garelli; S. Giani; R. Giannitrapani; D. Gibin; J.J. Gómez Cadenas; I. González; G. Gracia Abril; G. Greeniaus; W. Greiner; V. Grichine; A. Grossheim; S. Guatelli; P.
-

- Gumplinger; R. Hamatsu; K. Hashimoto; H. Hasui; A. Heikkinen; A. Howard; V. Ivanchenko; A. Johnson; F.W. Jones; J. Kallenbach; N. Kanaya; M. Kawabata; Y. Kawabata; M. Kawaguti; S. Kelner; P. Kent; A. Kimura; T. Kodama; R. Kokoulin; M. Kossov; H. Kurashige; E. Lamanna; T. Lampén; V. Lara; V. Lefebure; F. Lei; M. Liendl; W. Lockman; F. Longo; S. Magni; M. Maire; E. Medernach; K. Minamimoto; P. Mora de Freitas; Y. Morita; K. Murakami; M. Nagamatu; R. Nartallo; P. Nieminen; T. Nishimura; K. Ohtsubo; M. Okamura; S. O’Neale; Y. Oohata; K. Paech; J. Perl; A. Pfeiffer; M.G. Pia; F. Ranjard; A. Rybin; S. Sadilov; E. Di Salvo; G. Santin; T. Sasaki; N. Savvas; Y. Sawada; S. Scherer; S. Sei; V. Sirotenko; D. Smith; N. Starkov; H. Stoecker; J. Sulkimo; M. Takahata; S. Tanaka; E. Tcherniaev; E. Safai Tehrani; M. Tropeano; P. Truscott; H. Uno; L. Urban; P. Urban; M. Verderi; A. Walkden; W. Wander; H. Weber; J.P. Wellisch; T. Wenaus; D.C. Williams; D. Wright; T. Yamada; H. Yoshida; D. Zschesche. “Geant4—a simulation toolkit.” In: *Nucl. Instrum. Methods Phys. Research Section A: Accelerators, Spectrometers, Detectors and Associated Equipment* 506.3 (2003), pp. 250–303 (cit. on p. 134).
- [165] <http://geant4.cern.ch/> (cit. on p. 134).
- [166] Dawid Rosiak. “GEANT4 Monte-Carlo-Simulationen zur Optimierung der BGO-Compton-Suppression-Sield-Geometrie für die MINIBALL-Detektoren.” MA thesis. Albertus-Magnus Platz, Cologne, Germany: University of Cologne, 2014 (cit. on pp. 134, 136).
- [167] Iolanda Matea. Private Communication. IPN, Orsay, France, 2016-2018 (cit. on p. 138).
- [168] Iolanda Matea. Private Communication. IPN, Orsay, France, 2018 (cit. on pp. 140, 142–143).
- [169] M. Janecek; W. W. Moses. “Measuring Light Reflectance of BGO Crystal Surfaces.” In: *IEEE Transactions on Nuclear Science* 55.5 (Oct. 2008), pp. 2443–2449 (cit. on p. 140).
- [170] Hamamatsu Photonics K.K. Hamamatsu R3478 Photomultiplier Specifications. published online, <https://www.hamamatsu.com/us/en/R3478.html>. 2018 (cit. on p. 142).
- [171] Hamamatsu Photonics K.K. Photomultiplier Tubes: Basics and Application. published online, [https://www.hamamatsu.com/resources/pdf/etd/PMT\\_handbook\\_v3aE.pdf](https://www.hamamatsu.com/resources/pdf/etd/PMT_handbook_v3aE.pdf). Third Edition 3a. 2018 (cit. on p. 142).
- [172] User’s Manual: Digital Gamma Finder PIXIE-16. <http://www.xia.com/Manuals/Pixie16UserManual.pdf> (cit. on p. 149).

- [173] H. G. Thomas. “Entwicklung eines Germanium-CLUSTER-Detektors für das Gamma-Spektrometer EUROBALL.” PhD thesis. University of Cologne, 1995 (cit. on pp. 151–152).
- [174] Glenn F. Knoll. Radiation detection and measurement. John Wiley & Sons, Inc. , 3rd ed., 1999 (cit. on p. 153).



# List of Figures

1.	Two-neutron separation energy for isotopic chains including nuclei with magic neutron configuration . . . . .	12
2.	Excitation energies of the first excited state for nuclei around $^{208}\text{Pb}$ and $_{50}\text{Sn}$	13
3.	Comparison of energy levels from mean field shell models . . . . .	16
4.	Mass deviation between experimentally determined values and values calculated with the Bethe-Weizsäcker formula for isotonic and isotopic chains . .	18
5.	Quadrupole deformation of different nuclei with odd number of nucleons .	19
6.	Reduced transition strength in Weisskopf units for all even-even nuclei . .	22
7.	Illustration of Coulomb-scattering in the CM-system . . . . .	23
8.	Integrated non-relativistic Coulomb-excitation function $f_{\sigma,\lambda}(\xi)$ . . . . .	27
9.	First and second-order excitation and deexcitation processes for nuclei . . .	30
10.	Schematic nuclear chart with the magic numbers and one theoretical r-process path indicated . . . . .	32
11.	Nuclear abundance in the solar system and the s- and r-process path around $^{132}\text{Sn}$ . . . . .	33
12.	Shell-model orbitals forming the shell gaps at the magic numbers 50 and 82	34
13.	Excitation energies and reduced transition strengths for $2_1^+$ along the Sn chain	35
14.	Excitation energies and reduced transition strengths for $3_1^-$ along the Sn chain	36
15.	Excitation energies and reduced transition strengths for $2_1^+$ along the N = 82 isotonic chain . . . . .	37
16.	Excitation energies and reduced transition strengths $3_1^-$ along the N = 82 isotonic chain . . . . .	38
17.	$\gamma$ -ray spectrum and kinematics of the Coulomb excitation of $^{132}\text{Sn}$ performed at HRIBF . . . . .	40
18.	Beam and intensities available at the ISOLDE facility . . . . .	43
19.	CAD drawing of the ISOLDE HALL facility with its various experimental setups . . . . .	44
20.	Schematic figure of a typical primary ISOLDE target station with ion source	45
21.	Ionization efficiency of a FEBIAD source and a comparison between Sn ionization with RILIS and SnS ionization with an plasma source at ISOLDE	47
22.	Mass separators HRS and GPS at ISOLDE . . . . .	49
23.	CAD drawing of the REX- and HIE-ISOLDE part . . . . .	50
24.	Image of REXTRAP, a schematic cross-section and the working pinciple .	52
25.	Image of REXEBIS and a schematical illustration of the potential distribution inside REXEBIS . . . . .	53
26.	Extracted beam composition from REXEBIS for $^{129}\text{Cs}$ . . . . .	54
27.	Schematic illustration of the REXLINAC setup . . . . .	55
28.	Schematic illustration of the HIELINAC setup in the final version . . . .	57
29.	Time structure at ISOLDE . . . . .	58
30.	Schematic MINIBALL setup for the present experiment . . . . .	59
31.	MINIBALL and C-REX setup at ISOLDE . . . . .	60

32.	MINIBALL triple cluster and schematical illustration of the MINIBALL capsules . . . . .	61
33.	Double-Sided Silicon Strip Detector . . . . .	63
34.	Illustration of the data processing with MARABOU . . . . .	65
35.	DSSSD particle energy as a function of the MUX ID . . . . .	67
36.	Long-term stability of the DSSSD . . . . .	68
37.	Particle energy detected with the DSSSD as a function of the annular segments	69
38.	Annular segment 1 spectrum obtained with the DSSSD and DSSSD calibration	70
39.	Energy correlation spectrum of one DSSSD pixel . . . . .	71
40.	Energy correlation spectrum of one DSSSD pixel with two connected back-side segments . . . . .	73
41.	Energy correlation spectra of DSSSD pixels with 1 hit condition . . . . .	73
42.	Energy spectrum of particles detected in the innermost ring after energy correction . . . . .	74
43.	Comparison of $\gamma$ -ray spectra with different adjustments for the DSSSD. . .	75
44.	Long-term stability of the MINIBALL DAQ . . . . .	76
45.	$\gamma$ -ray spectrum of $^{66}\text{Ga}$ for energy and efficiency calibration . . . . .	77
46.	Fitted core signals of $^{66}\text{Ga}$ detected with one MINIBALL crystal . . . . .	78
47.	Quadratic energy calibration of the MINIBALL DGF modules . . . . .	79
48.	Relative detection efficiency of the MINIBALL array with the C-REX chamber	80
49.	Schematical illustration of the positioning parameters of the MB triple clusters	81
50.	Doppler correction for the $^{22}\text{Ne}$ data at segment level via a minimization algorithm . . . . .	82
51.	Doppler correction of the $^{22}\text{Ne}$ $\gamma$ -ray spectrum . . . . .	83
52.	FWHM of the target deexcitation as a function of the MINIBALL position parameters $\theta_i$ , $\phi_i$ and $\alpha_i$ . . . . .	84
53.	FWHM of the target deexcitation as a function of the DSSSD azimuth angle offset . . . . .	85
54.	FWHM of the $^{206}\text{Pb}$ deexcitation as a function of the virtual rotation of the DSSSD detector . . . . .	86
55.	DSSSD particle spectrum as a function of the scattering angle . . . . .	87
56.	Ratio of measured and calculated scattering cross section . . . . .	88
57.	$\gamma$ -ray energy as a function of the particle- $\gamma$ time difference . . . . .	89
58.	$\gamma$ -ray spectra before and after background subtraction . . . . .	90
59.	Nuclear chart around $^{132}\text{Sn}$ . . . . .	91
60.	<i>beta</i> -decay spectrum . . . . .	93
61.	Time dependent Beta-decay ratios . . . . .	94
62.	Low-energy beam-like $\gamma$ -ray spectrum Doppler corrected for $A = 132$ . . .	95
63.	$\gamma\gamma$ coincidence matrix . . . . .	96
64.	$\gamma\gamma$ coincidences with a gate on the $6^+ \rightarrow 4^+$ transitions of $^{166}\text{Yb}$ . . . . .	97
65.	Beam-like $\gamma$ -ray spectrum with Doppler correction for mass $A = 132$ enlarged around the $^{132}\text{Sn}$ transitions . . . . .	98
66.	Schematic activity as a function of time of $^{132}\text{Sn}$ and $^{132}\text{Sb}$ . . . . .	99

67.	Transitions from the Implantation measurement . . . . .	102
68.	Particle-energy spectrum of annular segments 4 and 8 . . . . .	104
69.	Particle energy as a function of the particle- $\gamma$ time difference . . . . .	105
70.	Particle energy vs. prompt $\gamma$ -ray energy for beam-like and target-like particles	106
71.	$\gamma$ -ray spectrum in coincidence with target-like particles with Doppler-correction for mass $A = 206$ . . . . .	107
72.	$\gamma$ -ray spectrum in coincidence with target-like particles without Doppler- correction . . . . .	108
73.	Beam-like $\gamma$ -ray spectrum with Doppler correction for mass $A = 132$ with restriction to safe Coulomb excitation . . . . .	109
74.	Particle cut conditions for conservative safe Coulomb excitation . . . . .	110
75.	$\gamma$ -ray spectra with complete beam-like and target-like separation. . . . .	111
76.	$\gamma$ -ray spectra including the total amount of the detected target deexcitation induced by all particles species. . . . .	112
77.	Particle energy of mass $A = 132, 166, 206$ as a function of the scattering angle calculated with LISE++ . . . . .	113
78.	Projections of the 3-dimensional $\chi^2$ -surface scans obtained with GOSIA2 . .	116
79.	$B(E2)$ value of $^{132}\text{Sn}$ as a function of the quadrupole moment . . . . .	118
80.	LSSM calculated $B(E2)$ transition decays and energy levels . . . . .	121
81.	MCSM T-plots of $^{130,132,134}\text{Sn}$ . . . . .	122
82.	Comparison between experimentally determined values and theory . . . . .	125
83.	$^{132}\text{Sn}$ wave function decomposition for the ground and first excitate state obtained from LSSM calculation. . . . .	126
84.	Wave function decomposition of the $4_1^+$ state of $^{132}\text{Sn}$ determined with LSSM	128
85.	MINIBALL spectrometer around COULEX target chamber at Cologne 2004.	133
86.	$\gamma\gamma$ matrix recorded with two MINIBALL triple clusters after $^{235}\text{U}(d,t)^{234}\text{U}$ reaction . . . . .	134
87.	GEANT4 predictions of the performance of a BGO escape-suppression shield for MINIBALL . . . . .	136
88.	CAD drawing of one MB triple with three BGO sub-systems . . . . .	138
89.	MINIBALL CAD drawings: Endcap and BGO crystal geometries. . . . .	139
90.	Bare BGO crystals at Orsay . . . . .	140
91.	BGO crystal wrapping . . . . .	141
92.	BGO carbon-fiber housing and assembly . . . . .	141
93.	Outlay of the photomultiplier voltage-divider circuit . . . . .	142
94.	“soft silicon cookies” for optical connection between photomultiplier and BGO crystals . . . . .	143
95.	BGO fixation with PMT housing . . . . .	144
96.	Assembled BGO prototype . . . . .	144
97.	Prototype measurement setup at Cologne . . . . .	145
98.	High-voltage supply box for the BGO prototype . . . . .	146
99.	Alignment box for escape-suppression shield and corresponding circuit diagram	147
100.	BGO signals with and without gain matching . . . . .	148

101. Comparison of a $^{137}\text{Cs}$ BGO sub-system spectrum with and without alignment	148
102. Pixie-16 modules . . . . .	150
103. BGO energy resolution spectrum and peak-to-valley spectrum . . . . .	151
104. $^{60}\text{Co}$ $\gamma$ -ray spectra with BGO shielded MINIBALL, but without Compton suppression . . . . .	154
105. HPGe and BGO energy correlation spectrum measured with a $^{60}\text{Co}$ source	155
106. HPGe and BGO energy correlation spectrum measured with a collimated $^{60}\text{Co}$ source . . . . .	156
107. Coincidence mode: $\gamma$ -ray spectrum with and without Compton suppression.	157
108. Time difference spectrum between one HPGe crystal and one BGO sub-system	158
109. <i>gamma</i> -ray energy detected in the HPGe as a function of the time difference between one HPGe and one BGO crystal . . . . .	159
110. Rejected $\gamma$ -ray spectra after Compton suppression and time cuts . . . . .	159
111. Free run mode: $\gamma$ -ray spectra before and after Compton suppression . . . .	160



## List of Tables

1.	Position parameters used for the center of each MINIBALL (MB) triple cluster for the Doppler correction. . . . .	84
2.	Observed $\gamma$ -ray transition energies following the corresponding $\beta$ -decay. . .	92
3.	Obtained efficiency corrected intensities for the decay of $^{132}\text{Sn}$ and $^{132}\text{Sb}$ nuclei during the decay and implantation time interval. For each nucleus the total amount of the decays is given by the sum of the obtained intensities.	103
4.	Determined excitation cross sections for $^{132}\text{Ba}$ and $^{166}\text{Yb}$ on $^{206}\text{Pb}$ corresponding to the observed $\gamma$ -ray transitions. . . . .	114
5.	Reduced transition strengths for $^{132}\text{Sn}$ determined in this work and from previous measurements. . . . .	117
6.	Relative energy resolution and peak-to-valley for all BGO crystals . . . . .	152



## Acknowledgements - Danksagung

Ich danke Herrn Prof. Dr. Peter Reiter für die Vergabe des vielseitigen und interessanten Promotionsthemas und für die Möglichkeit diese Arbeit in seiner Arbeitsgruppe am Institut für Kernphysik durchführen zu können. Ich bedanke mich für die vielfältige wissenschaftliche und methodische Unterstützung während der gesamten Bearbeitungsphase meiner Dissertation. Ich danke weiterhin herzlich Herrn Prof. Dr. Jan Jolie für die Übernahme des Koreferats sowie Herrn Prof. Dr. Andreas Schadschneider für die Übernahme des Vorsitzes der Prüfungskommission. Mein besonderer Dank geht an Herrn Dr. Michael Seidlitz, der mir stets mit Tatkraft und Fachwissen zur Seite stand. Ich danke für die gemeinsame Arbeit und die vielen Diskussionen zur Interpretation der erzielten Ergebnisse.

I owe special thanks to Prof. Dr. Frédéric Nowacki and Naidja Houda from the University of Strasbourg for providing results from large-scale shell-model calculations and the great collaboration. Furthermore, I would like to thank Mr. Yusuke Tsunoda, Tomoaki Togashi and Prof. Dr. Takaharu Otsuka from University of Tokyo, Japan for their Monte-Carlo shell-model calculations. Thank you for the great collaboration. I also wish to thank Prof. Dr. Gianluca Coló from the University of Milan, Italy for providing RPA calculations. Further thanks goes to Corinna Heinrich, Georgie Rainovski, Jacob Snäll, Tom Berry and Prof. Dr. Thorsten Kröll for support during the whole experiment. Special gratitude goes to Liam Gaffney whose expertise and commitment during the experiment was indispensable. I would also like to thank the ISOLDE operational staff, which were available 24/7 and led to a smooth operation of the HIE-ISOLDE accelerator and, thus, contribute a lot to the success of this experiment. I like to thank Iolanda Matea, Christine Le Galliard, Andrea Gottardo (now INFN-LNL) and Georgi Georgiev from the Institut de physique nucléaire Orsay for their contributions to the development of the MINIBALL escape-suppression shield prototype. Thank you very much for this fruitful and constructive collaboration.

Mein Dank geht an Herrn Dr. Nigel Warr für die viele Hilfe beim Aufbau und der Inbetriebnahme der MINIBALL Detektoren und deren Datenaufnahmesystem, sowie für die zahlreichen konstruktiven Diskussionen. Meiner gesamten Arbeitsgruppe gilt Dank für die zahlreichen fachlichen Gespräche, Ratschläge und Anmerkungen und für die freundliche und angenehme Arbeitsatmosphäre. Ganz besonders danke ich Herrn Dr. Herbert Hess und Herrn Dr. Jürgen Eberth für viele anregende Diskussionen und konstruktive Hilfestellungen. Ich danke auch insbesondere Herrn Konrad Arnswald, Herrn Rouven Hirsch, Herrn Levent Kaya, Herrn Lars Lewandowski, Herrn Michael Queiser, Herrn Burkhard Siebeck, Herrn Tim Steinbach und Herrn Andreas Vogt für die enge Zusammenarbeit, Hilfe und Unterstützung in vielen Projekten und Experimenten. Ich danke weiterhin Herrn Dr. An-

drey Blazhev und Herrn Dr. Karl-Oskar Zell für die Herstellung der Targets für das von mir durchgeführte Experiment an der HIE-ISOLDE Einrichtung am CERN bei Genf. Ich danke der Feinmechanikwerkstatt des IKP unter der Leitung von Herrn Stefan Thiel und der Elektronikwerkstatt des IKP unter der Leitung von Herrn Christoph Görgen für die großartige Zusammenarbeit. Ein ganz besonderer Dank gilt meinen Eltern und Großeltern sowie meiner Frau, die mich auf meinem Weg durch das Studium begleitet und unterstützt haben.

---

Diese Arbeit wurde finanziert von dem European Union's Horizon 2020 Forschungs- und Innovationsprogramm mit der Nummer 654002. Des Weiteren wurde die Arbeit finanziert vom Deutschen Bundesministerium für Bildung und Forschung unter der Vertragsnummer 05P15PKCIA und 05P2015.

---

# Eidesstattliche Erklärung

Ich versichere, dass ich die von mir vorgelegte Dissertation selbstständig angefertigt, die benutzten Quellen und Hilfsmittel vollständig angegeben und die Stellen der Arbeit – einschließlich Tabellen, Karten und Abbildungen –, die anderen Werken im Wortlaut oder dem Sinn nach entnommen sind, in jedem Einzelfall als Entlehnung kenntlich gemacht habe; dass diese Dissertation noch keiner anderen Fakultät oder Universität zur Prüfung vorgelegen hat; dass sie – abgesehen von unten angegebenen Teilpublikationen – noch nicht veröffentlicht worden ist sowie, dass ich eine solche Veröffentlichung vor Abschluss des Promotionsverfahrens nicht vornehmen werde.

Die Bestimmungen der Promotionsordnung sind mir bekannt. Die von mir vorgelegte Dissertation ist von Prof. Dr. Peter Reiter betreut worden.

**Teilpublikationen:** keine

Köln, den 28. Mai 2018

---

Dawid Rosiak



# Curriculum vitae

## Persönliche Daten

Name: David PawełRosiak  
Anschrift: Kohlsberger Starße. 50  
42657 Solingen  
Geburtsdatum: 29. November 1988  
Geburtsort: Solingen  
Eltern: Pawel Rosiak  
Krystyna Rosiak, geb. Wieczorek  
Nationalität: deutsch, polnisch  
Familienstatus: verheiratet, 1 Kind

## Hochschulstudium und Promotion

ab 2015 Promotion an der Universität zu Köln  
im Fach Experimentalphysik  
2012-2014 Studium der Physik an der Universität zu Köln  
(M.Sc. Physik)  
2009-2012 Studium der Medizinphysik an der Universität Düsseldorf  
(B.Sc. Physik)

## Arbeitsverhältnisse

ab 2015 Wissenschaftlicher Mitarbeiter am Institut für Kernphysik  
der Universität zu Köln  
2013-2015 Studentische Hilfskraft am Institut für Kernphysik  
der Universität zu Köln

## Schulbildung

1999-2008 ehem. Städtische Gesamtschule Solingen, seit 2015/2016 Alexander-  
Coppel-Gesamtschule, Solingen  
1995-1999 Städtische Grundschule Klauberg, Solingen